Rapid analytical methods based on colour change reactions

Shane O'Neill

Thesis submitted in Accordance with the Requirements for the degree of

Doctor of Philosophy

Dublin City University

Ollscoil Chathair Bhaile Átha Cliath

School of Chemical Sciences

Supervisor: Dr. Dermot Diamond

November 1998

Declaration

I hereby certify that this material, which I now submit for assessment on the programme of study leading to the award of DOCTOR OF PHILOSOPHY is entirely my own work and has not been taken from the work of others save and to the extent that such work has been cited and acknowledged within the text of my work.

Signed: 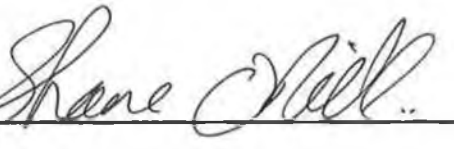 ***I.D. No. 95970801***

Dublin, 5th of November 1998.

For my parents and family.

For Ingrid.

Acknowledgements

I must acknowledge all the help and advice (And otherwise) I received from many many people while I was working on this thesis. I offer my sincerest thanks to each and every one.

- I want to thank my parents and family who supported me throughout my studies and for showing me the true path whenever I wandered. Without their help and guidance, this work and thesis would surely never have been finished.
- I must also thank everyone in 31 Woodcliff Heights for welcoming me each time (And there were many!) I called. A thanks also for showing me that family can extend beyond far beyond where you live.
- A most sincere and heartfelt thanks to Ingrid Leister. By just being there, and accepting when things were tough, constantly encouraging me an providing so many loving hugs.
- Thanks a million to a very energetic and considerate supervisor, Dr. Dermot Diamond. His help and trust has allowed so much of this work to be completed (or even attempted). His common sense and professionalism has shown me that scientists can be businessmen too. A sincere thank you for the freedom to imagine.
- I must thank John Fleming, Alan Farrell, Damien Lynch, Paul 'Coca Cola' , Brian (BOS) O'Sullivan, Graham Pidgeon, Yvonne Birney and others too numerous to mention for their willingness to listen an incredible amount of crap over coffee. Sometimes at least.
- Thanks also to the inhabitants of J207 and WG30(Both past and present), Patxi, Suzanne, Paddy (You call that music?), Darren (You call that hair?), Teresa, Tom, Fran 'The Man', Aogán, Brendan, Gaelle, Michael, Margret (G'day) and Kieran. Not only did they provide many opportunities for celebrations (Such as being Friday), they all offered genuine advice and guidance whenever any problems were encountered.

- Many thanks to the incredibly professional and underrated technicians in the School of Chemical sciences in DCU. Special thanks to Mick Burke, Maurice Burke, Ann Tinsley, Veronica Dobbyn, Ambrose and the effervescent Damien McGuirk.
- Thanks to Tony McKervey and everyone in his synthetic group in Belfast for synthesising many of the compounds used in this work.
- Thanks to the mechanical engineering technicians for machining the flow cells used.
- I would like to thank Dublin Bus (Formerly of C.I.E.) for making sure that each and every journey to work was an exciting adventure. I appreciate their attempt at dynamic timetables.
- Thanks to John Quinn and Aidan Doyle for collaborations and sharing ideas. Thanks also to Colm McAtamney for trusting me with his documents (And for being patient waiting for their return).

Contents

Figures

Tables

1 Overview

1.1 Ion-selective opt(r)odes

Optodes (or optrodes) are sensors whose optical properties change in some way in proportion to a change in the concentration of a target species (analyte). They consist of a membrane/film containing a receptor, which selectively binds with the target analyte. This binding is transduced optically. Typically the optical response is a change in an absorption spectrum or fluorescence spectrum but can also include other phenomena such as refractive index changes.

As the name implies, ion-selective opt(r)odes (optodes from here on) are optodes which exhibit a selective optical response to certain ions. While the vast majority of optode systems measure ions, some key optodes also measure neutral species such as amines and ethanol.

Optodes can be thought of as consisting of two types, those which respond to changes at the membrane: sample interface[1-5], and those which respond to changes in the bulk of the membrane[6-9]. The different features of these two types of optodes are discussed in the following sections.

1.1.1 Interfacial response optodes

Interfacial response optodes respond to changes at the sample: membrane interface. Examples of this type include those reported by Wolfbeis et al[1] in which a potential-sensitive dye (rhodamine C-18) incorporated into the membrane phase remains at the interface between the membrane and the aqueous solution. As the boundary potential increases due to the selective extraction of metal ions into the membrane, changes in the electronic structure of the potential sensitive dye occur and a change in the fluorescence emission is observed. Valinomycin was used as the ion-selective ligand in this case, resulting in a potassium selective optode. The membrane consists of two regions corresponding to the two moieties of the arachidic acid support after organisation into the bilayer structure shown in Figure 1.1. Lifetime of these potassium selective membranes was problematic, however, with approximately 5% loss per hour of the fluorescence signal occurring after several days use. Sensitivity was also quite poor with approximately only 10% reduction in fluorescence as maximum response. A similar system by the same authors, selective for calcium, using ETH 1001 (a commercially available calcium ligand) as the ion-selective ligand exhibited greater sensitivity than the potassium optode[2]. One of the limitations of this approach to optode measurements is the fact that, contrary to most optical systems, a reference membrane is required to distinguish the ion-selective response induced by the ion-selective carrier from responses due to non-selective ion diffusion into the membrane phase. Both indicator and reference membranes exhibit significant responses, and only the difference between them is due to a selective extraction of ions. Sensitivity has been improved by changing matrix from 1-octadecanol to PVC and using ionic additives within the membrane such as tetraphenyl borate anions[3]. The effect of the changing of membrane support results in a much more sensitive system as the matrix is much less hydrophilic (bis-2-ethylhexyl sebacate as plasticiser) and thus there is significantly less diffusion of non-complexed ions into the membrane. Also, the fluorescence signal generated by such potential sensitive dyes is far greater in a very lipophilic matrix such as bis-2-ethylhexyl sebacate. In addition, as non-selective ion

extraction is much reduced in the PVC plasticiser matrix, the difference between the reference membrane and the indicator membrane is greatly increased. The incorporation of the lipophilic anionic additives into the membrane results in a different response mechanism from those obtained previously and the mechanism of the signal generation is as yet unknown but is thought to involve micro-emulsions formed by aggregation of the anionic site, potential sensitive dye and ion-selective ligand within the membrane.

Similar work has been reported by Ishibashi et al for potassium and ammonium using acridine orange as the potential sensitive dye[4,5]. The sensors exhibited a good sensitivity (approx 35% reduction in fluorometric signal maximum) and lifetimes were of a similar magnitude to those reported by Wolfbeis et al. The addition of long alkyl chains to the indicator molecule (acridine orange) resulted in much increased lifetimes over those initially reported by this group. The method of operation here is due to the difference in polarity of the indicator molecule. It is thought that the acridine moiety of the indicator exists within the membrane phase. As the amount of ions entering the membrane increases, and thus the positive charge within the membrane increases, the indicator moiety leaves the membrane phase, with the alkyl chains present preventing complete solvation in the aqueous phase. Since the fluorescence of the acridine moiety in aqueous medium is only 2.5% of that in the PVC membrane phase, the drop in fluorescence of the membrane accompanying the relocation of this moiety is used as an indication of ion extraction. Polynactin was used as ionophore for ammonium and valinomycin for potassium.

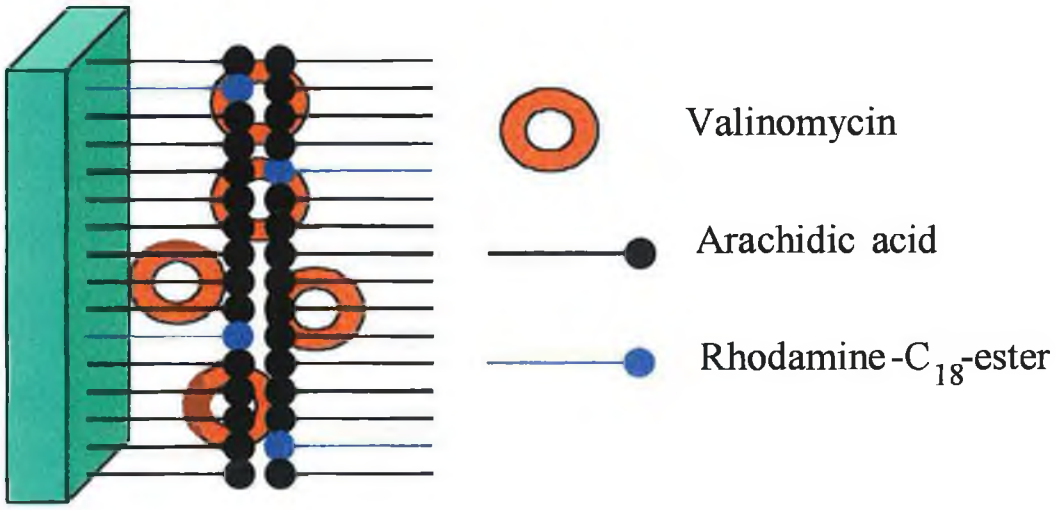

Figure 1.1: Diagram of the structure of the interfacial potential-sensitive optode reported by Wolfbeis et al.

1.1.2 Bulk response optodes

Walt et al.[6] reported a bulk optode for penicillin in which a pH dye was immobilised within a membrane phase along with an enzyme (Penicillinase). Working on the principle that the product of the penicillin-penicillinase reaction is a proton (H^+), the system responded to changes in penicillin concentration by means of the associated pH optode. However, due to the method of operation, not only is the pH of the sample buffer important, but also the buffer capacity, as this can have a dramatic effect on the sensitivity by masking the pH changes within the membrane phase. Polster et al.[7] outlined another approach to optical penicillinase measurement with a reverse-phase optode (Where components dissolved in an aqueous film are used to sense changes in organic solvents) which exhibits very fast response times (ca. 10 seconds). Again, pH and buffer strength must be carefully controlled.

Simon et al.[8] have described the principles and mechanism of ion-selective optodes, based on work published earlier by the same group[9]. This class of sensor consists of a plasticised PVC membrane with three main components, an ion-selective ligand, a pH indicator and a lipophilic anion (Figure 1.2). Some of the features of this class of optodes include

- All active components are lipophilic, entrapped in a lipophilic membrane phase which is assumed to be homogenous in composition.
- The membranes respond to the activity of the ions of interest. This is an important factor as, unlike concentration, the activity coefficient is dependent on the ionic strength of the solution.
- The ion-sensing agent within the membrane phase is separate from the optically responsive agent. Coupling between the two reactions is brought about by the maintenance of electroneutrality within the membrane phase.

It is clear from this description of membrane response mechanism that the concentration ratio of the active components to each other is crucial in creating a reliable and stable sensor, and therefore loss of components from the membrane into the aqueous solution cannot be tolerated. The lipophilicity of the membrane components was quickly targeted as an extremely important factor in determining the lifetime of these sensors[10]. Simon et al. investigated the effect of various components within the membrane on the lifetime of the systems. A result of this was the discovery that the characteristics of the plasticiser (which makes up 66% of the membrane) is crucial. The lifetime of the membrane is dependent on the partition coefficient of the key components between the aqueous phase and the organic membrane phase (i.e. the plasticiser). The lipophilicity of the membrane is assumed to be roughly equal to that of the plasticiser and so it seems reasonable that the more lipophilic the plasticiser the longer the lifetime of the system. However, as the lipophilicity (and also the viscosity, typically due to long alkyl chains present) of the plasticiser increases above log P ~ 20 then the diffusion of the components is limited[11] and longer response times result. Since leaching from the membrane phase to the aqueous phase can never be totally prevented, covalent immobilisation of some of the key membrane components was attempted. Simon et al.[12] investigated the effect of covalent immobilisation of different components within the membrane. The key findings were that very similar responses between the covalently immobilised system and the normal system albeit with greatly increased response times. While the membrane thickness can be reduced to yield faster responses (due to diffusion-limiting processes), the membranes cannot be made infinitely thin, as plasticiser leakage becomes an important issue below 1 μm thickness. Related to this is the problem of a reduced pathlength resulting in reduced absorption signals. The length of the covalent spacers were found to be important as regards immobilisation of the indicator dye while immobilisation of the anionic site gave rise to slight peak splitting in the absorbance spectrum of the pH dye. The dye also exhibited a smaller extinction coefficient and a slightly shifted absorbance maximum with this scheme.

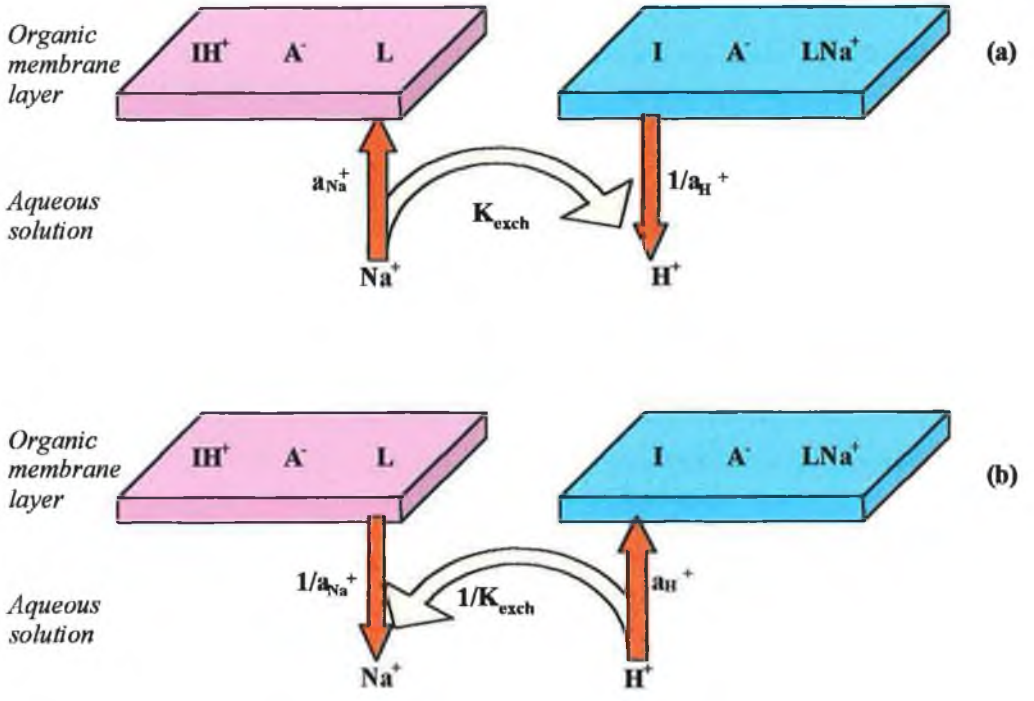

Figure 1.2: Schematic representation of the process involved in (a) deprotonation of the membrane and (b) protonation of the membrane. I represents a lipophilic pH dye, A represents a lipophilic anionic site while L represents a lipophilic ion-selective ligand. $a_{H}+$ and $a_{na}+$ represent the aqueous activities of protons and sodium respectively. K_{exch} is proportional to a_{Na+}/a_{H+}.

Simon et al defines equations describing membrane response and the theory and assumptions behind them. The main assumptions in the derivation of this theory are as follows.

1. Solid support. The membrane layer is exposed on one side to the sample solution and on the other to a solid support. The support is assumed to be chemically inert and impermeable for all species involved.
2. Equilibrium. The optodes as discussed are reversible equilibrium systems. At equilibrium there are no concentration gradients either within the membrane or the sample. No membrane components can be present in the sample and all analyte within the membrane phase is completely complexed by the carrier.
3. Impurities. Impurities within the membrane are not considered to play any part in the response mechanism.
4. Interface. The size of the interfacial region is assumed to be only a small fraction of the membrane thickness.
5. Stoichiometry. It is assumed that the stoichiometries of complexes and equilibria involved do not change over the range of analyte measurement.
6. Activity coefficients The activity coefficients of the membrane components are assumed to be either unity or constant at all times.

Response characteristics of optode membranes include a variable sensitivity of the membrane i.e. sensitivity is not constant over the measuring range and at no time is the response truly linear. The response time also varies with activity of the primary ion, with longer response times occurring at lower activities.

Even with these constraints, many improvements can yet be made. The pH dye is a very important part of this type of sensor, as the characteristics of the other components are well understood from extensive use in ion-selective electrodes. Simon et al. report the synthesis of several different lipophilic pH dyes for use in these sensors. A point of note is the change in response characteristics of the membranes when incorporating dyes of differing pK_a. An increased affinity for

protons allows the membrane to remain protonated in higher pH solutions and/or higher ion activities. The result is a sensor with a higher limit of detection or a sensor with the same limit of detection but operating at a higher pH. The opposite effect is seen if the dye has a low affinity for protons. Bakker et al.[13,14] report a method where different dyes are used for the determination of selectivity coefficients where no such measurement would ordinarily be available. They also report on the ability to shift ion-selective optode responses to very low levels by careful selection of membrane composition (pH dye in particular) and pH. By incorporating dyes with different pK_as, the authors were able to perform measurements at different pHs, and through the equations defined by Simon et al, calculate back to the original membrane composition and pH to estimate membrane responses at very low levels. One drawback of this is the resulting response times of ca. 30 hours for a nanomolar sample. The reason for this long response time is most likely due to depletion of the analyte from the membrane/ sample interface.

The lipophilicity of these pH dyes is paramount, with UV stability, extinction coefficient, pK_a and general chemical stability all being important factors in choosing the right dye.

1.1.2.1 Effect of permittivity of the plasticiser

In a simple two phase system (organic and aqueous layers) the ability of any given ion to transfer from aqueous medium to lipophilic is affected by the difference in permittivity between the two media[15] (Equation 1.1 to Equation 1.3[16]). Equation 1.3, estimates the effect of permittivity (Fm^{-1}) on the solvent's ability to discharge the charge of an ion's surface. The work performed in this operation is given in equation 1.1. The non-charged ion is then transported into the second solvent (organic phase) where no work is lost or gained. Once in the second solvent, the work required to re-establish the ion's surface charge is given in equation 1.2. Since the permittivity, ε, of most plasticisers is much less than that of water (Permittivity of dioctyl sebacate ε_{DOS}=4.8, Permittivity of water ε_{water}=78.4) and

taking equation 1.3 into account, the energy associated with solvation within a medium of low permittivity is greater than that of a medium of higher permittivity[17]. The probability of a free ion entering an organic phase can thus be estimated in part by the difference in solvation energies between the two solvents. In contrast, ions complexed by the ion-selective ligand do not require solvation and as such the energies required are smaller. It follows then that in membranes with low permittivities the ion-selective ligand dominates the ion-transport into the membrane.

$$w_1 = \frac{1}{4\pi\varepsilon_0 r_i}\int_{z_i e}^{0} q\,dq = \frac{(z_i e)^2}{8\pi\varepsilon' r_i} \qquad \textbf{Equation 1.1}$$

$$w_2 = \frac{1}{4\pi\varepsilon_0 r_i}\int_{z_i e}^{0} q\,dq = -\frac{(z_i e)^2}{8\pi\varepsilon'' r_i} \qquad \textbf{Equation 1.2}$$

$$\Delta G_{s,i} = N_A(w_1 + w_2) = -\frac{(z_i e)^2 N_A}{8\pi r_i}\left(\frac{1}{\varepsilon'} - \frac{1}{\varepsilon''}\right) \qquad \textbf{Equation 1.3}$$

where e_0 is the permittivity of a vacuum, r_i is the radius of the ion, q is the charge of the ion which varies during discharge, z_i is the nominal charges of the ion, e is the elementary charge of a proton and ε' and ε'' are the permittivities of water and plasticiser respectively, $\Delta G_{s,i}$ is the change in Gibbs free energy for the transfer, N_A is the number of molecules involved and w_1 and w_2 are the work done when transferring from water and to plasticiser respectively.

In membranes with low permittivities, the free ion activity within the membrane is greatly suppressed and ion-pairing is favoured. This is shown to be true in bulk optodes given the unusually high solubility of tetraphenyl borate anions within the membrane phase[18]. Ordinarily, the lipophilicity of these compounds is not sufficient to allow prolonged use, but the observed lipophilicities of these species within the membrane suggests strongly that they are ion-paired at all times with the more lipophilic ion-selective ligand or pH dye[18]. An equation defining the

relationship between the association constant for solvents and the permittivity is given in Equation 1.4

$$\ln K_{ass} = \ln\left(4\pi N_A a^3\right) - \frac{z_i z_k e^2}{4\pi kTa}\frac{1}{\varepsilon} \qquad \textbf{Equation 1.1.4}$$

where K_{ass} is the association constant, N_A is the number of molecules involved, a is the minimum approach distance of the ions, z_i and z_k are the charges of the two oppositely charged ions, e is the elementary charge of a proton, k is the Boltzmann constant, T is the temperature (Kelvin) and ε is the permittivity of the relevant solvent.

The linear relationship between K_{ass} and $1/\varepsilon$ has been shown experimentally, but with some exceptions. There are also some assumptions such as all ions being perfectly spherical, that the dielectric constant in the vicinity of the ions is identical to the bulk, and the effect of solvation of the ions during formation of ion pairs id not considered.

1.1.2.2 Target markets

With so many particular features and characteristics, the preferred target market for the commercialisation of such sensors has been identified as being the one-shot sensor, most likely for the clinical market[19]. The optimum pH of 7-8 for most optodes of this type, the short lifetimes in anything other than pure aqueous samples and the ability to measure some clinically relevant ions (potassium, sodium, calcium, lithium) serve to make these sensors most suited to this market. Again, membrane lifetime is recognised as the principle reason against such sensors being used in continuous or long-term sensor applications.

1.2 Sensor applications

1.2.1 pH sensing

pH measurement via optical methods has been of particular interest for a number of years. Hartmann et al.[20] outline the possibilities and limitations of such pH measurements with both fluorometric and absorbance transduction. Problems associated with optical pH measurements include the following.

- Physical and chemical interferences. In many pH sensors, the ionic strength of the sample being measured has an influence on the sensor response. While the activity of protons will change in a defined manner with changing ionic strength, unaccounted changes in the membrane matrix result in the sensor generating signals which deviate from the expected. Work reported by Wolfbeis et al.[21] demonstrates a pH sensing system which is sensitive to ionic strength changes when the support is non-charged, but is relatively unaffected by ionic strength when the support is highly charged.
- Dynamic range. The indicator in many types of pH optode is an acidochromic dye. The dynamic range of these devices is generally limited to a restricted pH range determined primarily by the pK_a of the dye used. Because of this, pH optodes are generally targeted at specific pH ranges, i.e. 6.5-8 for clinical measurements.
- Accuracy. Many pH optodes are based on evanescent wave interrogation via coated fibre optic cables. The propagation of the light through this medium is dependent on the angle of the fibre, and any bending of the fibre can induce loss of radiation and thus an accompanying change in the absorbance or fluorescence spectrum. Lehmann et al propose that changes of 1.45% of the signal are due to fibre bending, with only 0.56% and 0.22% resulting from light source fluctuations and ambient light respectively. This clearly illustrates the importance of fibre-bending on the accuracy of fibre optic pH sensors.

- Calibration. Due to the non-linear nature of the response of most pH optodes, two point calibrations which are possible with glass pH electrodes are not sufficient in these cases.
- Lifetime. As with many optode sensors, the lifetime of the sensor is problematic due to leaching of the active components from the membrane phase to the sample phase. Because of this, considerable work has been done on immobilisation of the sensing groups within the membranes. Because of the bulk response of these optodes, the membrane thickness is crucial in determining the response time of the sensor. Thinner membranes result in rapidly responding optodes, but with reduced lifetimes due to leaching.

Despite these obstacles, optical pH sensors have been developed for a variety of purposes including gastric measurements[22], gastro-oesophageal measurements[23], high pH values[24], low pH values[25], intermediate pH values[26], and general physiological use[27]. None of these sensors solve all of the problems listed above but rather accept their limits and target areas and applications where these limitations are not crucial. Suzuki et al. outline the possibilities of using pH optodes in flow systems[28].

An extension of this method for pH measurement is the ability to couple a pH optode to another system whose response does not generate an optical signal. For example, Wolfbeis et al report an optode with an enzyme layer (urease). As the enzyme-substrate reaction generates protons, the course of the reaction can be monitored with a pH sensitive optode (Equation 1.1.5). The sensor measures the production of protons generated when the enzyme urease converts urea to ammonia. Thus, the sensor is measuring the reaction of the urease enzyme, which is taken as an indicator of the concentration of urea within the sample.

$$H_2NCONH_2 + 2H_2O + H^+ \xrightarrow{\text{urease}} 2NH_4^+ + HCO_3^-$$

Equation 1.1.5: Reaction scheme proposed by Wolfbeis et al. for monitoring of urease activity by monitoring the production of protons.

1.3 Bulk membrane components

1.3.1 pH Dyes

The pH dye used in these systems can have a very important effect on the overall membrane response. It is the dye which, after all, determines the magnitude of the membrane signal, and also the effective pH range of the device. It is no surprise therefore that many different pH dyes have been investigated for use in these systems. Simon et al[29]. have synthesised and characterised a range of neutral carrier pH dyes (Figure 1.5) including N,N- diethyl-5-(octadecanoylimino)-5H-benzo[a]phenxazin-9-amine (ETH 5294, Dye ETH1), N,N-(diethyl)-5-[(2-octadecyl)imino]-5H-benzo[a]phenoxzain-9-amine (ETH 5350, Dye ETH2) and 11-[(1-butylpentyl)oxyl]-11-oxoundecyl 4-{[9-(dimethylamino)-5H-benzo[a]phenoxazine-5-ylidene]amino}benzeneacetate (ETH 2439, Dye ETH3). These three dyes have proven very popular as indicators in optodes because of their high lipophilicities and very high molar absorption coefficients (All three dyes presented have molar absorption coefficients of in excess of 70,000). Their structures and basicities are shown in Figure 1.5. The reason for the differences in the pK_a of the different dyes can be explained by means of the ability of the nitrogen to donate electrons. While a π-conjugated system is rich in electrons, it is essentially an electron withdrawing group, reducing the electron density at the protonation site. All three dyes have alkyl chains present at the site of protonation, which are electron donating. The degree of the electron donating nature is proportional to the length of the chain, and thus ETH 2439, which has only methyl groups present has a lower basicity than the other two which have ethyl chains.

A feature common to these dyes presented is that they are not very photo-stable especially in the presence of low wavelength radiation (100-300 nm) and oxygen. Careful storage and experimental arrangement is often required in order to prolong lifetimes[29]The same group also showed that the lipophilicity of the dyes

decreases significantly when protonated as they then have an overall positive charge. As a result, the lifetime is also dependent on pH. None of the dyes synthesised managed to exhibit lipophilicities above the desired minimum in both protonated and deprotonated forms. The minimum lipophilicity of $\log k \geq 9.3$ was calculated as a minimum lipophilicity required to allow only 1% decrease in absorbance over 1 month in a 2 μm thick membrane. More recently, Spichiger et al[30]. have developed a new group of pH dyes for pH sensing. The design of long wavelength absorbing dyes has become particularly interesting due to the recent development of long wavelength laser diodes allowing the production of very affordable, compact instruments[31,32,33]. Other methods also exist to allow measurements to be made in the long wavelength region, namely fluorescence resonance energy transfer (FRET)[34,35] and the inner filter effect[36] . Both of these methods allow the signal from an indicator dye to be shifted from fluorescence to long wavelength fluorescence. The method of operation is similar in both cases. Two dyes are incorporated into the membrane phase. Either one or both of these can be fluorescent. The first dye is responsible for interacting with the equilibrium state of the membrane much the same way as described by Simon et al above. The second dye, whose excitation band overlaps with the first dyes emission (or absorbance) peak, does not change its fluorescent state. Instead, it is dependent on the emission of the first dye for excitation. In this way, the emission of the second dye at longer wavelengths can be used as the indicator (Figure 1.3).

Fluorescence resonance energy transfer is a radiationless method of energy transfer between two molecules which allows an excited electron to transfer between two molecules. Because of this, the two chromophores must be homogeneously dissolved in the same medium as a FRET process can occur over a maximum distance of ca. 40 Å. The Inner filter effect operates by means of the simple fact that the radiation fluoresced by the fluorophore is re-absorbed by the pH dye (Figure 1.4). Because of this, the two chromophores do not have to be in such close proximity as in the case of FRET.

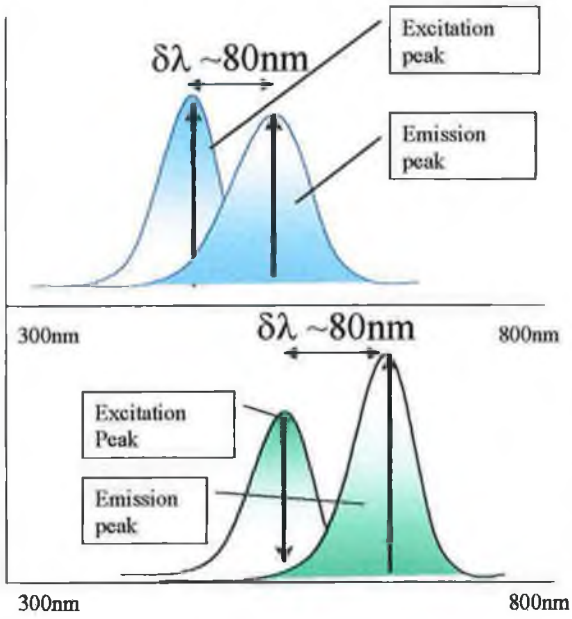

First fluorophore. This fluorophore partakes in the equilibrium system of an ion-selective optode as described previously. Its fluorescence is dependent on the state of equilibrium within the membrane.

Second Fluorphore. The greater the fluorescence from the first fluorophore, the greater the excitation of this molecule, and thus the greater the long-wavelength emission.

The excitation peak of the first fluorophore and the excitation peak of the second fluorophore overlap to a large extent.

Figure 1.3: Schematic of the relative dye/wavelength relations required for the inner filter effect. The example shown here is for the fluorescence/fluorescence model

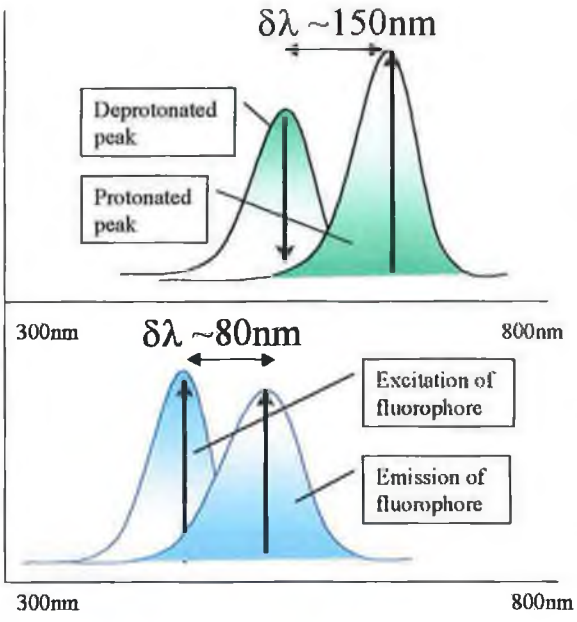

pH indicator, protonated and deprotonated forms interchange. The greater the absorbance peak, the less radiation is transmitted.

Fluorescent dye, as the light exciting the fluorophore increases, so does the emission. The fluorophore is not pH sensitive.

The protonated peak of the pH indicator and the excitation peak of the fluorophore overlap to a large extent.

Figure 1.4: Schematic of the relative dye/wavelength relations required for the inner filter effect. The example shown here is for the mixed fluorescence/absorbance model.

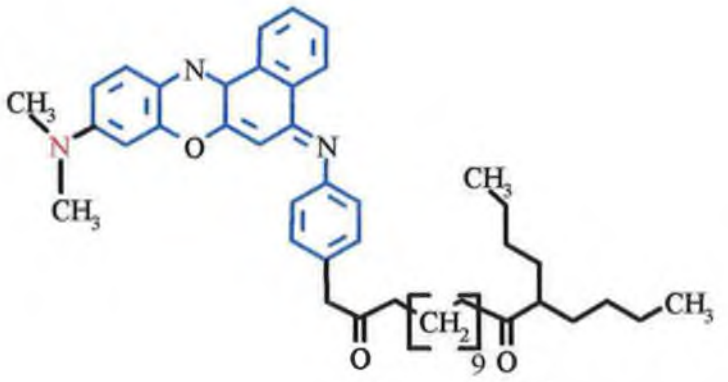

Dye 1a (ETH 2439) pK_a 8.3

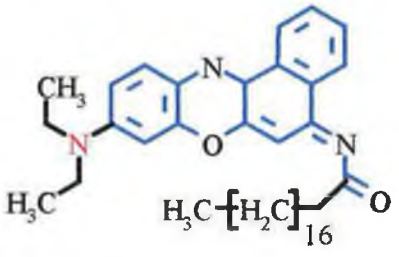

Dye 1 (ETH 5294) pK_a 10.6

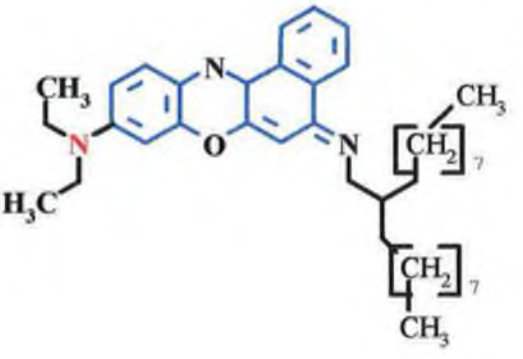

Dye 1b (ETH 5350) pK_a 11.4

Figure 1.5: Structures of pH dyes synthesised by Simon et al. Blue hghlights the π conjugated system responsible for the absorbance properties of the dye, Red highlights the site of protonation within the dyes.

1.3.2 Anionic Site (Ion-exchanger)

Within an ion-selective optode membrane, the anionic site is responsible for providing and controlling the amount of negative charges present within the membrane phase. When either the ion-selective ligand or the pH dye become positively charged through complexation/protonation respectively, it is the role of the anionic site to provide lipophilic negative charges within the membrane to allow these positively charged species to exist without residual charge build-up.

Traditionally (in ion-selective electrodes) tetraphenyl borates have been used to provide this function (Figure 1.6). However, the tetraphenyl borate employed in ISEs for many years has some serious limitations when used in ion-selective optode membranes. The tetraphenyl borate compound undergoes an acid catalysed degradation to yield neutral benzene and a neutral triphenyl borate (Figure 1.7). Because this results in the removal of the negative charges from within the membrane phase, it limits the ability of the membrane to respond. In order to maintain charge balance, a portion of the neutral dye molecules will no longer be able to be protonated. To correct for this, several more stable tetraphenyl borates are now available with much reduced susceptibility to acid-catalysed degradation such as Anionic site b in Figure 1.6. The increased amount of electron withdrawing groups within the aromatic system results in more charge delocalisation from the central boron atom, and therefore, the acid catalysed attack shown in Figure 1.7 becomes less favourable.

While lipophilicity is crucial for both the ion-selective ligand and the pH dye, even sparingly lipophilic anionic sites seem to work well when incorporated into ion-selective optode membranes. It is postulated that this is due to the formation of ion pairs within the membrane phase between the anionic site and the lipophilic ion-selective ligand or the pH dye.

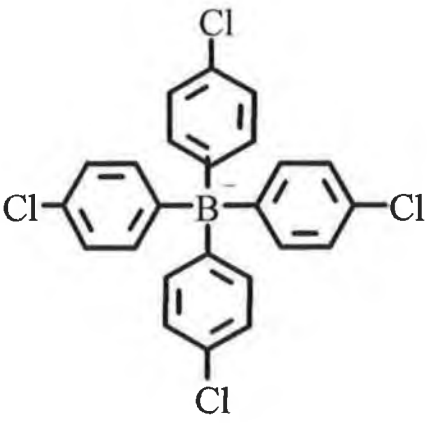

4-chloroplenyl Borate

A

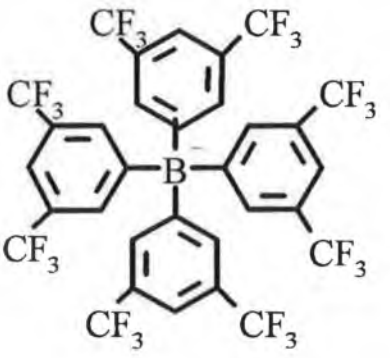

3,5 Trifluoromethylphenyl Borate

B

Figure 1.6: Some structures of anionic sites used in the literature

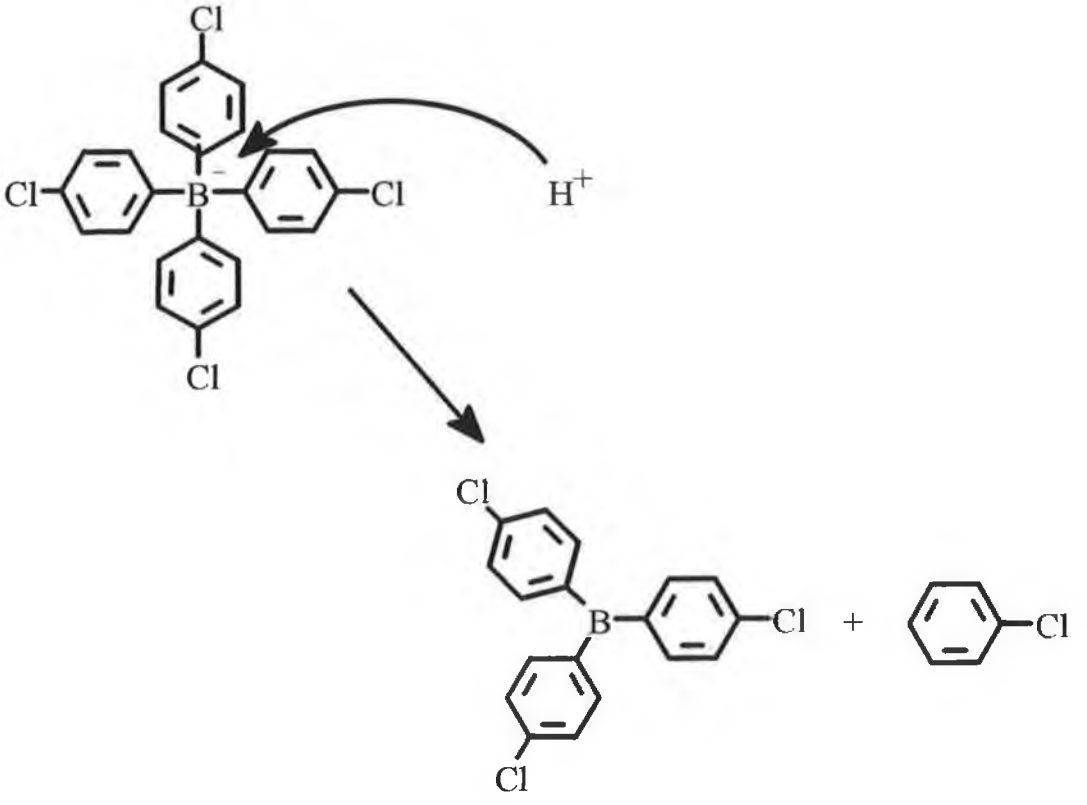

Figure 1.7: Acid-catalysed degradation of tetraphenyl borate

1.3.3 PVC support

The polyvinylchloride support gives the membrane mechanical strength so that thin films may be cast. It also provides a matrix for immobilisation of the lipophilic components within the organic membrane phase via the plasticiser. Modified PVCs such as carboxylated PVC and hydroxylated PVC have been used for membrane support either to provide inherent anionic sites or increase membrane adherence respectively.

1.3.4 Plasticiser

The plasticiser is added to allow the PVC membranes to reduce the glass transition temperature (Tg) to around –20°C. This results in a flexible membrane at room temperature. Choice of plasticiser is important for a number of reasons. It is the plasticiser that determines what refractive index the membrane phase has, which is crucial when designing a membrane for use with ATR or evanescent wave techniques of interrogation.

The lipophilicity of the plasticiser must be sufficient to allow for a phase barrier between the membrane and the aqueous sample solution. A plasticiser of insufficient lipophilicity will allow rapid leaching of the lipophilic active components. The more lipophilic plasticisers generally have long non-polar chains and are quite viscous and therefore, a plasticiser of extreme lipophilicity is thought to inhibit diffusion through the membrane phase, and thus significantly increase response times.

Finally, since the plasticiser composes typically 66% of the membrane bulk, its innate ion-selective capabilities must be known. Certain plasticisers have been found to affect the extraction of certain ions. Because of this, certain plasticisers may or may not be suitable for targeting a particular ion.

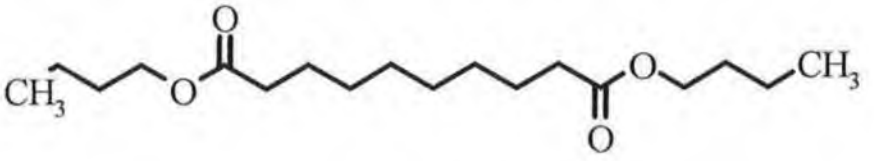

Dibutyl sebacate. Refractive index = 1.441

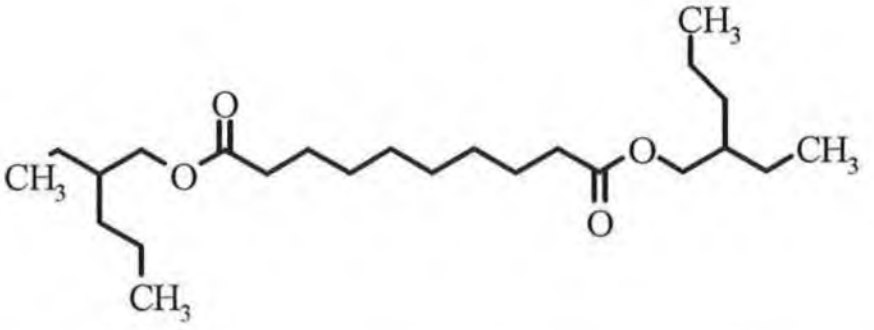

Bis 2-ethylhexyl sebacate (Dioctyl sebacate). Refractive index = 1.450 ε=4.8

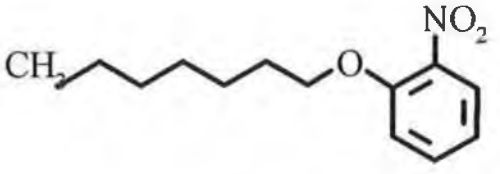

Nitrophenyl octyl ether. Refractive index = 1.511 ε=14

Figure 1.8. Structures of some commonly used plasticisers

1.4 Ion analysis applications

The advanced stage of pH optode development and pH dye synthesis and characterisation has undoubtedly been a factor in the development of ion-exchange optode systems as described by Simon et al[8,9]. The same group has reported a calcium-selective membrane using ETH 5294 as the indicator dye[37]. It operates by the method of cation-exchange described elsewhere[38]. Other optodes employing the same exchange mechanism have been reported for thiamine[39], zinc[40], sodium[41,42,43,44,45,46], silver[47,48], potassium[46,49,50], calcium[46], chloride[46], chiral enantiomers[51], ammonium[52,53] and lysine[54]. Theoretically similar ion coextraction membranes have also been prepared for hydrogensulfite[55], sodium[56], potassium[57], calcium[58], heavy metals[59] and anions such as chloride[60].

1.5 Calixarenes

Calixarenes are a group of macrocyclic oligomers consisting of the general structure shown in Figure 1.9. The word calixarene itself is derived from the Greek word 'calix' meaning a vase or chalice. This description relates to the ability of the calixarenes to act as a host for ions within a non-polar environment[6162]. The number of units within the ring of a calixarene is stated by placing [n] in the name, i.e. Calix[4]arene is a four-unit calixarene.

A wide variety of calixarenes exist which exhibit selective responses to many different ions. This variety is made possible due to the relatively simple chemical modification pathways available[63646566] and the pre-organised cavity ideally disposed to encapsulating ionic or neutral guests. Many different functional groups have been used in conjunction with these compounds, each giving rise to slightly different ligand properties. The nature of these groups in conjunction with the cavity size of the calixarene dictated by the number of repeating units in the ligand combine to impart different ion recognition properties. The application of calixarene compounds to sensors has been comprehensively reviewed by Diamond and McKervey[67,68].

The size of the cavity of a calixarene ionophore has been shown to be very important in defining its selectivity. Ester-modified calix[4]arenes have been shown by Diamond et al. to be selective for sodium whereas similar calix[6]arene esters were caesium selective. This is related to the increase in ionic radius of the two respective ions, with sodium having an ionic radius of only 1.54 Å compared to caesium's 2.35 Å.

The cavity size of the calixarene is not the only factor in deciding the ion of preference. The chemical nature of the groups on the lower rim (pendant groups) has been shown to have a significant influence on the selectivity of the ligand. Studies performed by Diamond et al. show that in particular, calixarenes with ketone groups present in the pendant groups have significant preference for

sodium. It is proposed that a cation of the appropriate size interacts most strongly with the cavity defined by the negatively polar carbonyl oxygens and phenoxy oxygen atoms. This selectivity is not seen however when the carboxy groups are replaced by ether analogues. In this case, no particular ionophoric activity is observed. In a similar vein, when the ketone groups are replaced by esters, the response characteristics do not change significantly, indicating that the carbonyl groups are the single most important feature of the pendant group.

In another study on calixarenes designed to synthesise a suitable ionophore for extraction of lanthanides and actinides from nuclear waste, calixarenes with phosphine oxide groups were synthesised by McKervey et al. Many of these ligands have been shown to be superior thorium and europium extractants than existing structures. The effect of chemical modification is again evident in this case as McKervey et al. have shown that if the tertiary butyl groups in this ligand on the upper rim are replaced with hydrogens, the selectivity shifts from europium to thorium. The ligand has been shown to exist in a stable cone conformation (Figure 1.11 and Figure 1.10[a]). During screening experiments it was found however that ligand 5(a) presented in this work was in fact a reasonable calcium ionophore (Chapter 2, Figure 2.15), and Diamond et al. have shown that this ligand can be used to make excellent calcium-selective electrodes[69].

[a] Molecular modelling studies were carried out by P. Kane and D. Fayne, Dublin City University.

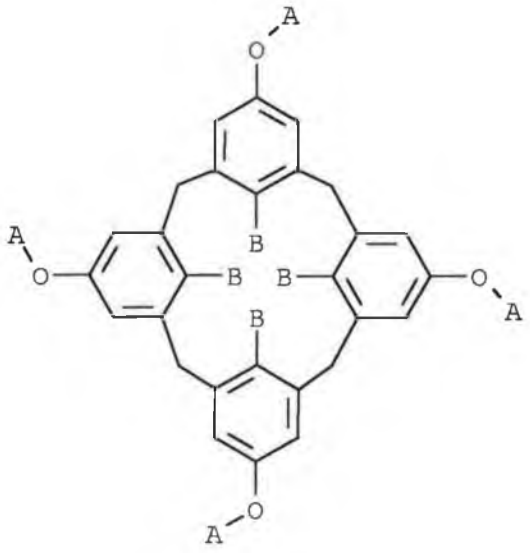

Figure 1.9: General structure of a calix[4]arene. A and B groups can be modified with the modified B generally consisting of either H of $C(CH_3)_3$ groups.

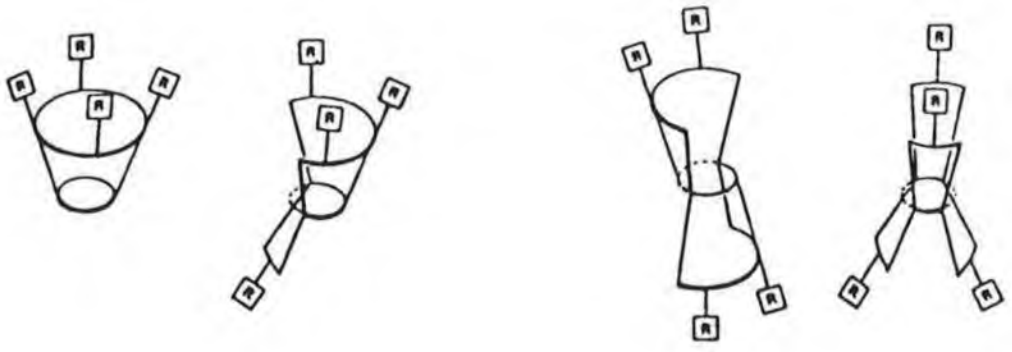

Figure 1.10: Four principle conformations of calixarenes proposed by Gutsche

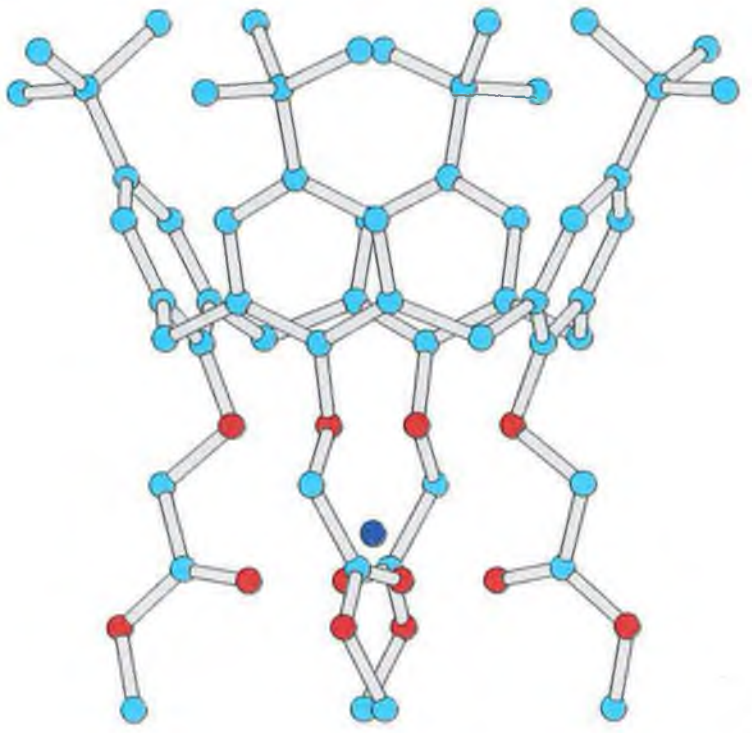

(a)

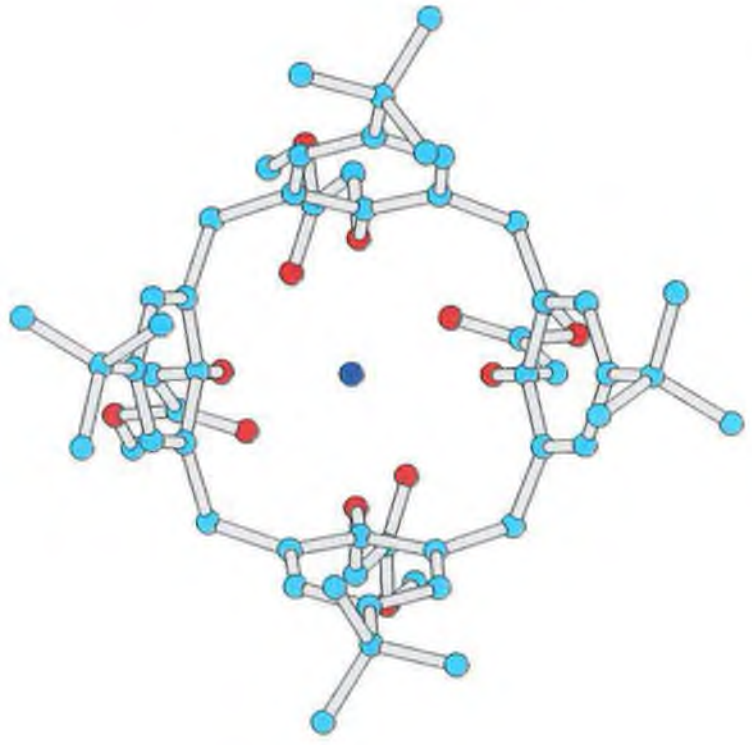

(b)

Figure 1.11: 3-D side-view (a) and top view (b) sodium ion: calixarene complex. This is an energy minimised structure of a tetramethoxyethyl ester calix[4]arene[70].

1.5.1 Chromogenic ligands

Even though the theory of operation of optode membrane systems is so well defined and understood, the neccessity to maintain constant component ratios within the membrane phase is perhaps the most significant limiting factor. With three different components in the membranes adhering to the model put forward by Simon et al., (ion-selective ligand, pH dye and anionic site) this can be very difficult to achieve in practice. Tóth et al.[71] have attached an azo dye to an existing sodium ion-selective ligand (Figure 1.12), with tridodecylamine as the counter species in the membrane. In this example, it is the ion-selective ligand which gives rise to any spectral properties the membrane may have, even though the response characteristics are the same as before and the same basic rules and equations apply[71]. The ligand with the azo dye incorporated shows good response in accordance with the theory of operation of these membranes, but the selectivity of the ligand is impaired by the effect of the chemical modification. The optode also seems to respond over a narrower range of activities, although for clinical analysis where accepted ranges are very small, this may not prove to be a problem. More recently, the same author has further refined this idea with a strongly absorbing, rapidly responding membrane, again incorporating a derivatised calix[4]arene[72]. Selectivity continues to be mediocre however. Similar work has also been carried out by Diamond et al. with respect to the analysis of lithium and sodium[73]. A different method for this, that should overcome the problem with decreased selectivity, was attempted by Sutherland et al[74]. In an attempt to create a chromogenic ion-selective ligand without reducing selectivity of an existing ligand, a group of chromogenic ligands were designed with the chromogenic moiety as an integral part of the recognition mechanism rather than an addition to an existing ligand. This helps to both prevent unforeseen effects on the ligand selectivity after incorporation of a chromogenic moiety and that the interaction between the recognition site and the chromogenic moiety is strong. Extensive use of molecular modelling was employed in this work.

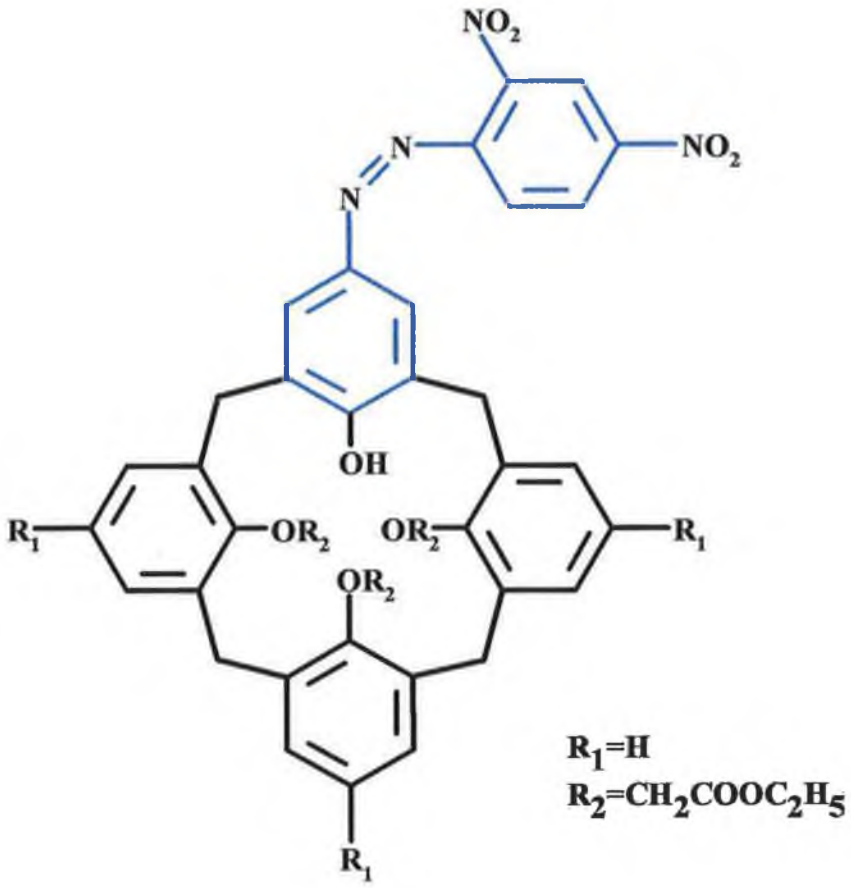

Figure 1.12: Structure of the chromogenic calix[4]arene reported by Tóth et al. The chromogenic moiety is highlighted in Blue.

1.6 LabVIEW

The development of the LabVIEW package and the idea of the virtual instrument (vi) began with James J. Truchard and Jeffrey L. Kodosky way back in 1984. The spur that set the ball in motion was the fact that a bias was becoming evident in the professional software market. Scientists had to slug it out with computer systems and programming languages in order to interface even the simplest of experiments to computer. Meanwhile businessmen and financial advisers had the following of a large group of software developers and were, using their latest commercially available spreadsheet software, able to draw up spreadsheets and the like in seconds.

The fact that commercial software developers obviously did not have the interest in the scientific area of the market, Kodosky and Truchard decided to redress the balance. They were both familiar with the concept of the virtual machine and were therefore also aware that its ease of use and flexibility would be invaluable in the process of making the scientists' and engineers' job that much easier. The real requirement, was to develop a truly friendly human-computer interface. Until then, even the best of the available programming languages required additional learning, training and familiarisation time. No longer would the users be required to be programmers to take advantage of their hardware.

LabVIEW (Laboratory Virtual Instrument Engineering Workbench) is a product from National Instruments for development of data acquisition systems incorporating real-time displays. Originally developed for the Apple Macintosh, it has since been ported to several other platforms including Power Macintosh, IBM PC, DEC Alpha systems and SUN Sparc stations. Its primary advantage over its competitors is its flexibility and ease of use. Using a totally graphical interface, the tiresome lines of obtuse code and functions are replaced by icons and pictures representative of their function. In this way debugging is made much simpler with data paths and types visible at a glance. This is where LabVIEW comes into its own. A program 'written' in LabVIEW by one programmer can

much more easily be understood than an equivalent line-based program. One of the features which allows this incredible user-friendliness is Object Oriented Programming (OOP).

Programming with LabVIEW is not like programming with traditional line-based systems. Programs written with LabVIEW are called Virtual Instruments (VIs). Instead a 'block diagram' must be constructed to create the code. This controls how the VI works. The whole thrust of the LabVIEW programming experience revolves around the manipulation and linking of icons representing whatever functions are required by the user. The icons are linked by 'wires' - software analogies of electronic wiring. An example of the front panel of a virtual instrument can be seen in Figure 1.13. The various buttons and displays, when added to the front panel, are automatically entered to the block diagram of the code (Figure 1.14). Here, these indicators can be updated, and the control states of the buttons read. For example, when a value is passed to the icon labelled 'Time' in Figure 1.14, the large numeric display in the right hand side of Figure 1.13 is updated instantaneously with that value. Conversely, if the button labelled 'Start' on the front panel (Figure 1.13) is pressed, the icon labelled 'Start' in the code is updated with the relevant true or false Boolean state. Other variables can be added to the block diagram if needed, but every item on the front panel is always represented in the code. A more detailed discussion can be found in Chapter 4.

Everything from addition functions to Fourier transforms to data acquisition operations is represented as icons, and data connected via wires on-screen. These wires are analogous to wires on an electronic circuit. Their size, pattern and colour allow the user to instantly determine what data type passed through them. Each publication incorporating LabVIEW documents the user-friendliness of the programming language to be a real asset in designing an interface to perform the purpose required by the scientist. The keywords used in these articles to describe the experience of having used LabVIEW are 'flexibility', 'rapid data acquisition', 'accurate', 'sensitive', 'user-friendly', 'robust', and 'rapid development'[75-93].

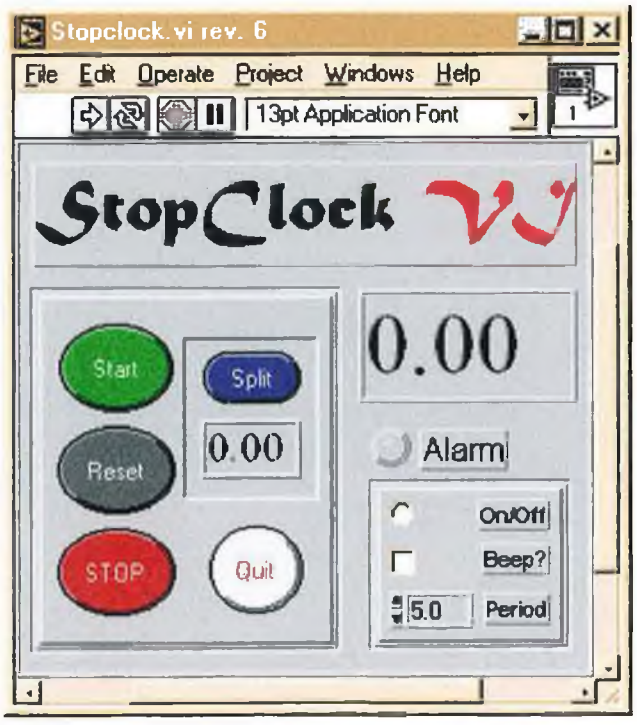

Figure 1.13: Example of front panel for a LabVIEW virtual Instrument.

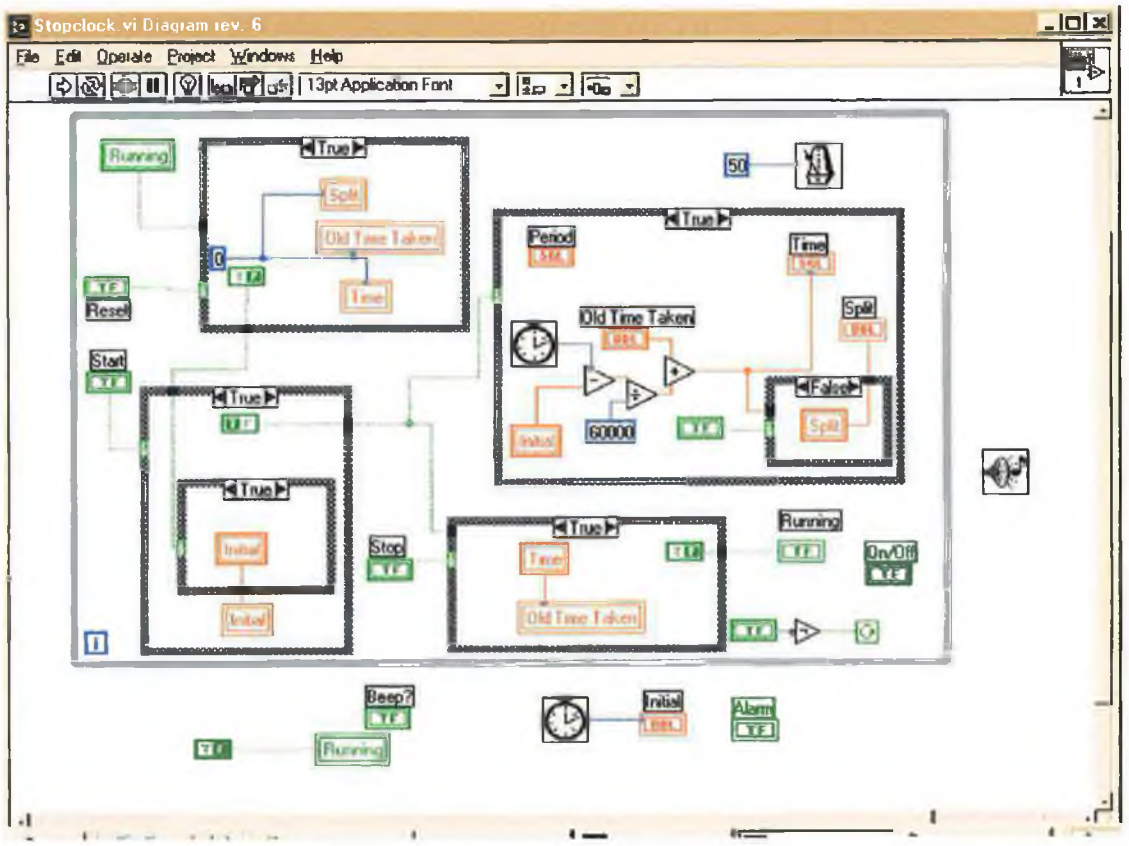

Figure 1.14: Example of block diagram code for LabVIEW Virtual Instrument.

1.6.1.1 Uses in research and industry

There have been numerous applications of the LabVIEW package in research. The areas where this is used range from measurement of magnetic fields to gas chromatography control to fed-batch process control in biotechnology. Some examples from the literature include;

- Testing component parts for Harley-Davidson motorcycles[75].
- Velocity programming for capillary Electrophoresis[76].
- Fed-batch bioprocess control[77].
- Control and data acquisition system for single photon counting fluorimeter[78].
- Measurement of the characteristics of magnetic materials[79].
- Instantaneous power measurements[80].
- Flow injection analysis with sensor array detection[81].
- Flexible pulse programmer for NMR spectrometer[82].
- Instrument simulation[83].
- Resolution improvement in spectroscopy measurements[84].
- Engineering education[8586].
- Monitoring of nuclear reactor refuel process[87].
- On-line chemical analysis[88].
- Multi-component analysis[89].
- High speed cardiac mapping system[90].
- In-vitro fertilisation automation[91].
- Postprocessing of MRI imaging[92].
- General tools ie. file format conversion between different packages[93].

1.7 Digital Cameras

A digital camera is composed of a 2-dimensional array of charge coupled device detectors (CCD). Smith and Boyle first reported CCDs in 1970[94]. The ability of the CCD to return a signal proportional to the intensity of light incident on the detector and the ability to create 1-d[9596] or 2-d arrays[9798] of these detectors led to their adoption by analytical instrument manufacturers[99].

Linear arrays of CCD detectors are used extensively in conjunction with dispersion optics to provide affordable spectrometer systems with rapid and sensitive responses. These systems have been applied to many different analytical techniques including ion-selective optodes[45], humidity sensors[100], UV-vis spectroscopy[101102], raman spectroscopy[103], and investigation of thin film mass transport[104]. Diode array UV-Vis is now employed extensively in HPLC to provide 3-d displays of time vs. absorbance vs. wavelength.

It is with 2-d arrays however that the CCD device excels. It is possible to generate 2-d topographical images of a target with this approach, or to create a 1-dimensionally resolved spectrometer[105]. However, it is in the area of imaging that CCD cameras have had most impact. Chan et al.[106] have used CCD cameras to record images of electrophoresis gels and report a detection limit of 5 ng of DNA per band. Hoke[107] and Unger[108] have also reported the use of CCD cameras with electrophoresis systems. Hardisky et al.[109], and Amato[110] report on the use of a CCD camera for remote monitoring of coastal wetlands. Combined with microscope systems, CCD cameras offer immediate distortion free images. Many articles are available outlining the advantages of CCD cameras in these applications[111,112,113,114,115,116].

1.8 References

[1] O.S. Wolfbeis, B.P.H. Schaffar, Anal. Chim. Acta, 198, 1987, 1-12

[2] B.P.H. Schaffar, O.S. Wolfbeis, Anal. Chim. Acta., 217, 1989, 1-9

[3] O.S. Wolfbeis, Sens. And Act. B., 29, 1995, 140-147

[4] Y. Kawabata, R. Tahara, T. Kamichika, T. Imasaka, N. Ishibashi, Ana. Chem., 62, 1990, 1531

[5] Y. Kawabata, R. Tahara, T. Kamachika, T. Imasaka, N. Ishibashi, Anal. Chem., 62, 1990

[6] T.J. Kulp, I.Cummins, S.M. Angel, C. Munkolm, D.R. Walt, Anal Chem, 59, 1987, 2849-2853

[7] W. Höbel, A. Papperger, J. Polster, Biosens. And Bioelectronics, 7, 1992, 549-557

[8] K. Seiler, W. Simon, Sens. And Act. B., 6, 1992, 295-298

[9] K. Seiler, W.E. Morf, P.R. Sørensen W. Simon, Ion-selective electrodes, 5, 1989, 141-152

[10] O. Dinten, U.E. Spichiger, N. Chaniotakis, P. Gehrig, B. Rusterholz, W.E. Morf, W. Simon, Anal. Chem, 63, 1991, 596-603

[11] U. Oesch, W. Simon, Helv. Chim. Acta, 62(3), 1979, 754

[12] T. Rosatzin, P. Holý, K. Seiler, B. Rusterholz, W. Simon, anal. Chem., 64, 1992, 2029-2035

[13] M. Lerchi, E. Bakker, B. Rusterholz, W. Simon, Anal. Chem., 64, 1992, 1534-1540

[14] E. Bakker, M. Willer, E. Pretsch, Anal. Chim. Acta., 282, 1993, 265-271

[15] U. Spichiger, W. Simon, E. Bakker, M. Lerchi, P. Bühlmann, J. Haug, M. Kuratli, S. Ozawa, S. West, Sens. And Act. B., 11, 1993, 1-8

[16] Principles of electrochemistry, J. Koryta, J. Dvorák, Wiley, 1987, ISBN 0471912115

[17] U. Schaller, E. Bakker, E. Pretsch, Anal. Chem., 67, 1995, 3123-3132

[18] P. Bühlmann, S. Yajima, K. Tohda, K. Umezawa, S. Nishizawa, Y. Umezawa, Electroanalysis, 7(9), 1995, 811-816

[19] U.E. spichiger, D. Freiner, E. Bakker, T. Rosatzin, W. Simon, Sens. And Act. B., 11, 1993, 263-271

[20] M.J.P. Leiner, P. Hartmann, Sens. And Act. B., 11, 1993, 281-289

[21] O. Wolfbeis, H. Offenbacher, Sens. And act. B., 9, 1986, 85

[22] E.J. Netto, J.I. Peterson, M. McShane, V. Hampshire., Sens. And Act. B., 29, 1995, 157-163

[23] F. Baldini, P. Bechi, S. Bracci, F. Cosi, F. Pucciani, Sens. And Act. B., 29, 1995, 164-168

[24] A. Safavi, H. Abdollahi, Anal. Chim Acta., 367, 1998, 167-173

[25] T. Werner, C. Huber, S. Heinl, M. Killmannsberger, J. Daub, O.S. Wolfbeis., Fres. J. Anal. Chem., 359(2), 1997, 150-154

[26] H. Lehmann, G. Schwotzer, P. Czerney, G.J. Mohr., Sens. And Act. B., 29, 1995, 392-400

[27] A. Song, S. Parus, R. Kopelman, Anal. Chem., 69, 1997, 863-867

[28] H. Hisamoto, M. Tsubuku, T. Enomoto, K. Watanabe, H. Kawaguchi, T. Koike, K. Suzuki, Anal. Chem., 68, 1996, 3871-3878

[29] E. Bakker, M. Lerchi, T. Rosatzin, B. Rusterholz, W. Simon., Anal. Chim. Acta., 278, 1993, 211-225

[30] D. Citterio, S. Rásonyi, U.E. Spichiger, Fres. J. Anal. Chem., 354(7/8), 1996, 836-840

[31] I. Oehme, B. Prokes, I. Murkovic, T. Werner, I. Klimant, O.S. Wolfbeis, Fres. J. Anal. Chem., 350(7-9), 1994, 563-567

[32] H. Lindauer, P. Czerney, G.J. mohr, U.W. Grummt, Dyes and Pigments, 26, 1994, 229-235

[33] G. Patonay, J. Zen, T. Czuppon, Environ. And Proc. Monitoring Tech., 1637, 1992, 142-150

[34] H. Zeng, K. Wang, R. Yu, Anal. Chim. Acta., 298, 1994, 271-277

[35] S.B. Bambot, J. Sipior, J.R. Lakowicz, G. Rao, Sens. And Act. B, 22, 1994, 181-188

[36] H. He, H. Li, G. Mohr, B. Kovács, T. Werner, O.S. Wolfbeis, Anal. Chem., 65, 1993, 123-127

[37] W.E. Morf, K. Seiler, B. Rusterholz, W. Simon, Anal. Chem., 62, 1990, 738-742

[38] P.C. Hauser, P.M.J. Périsset, S.S.S. Tan, W. Simon, Anal. Chem., 62, 1990, 1919-1923

[39] H. He, G. Uray, O.S. Wolfbeis, Anal. Letters, 25(3), 1992, 405-414

[40] E. Lindner, M. Horváth, K. Tóth, E. Pungor, Anal. Letters, 25(3), 1992, 453-470

[41] W.H. Chang, A.W.M. Lee, C.M. Lee, K.W. Yau, K. Wang, Analyst, 120, 1995, 1963-1967

[42] K. Seiler, K. Wang, E. Bakker, W.E. Morf, B. Rusterholz, U.E. Spichiger, W. Simon, Clin. Chem. 36(8), 1991, 1350-1355

[43] W.H. Chan, A.W.M. Lee, D.W.J. Kwong, Y. Liang, K. Wang, Analyst, 122, 1997, 657-661

[44] M. Shortreed, E. Bakker, R. Kopelman, Anal. Chem, 68, 1996, 2656-2662

[45] S. O'Neill, P. Kane, M.A. McKervey, D. Diamond, Anal. Comm., 35, 1998, 127-131

[46] H. Hisamoto, N. Miyashita, K. Watanabe, E. nakagawa, N. Yamamoto, K. Suzuki, Sens. And Act. B, 29, 1995, 378-385

[47] H. Hisamoto, E. Nakagawa, K. Nagatsuka, Y. Abe, S. Sato, D. Siswanta, K. Suzuki, Anal. Chem, 67, 1995, 1315-1321

[48] M. Lerchi, F. Orsini, Z. Cimerman, E. Pretsch, D.A. Chowdhury, S. Kamata, Anal. Chem, 68, 1996, 3210-3214

[49] M.R. Shortreed, S. Dourado, R. Kopelman, Sens. And Act. B, 38-39, 1997, 8-12

[50] K. Wang, K. Seiler, W.E. Morf, U.E. Spichiger, W. Simon, E. Lindner, E. Pungor, Anal. Sci., 6, 1990, 715-720

[51] H. He, G. Uray, O.S. Wolfbeis, Anal. Chim. Acta, 246, 1991, 251-257

[52] C. Stamm, K. Seiler, W. Simon, Anal. Chim. Acta, 282, 1993, 229-237

[53] H. Li, O.S. Wolfbeis, Anal. Chim. Acta, 276, 1993, 115-119

[54] H. Li, H. He, O.S. Wolfbeis, Biosens. And Bioelec., 7, 1992, 725-732

[55] M. Kuratli, M. Badertscher, B. Rusterholz, W. Simon, Anal. Chem., 65, 1993, 3473-3479

[56] H. Hisamoto, S. Sato, K. Sato, S. Siswanta, K. Suzuki, Anal. Sci., 14, 1998, 127-131

[57] C. Krause, T. Werner, O.S. Wolfbeis, Anal. Sci., 14, 1998, 163-167

[58] H. Hisamoto, K. Watanabe, E. Makagawa, D. Siswanta, Y. Shichi, K. Suzuki, Anal. Chim. Acta, 299, 1994, 179-187

[59] R. Czolk, J. Reichert, H.J. Ache, Sens. And Act. B. 7, 1992, 540-543

[60] M.R. Shortreed, S.L.R. Barker, R. Kopelman, Sens. And Act. B., 35-36, 1996, 217-221

[61] D. Diamond, M.A. McKervey, Chem. Soc. Reviews, 1996, 15

[62] R.J. Forster, A. Cadogan, M. Telting Diaz, D. Diamond, S.J. Harris, M.A. McKervey, Sens. And Act. B., 4, 1991, 325

[63] M.A. Mckervey, E.M. Seward, G. Ferguson, B. Ruhl, S.J. Harris, Chem. Soc. Chem. Commun., 1985, 389

[64] O. Aleksiuk, S.E. Biali, Tetrahedron Lett., 1993, 34, 4857

[65] S. Shinkai, H. Kawabata, T. Arimura, T. Matsuda, H. Satoh, O. Manabe, J. Chem. Soc. Perkin. Trans., 1, 1989, 1073

[66] S. Shinkai, Y. Shirahama, T. Tsubaki, O. manabe, J. Chem. Soc. Perkin. Trans., 1, 1989, 1859

[67] A. Cadogan, D. Diamond, M.R. Smyth/, M Deasy., M.A. McKervey., S.J. Harris., Analyst, 114(12), 1989, 1551-1554.

[68] M. Telting-Diaz., D. Diamond., M.R. Smyth., E.M. Seward., A.M. McKervey., Electroanalysis., 3(4-5), 1991, 371-375

[69] T. McKittrick, D. Diamond, D.J. Marrs, P.O'Hagan, M.A. McKervey, *Talanta*, **43**, (1996), 1145-1148

[70] P. Kane., K. Kincaid., D. Fayne., T. McKittrick., D. Diamond., In preparation..

[71] K. Toth, B.T.T. Lan, j. Jeney, M. Horváth, I. Bitter, A. Grün, B. Ágai L. Tóke., Talanta, 41, 1994, 1041-1049

[72] B.T.T. Lan, K. Tóth, Anal. Sci., 14, 1998, 191-197

[73] M. McCarrick, S.J. Harris, D. Diamond, Analyst, 118, 1993, 1127-1130

[74] K.R.A.S. Sandanayake, I.O. Sutherland, Sens. And Act. B., 11, 1993, 331-340

[75] P. Korth, *EDN* October 1993

[76] J.B. Shear, L.A. Colon, R.N. Zare, *Anal Chem.*, **65,** 1993, 3708

[77] M.E. Gregory, P.J. Keay, P. Dean, M. Bulmer and N.F. Thornhill, *Journal of Biotechnology* **33,** 1994, 233

[78] W.J. Stryjewski, *Rev. Sci. Instrum.*, **62**(8), 1991

[79] E. Carminati, A. Ferrero, *IEEE transactions*, **41**, 1992

[80] D.R. Zrudsky, J.M. Pichler, *IEEE transactions*, **41**, 1992

[81] F.J. Saez de Viteri, D. Diamond, *Anal. Proc.*, **31**, 1994

[82] X.W. Donald, A. Patterson, L.G. Butler, J.B. Miller, *Rev. Sci. Instrum.* **64** (5), 1993

[83] R.E. Abdel-Aal, Meas. Sci. Technol., 3, 1992, 959

[84] R.E. Abdel-Aal, Meas. Sci. Technol., 3, 1992, 1133

[85] D.N. McStravick, J.L. Kelly, Lab. Robotics and Automation, 10(2), 1998

[86] J.P. Osborne, B. Erwin, M. Cyr, C. Rogers, Lab. Robotics and Automation, 10(2), 1998

[87] G.L. Hurd, M.C. Haun, Lab. Robotics and Automation, 10(2), 1998

[88] M. Collins, P. Hope, Lab. Roborics and Automation, 10(2), 1998

[89] C.J. Chapo, Lab. Robotics and Automation, 10(2), 1998

[90] S. Conquergood, Lab. Robotics and Automation, 10(2), 1998

[91] L. Butler, J. Conia, Lab. Robotics and Automation, 10(2), 1998

[92] F.E. Boada, J.S. Gillen, D.C. Noll, G.X. Shen, K.R. Thulborn, Int. J. of Imag. Systems and Techn., 8(6), 1997

[93] T. Starn, Lab. Robotics and Automation, 10(2), 1998

[94] W. Boyle , G. Smith, Bell Systems Technical Journal, 49, 1970, 587

[95] K.L. Ratzlaff, S.L. Paul, Apl. Spectrosc., 33, 1979, 240

[96] P.M. Epperson, R.D. Jalkian, M.B. Denton, Anal. Chem., 61, 1989, 282

[97] J.H. Kinney, Q.C. Johnson, U. Bonse, R. Nusshardt, M.C. Nichols, Proc. SPIE-Int. Soc. Opt. Eng., 43, 1986, 691

[98] R.W. Leach, Opt. Eng., 26, 1987, 1061

[99] I. Nir, Y. Talmi, Laser Focus World, 8, 1991, 111

[100] T.E. Brook, M.N. Taib, R. Narayanswamy, Sens. And Act. B., 38-39, 1997, 272

[101] R.D. Waterbury, W. Yao, R.H. Byrne, Anal. Chim. Acta., 357, 1997, 99

[102] J.J. Sullivan, B.D. Quimby, Anal. Chem., 62, 1990, 1034

[103] Y. Wang, R.L. McCreery, Anal. Chem., 61, 1989, 2647

[104] N.F. Fell Jr., P.W. Bohn, Anal. Chem., 65, 1993, 3382

[105] J.W. Olesik, G.M. Hieftje, Anal. Chem., 57, 1985, 2049

[106] K.C. Chan, L.B. Koutny, E.S. Yeung, Anal. Chem., 63, 1991, 746

[107] F. Hoke, The Scientist, 8(6), 1994, 18

[108] T.F. Unger, S. Beck, The Scientist, 11(24), 1997, 18

[109] M.A. Hardisky, M.F. Gross, V. Klemas, Bioscience, 4, 1986, 453

[110] I. Amato, Anal. Chem., 60(23), 1988, 1339

[111] H. Goldner, The Scientist, 9(3), 1995, 18

[112] R. Lewis, The Scientist, 10(21), 1996, 18

[113] L. Krumenaker, The Scientist, 8(19), 1994, 17

[114] H. Ahern, The Scientist, 9(21), 1995, 18

[115] R. Finn, The Scientist, 10(4), 1996, 18

[116] R.R. Klevecs, The Scientist, 12(15), 1998, 22

2 Comparison of the performance of Calix[4]arene Phosphine Oxide and Ester Derivatives in Ion-Selective Optode Membranes

2.1 Introduction

In 1972, the first ion-selective membrane electrode clinical analyser system was marketed by STAT-ION (STAT-ION, Technicon, Tarrytown, NY/Photovolt Corp., Indianapolis, IN, USA). The market for ion-selective electrodes is quite large and it is estimated that by 1990, about 65 million potassium-selective electrodes based on Valinomycin had been sold[1]. Many other ion-selective membranes are also available, incorporating neutral carriers in a plasticised PVC membrane. The selectivity of such systems arose from the recognition pattern of the ionophore used in the construction of the electrodes. In 1982 an american company, AMES, introduced a solid-state clinical analyser based on valinomycin and a pH dye immobilised on a test strip. The interaction between valinomycin and potassium led to a change in colour of the test kit due the dye exchanging protons. This system's principle of operation was later developed and expanded by Morf et al[1] and became the model of the ion-selective optode membrane. Since then, the response mechanism has been altered and improved. There are now sensors of this type available for many different ions (see Chapter 1).

Modelling of the optical responses is made possible by the relatively simple mode of operation which is discussed in Chapter 1. Many of the assumptions have been vindicated by the virtue of the ability of these models to accurately predict the behaviour of the sensors.

In this work two novel ion-selective optodes are investigated containing calix[4]arene ion-selective ligands. Their performance and response characteristics are compared and some insight into the differences observed is given based on the molecular structure of the calixarene receptors.

2.1.1 Absorbance as a transduction mechanism

Optical signals are impervious to electrical noise and can be transmitted over very long distances with little or no loss of signal. Throughout this work, absorbance is used as the transduction mechanism. The relation between absorbance and concentration is given by the Beer-Lambert law

$$\ln\frac{P_0}{P} = kbC$$ Equation 2.1: Beer-Lambert law.

Where P_0 and P are the radiation power before and after absorbance of the sample
k is a constant which is a measure of how strongly the sample absorbs ($cm^{-1}M^{-1}$)
b is the pathlength of the sample (cm)
C is the concentration of the sample being measured (M)

By modifying the equation to include base-10 logarithms instead of natural logarithms, and redefining the proportionality constant to a we get the accepted mathematical definition of absorbance.

$$\log\frac{P_0}{P} = abC$$ Equation 2.2

where P_0, P, b and C are as before
and a is now the molar extinction coefficient ($cm^{-1}M^{-1}$)

The optode membranes exhibit selective absorption, meaning that the sensing layer absorbs certain wavelengths more than others. In this case, each measured wavelength must have its own proportionality constant a, often expressed as the molar extinction coefficient.

The Beer-Lambert law can be used to relate changes in absorbance to changes in concentrations of the relative absorbing species in a given sample. The law states that an arithmetically increasing concentration of an absorbing species gives rise to an arithmetically increasing absorbance signal. In this way, the absorbance is

directly proportional to the concentration of the absorbing species. Absorbing systems tend to deviate from the Beer-Lambert law however as the concentration increases (Figure 2.1). This deviation is caused by changes in refractive index and the extinction coefficient of the solution. Kortum and Seiler point out that solutions at or below 10^{-3}M can be assumed to have constant refractive index[2]. In solutions which have a high degree of radiation scattering (normally non-homogenous samples such as whole blood) then the typical response profile changes. This occurs because the radiation lost through scattering A_s can be greater than that through actual sample absorbance. In the work presented here the assumption that $A>>A_s$ is made.

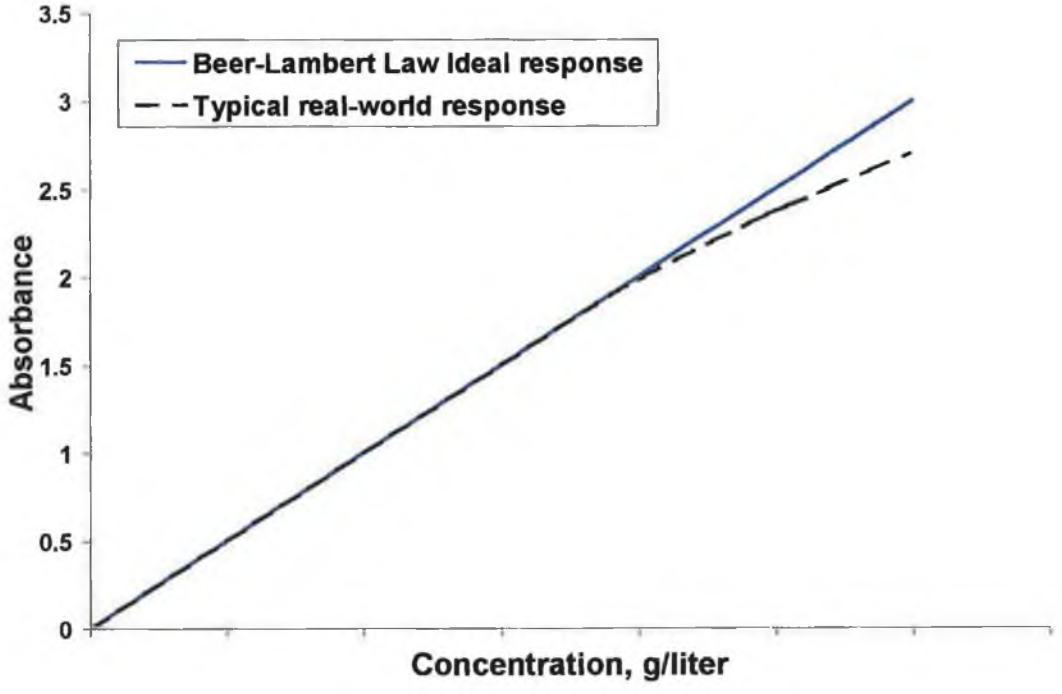

Figure 2.1: Deviation of real samples from the Beer-Lambert law at high concentrations.

2.1.2 Activity coefficient

From the optode response equation (Equation 2.9), it can be seen that the membrane response is related to the activity of the target ion in solution, a_i. The activity of an ion is not the same as its concentration but is related directly to it

$$\mathbf{a_i = f_i c_i} \qquad \text{Equation 2.3}$$

where for a particular ion, i, a_i is the activity, c_i is the concentration, and f_i is the activity coefficient. The activity coefficient f_i is a measure of the deviation of an ideal solution from the ideal situation. For a particular ion in a solvent (usually water), the value of this coefficient depends only on the ionic strength of the solution involved (I).

$$\log f_i = -Az_i^2\left(\frac{\sqrt{I}}{1+\sqrt{I}} - 0.2I\right) \qquad \text{Equation 2.4}$$

Where A is a solvent dependency constant with a value of 0.512 for water.

$$I = \frac{1}{2}\sum c_i z_i^2 \qquad \text{Equation 2.5}$$

where c_i = the molar concentration of the ion i, and z is the charge on the ion.

The activity coefficient is then calculated from the ionic strength from Equation 2.4

2.1.3 Modelling of experimental data

In order to be able to test response mechanisms, we can use mathematical modelling of the experimental data which may yield important information about the system. Fitting these equations to data allows us to estimate quantities such as membrane thickness, diffusion constants, overall membrane exchange constants and so on. The SOLVER method available within Microsoft Excel was used throughout this work for modelling studies.

2.1.3.1 Microsoft Excel SOLVER function

SOLVER is an iterative optimisation routine incorporated into Microsoft Excel, which allows the user to attempt to estimate model parameters by iteratively varying pre-defined variables which govern the value of the required target. The method by which SOLVER works is usually by minimisation of the sum of squared residual error between a predicted model and an equivalent experimental data array. SOLVER requires the address on the spreadsheet of the variables involved in the model prediction and will vary the values stored in these variables until the error has been minimised.

The SOLVER method searches for a minimum error condition by varying the values involved, but it is possible, as is with many modelling techniques, that the end result will not correlate with the experimental data. Part of the reason for this is to do with the initial conditions from which the minimisation starts. Due to the presence of local and global minima the initial position of the search can be important[3]. Fortunately, the variables optimised by SOLVER in the instances reported here are all expected to be within certain boundaries, and so setting the initial values to values approximating those expected proved to remedy this.[4,5].

2.2 Experimental

2.2.1 Chemicals and reagents

High molecular weight polyvinyl chloride (PVC), dibutyl sebacate (DBS), potassium tetrakis[(4-chloro)phenyl]borate (KpTClPB) and 9-(Diethlyamino-5-octadecanoylimino-5H-benzophenoxazine (ETH 5294) were obtained from Fluka, Buchs, Switzerland.
Sodium chloride, potassium chloride, calcium chloride, lithium chloride and magnesium chloride were also obtained from Fluka, and were of the highest purity available. Water from a Barnstead RO/RF ultrapure water system was used throughout. The ligands were synthesised as reported previously[6,7].

2.2.2 Equipment and apparatus

UV-vis spectra were obtained with a Hewlett Packard HP5428A photodiode array spectrometer (Hewlett Packard, Filton Road, Stoke Gifford, Bristol, BS12 6QZ UK. The membranes were prepared by accurately weighing out the quantities shown in Table 2.1 and dissolving in tetrahydrofuran. From these solutions, membranes of approximately 4μm thickness (estimated by curve fitting to dynamic membrane response, Appendix 2) were obtained by spin coating onto a glass slide using a spin-coater with vacuum attachment (Laurell Technologies Corporation 850 North Wales Road, Lansdale, PA 19446-6104, USA). The membrane-coated slide was placed into a standard UV-Vis cuvette and retained in position using spacers in the base and lid of the cuvette cell (Figure 2.2). All measurements were made in the transmission mode.

All solutions were buffered at pH 8 using Tris/TrisHCl using quantities as predicted by the Henderson-Hasselbach equation (assuming a pK_a for Tris of 8.3).

The pH values of samples and buffers were verified using an EDT RE357 pH meter and glass combination electrode (EDT Instruments Limited, Lorne Road, Dover, Kent, CT16 2AA, England).

All solutions used for calibration measurements were buffered at pH 8.0. This pH was chosen as it was sufficiently acidic to ensure the dye is fully protonated[8] in the absence of any complexation of metal ions by the calixarene ionophores. Calibration was carried out by serial injections of increasingly concentrated standards of either NaCl or $CaCl_2$, depending on which ligand was used (also pH buffered) into the buffer solution in the cuvette. The volume and concentration of the additions was calculated previously to give half-logarithmic steps from 10^{-6}M primary ion to 10^{-1}M primary ion. The addition scheme is outlined in Table 2.2. The time of each addition was noted, and used in later processing.

During the experiments, wavelength scans were performed every few seconds from 400nm to 800nm and zeroed at 800nm. Once the experiment was completed, cross-sections of the wavelength traces were taken (normally at 660nm, the most sensitive portion of the spectrum) in order to obtain the response of the membrane with time. From the resulting plot, the values of the steady-state portions were taken and correlated back to the respective concentration of primary ion according to the times of 'spiking' recorded during the experiment.

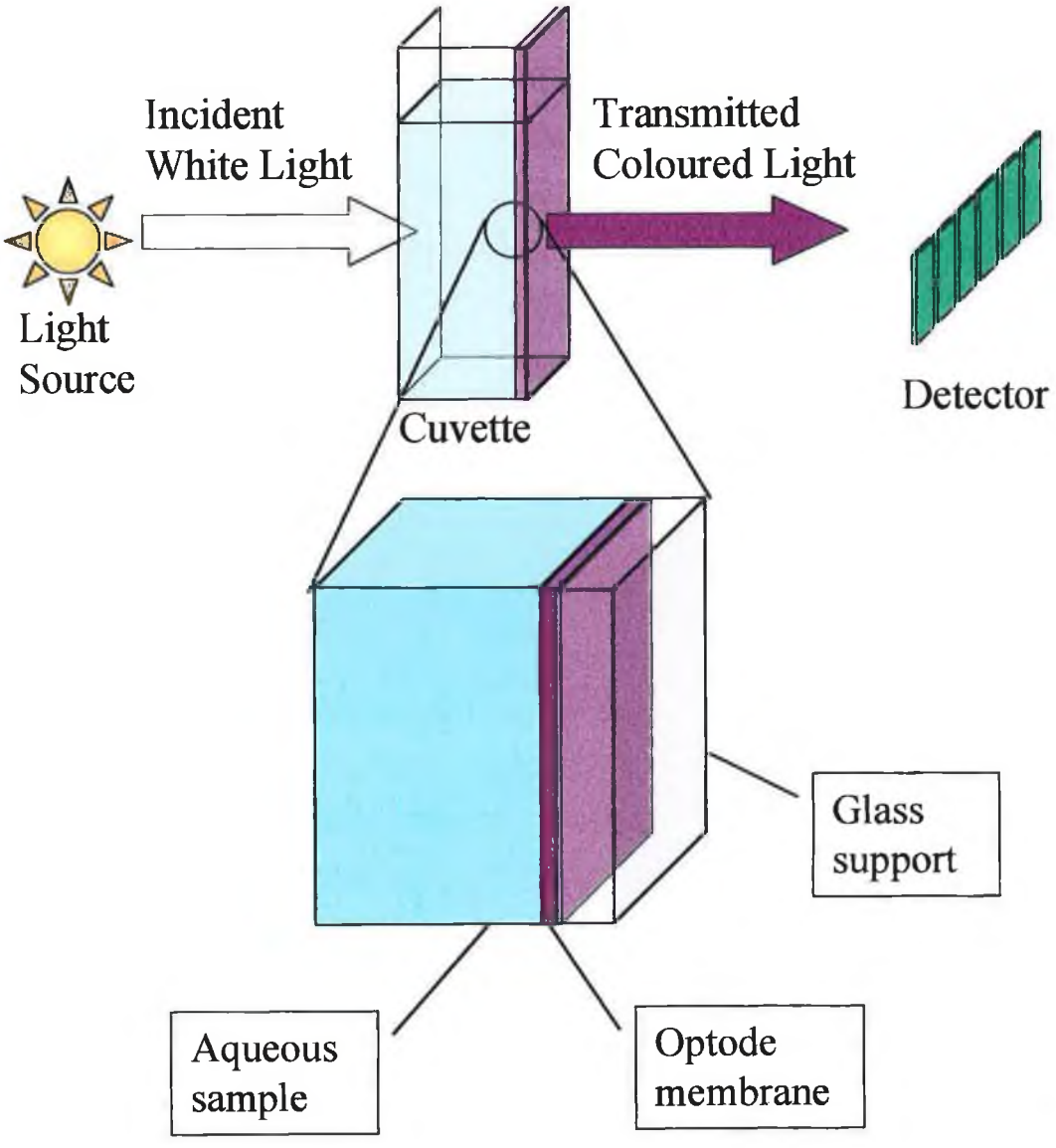

Figure 2.2: Schematic of the experimental setup used in these experiments

2.3 Modelling of membrane steady-state response

Fitting of the theoretical data to the experimental by means of error minimisation (Appendix 1) proved quite successful. Obviously, the quality of the original experimental data is of extreme importance in determining the effectiveness of this process. As can be seen in Figure 2.3 and Figure 2.4, the fit is not perfect, but is adequate to provide an approximation of the actual parameters required. This method of modelling allows us to estimate three values, A_0, A_t and K_{exch}(Appendix 1). However, it serves another function beyond this.

The model, when treated with different pH values yields a significant change in response. The model predicts that, according to the current equation, the response of the membrane system will move one logarithmic unit lower for every pH unit raised. The response of the membrane over the entire activity range is shifted by the same magnitude. The shift has no effect on the shape of the response curve at all. We can also say that the limit of detection (Which will be equal to a particular value of α in a given system) will also be affected in the same way. Thus a membrane with a limit of detection of 10^{-5} at pH 8 should have a limit of detection of 10^{-6} at pH 9. In general, this has proved to be true. However, one problem associated with raising the pH of the solutions used is that eventually, the pH is no longer low enough to protonate the dye within the membrane fully. Once this happens, the analytical signal disappears, as the deprotonation normally due to complexation of the relevant cation cannot take place. Also, each ligand appears to have its own inherent limit of detection. However, this approach has been used to generate sensors with sub-nanomolar limits of detection[9]. The limit of detection of such systems can be defined in many ways. One of the most convenient ways is to express the LOD as a particular fraction of the variable α. Since any pH shifts or other changes in the operating range affects all values of α equally, any one value can be chosen as an indicator of the respective LOD changes. In this work, a value for α of approximately 0.85 was used.

This problem aside, the model has proven useful in predicting how different pHs will affect the response of the membrane (Figure 2.5). This diagram shows how the experimental and theoretical data from the same membrane over the same ion activity range varies with pH. The dashed lines are the theoretical fit, and the solid points are the actual experimental points.

Clearly, some of the terms included in these equations are static during the course of an experiment such as the concentration of the three main components within the membrane (L, I, and R^-). These values are determined at the time of preparing the membrane mixture before preparing the optode slides. Buffering the pH controls the activity of the H+ ions and is known for all solutions used. In the work presented here, variables whose values are determined experimentally are pH of the solutions, concentrations of the components within the membrane (As determined by the amounts weighed out initially), ion activities and the absorbance of the membrane at a particular wavelength and ion activity.

The term α within the model (Equation 2.12, Appendix 1)is a value representing the degree of protonation of the pH dye within the membrane phase. Its value can range from 0 to 1. As we can see (Equation 2.9,Appendix 1), the term α, present in the model equation is related to the current absorbance of the system (Abs) and the limiting absorbances of the membrane (Abs_t and Abs_0). Initially, it was attempted to determine the absorbance limits Abs_t and Abs_0 of the membrane experimentally by exposing the membrane to 0.1M acid and base respectively. While this ensured complete protonation and deprotonation respectively, it was found to reduce the lifetime of the membrane considerably due to acid-catalysed degradation of the anionic site and often resulted in ion-pairs to enter the membrane (Due to a limiting concentration of anionic site to offset the full protonation of the pH dye. After preliminary investigations to ensure accurate modelling of these parameters, it was decided they should be estimated using SOLVER.

This leaves the values of K_{exch}. This value is the overall equilibrium constant for the membrane and is calculated by error minimisation via the SOLVER method of mathematical modelling given that the other variables present in (Equation 2.12,Appendix 1) are known.

In summary, the SOLVER method is required to optimise three values, Abs_t, Abs_0 and K_{exch}. After modelling, a manual check is performed to ensure the values for Abs_t and Abs_0 are acceptable. If these values do not seem to be in accordance with the data i.e. Abs_t of >1 or Abs_0<=0.5, the model is re-optimised with more suitable starting values.

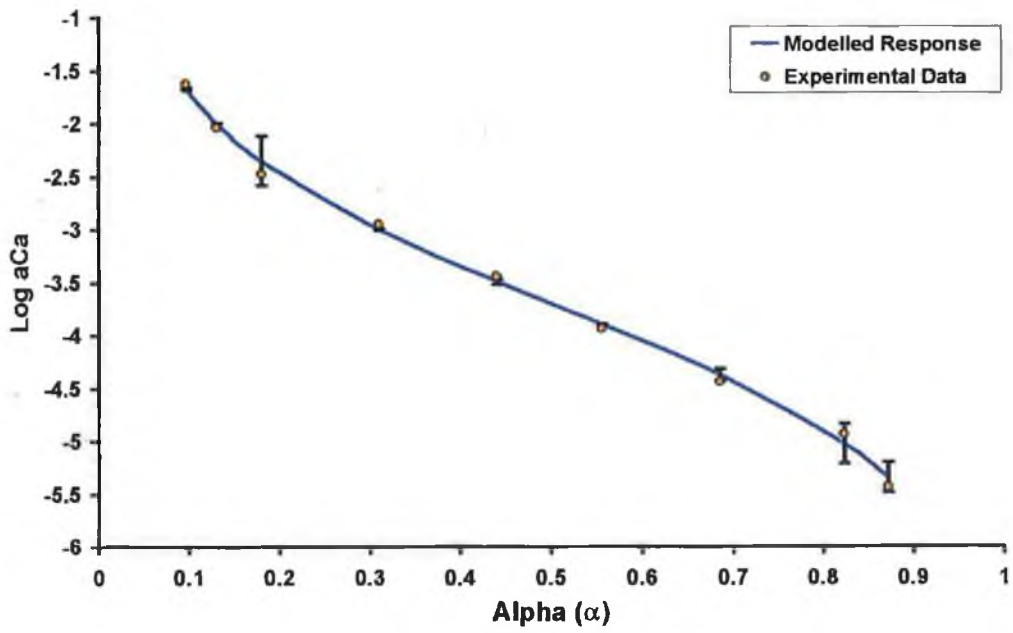

Figure 2.3: Fit of experimental and theoretical data.

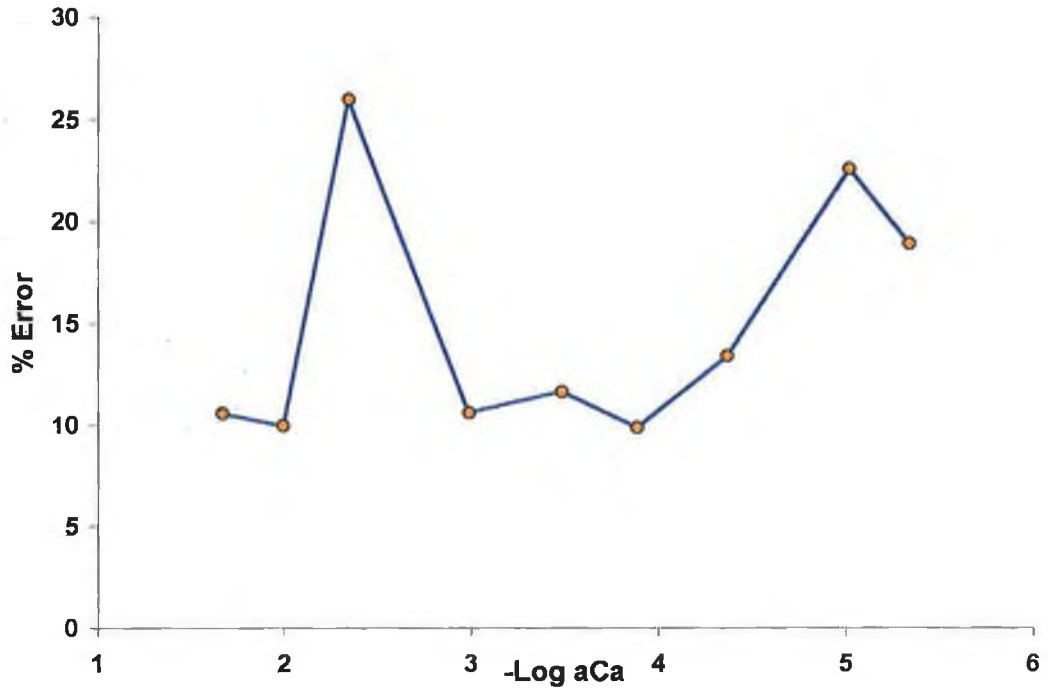

Figure 2.4: Plot of residual error (%) of model fit shown above.

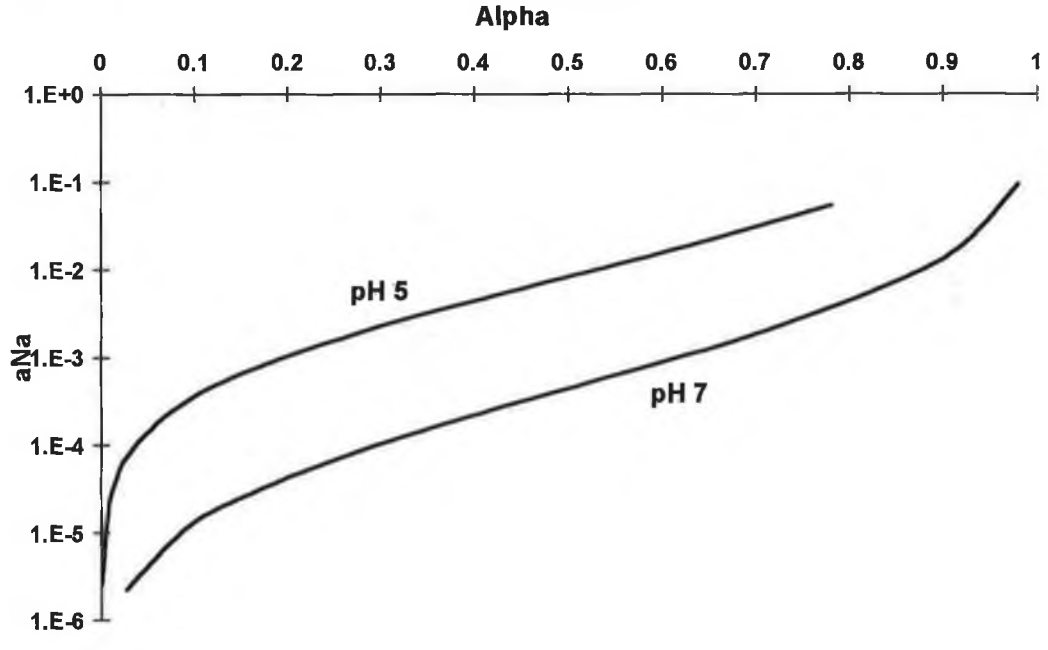

Figure 2.5: Theoretical response of a membrane with a K_{exch} of $9.4x10^4$ to sodium solutions at pH 5.0 and 7.0.
The higher pH allows for lower limits of detection, and the relationship between them is given in Equation 2.6.

2.4 Modelling of dynamic membrane response

The modelling method chosen in this work was that of fitting the experimental data to the theoretical response by minimising the errors between them using the SOLVER function in Microsoft Excel**3** (Appendix 2).

The values from fitting to the model optimised by SOLVER are

- D, the diffusion coefficient within the membrane (cm^2/sec)
- d, the thickness of the membrane (m)
- k, a constant denoting the size of the absorbance change monitored
- T_0, the theoretical start of membrane response

Values of D expected for PVC membranes are in the region of $1x10^{-14}$. This value is affected greatly by the plasticiser used. The thickness of the membranes was expected to be around 4 μm. T_0 and k are modelling constants for a particular modelling situation and are of no analytical interest in this study.

These fit of the experimental and theoretical data proved quite successful (Figure 2.6).

The diffusion coefficients obtained were around $1x10^{-14}$ cm^2s^{-1}. The difference between this value and the suggested values in literature may be due to the choice of plasticiser in the experiments. However, it is in the region of diffusion coefficients expected for plasticised PVC membranes.

The thickness of the membrane according to the model is ca. 3 microns. This agrees well with the thickness expected due to the membrane preparation and comparison to such procedures in the literature.

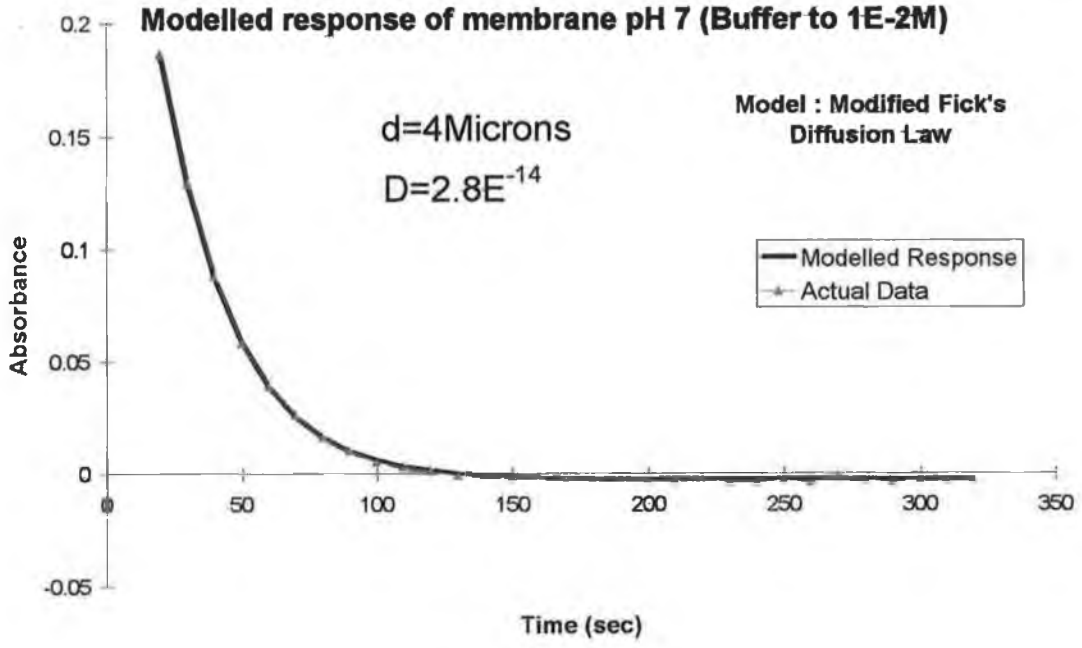

Figure 2.6: fit of experimental and theoretical data for membrane dynamic response.

Component	Membrane 1	Membrane 2
Ligand **1**	12.5 mg	-
Ligand **2**	-	18.3 mg
Anionic Site (KtpClPB)	7.02 mg	7.02 mg
Dye (ETH 5294)	5.97 mg	5.97 mg
PVC (high molecular wt.)	483 mg	483 mg
Plasticiser (di-butyl sebacate (DBS))	238 mg	238 mg

Table 2.1: Membrane compositions as used in preparation of the membranes used in this study.

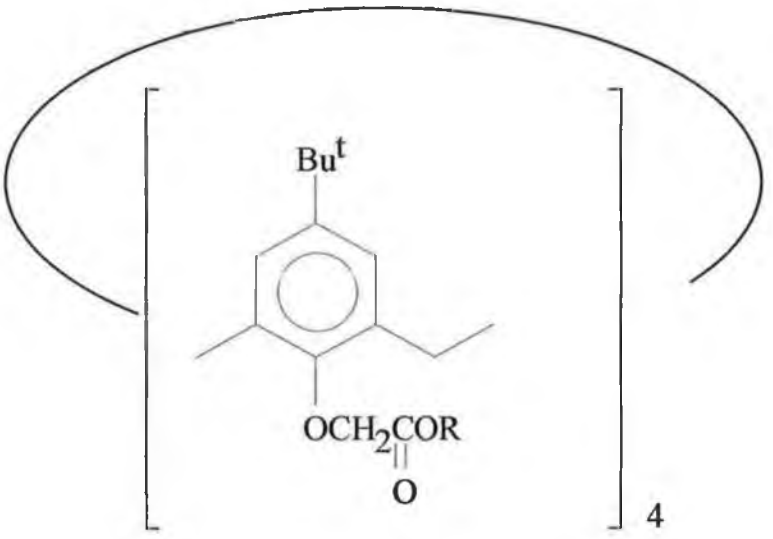

R = $CH_2CH_2OCH_3$

p-tert-butylcalix[4]arene methoxyethylester

Ligand 1

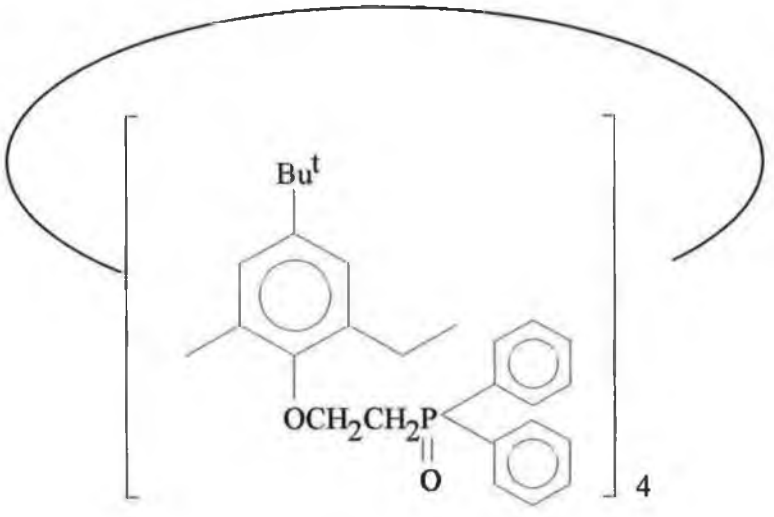

p-tert-butylcalix[4]arene ethyleneoxydiphenylphosphine oxide

Ligand 2

Figure 2.7: Structures of the two Calix[4]arene ligands used in this study.

Required conc. (M)	*Total volume (μl)*	*Addition(μl)*	*Conc. Of addition(M)*	*Actual conc.(M)*
0	3000	0	0	
0	3000	31	1.00E-04	0.000E+00
1E-06	3031	6	1.00E-03	1.023E-06
3E-06	3037	23	1.00E-03	2.998E-06
1E-05	3060	12	1.00E-02	1.051E-05
5E-05	3072	16	1.00E-02	4.958E-05
1E-04	3088	63	1.00E-02	1.014E-04
3E-04	3151	23	1.00E-01	3.013E-04
1E-03	3174	65	1.00E-01	1.026E-03
3E-03	3239	23	1.00E+00	3.033E-03
1E-02	3262	67	1.00E+00	1.008E-02
3E-02	3329	253	1.00E+00	3.021E-02
1E-01	3582	0		1.008E-01

Table 2.2: Spiking scheme for addition of standard solutions for construction of standard curve with membranes 1 and 2.

The first column contains the target concentration of the solution. The second column contains values recording the current total volume in the cuvette, used in calculating the true concentration of the solution after addition. The third column contains the amount of standard to be added to achieve the next required concentration while the fourth column contains the concentration of the solution required for this addition.

The last column contains the actual concentration achieved by this method.

All resulting concentrations were generally within 5% of the required concentration.

2.5 Results and discussion

The response of the membrane containing ligand 1 to increasing concentrations of NaCl (10^{-6}M to 0.1 M) is shown in Figure 2.8. The typical spectral changes caused by deprotonation of ETH 5294 are apparent, with an isosbestic point at 560 nm, an increasing absorbance below this wavelength, and a decrease in the absorbance at wavelengths above it

In Figure 2.9, the same membrane exhibits virtually no response to increasing $CaCl_2$ concentrations, demonstrating that the excellent potentiometric selectivity of this calix[4]arene tetraester[10] based membrane for sodium ions is retained in these optode membranes. The value obtained for the K_{exch} of this system ($K^{exch}=2.08x10^5$) agrees well with similar membranes incorporating calixarenes reported in the literature[11].

Figure 2.10and Figure 2.11 illustrate the response of membranes based on ligand 2 to increasing concentrations of calcium and sodium ions, respectively. Clearly, there is a striking reversal of the selectivity shown in Figure 2.8 and. Figure 2.10 These results show that the previously reported calcium selectivity of the ligand obtained with ion-selective electrode is retained.

Furthermore, as with the potentiometric results, the sodium membrane exhibits a greater selectivity than the calcium membrane. Selectivity for the sodium membrane over some other ions is in the order Mg>K>Li>Ca with none of these ions showing any significant response. For the calcium membrane the order of selectivity is K>Mg>Na>Li with lithium being the only ion to show any significant response, although this is still much less than that generated by calcium ions. These results are also in accordance with potentiometric selectivity patterns reported for both membranes. Modelling based on a 1:1 calixarene:ion ratio gives a value for the K_{exch} of $6.7x10^{11}$.

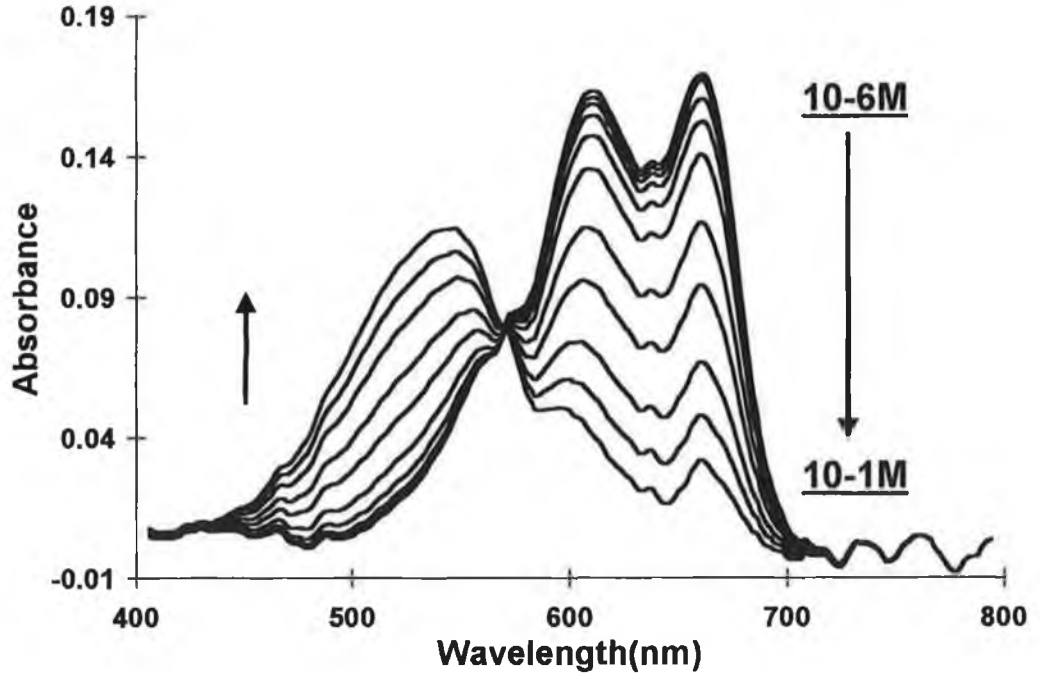

Figure 2.8: Spectral response of membrane based on ligand 1 to sodium solutions at pH 8.0

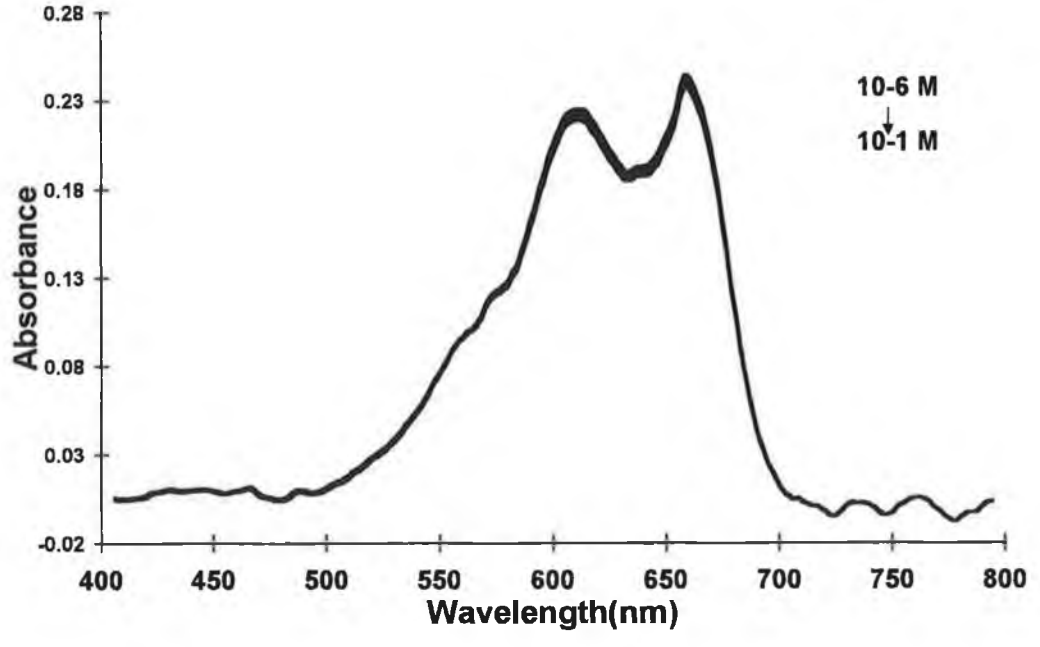

Figure 2.9: Spectral response of membrane based on ligand 1 to calcium solutions at pH 8.0

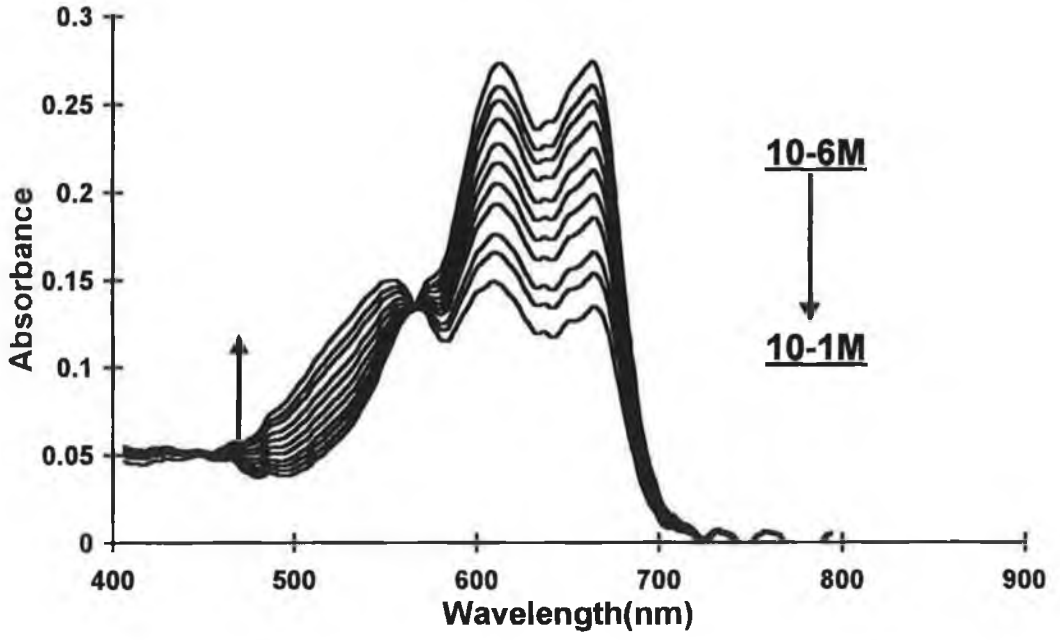

Figure 2.10: Spectral response of membrane based on ligand 2 to calcium solutions at pH 8.0

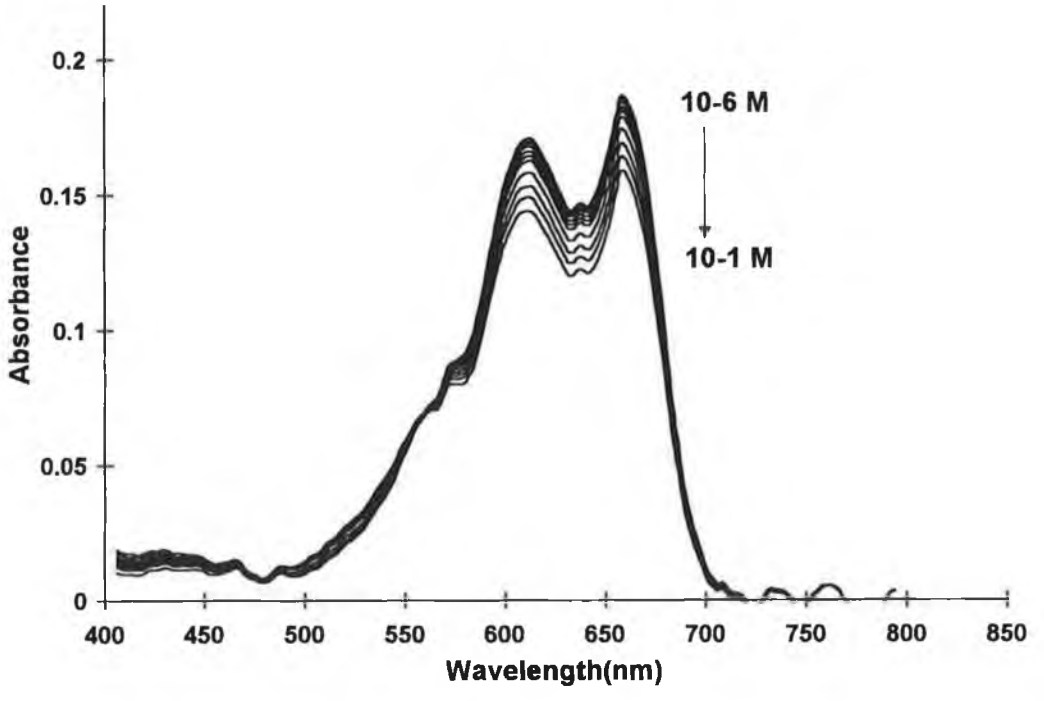

Figure 2.11: Spectral response of membrane based on ligand 2 to sodium solutions at pH 8.0

Figure 2.12 shows a calibration curve for membrane 1 to sodium solutions at pH 8. Clearly the linear range is somewhat less and the limit of detection an order of magnitude higher than is than that typically obtained with equivalent potentiometric systems. The limit of detection can easily be shifted to lower activities by a change of the pH of the solutions used for calibration and analysis. The limited dynamic range is characteristic of ion-selective optode membranes and while it limits the ability to measure over large ranges of activity, it does allow the production of sensors with increased sensitivity over well defined ranges.

Figure 2.13 shows a calibration curve for a membrane 2 to calcium solutions at pH 8. In this case, a greater linear range is exhibited, and a limit of detection significantly lower than that obtained with membrane 1 is evident. Conversely, the sensitivity of membrane 1 is approximately the same as that of membrane 2, although the difference in magnitude of the wavelength scans suggests that membrane thickness should be considered. As a result, the true sensitivity is actually ca. half that of membrane 1. While theory predicts that a doubly charged ion will generate a more sensitive response in this type of sensing scheme, the opposite is evident here. A possible situation suggested by these results is the formation of a calixarene:ion complex of other than 1:1 ratio. While NMR titration studies have shown the tetraphosphine oxide to be able to form a 2:1 complex ratio with some ions, a 1:1 ratio has been found in the case of calcium[12].

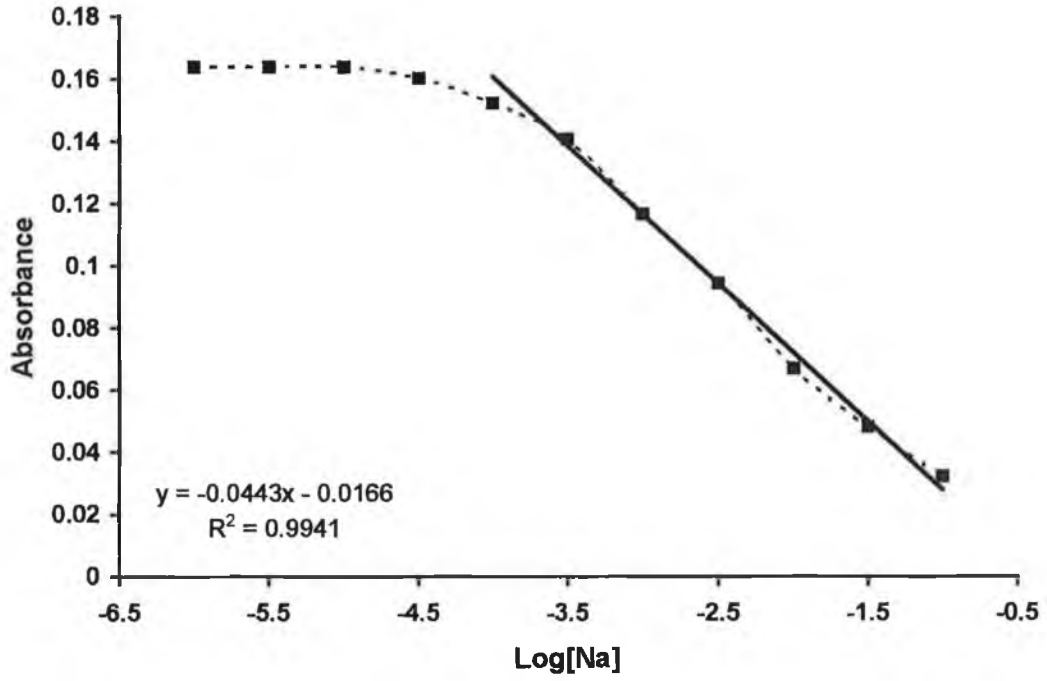

Figure 2.12: Calibration curve for membrane 1 to sodium solutions at pH 8.0

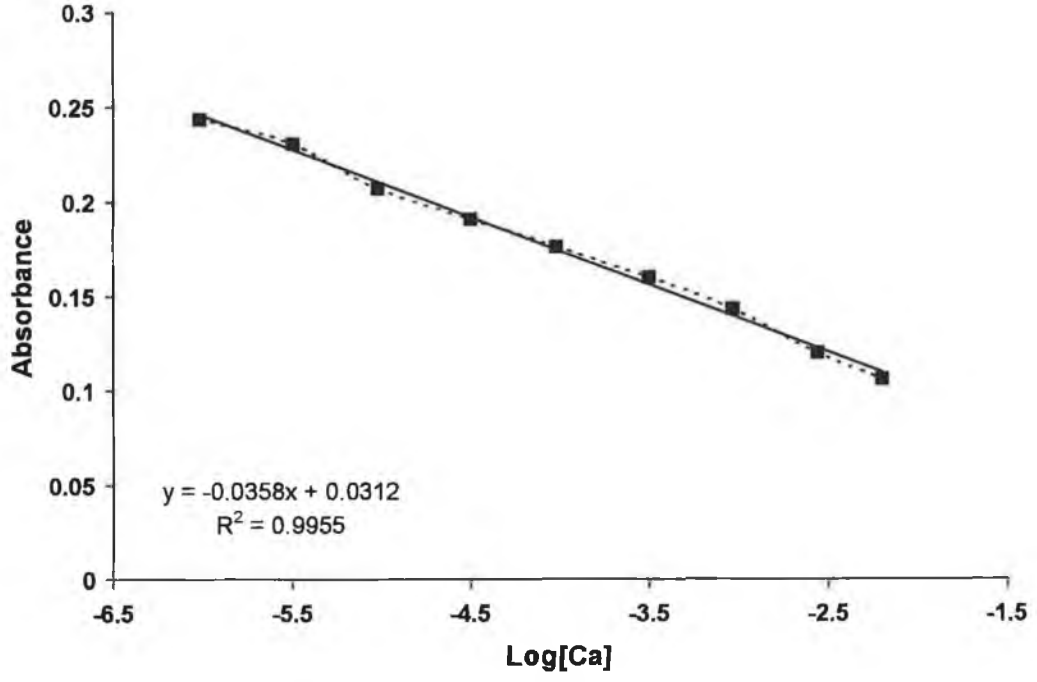

Figure 2.13: Calibration curve for a membrane 2 to calcium solutions at pH 8.0

2.6 Response mechanism and characteristics

Some insight into the underlying reason for the striking reversal of selectivity is provided by the energy-minimised structures shown in figures 6 and 7. In the case of the complex between the tetraester derivative (Figure 2.7, 1) and sodium (Figure 2.14), the sodium ion appears to be bound electrostatically in the polar cavity defined by the four ethereal oxygen atoms on the calixarene lower rim and the four carbonyl oxygen atoms of the esters. This is supported by experimental results which show that similar tetraketone derivatives (which contain the same eight oxygen atoms in approximately the same conformation) exhibits excellent sodium selectivity over other Group I and Group II ions[13], whereas a simple tetraether derivative (which does not possess the carbonyl atoms) is not sodium selective[14].

In the case of the tetraphosphine oxide derivative (Figure 2.1, 2), the energy minimised structure (Figure 2.15) suggests that the calcium ion is located at a much lower position in the calixarene cavity, and interacts solely with the four phosphine oxide oxygen atoms. It seems that the distance between these oxygen atoms and the four ethereal oxygen atoms at the calixarene lower rim (defined by the two methylene spacer groups) is too large to enable the sodium ion to interact simultaneously with all eight oxygen atoms, and the basis of the exquisite sodium selectivity of many calix[4]arene tetraesters is lost.

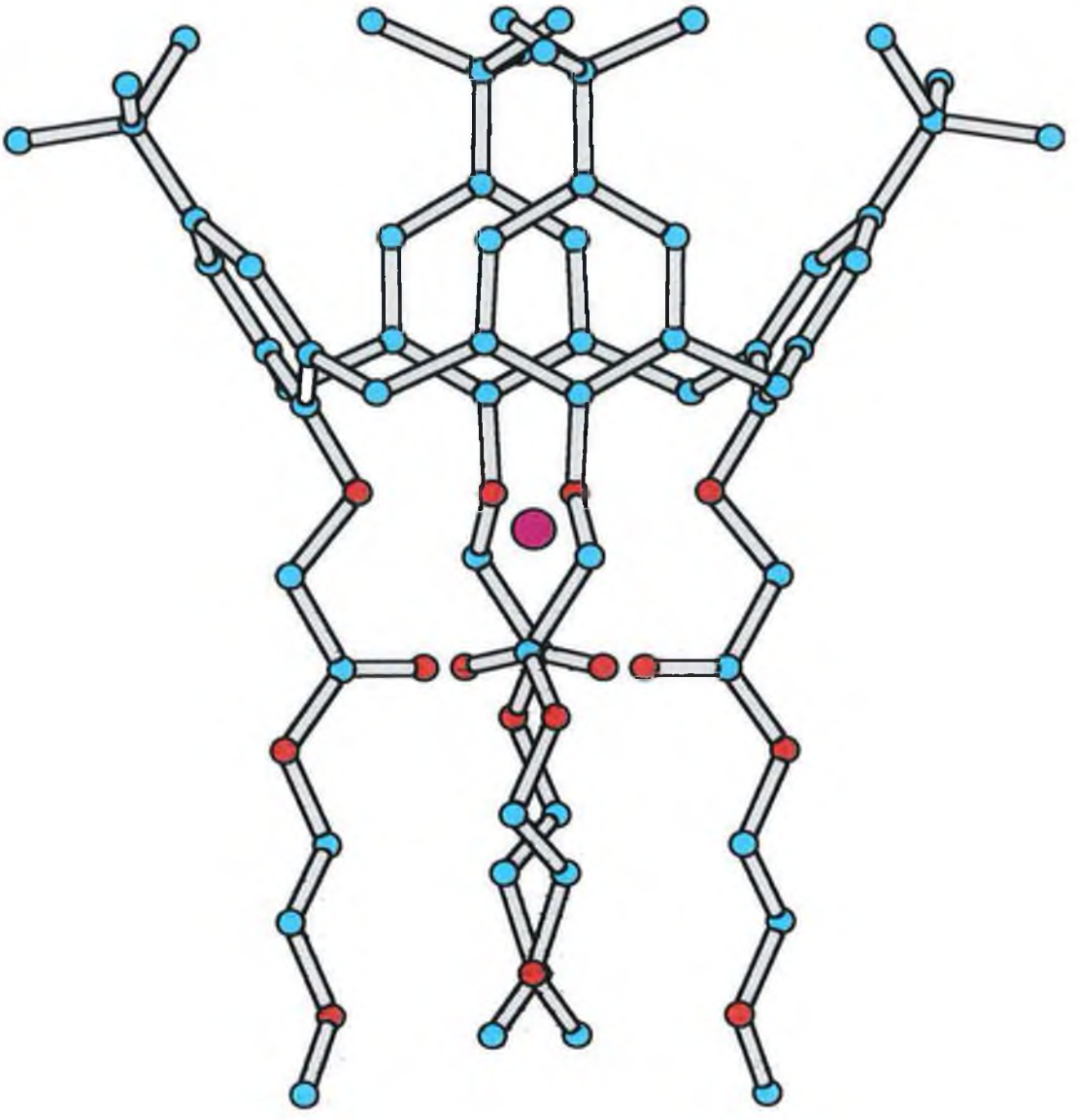

Figure 2.14: Side view of 3-d structure of the ligand 1:Na^+ complex (Hyperchem V4.0).
The energy minimised structure suggests the sodium ion is located in a negatively polarised cavity defined by the four phenyl oxygen atoms immediately below the calixarene lower rim.
(key: oxygen atoms: red; carbon atoms: light blue; sodium ion: purple, hydrogen atoms omitted for clarity).

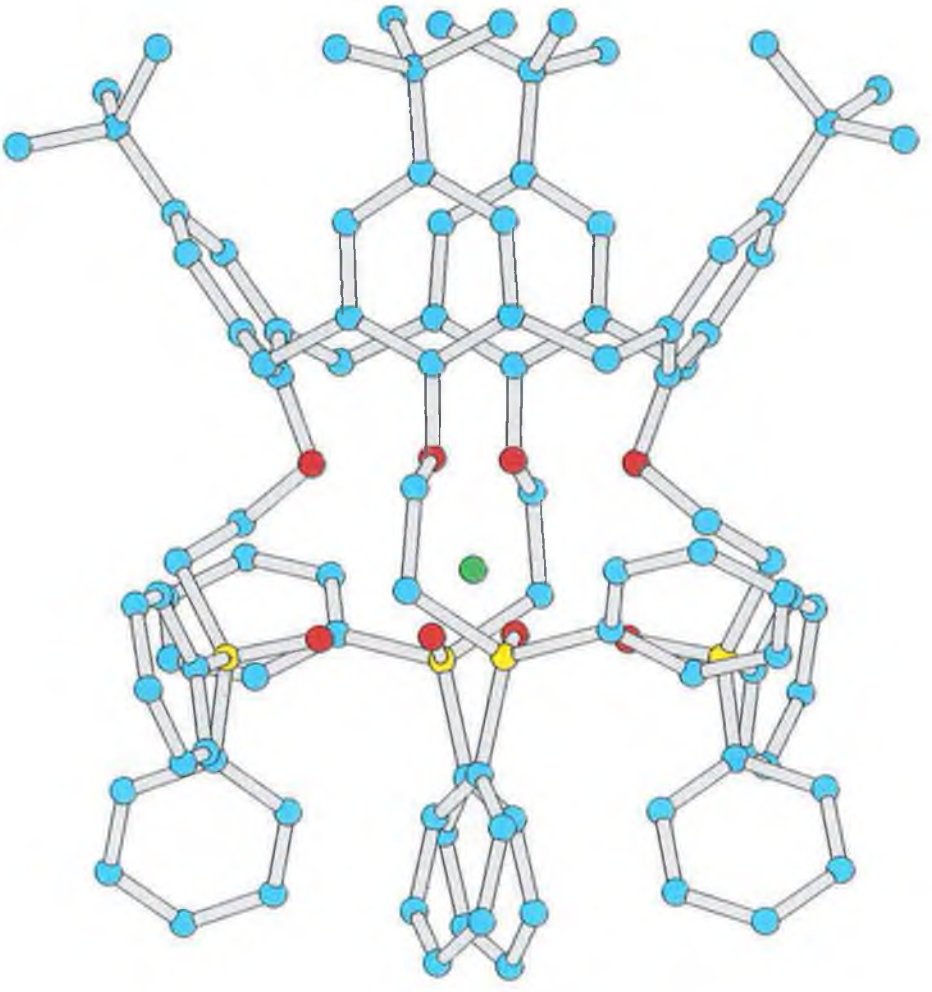

Figure 2.15: Side view of 3-d structure of the ligand 2:Ca^{2+} complex (Hyperchem V4.0).
The energy minimised structure suggests the calcium ion is located in a negatively polarised cavity defined by the four phosphine oxide oxygen atoms well below the calixarene lower rim and there is no interaction with the four phenyl oxygen atoms which are separated from this region by two methylene groups in each pendent chain
(key: oxygen atoms: red; carbon atoms: light blue; calcium ion green, phosphorus atoms: yellow; hydrogen atoms omitted for clarity)

2.6.1 kinetics

Theory dictates that an ion's diffusion through a lipophilic medium is affected significantly by it's charge density and its ionic radius. An ion with a highly concentrated charge density will diffuse more slowly through a medium of this type, whereas a sparsely charged ion will have a much greater freedom of movement.

This is evident in the response traces of the membranes presented here. We can see from Figure 2.16 that the response time of membrane 1 to a solution change of approximately 0.5 Log units of sodium at constant pH is less than 50 seconds.

The response of membrane 2 however is in the region of >400 seconds, with an initial interfacial response being completed in ca. 75 seconds (Figure 2.17). The extended response time is due to diffusion-limited effects. This is in complete contrast with membrane 1 where the response times are much shorter. However, we see that when we expose membrane 2 to sodium (an ion with a smaller charge density), we see a striking difference in response time (Figure 2.18). The membrane now has a response time of under 100 seconds. While this is still not as quick as membrane 1 with sodium, the sodium ion is not the preferred ion of the tetraphosphine oxide, and therefore incurs a less favourable interaction and hence a slightly slower response time.

By modelling the dynamic response according to an equation presented by Spichiger et al.[15], diffusion constants of $6.9\pm0.3\times10^{-14}cm^2s^{-1}$, $7.0\pm0.4\times10^{-15}cm^2s^{-1}$, $1.1\pm0.3\times10^{-14}cm^2s^{-1}$ for membrane 1 with sodium, membrane 2 with calcium and membrane 2 with sodium respectively.

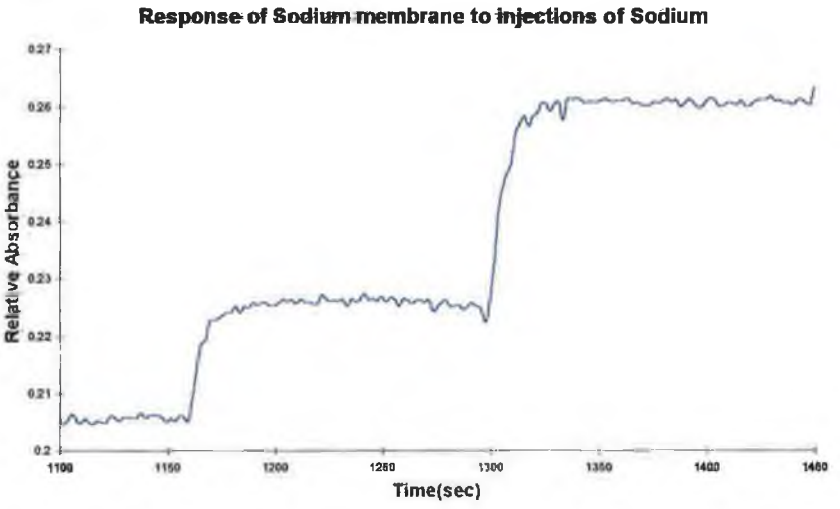

Figure 2.16: Dynamic response of Membrane I to sodium chloride. Membrane thickness of 3.2 μm, and a diffusion constant of $6.9x10^{-14}cm^2s^{-1}$ were estimated by modelling.

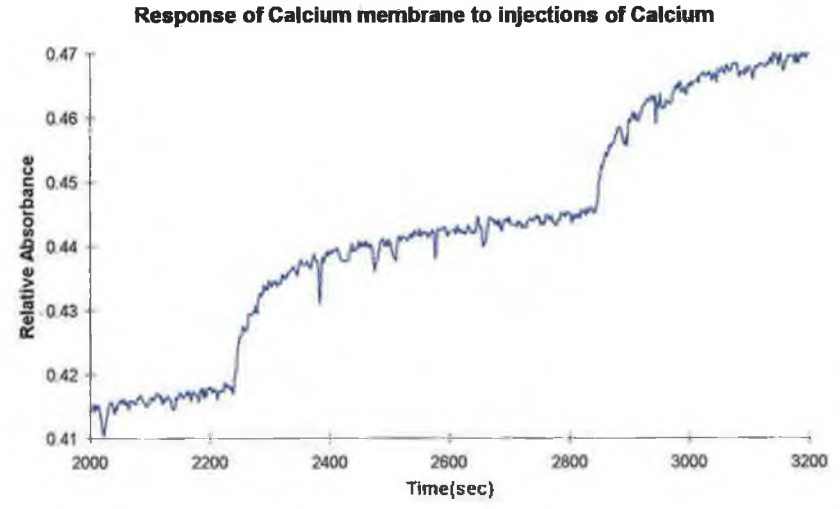

Figure 2.17: Dynamic response of Membrane II to calcium chloride. Membrane thickness of 3 μm and a diffusion constant of $7.0x10^{-15}$ cm^2s^{-1} were estimated by modelling.

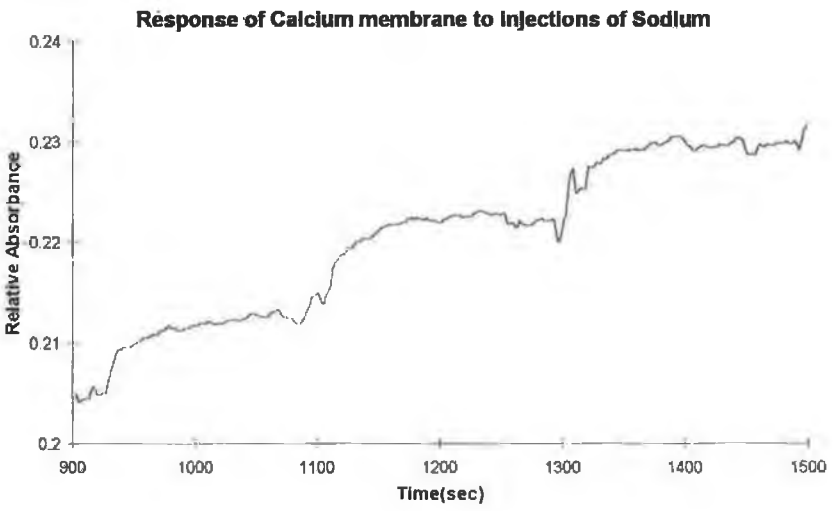

Figure 2.18: Dynamic response of Membrane II to sodium chloride. Membrane thickness of 2.6 μm, and a diffusion constant of $1.1x10^{-14}$ cm^2s^{-1} were estimated by modelling.

2.6.2 Effect of pH on membrane response

In order to investigate the response of pH on the response of membranes 1 and 2, calibration were carried out for ions at pH 7.0. The responses can be seen in Figure 2.19 and Figure 2.20 for membrane 1 and Figure 2.21 and Figure 2.22 for membrane 2.

We see for membrane 1 that the response is somewhat different from that at pH 8.0. The limit of detection has shifted from lower activities to higher activities. The shift in response is ca. 1 log unit. This is in accordance with theory, which states that a decrease in pH is accompanied by a raising of the detection limit by 1 log unit for a singly charged ion.

The response for membrane 2 is significantly different at pH 7.0 than at pH 8.0 for one main reason. The limit of detection of this membrane is now visible in the response. Clearly the limit of detection at pH 8.0 was just below the ion activity range investigated. Again however, we see that membrane 1 has a higher sensitivity than that of membrane 2.

These results are in good agreement with both theoretical descriptions of the membrane response and other works published.

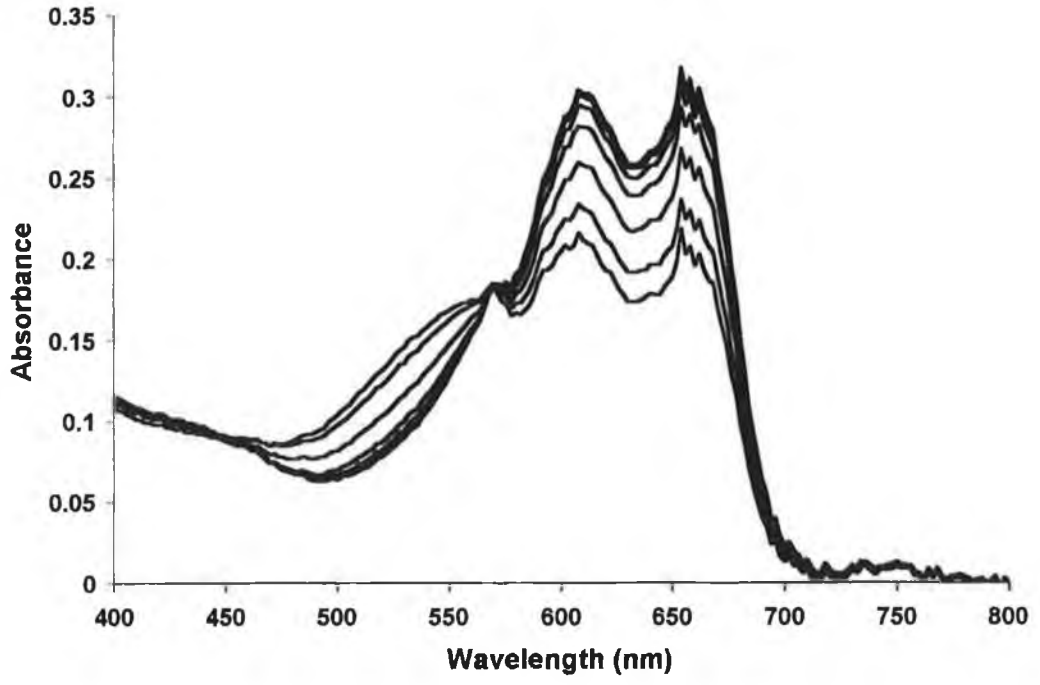

Figure 2.19: Spectral response of membrane 1 to sodium solutions pH 7.0

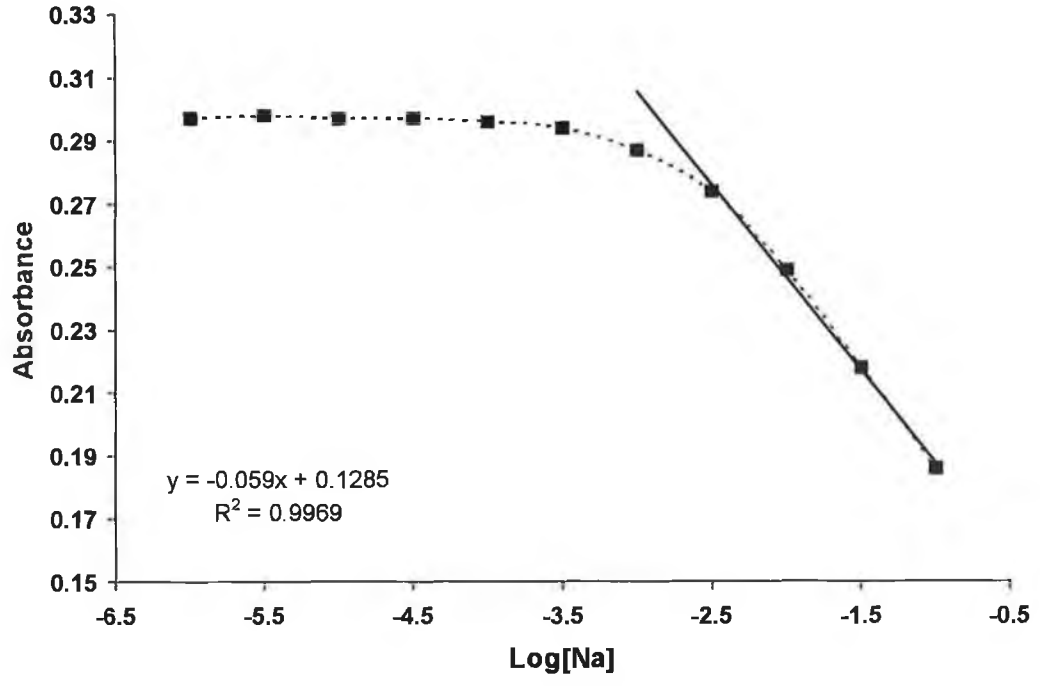

Figure 2.20: Response of membrane 1 to sodium solutions pH 7.0 @ 660 nm

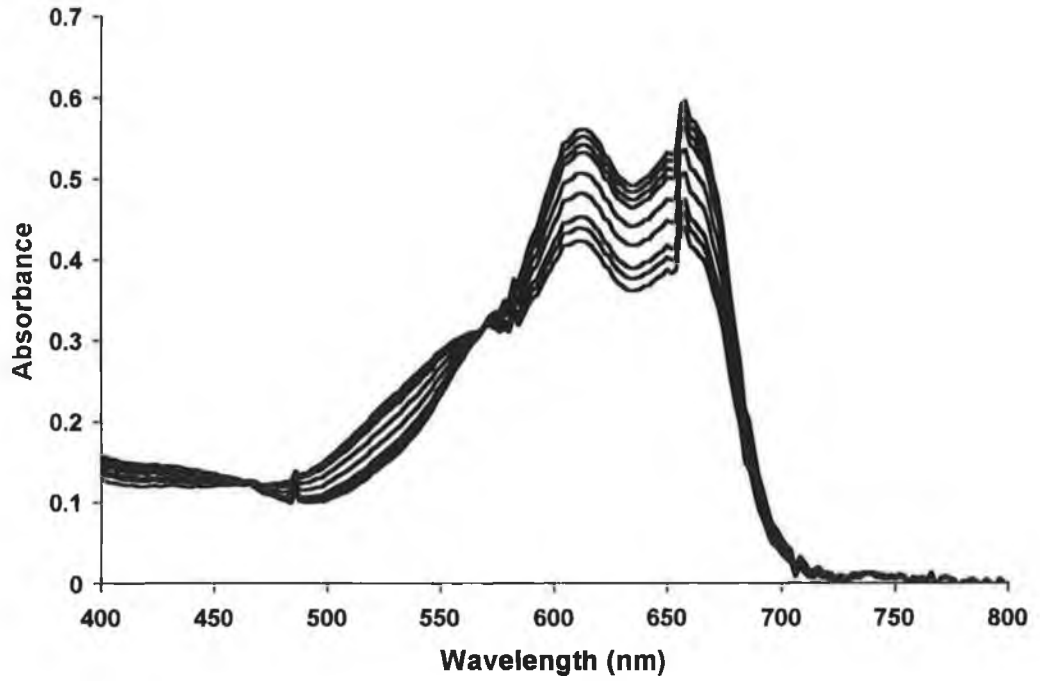

Figure 2.21: Spectral response of membrane 2 to calcium ions pH 7.0

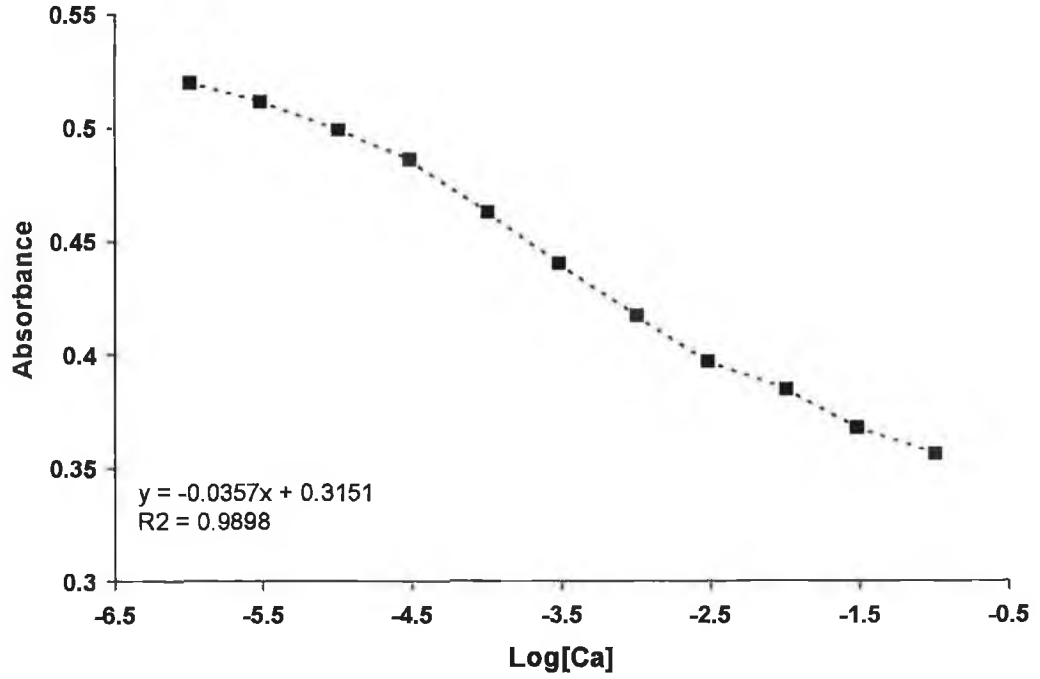

Figure 2.22: Response of membrane 2 to calcium solutions pH 7.0

2.6.3 Lifetimes

The lifetime of these membranes was found to be quite short with a noticeable (~10%) decrease protonation of the membrane in buffer visible after 1-2 hours. This is clearly not sufficient to allow many measurements to be made with single membranes and made it necessary to use fresh membranes for each calibration.

The lipophilic anionic site is responsible for controlling the number of positively charged species within the membrane, and any decrease in the concentration of this is accompanied with a corresponding decrease in protonation within the membrane. The acid-catalysed decomposition of this component is a problem in these membrane. Substituting a more stable version of this anionic site is the best way of negating this problem. One such compound reported is sodium tetrakis[3,5-bis(trifluoromethyl)phenyl]borate.

The lipophilic dye ETH 5294 is quoted as being susceptible to degradation by a combination of UV light and oxygen. Thus the lifetime of this species is limited since the membrane exists for much of it's time directly in a UV/VIS lightpath. One way of possibly counteracting this problem is by degassing all solutions before use and maintaining either a vacuum or an inert gas atmosphere for the duration of the experiment. Neither of these approaches were taken as the lifetime of the membranes were not likely to be improved by a significant amount since the anionic site degradation was likely to remain the most significant problem.

All active components within the membrane are susceptible to leaching. All of the active components (Calix[4]arene, anionic site, ETH dye) are maintained in the membrane purely by means of the fact that they are more soluble in organic medium (membrane) than in aqueous media (sample). However, none of the components or plasticisers are infinitely lipophilic, so a certain amount of leaching is to be expected. While this may not be an immediate problem with potentiometric membranes, the problem is exaggerated in optodes because of the very thin nature of the membranes involved.

2.7 .Conclusion

The optical membranes reported respond well to increasing concentrations of the primary ion of the relevant ionophore and retain their general potentiometric selectivity behaviour except for the inherent sensitivity of the optode membranes to pH. This indicates that, in accordance with the assumptions made in the derivation of the proposed membrane response mechanism, the ion-selective ligand incorporated into the membrane phase dominates the ion-exchange patterns.

The dependence of the membranes to pH has been shown to agree well to the theoretically derived relationship. Increasing the sample pH has been shown to result in a signal which allows lower activities of primary ion to be investigated. The opposite also holds true.

Preliminary investigations into the dynamic response of the membranes shown the system to be diffusion-limited, with a good agreement found between a theoretically derived diffusion equation and experimental data.

The presence of an ionic site susceptible to acid catalysed degradation within the membrane has been identified as a major source of drift in the sensor. Substitution of this species with a more stable anionic site may yield a more stable sensor signal.

2.8 Appendix 1: Derivation of steady state response model

Taking sodium as an example ion and assuming a 1:1 ligand:ion ratio, the following general equilibrium can be used to describe the optode response process.

$$Na^+_{(aq)} + HI^+_{(org)} + L_{(org)} \xleftrightarrow{K_{exch}} NaL^+_{(org)} + H^+_{(aq)} + I_{(org)}$$

where (aq) and (org) denote species in the aqueous and organic phases respectively, and L and I are the ligand and indicator dye respectively.

From this equation the following can be stated

$$K_{exch} = \frac{(a_{Na^+})[HI^+][L]}{[NaL^+](a_{H^+})[I]} = \frac{(\beta_{HI} + k_{H^+})}{(\beta_{NaL^+} + k_{Na^+})}$$

Equation 2.6

Where a_{Na^+} and a_{H^+} are the aqueous activities of sodium and protons respectively,

$[HI^+]$, [L], $[NaL^+]$, [I] are the membrane-immobilised concentrations of the protonated dye, free ligand, complexed ligand and deprotonated dye respectively,

β_{HI^+} and β_{NaL^+} are the complex formation constants for the pH dye and the ion-selective ligand respectively,

k_{H^+} and k_{Na^+} are the analytical concentrations within the membrane of free protons and sodium ions respectively and

K_{exch} is the overall exchange constant as described in Equation

With [A⁻] as the net concentration of negative sites in the membrane, the electroneutrality condition leads to the following concentration relationship

$$[HL^+] + [NaL^+] = [A^-]$$
$$\therefore [HL^+] = [A^-] - [NaL^+]$$
$$\therefore [NaL^+] = [A^-] - [HL^+]$$

Equation 2.7

If the concentration ratios of complexed relative to total ionophore present in the membrane phase are denoted by α (pH dye) and α' (Ion-selective ligand), then

$$[I] = \alpha\, L_T;\ [HI^+] = (1-\alpha)L_T$$
$$[L] = \alpha'\, I_T;\ [NaL^+] = (1-\alpha')I_T$$

Equation 2.8

Where I (pH dye) and L (Ion-selective ligand) are the total concentrations of the different neutral carrier ligands in the membrane.

The absorbance of the membrane system is obviously related to the fraction α of the deprotonated pH dye I :

$$Abs = Abs_1\alpha + Abs_0(1-\alpha)$$
$$\alpha = \frac{(Abs - Abs_0)}{(Abs_1 - Abs_0)}$$

Equation 2.9

where Abs_1 and Abs_0 are the limiting absorbance values for the system (Figure 2.23).

Then, taking Equation 1 and substituting with notice to Equation 3 we get

$$\frac{1}{K_{exch}}\frac{(a_{Na^+})}{(a_{H^+})}=\frac{(A_T-(1-\alpha)I_T)(\alpha)}{(1-\alpha)[L]}$$

Equation 2.10

Then, considering

$$[L]=L_T-[NaL^+]=L_T-(A_T-[HI^+])$$

Equation 2.11

we can then substitute this for the term [L] in equation 5 to ultimately yield

$$\frac{1}{K_{exch}}\frac{(a_{Na^+})}{(a_{H^+})}=\frac{(\alpha^2)(R_T-(1-\alpha)I_T)}{(1-\alpha)(L_T-R_T-(1-\alpha)I_T)}$$

Equation 2.12

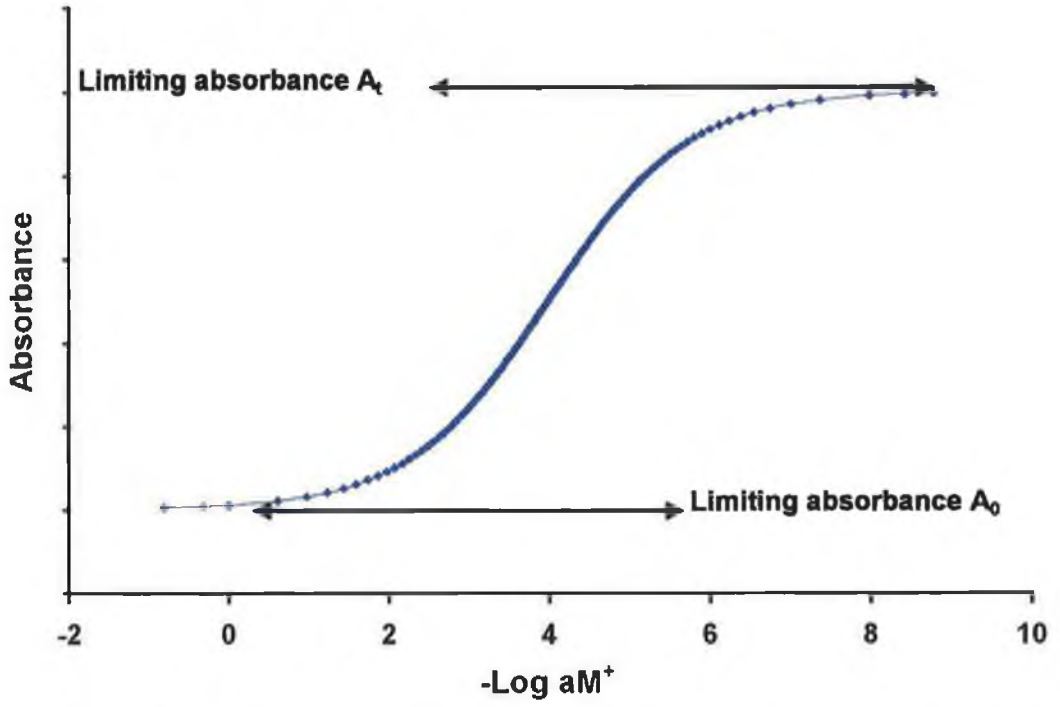

Figure 2.23: Schematic of the limiting absorbances Abs_t and Abs_0 with regard to the defined response curve for ion-selective optode membranes.

2.9 Appendix 2: Modelling of membrane dynamic response

Modelling of the dynamic response of the membranes was performed using a modified Fick's diffusion law. It is assumed that diffusion through the PVC layer is the rate-determining step in the response of such membranes.

$$Flux = -D_i \frac{d\ c_i}{\delta x}$$

Equation 2.13: Fick's first law
Where D is the diffucion constant, c_i is the concentration of the diffusing species and x is the depth of diffusion

Fick's first law states that the net movement of molecules per unit time is proportional to the concentration gradient

Fick's second law pertains to the change in the concentration gradient as a function of time. It is derived from the first law by noting that the change in concentration at a location is given by the differences in the flux into and the flux out of an element of width dx.

$$\frac{\delta c_i}{\delta t} = D_i \frac{\delta^2 c_i}{\delta x^2}$$

Equation 2.14: Fick's second law
Where D is the diffusion constant, c_i is the concentration of the diffusing species and x is the depth of diffusion

The model employed in this research is based on this second law with some assumptions made pertaining to planar solid-state membranes

- Diffusion is assumed to be only into the membrane perpendicular to the membrane/solution interface. Any diffusion longitudinally across the

membrane is ignored or assumed constant. This is based on the assumption that any solution in contact with the membrane is homogenous in composition and that no concentration gradients exist within the sample.

- The flux of molecules, once it has reached the limit of the PVC layer (glass slide in this case) is reversed in direction. The reversal of ion/molecule direction is due to the assumption that the glass support for the membrane is totally impermeable to the species present within the membrane.

Once these assumptions have been taken into account, the following equation is achieved[15].

$$X_t = \left[k\left(1-\frac{4}{\pi}\right)\right]\left[\sum_{n=0}^{\infty}\left(\frac{-1^n}{2n+1}\right)e^{\left(-(2n+1)^2(\pi)^2\left(\frac{t-t_0}{4}\right)\left(\frac{D}{d^2}\right)\right)}\right]$$

Equation 2.15:

Where X_t is the response at time t, k is a constant for a given response, t is the time since the start of the response, t_0 is the initial point of response, D is the diffusion constant and d is the thickness of the membrane layer.

Since the summation from 0 to infinity is not practical to implement, the first 20 iterations were chosen as any values past this tended rapidly to zero.

2.10 References

[1] W.E. Morf, K. Seiler, B. Lehmann, Ch. Behringer, K. Hartmann, W. Simon, Pure appl. Chem., 1989, 61, 1613-1618

[2] Kortum, G., M.T. Seiler, Angew. Chem., 52, 1939, 687

[3] Non-linear computer modelling of chemical and biochemical data, J.F. Rusling, T.F. Kumosinski, Acedemic Press, ISBN 0126044902.

[4] Walsh, S. and Diamond, D., *Talanta*, **42(4)**, 1995, 561-572

[5] Diamond, D., Hanratty, V., "Spreadsheet applications in chemistry using Microsoft Excel" 244p, 1997, ISBN 0471140872

[6] J. F. Malone, D. J. Marrs, M.A. McKervey, P. O'Hagan, N. Thompson, A. Walker, F. Arnaud-Neu, O. Mauprivez, M.-J. Schwing-Weill, J.-F Dozol, H. Rouquette and N. Simon, J. Chem. Soc. Chem. Commun., 1995, 2151

[7] F. Arnaud-Neu, G. Barrett, S. Cremin, M. Deasy, G. Ferguson, S.J. Harris, A.J. Lough, L. Guerra, M.A. McKervey, M.J. Schwing-Weill, and P. Schwinte, J. Chem. Soc, Perkin Trans., 1992, 2, 1119

[8] E. Bakker, M. Lerchi, T. Rosatzin, B. Rusterholz, W. Simon., Anal. Chim. Acta 1993 278, 211-225

[9] M. Lerchi, E. Bakker, B. Rusterholz and W. Simon Anal. Chem. 1992, 64, 1534-1540

[10] K. Cunningham, G. Svehla, S.J. Harris and M.A. McKervey, Analyst, 1993, 118, 341

[11] W.H. Chan, A.W.M. Lee, C.M. Lee, K.W. Yau, K. Wang, Analyst, 120, 1995, 1963

[12] P. Kane, K. Kincaid, D. Fayne, T. McKittrick, D. Diamond, In preparation.

[13] R.J. Forster, A. Cadogan, M. Telting-Diaz, D. Diamond, S.J. Harris, M.A. McKervey, Sensors and Actuators B, 1991, 4, 325

[14] S. Chang and I. Cho, J. Chem. Soc. Perkin Trans, 1986, 1, 211

[15] U. Spichiger., D. Citterio., M. Bott., E. Pretsch., invited lecture at Environmental sefety conference., Munich, 1992..

3 Ion-selective optode membranes using a novel 9-(4-Diethylamino-2-octadecanoatestyryl)-acridine acidochromic dye

3.1 Introduction

Neutral carrier ion selective optode membranes have been the target of significant research. Sensors of this type have been reported for many analytes such as calcium[1,2,,3], sodium[3,2,4,5] , potassium[2,6,7,8], ammonium[9,10,11], silver[12] and lead[13], among others. Various types of ligand have been used but in this research, we focus on calixarene receptors. Calix[4]arenes[14,15] and calix[6]arenes[16] are already established as ionophores for potentiometric ion-selective electrodes. The ligands presented here, tetramethoxy ethyl ester (Ligand 1) and tetraphosphine oxide (Ligand 2) calix[4]arene derivatives, have previously been reported by the authors[3] in ion-selective optode membranes incorporating the acidochromic dye ETH 5294.

Two ion selective optode membranes incorporating the novel acidochromic dye are presented and ligands for sodium and calcium were investigated in this research. Their performance is compared to identical membranes with the commercially available dye (ETH 5294, dye 1). In particular, the difference in lifetime of the two dyes in discussed.

Modelling of both the steady-state and dynamic responses of these membranes is undertaken. The modelling is done in accordance with the methods outlined in Chapter 2.

3.2 Experimental

3.2.1 Equipment and Apparatus

UV-vis spectra were obtained with an Ocean Optics PS1000 miniature photodiode array spectrometer (Ocean Optics Inc. 1237 Lady Marion Road, Dunedin, Florida, USA 34698-5314). The membranes were prepared by accurately weighing out the quantities shown in Table 1 and dissolving in tetrahydrofuran. From these solutions, membranes of approximately 4μm thickness were obtained by spin coating onto a glass slide using a spin-coater with vacuum attachment (Laurell Technologies Corporation 850 North Wales Road, Lansdale, PA 19446-6104, USA). Two such coated slides were placed into a flow-through cell as shown in Figure 3.1. The flow-through cell was mounted in a custom-made holder to allow optical interrogation of the membranes immobilised within the cell. By properly immobilising the membrane in such a flow cell as opposed to the method employed in chapter 1, reproducibility and lifetime studies were now possible. All measurements were made in the transmission mode.

All solutions were pH buffered tris/trisHCl (pH 7.3) using quantities as predicted by the Henderson-Hasselbach equation (assuming a pK_a for Tris of 8.1at 25°C[17]) and Lithium Acetate/Acetic acid (pH 5.0). The pH values of samples and buffers were verified using an EDT RE357 pH meter and glass combination electrode (EDT Instruments Limited, Lorne Road, Dover, Kent, CT16 2AA, England).

High molecular weight polyvinyl chloride (PVC), dibutyl sebacate (DBS), sodium tetrakis[3,5-bis(trifluoromethyl)phenyl]borate (NaTFM) and 9-(Diethlyamino0-5-octadecanoylimino-5H-benzo[a]phenoxazine (ETH 5294, dye 1, Chapter 1 Figure 3) were obtained from Fluka, Buchs, Switzerland. Nitric acid used was of Analar

grade (69% w/v) and obtained from BDH (BDH Ltd. Poole, England). Methanol was of HPLC grade and supplied by Lab-Scan (Stillorgan, Dublin).

All chloride salts were obtained from Fluka, Buchs, Switzerland and were of the highest purity available. Water from a Barnstead RO/RF ultrapure water system ($18.3M\Omega cm^{-1}$) was used throughout. Ligands 1 and 2 were synthesised as reported previously[18,19]. The acidochromic dye (9-(4-Diethylamino-2-octadecanoatestyryl)-acridine, dye 2 was synthesised in-house. Conc. Nitric acid used was of Analar grade and obtained from BDH (BDH Ltd. Poole, England). Methanol was of HPLC grade and supplied by Lab-Scan (Stillorgan, Dublin). The three versions of the precursor of dye 2 were synthesised in-house and their structures are given in Figure 3.3.

Mathematical modelling of membrane dynamic and steady state responses was performed as discussed in Chapter 2 Appendices 1 and 2.

3.2.1.1 Determination of dye pK_a

The solution containing the dissolved dye was circulated through a custom-made flow cell giving rise to an optical path-length of approx. 2mm. After each addition of acidified MeOH from the burette the resulting spectrum was relayed to an Ocean Optics spectrophotometer controlled by a national instruments Daq-Pad 700 I/O card connected to a laptop computer.

Approx. 7mg of dye was accurately weighed out and dissolved in 25ml of methanol:water 50:50. The flow cell incorporating two blank glass slides was used as the measuring cell. The resulting solution was then continuously pumped through the flow cell as shown in Diagram 3.1. During the course of the titration with acidified methanol: water (Using nitric acid in 50:50 methanol: water), the absorbance spectrum was measured after each addition (Figure 3.4, Figure 3.6, Figure 3.8) and the absorbance maximum was plotted versus acid added (Figure 3.5, Figure 3.7, Figure 3.9). The equivalence point was obtained by linear

extrapolation of the rising and constant portion of the plot. The difference between the absorbance at this point and the expected 100% absorbance allows estimation of the amounts of each species present at equilibrium and from this, a value of the k_a can be estimated via the mole ratio method (Appendix 3).

	Membrane I	Membrane II	Membrane III	Membrane IV
Ligand 1	6.9 mg	-	6.9 mg	-
Ligand 2	-	18.7 mg	-	18.7 mg
NaTFM	5.4 mg	5.4 mg	5.4 mg	5.4 mg
dye 1	3.6 mg	3.6 mg	-	-
dye 2	-	-	3.9 mg	3.9 mg
Dibutyl Sebacate	250 mg	250 mg	250 mg	250 mg
Polyvinyl Chloride	125 mg	125 mg	125 mg	125 mg

Table 3.3: membrane compositions.

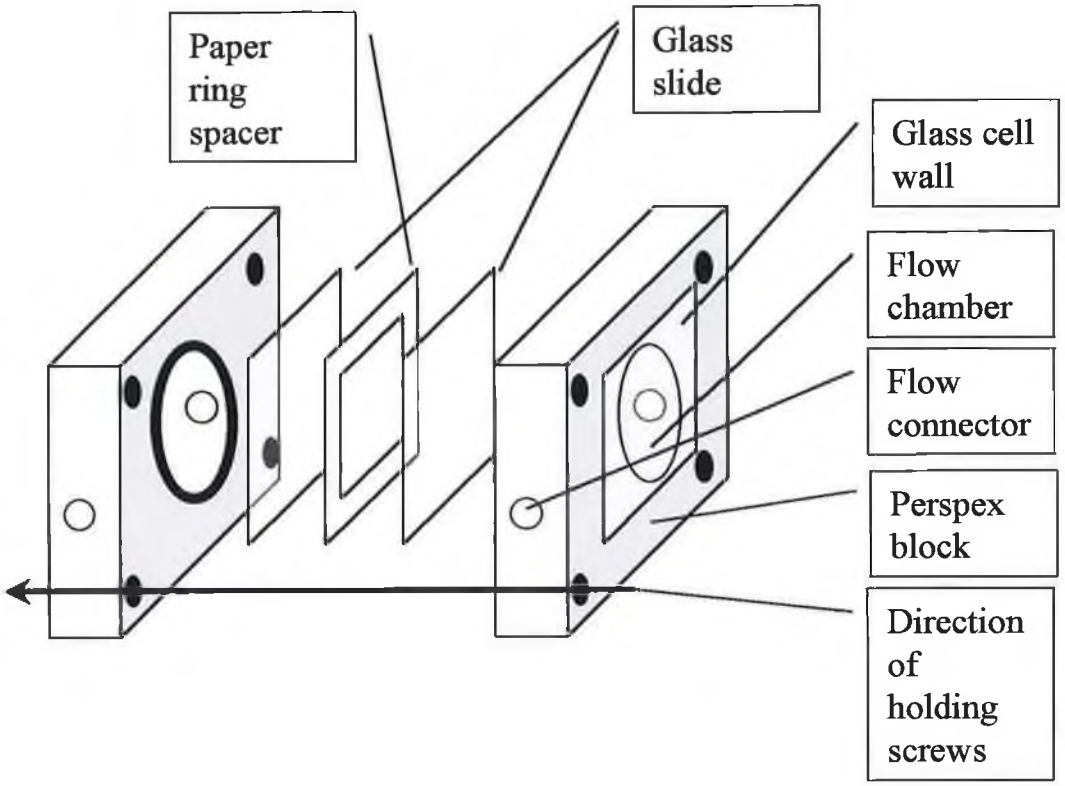

Figure 3.1 : Schematic of Flow cell diagram

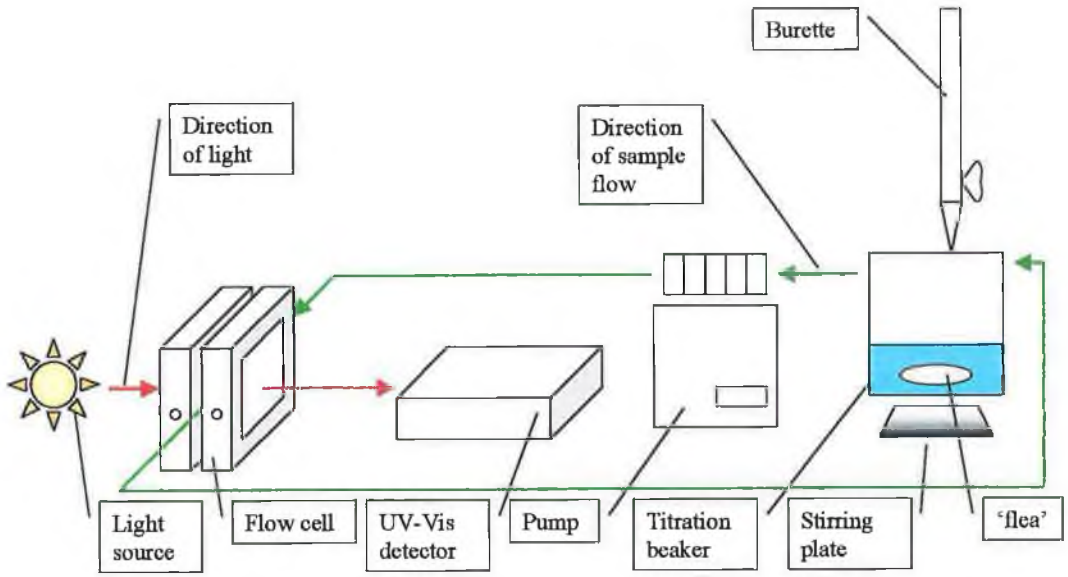

Figure 3.2: Schematic of experimental setup for determintaion of dye Pk_a.

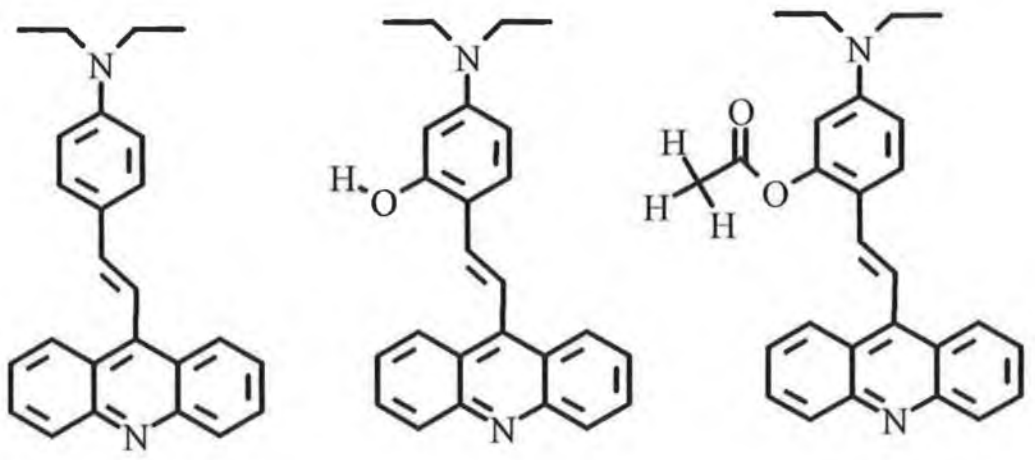

Figure 3.3: Structure of three dyes investigated.

3.3 Results and discussion

3.3.1 Spectral response

The change in spectrum upon introduction of acid is quite dramatic. The peak present initially (450nm deprotonated) decreases in magnitude and a much larger peak (600nm protonated) emerges. The degree of change in spectrum is proportional to the amount of acid added. After complete titration, the dye is present only in its protonated form. On addition of a large excess of acid, a second change occurred. This time the protonated peak at 600nm disappears and a peak similar to the initial deprotonated peak is generated (425nm). The spectral change during the titration for the three dyes is shown in figures 1,2 and 3. The accompanying colour change during the titration is Yellow to Blue.

Using the initial change in absorbance at the absorbance maximum (~600nm) as the measure of change in spectrum, a titration curve was constructed for each dye (Figures 2,3,and 4). The difference between the absorbance at equivalence and the maximum absorbance was used to estimate the pKa of the dye.

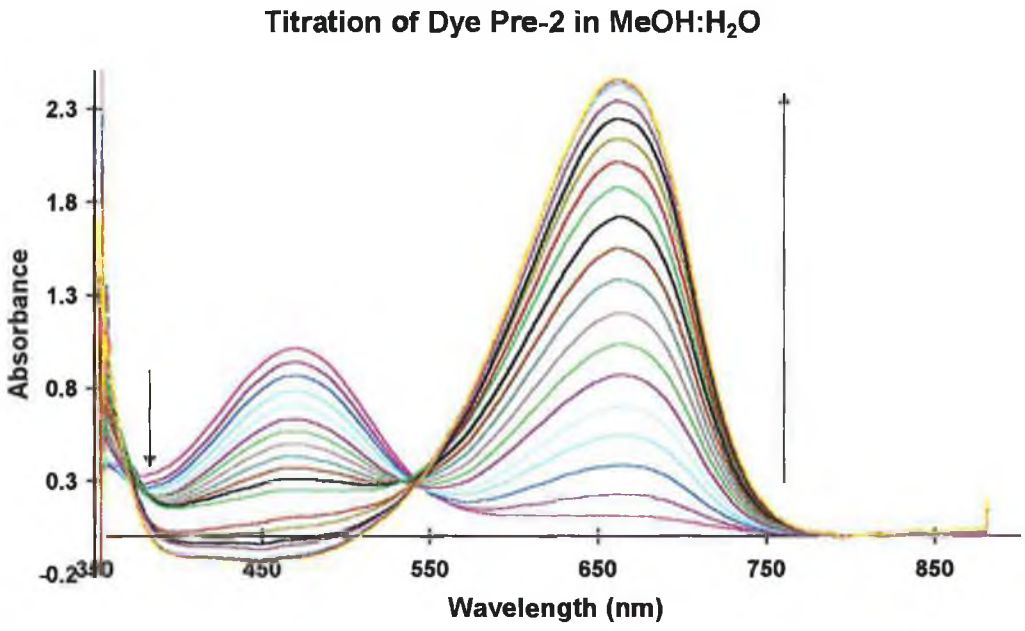

Figure 3.4: Spectral change associated with titration of dye Pre-2 with HNO_3.

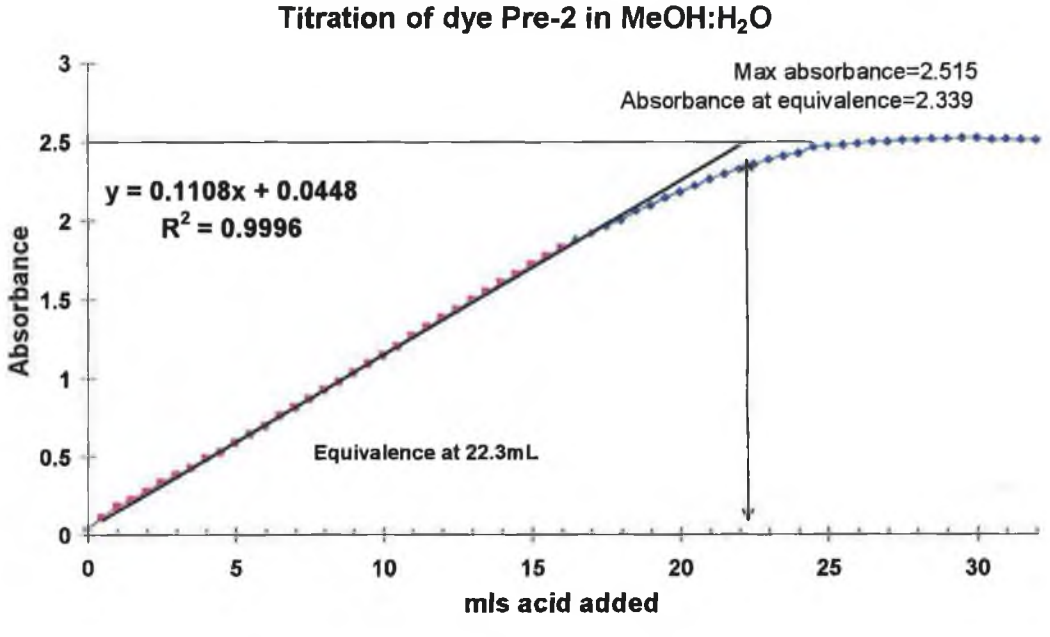

Figure 3.5: Plot of absorbance versus acid added for titration of dye Pre-2.

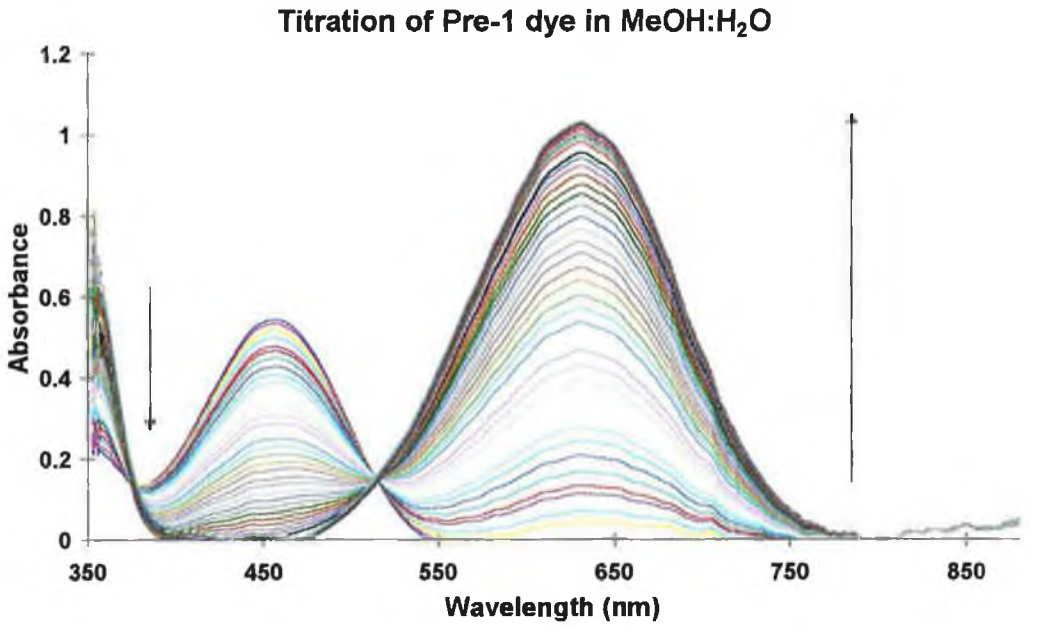

Figure 3.6: Spectral change associated with titration of dye Pre-1 with HNO_3.

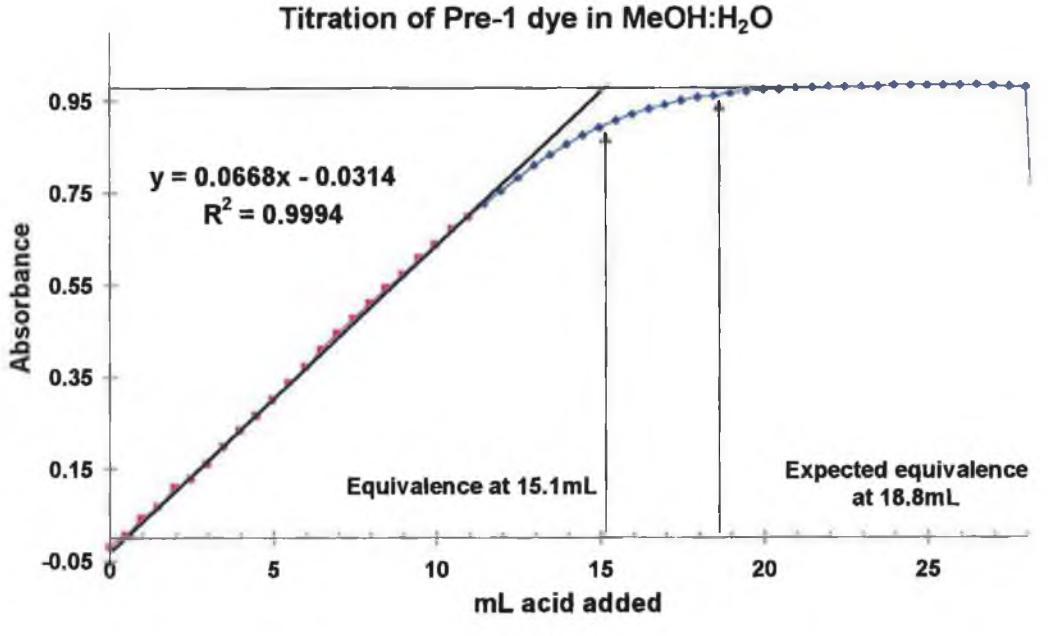

Figure 3.7: Plot of absorbance versus acid added for titration of dye Pre-1.

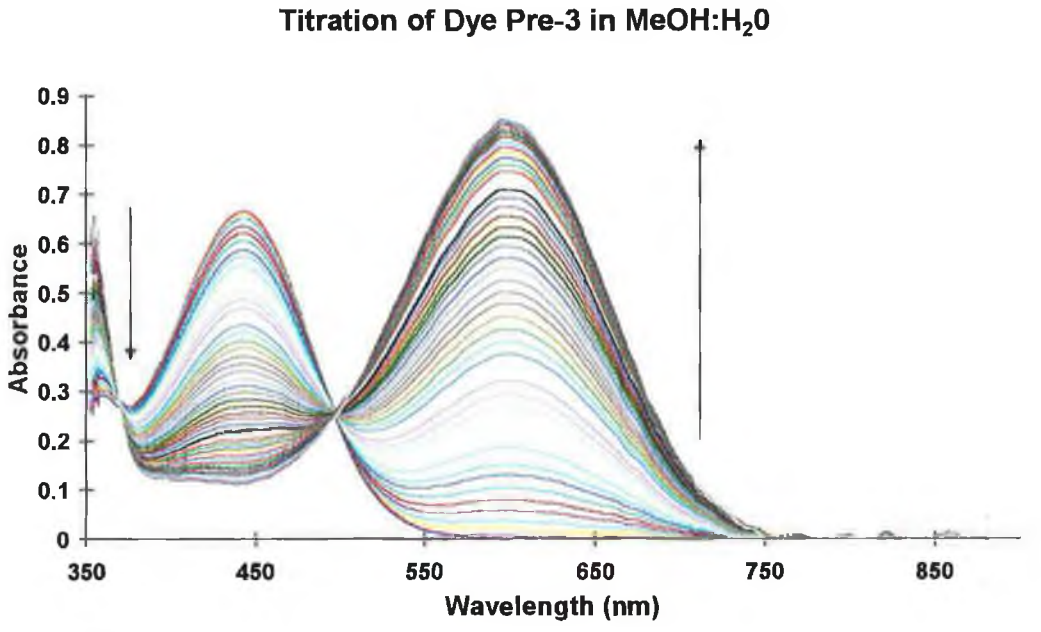

Figure 3.8: Spectral change associated with titration of dye Pre-3 with HNO_3.

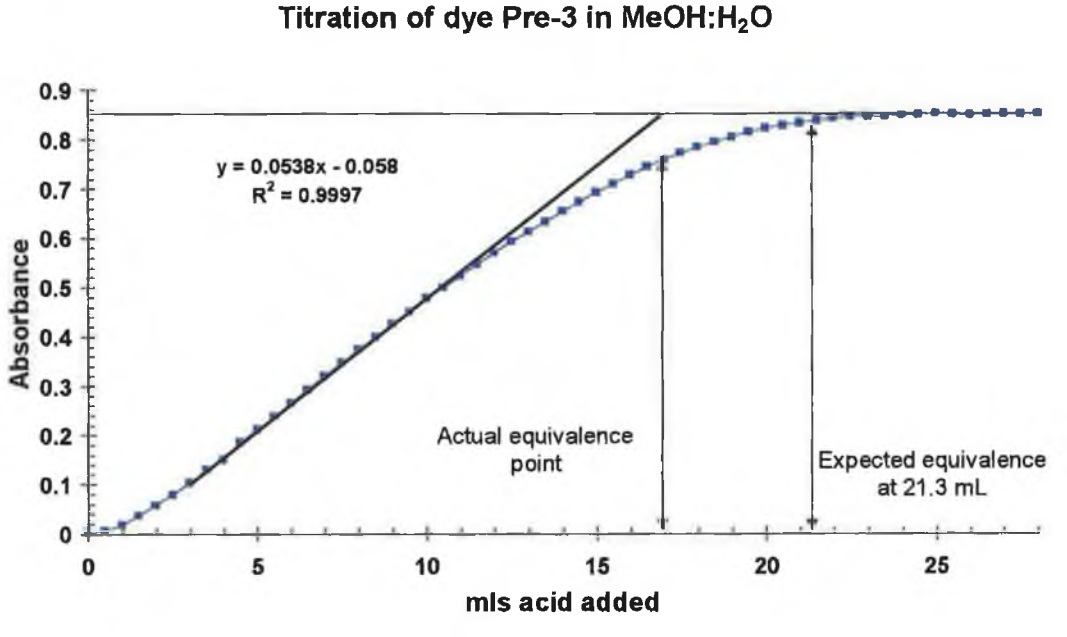

Figure 3.9: Plot of absorbance versus acid added for titration of dye Pre-3.

dye Pre-1	5.43±0.05 pK_a with 80.3% estimated purity.
dye Pre-2	5.53±0.04 pK_a with 100% estimated purity.
dye Pre-3	5.27±0.06 pK_a with 78% estimated purity.

The purities of the compound mixtures were estimated by comparing the theoretical equivalence (From the amount weighed out for the experiment) to the actual experimental equivalence. This assumes of course that any impurities do not react with the HNO_3 added during the course of the experiment.

The pK_a values found here compare well with those in the literature for similar compounds[20].. The value of 5.2-5.4 also equates well with the pK_a of acridine, whose structure is shown in Figure 3.10. This compound is an important moiety within the dye 2, and the similarity between the pK_as found here and the pKa of this compound suggest strongly that it is the acridine nitrogen that is protonated. Literature supports this as the observed pK_a in isopropanol : water was found to be 5.65, while the true pK_a in the membrane phase phase was found to be 7.8[20]. The solvent used can be assumed to play a role in the effective pK_a of the dye.

Dyes similar in structure to those presented here have also been used in PVC films as pH sensitive sensors[21].

Dye Pre-2 was made more lipophilic in order to facilitate membrane-bound systems in later experiments. This was chosen due to its high estimated purity. The synthetic pathway is reported in the literature[22]. The structure of this modified compound can be seen in Figure 3.11.

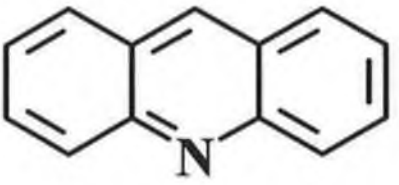

Figure 3.10: Structure of Acridine, pK_a 5.6.

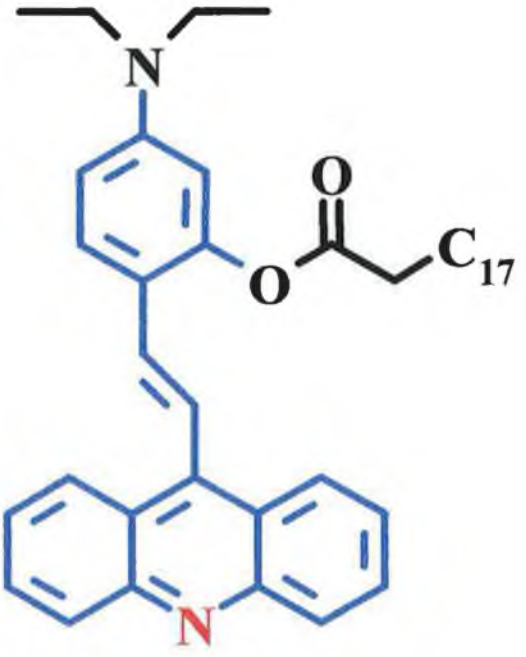

Dye **2**

Figure 3.11: Structure of lipophilicised dye 2.
The chromogenic part of the dye is hghlighted in blue while the protonateion site is highlighted in red.

3.3.2 Selectivity and Sensitivity

Due to the large difference in pK_a for the two dyes under investigation (10.6 for dye 1 and 5.5 for dye 2) it is evident that membranes incorporating the different dyes will have a different optimum pH. This is illustrated in Figure 3.13 where the response of membranes incorporating dye 1 and 2 are shown at pH 7. The large shift in response is due mainly to the difference in pK_a of the two dyes. Because of this shift in response and the accompanying change in membrane K_{exch}, it was decided measurements with membranes incorporating dye 1 would be performed at pH 5.0 and those with dye 2 at pH 7.3.
An overlay of the calibration plot for membranes I and III (both incorporating Ligand 1) does not yield the same dynamic range for the membranes (Figure 3.14). There is a clear difference in the limit of detection of these two membranes with membrane III having the lower limit of detection. Calibrations with membranes II and IV (both incorporating Ligand 2) display very similar responses over the same activity range (Figure 3.15) with no discernible differences in dynamic range or detection limit. The change in the visible spectrum accompanying this calibration are visible in Figure 3.16 for membrane I and Figure 3.17 for Membrane III. The increased concentration of ligand 2 within these membranes compared to Chapter 2 yields a more sensitive response (Figure 3.15).

Selectivity values for the membranes were estimated by curve fitting to a theoretical model shown in Chapter 1 using the SOLVER function within Microsoft Excel. The difference in K_{exch} obtained between the different ions was used to estimate selectivity[23]. Selectivity values obtained are in good agreement as most interfering ions tested (Table 3.4) giving no discernable response over the activity range tested (10^{-6}M to 0.1M). Where an ion shows no response at all in the activity range chosen, the selectivity is set as being greater than a maximum selectivity value guaranteed to exhibit a response. The values obtained for calcium selectivity show a significant change between the two membranes with

the presence of potassium (A minor interferent) in the pH 5 buffer most likely affecting this result. Selectivity values of ion-selective electrodes incorporating the same two ionophores yield similar selectivities, although there ae some notable differences[24]. Sodium in particular for the membrane incorporating Ligand 2 has markedly different selectivity (2.2 vs. >4). One factor which may be responsible for the disparity between ion-selective electrode and ion-selective optode selectivities is the absence of an internal filling solution. It has been known for some time that the internal filling solution of an ISE affects the selectivity and general response of the sensor.

Values obtained for membrane thickness (4μm±0.2μm) and diffusion constants (10^{-14} cm^2/sec) obtained through mathematical modelling of the optode response are consistent with values expected. The membranes all have 95% response times of <10 seconds at this membrane thickness. However, quoting values for diffusion and response time within these membranes is not entirely representative as the response times vary with both pIon and pH.

3.3.2.1 Effect of pH on dynamic response of the membranes

It was noted during the course of the experiments performed throughout that the response time of the membrane seemed to vary with different activity of metal ion. It was postulated that the same might be true for different pH values. To investigate this, a time-trace of a membrane at two different pHs, 5 and 7, were taken and modeled.

The values obtained suggested that there is indeed an effect on the rate of response depending on the pH of solution (Figure 3.12). The difference between the diffusion coefficients obtained for a difference of 2 pH units was approximately 30%. The faster response to increasing activity of metal ion was obtained at the higher pH value. The diffusion coefficient obtained for pH 5 was $3.7\pm0.2 \times 10^{-14}$ cm^2s^{-1} while that for pH 7 was $4.8\pm0.3 \times 10^{-14}$ cm^2s^{-1}.

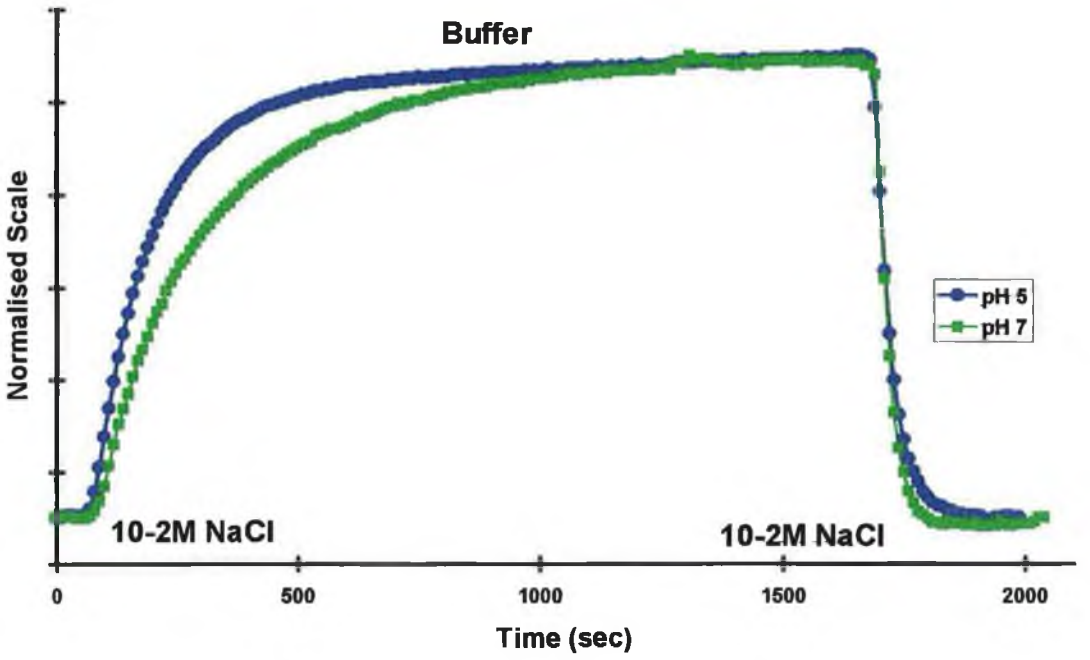

Figure 3.12 : Comparison of membrane 1b (thickness approx. 5μm) kinetics at pH 5 and 7.
There is approximately a 30% difference in the observed rate of diffusion between these two pHs.

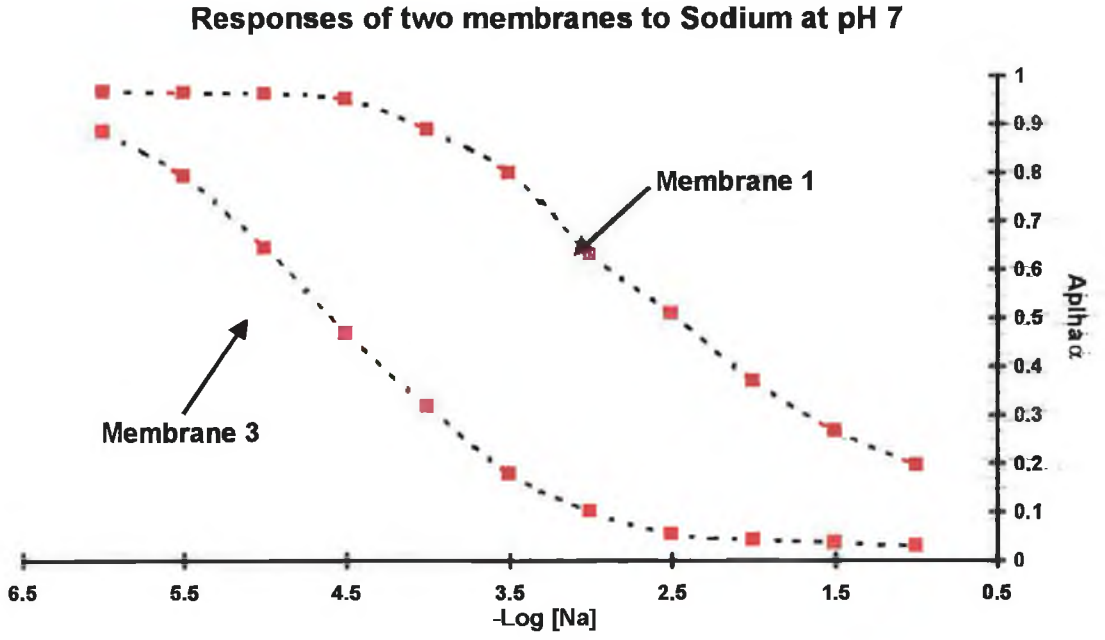

Figure 3.13 : comparison of membrane 1 and 3 dynamic ranges at pH 7.

The visible shift in the dynamic range is due to the difference in Ka between the two dyes used.

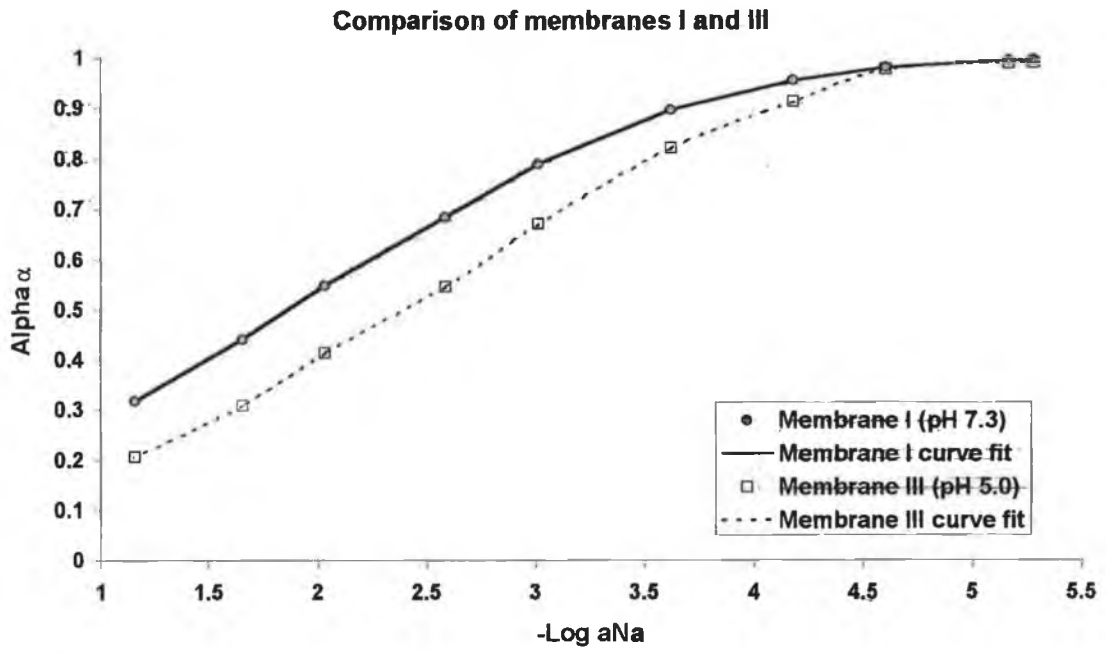

Figure 3.14 : Comparison of Membrane I and III modelled responses at pH 7.3 and 5.0, respectively and fits to these data based on Equation

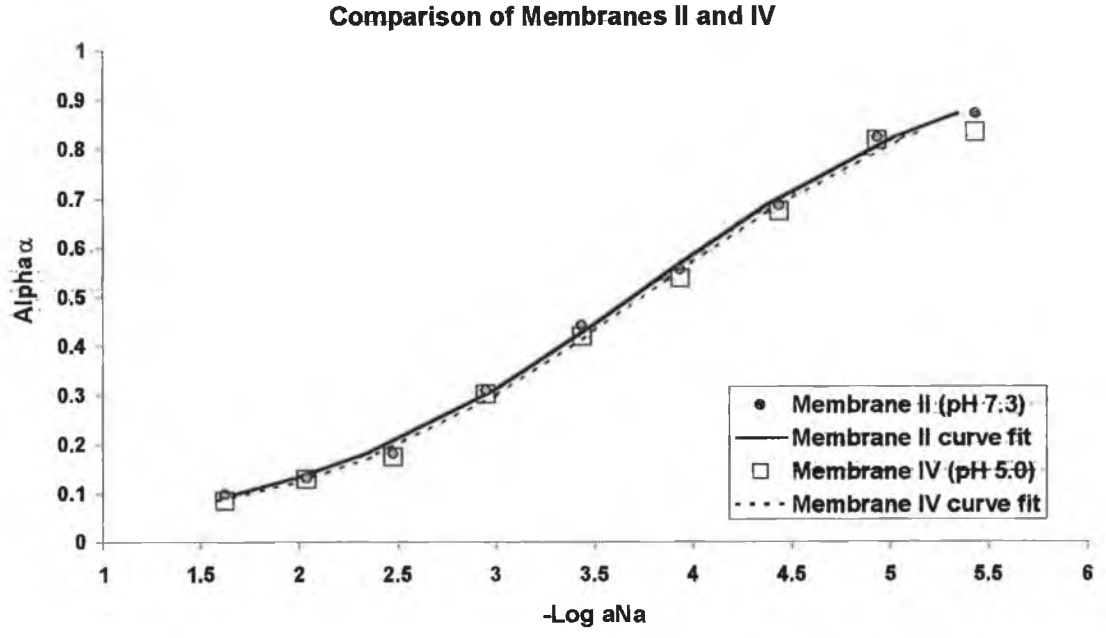

Figure 3.15 : Comparison of membrane II and IV modelled responses at pH 7.3 and 5.0, respectively and fits to these data based on Equation

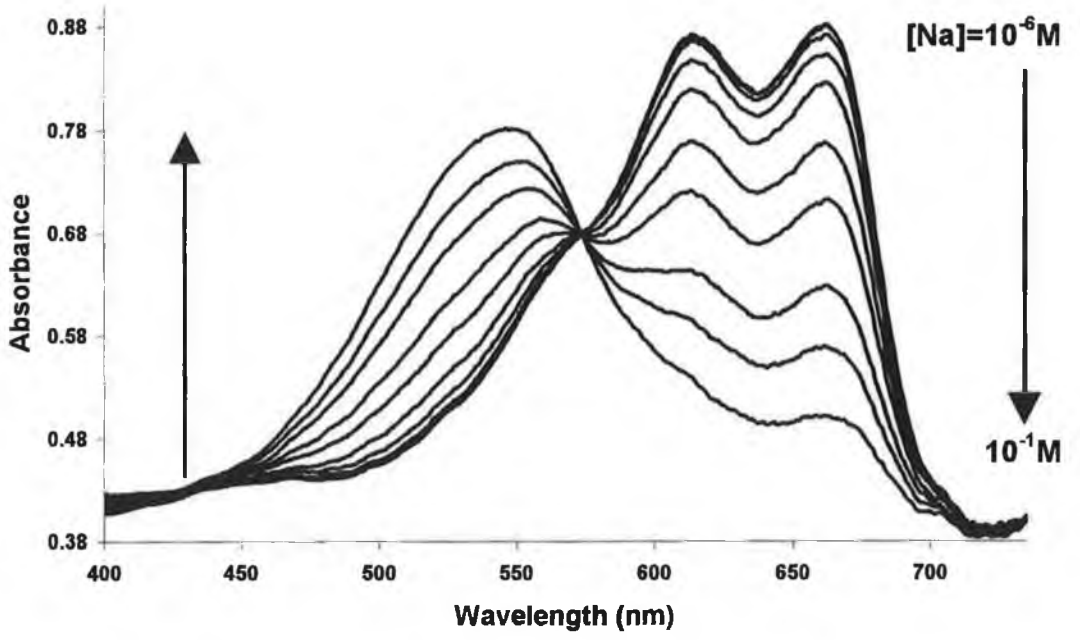

Figure 3.16 : Response of membrane 1 to sodium solutions (pH 7.3)

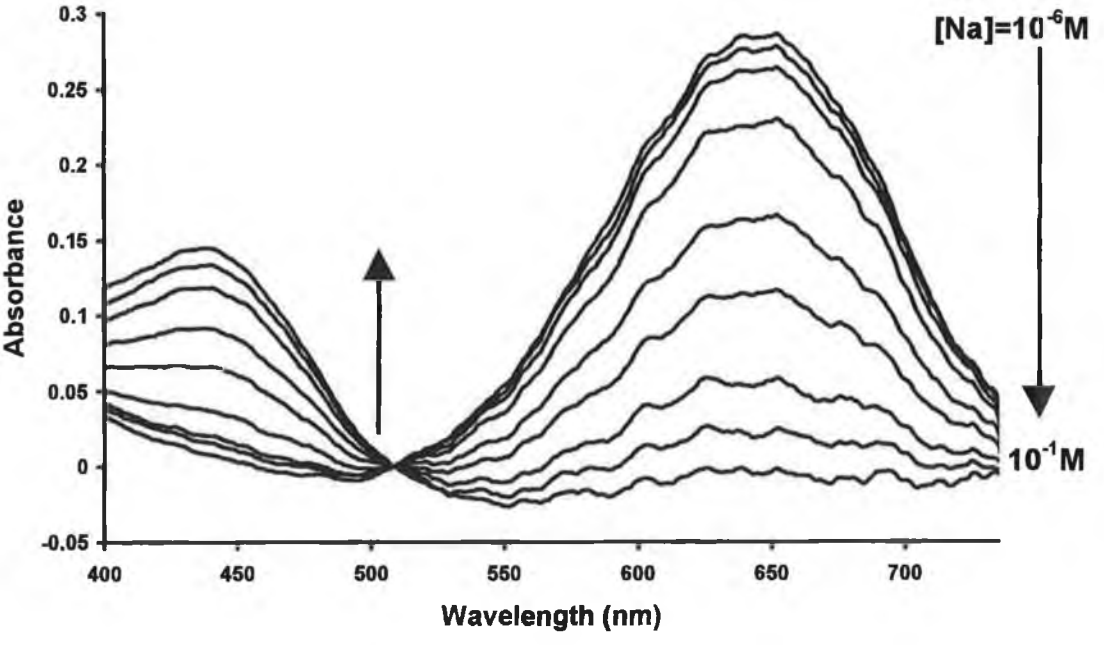

Figure 3.17 : spectral response of membrane 3 to sodium solutions (pH 5)

3.3.3 Dye stability

Reproducibility studies performed on membranes incorporating dye 2 showed no short-term reproducibility problems (Figure 3.20). Baseline stability approaches that of the instrumentation used for measurement (0.15% RSD). Inter-measurement stability was also very good at 0.5% RSD). Longer-term studies showed no measurable decrease in signal over a 72 hour period suggesting that the lipophilicity of the dye is sufficient for prolonged use in aqueous media. Experiments to determine the dye's UV stability proved encouraging. In comparison to dye 1 when exposed to UV radiation over 17 hours (using membranes of equal thickness), dye 2 showed less than 5% degradation while the dye 1 showed approximately 70% degradation (Figure 3.21).

In the pursuit of a long-life optode membrane, a stable lipophilic pH dye is desirable. Initial observations seem to suggest that dye 2 has a longer shelf-life than the dye 1. When stored either as a membrane or dissolved in THF, a mixture containing the dye 1 becomes reddish in colour after approximately 5-6 days. Since normal operation of the membranes incorporating this dye do not generate a red colour, it can be assumed this red colour is due to decomposition of the dye. The membranes produced from this red mixture do not perform well as ion-selective optodes (Figure 8). No spectral change is observed when the membranes resulting from this mixture are exposed to changes from buffer to 0.1M NaCl. The spectral shape also appears radically different indicating that some chemical modification of the dye has occurred.
in contrast, membranes cast from a similarly aged mixture incorporating dye 2 kept in identical conditions perform well as ion-selective optodes with no corruption of the spectrum suggesting there was no decomposition of the dye during the period investigated.

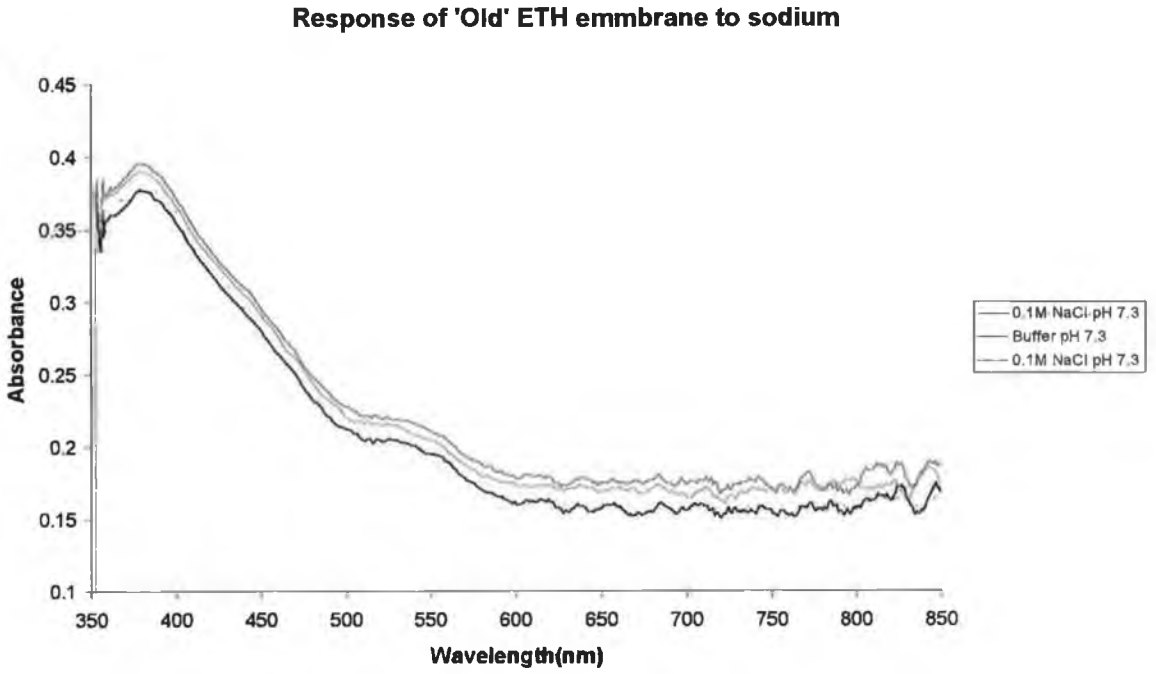

Figure 3.18: Spectral (non-) response of 'Old' dye 1 sodium membrane to sodium

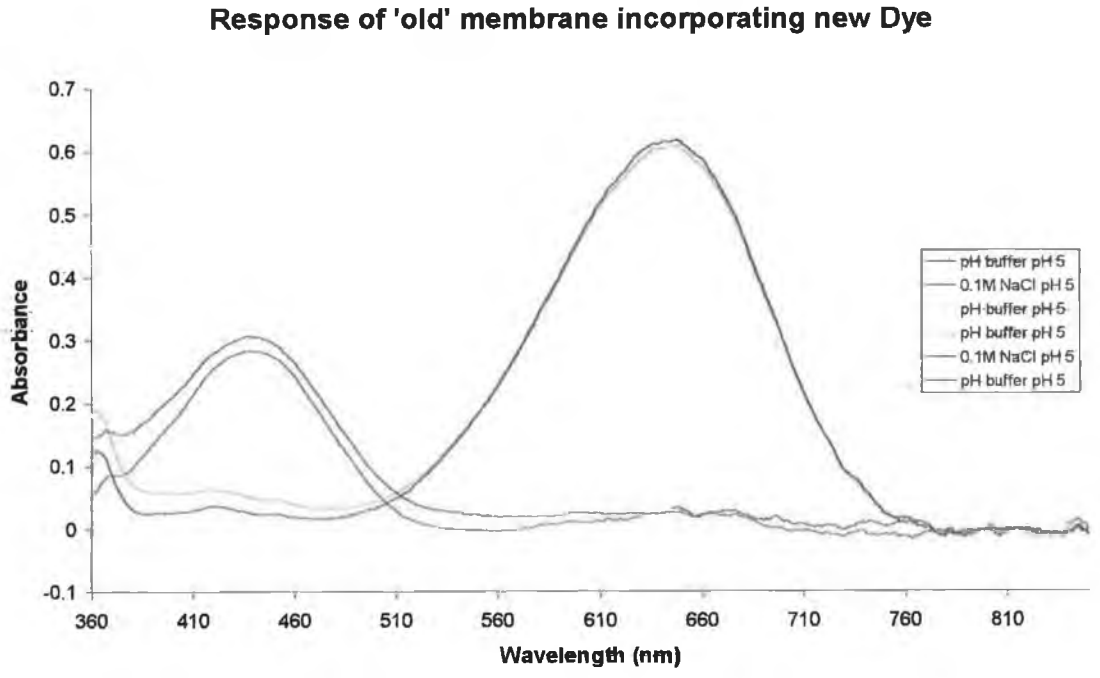

Figure 3.19: Spectral response of 'Old' dye 2 membrane to sodium

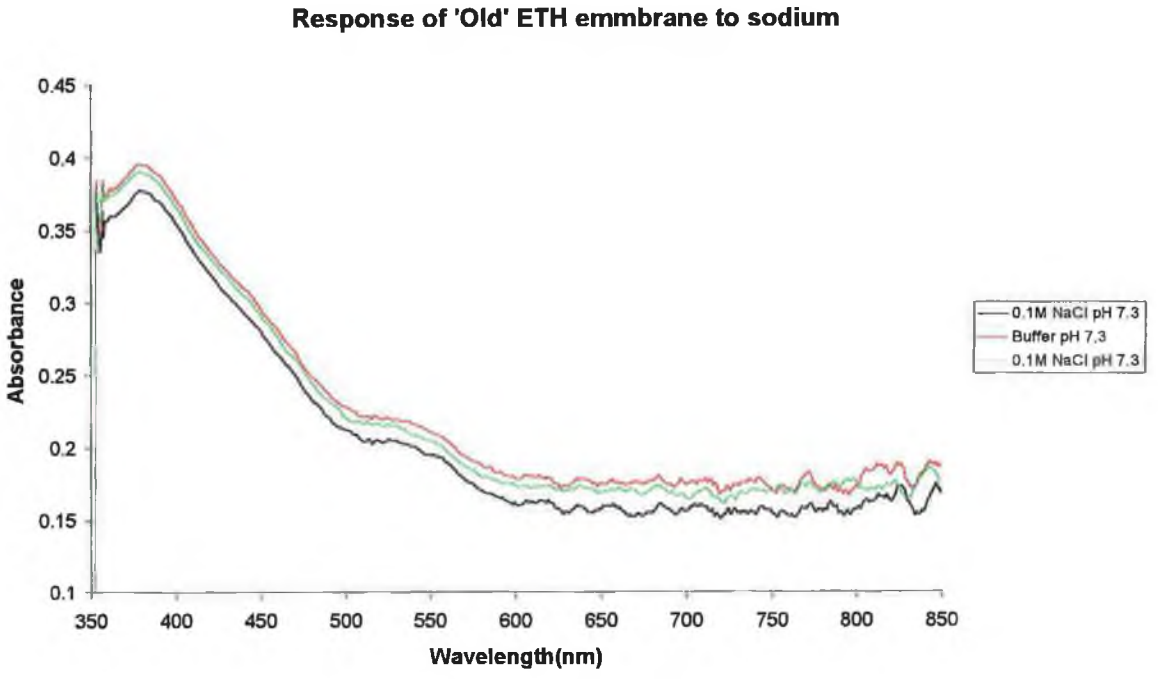

Figure 3.18: Spectral (non-) response of 'Old' dye 1 sodium membrane to sodium

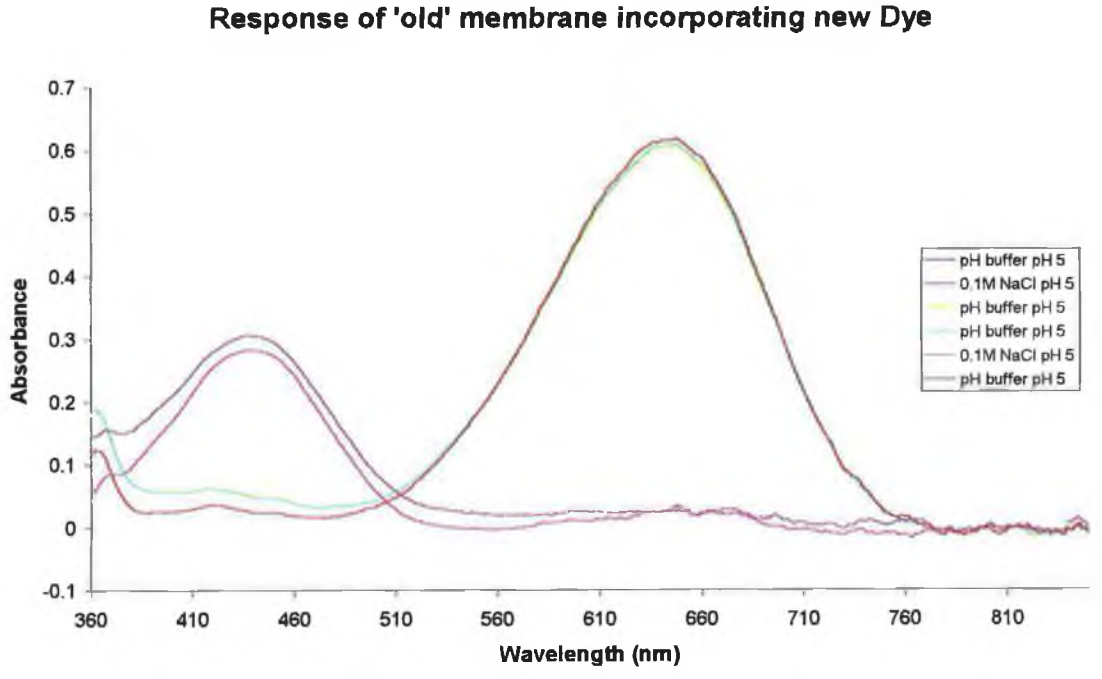

Figure 3.19: Spectral response of 'Old' dye 2 membrane to sodium

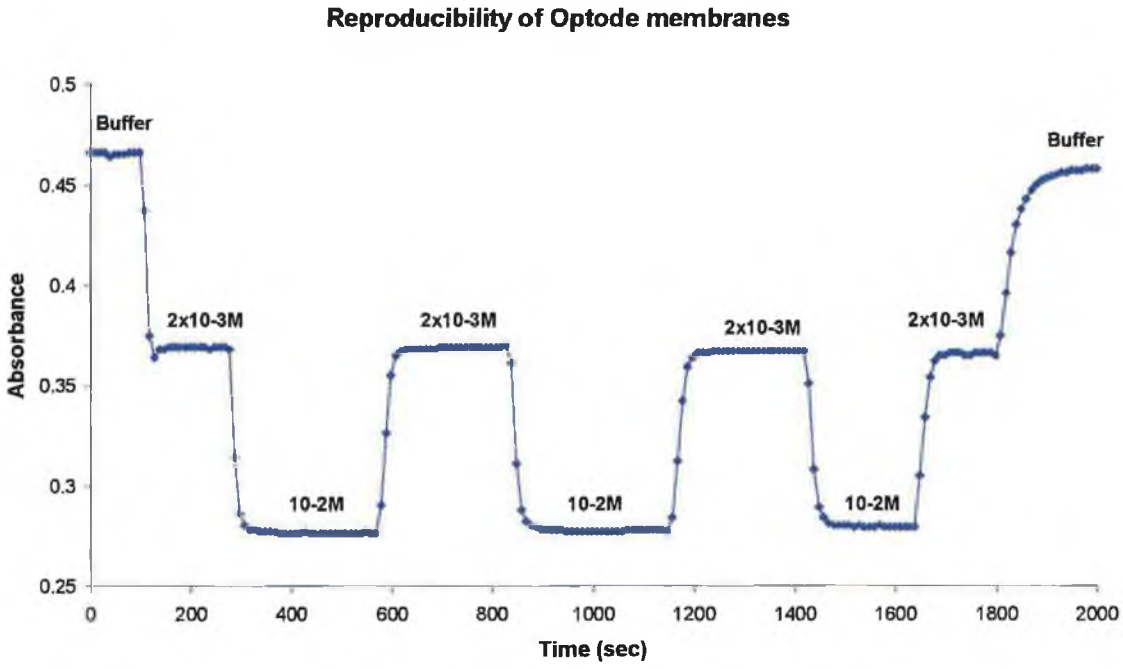

Figure 3.20 : Repeatability of membrane 3 measurements. %RSD within measurements = 0.15%, %RSD between measurements = 0.5%

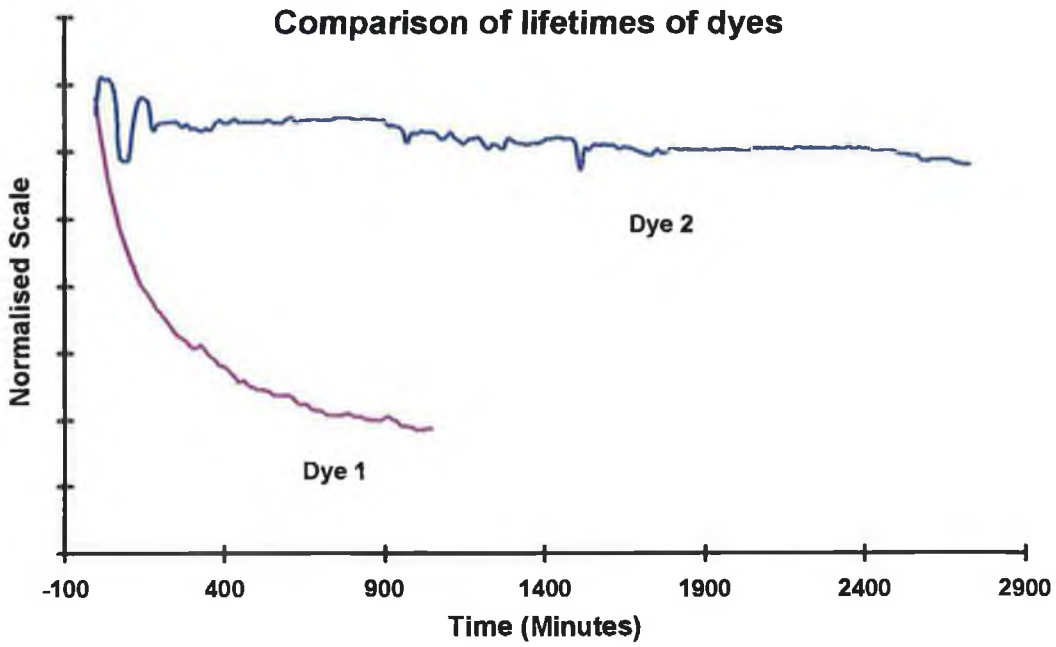

Figure 3.21 : comparison of dye decay profiles vs. time at the respective wavelength maximum (560 for dye 1 and 650 for dye 2)

3.4 Conclusions

Ion-selective optode membranes have been presented which incorporate a novel pH chromoionophore. The performance of membranes employing this dye and a reference dye (Dye 1) show very similar characteristics suggesting an absence of any unwanted dye-ligand interactions.

The pK_a of the dye has been estimated at 5.53, which agrees well with other similar dyes quoted in literature (5.65). This suggests that the acridine nitrogen is the primary basic group within the dye.

The UV stability has been shown to be superior to dye 1 with very little degradation observed over a 17 hour period while the reference dye demonstrated 70% degradation over the same period. The lipophilicity of the dye has been demonstrated to be sufficient to allow prolonged measurement in aqueous media.

	Na^+	Ca^{2+}	K^+	Mg^{2+}	Li^+	Ba^{2+}	NH_4^+
Membrane 1	-	2.30	2.09	>3.6	3.18	>3.6	>3.6
Membrane 2	-	>3.2	3.06	>3.2	>3.2	>3.2	>3.2
Electrode 1*	-	3.50	2.70	3.70	2.90	N/a	3.50
Membrane 3	4.77	-	3.84	1.39	2.30	1.14	3.65
Membrane 4	4.11	-	3.93	1.59	1.93	1.47	1.79
Electrode 2[$]	2.20	-	2.70	2.60	1.60	N/a	2.0

Table 3.4 : Selectivity values estimated for optical membranes 1-4 calculated from K_{exch} values obtained from fitting experimental data to a theoretical model (equation 1) and selectivity coefficients for potentiometric membranes incorporating TMEE (Electrode 1) and TPO (Electrode 2)[24].

	Ligand 1	Ligand 2
Dye 1	6.13×10^{-6}	5.36×10^{-4}
Dye 2	1.24×10^{-3}	5.89×10^{-2}

Table 3.5: K_{exch} values obtained from membrane model (Equation 1) for primary ion calibrations at the appropriate pH (pH 7.3 for dye 1 and pH 5.0 for dye 2)

3.5 Appendix 3: Derivation of method for estimation of dye pka.

At equivalence in the Dye/acid titration, we know that the following is true

$[HA]_{Total}=[Dye]_{Total}$ (1)

where :

$[HA]_{total}$ is the total analytical concentration of acid added,

$[Dye]_{total}$ is the total analytical concentration of dye in the solvent,

And according to the charge balance equation:

$[A^-]=[DyeH^+]$ (2)

where :

$[A^-]$ is the concentration of dissociated acid,

$[DyeH^+]$ is the concentration of protonated dye

At 600nm, where the extinction coefficient of the deprotonated form of the dye is ≈ 0, and the absorbance of the solution at this wavelength is due only to the concentration of the protonated form of the dye. At the point where the acid and dye total concentrations are equal, less than 100% of the dye has been protonated. From the total absorbance (where there is an excess of acid) and the absorbance at this point, the ratio of protonated to deprotonated dye present in solution can be estimated. With knowledge of the total dye concentration we can work out the concentration of protonated and deprotonated dye forms.

Also, from Eqns. 1 and 2 :

$[H^+]=[HA]_{Total}-[A-]$ (3)

Substituting (1) and (2) into the Henderson-Hasselbach equation:

$$pH = pK_a + Log\frac{[A^-]}{[HA]} \quad (4)$$

where pK_a is the association constant of the conjugate acid

, and assuming $[H^+]$=[HA] (equivalence),

$$-Log([HA]) = pK_a + Log\frac{[A^-]}{[HA]} \quad (5)$$

The absorbance taken at 660nm is a measure of the amount of protonated dye $[DyeH^+]$. As a consequence of this, the ratio of $[DyeH^+]$ to $[Dye]_{total}$ is the same as the ratio of the absorbane at the equivalence point to the final absorbance. Thus :

$$\frac{Abs_{total}}{Abs} = \frac{[Dye]_{total}}{[DyeH^+]} \quad (6)$$

Because the absorbance measurement is a direct measurement of the relative amounts of protonated and deprotonated dye, the following can be stated

$$\frac{[Dye]}{[DyeH^+]} = \frac{Abs_{Total} - Abs}{Abs} \quad (7)$$

As the nitric acid is totally dissociated in this medium :

$$pH \approx -Log([Dye]_{total} - [DyeH^+]) \quad (7)$$

and

$$[DyeH^+] = [Dye]_{total} \times \frac{Abs}{Abs_{total}} \quad (8)$$

Substituting (7) and (8) into (5) and bearing in mind (1)

$$pK_a = \left(-Log\left([Dye]_{Total} - \left([Dye]_{Total} \times \frac{Abs}{Abs_{Total}}\right)\right)\right) - Log\frac{Abs_{Total} - Abs}{Abs} \quad (9)$$

3.6 References

[1] H. Hisamoto, K. Watanabe, E. Nakagawa, D. Siswanta, Y. Shichi, K. Suzuki, *Anal. Chim. Acta*, **299**, (1994) 179-187

[2] H. Hisamoto, N. Miyashita, K. Watanabe, W. Nakagawa, N. Yamamoto, K. Suzuki, *Sens. And Act. B*, **29**, (1995), 378-385

[3] S. O'Neill, P. Kane, M.A. McKervey, D. Diamond, *Anal. Comm.*, **35**, (1998), 127-131

[4] K. Toth, B.T.T. Lan, J. Jeney, M. Horvath, I. Bitter, A. Grun, B. Agai, L. Toke, *Talanta*, **41**, (1994), 1041-1049

[5] K.Seiler, K. Wang, E. Bakker, W.E. Morf, B. Rusterholz, U.E. Spichiger, W. Simon, *Clin. Chem*, **36/8**, (1991), 1350-1355

[6] O.S. Wolfbeis, B.P.H. Schaffar, *Anal. Chim. Acta*, **198**, (1987), 1-12

[7] M.R. Shortreed, S. Dourado, R. Kopelman, *Sens. And Act. B*, **38-39**, (1997), 8-12

[8] K. Toth, G. Nagy, B.T.T. Lan, J. Jeney, S.J. Choquette, *Anal. Chim. Acta*, **353**, (1997), 1-10

[9] C. Stamm, K. Seiler, W. Simon, *Anal. Chim. Acta*, **282**, (1993), 229-237

[10] H. Li, O.S. Wolfbeis, *Anal. Chim. Acta*, **276**, (1993), 115-119

[11] Y. Kawabata, T. Kamichika, T. Imasaka, N. Ishibashi, *Anal. Chem*, **62**, (1990), 2054-2055

[12] H. Hisamoto, E. Nakagawa, K. Nagatsuka, Y. Abe, S. Sato, D. Siswanta, K. Suzuki, *Anal. Chem*, **67**, (1995), 1315-1321

[13] E. Bakker, M. Willer, E. Pretsch, *Anal. Chim. Acta.*, **282**, (1993), 265-271

[14] K. Toth, B.T.T. Lan, J. Jeney, M. Horvath, I. Bitter, A. Grun, B. Agai, L. Toke, *Talanta*, **41**, (1994), 1041-1049

[15] K.R.A.S. Sandanayake, I.O. Sutherland, *Sens. And Act. B*, **11**, (1993), 331-340

[16] Y. Kawabata, T. Yamashiro, Y. Kitazaki, T. Imasaka, *Sens. And Act. B*, **29**, (1995), 135-139

[17] *Aldrichimica Acta*, **16**, 1983, 35

[18] Arnaud-Neu, F., Barrett, G., Cremin, S., Deasy, M., Ferguson, G., Harris, S.J., Lough, A.J., Guerra, L., Mc. Kervey, M.A., Schwing-weill, M.J., and Schwinte, P., J. Chem. Soc. Perkin Trans. **2**, 1992, 1119

[19] Malone, J.F., Marrs, D.J., Mc Kervey, M.A., O'Hagan, P., Thompson, N., Walker, A., Arnaud-Neu, F., Mauprivez, O., Schwing-Weill, M.J., Dozol, J.F., Rouquette, H., and Simon, N., J. Chem. Soc. Chem. Commun., 1995, 2151

[20] H. Lindauer, P. Czerney, G.J. Mohr and U.W. Grummt Dyes and Pigments 26 (1994) 229-235

[21] H. Lehmann, G. Schwotzer, P. Czerney and G.J. Mohr Sensors and Actuators B 29 (1995) 392-400

[22] S. O'Neill, S. Conway, O. Egan., D. Diamond., In Preparation.

[23] E. Bakker, W. Simon, Anal. Chem., 64, 1992, 1805

[24] T. McKittrick, D. Diamond, D.J. Marrs, P.O'Hagan, M.A. McKervey, *Talanta*, **43**, (1996), 1145-1148

4 Real-time sensor for biological interaction monitoring

4.1 Introduction

Monitoring biological interactions is important in many different areas of research. Molecular recognition is the dominant factor behind many biological interactions such as enzymes and substrates and also for antigens and target antibodies[1,2,3,4]. The activity of many drugs is controlled by 'best-fit' interactions with certain proteins. In order to be able to monitor the interaction of different biomolecules, there are many methods available. One of these is surface plasmon resonance[5,6,7,8].

4.1.1 Surface plasmon resonance

A surface plasmon is a transverse charge-density wave which propagates along the interface of two different media, one of which is assumed to be a metal, and the other a dielectric (Figure 4.1). The dispersion of this charge-density wave along the interface between the metal (dielectric function $\varepsilon(\omega)$) and the dielectric (dielectric constant ε_a) can be written as

$$k_{sp} = \frac{\omega}{c}\left(\frac{\varepsilon(\omega)\varepsilon_a}{\varepsilon_a + \varepsilon(\omega)}\right)^{1/2}$$

Equation 4.1

Where ω is the frequency of the incident radiation, $\varepsilon(\omega)$ is the dielectric function of the metal layer, ε_a is the dielectric constant of the bulk dielectric, c is the speed of light and K_{sp} is the wave vector for the surface plasmon.

The surface plasmons can only be excited when the vector of the surface plasmon at the interface and the wave vector of the sample are equal. Without the

dielectric, this is not possible as the vector of the ambient is always smaller than that of the dielectric-metal interface.

$$k_a = \frac{\omega}{c}\sqrt{\varepsilon_a} << \frac{\omega}{c}\sqrt{\frac{\varepsilon(\omega)\varepsilon_a}{\varepsilon_a + \varepsilon(\omega)}}$$

Equation 4.2
Where k_a is the ambient vector.

With attenuated total reflection, the light is reflected at angles greater than the critical angle for total reflection Φ_c. At these angles, the majority of the light is reflected, although a small portion of the light penetrates beyond the medium and this is called an evanescent wave. This wave allows us to communicate optically with the interface and to initiate a surface plasmon, provided the metal layer is thin enough. There then occurs an incident angle of radiation corresponding to resonance with surface plasmons, and this angle can be defined as

$$\sqrt{\varepsilon_g}\sin\Theta_{sp} \approx \sqrt{\frac{\varepsilon'(\omega)\varepsilon_a}{\varepsilon_a + \varepsilon'(\omega)}}$$

Equation 4.3
Where ε_g is the refractive index of the sample, and Θ_{sp} is the angle of incident light which excites surface plasmons, and where only the real part ($\varepsilon'(\omega)$) of the imaginary dielectric function $\varepsilon(\omega) = \varepsilon'(\omega) + i\varepsilon''(\omega)$. While the imaginary part of this function is never zero, it proves a very useful approximation since $|\varepsilon'(\omega)| >> |\varepsilon''(\omega)|$.

Where the vectors of the incident radiation and the surface plasmons are equal, energy is transferred from the incident light to the surface plasmons. This manifests itself in a dip in the reflected light at a particular angle of reflectance which depends on the refractive index of the sample being interrogated.

Therefore, the refractive index of our sample ε_g alters the angle of resonance. Experimentally, where the refractive index of the sample is unknown, this angle (or wavelength) can be measured and treated as an indicator of the refractive index of the sample.

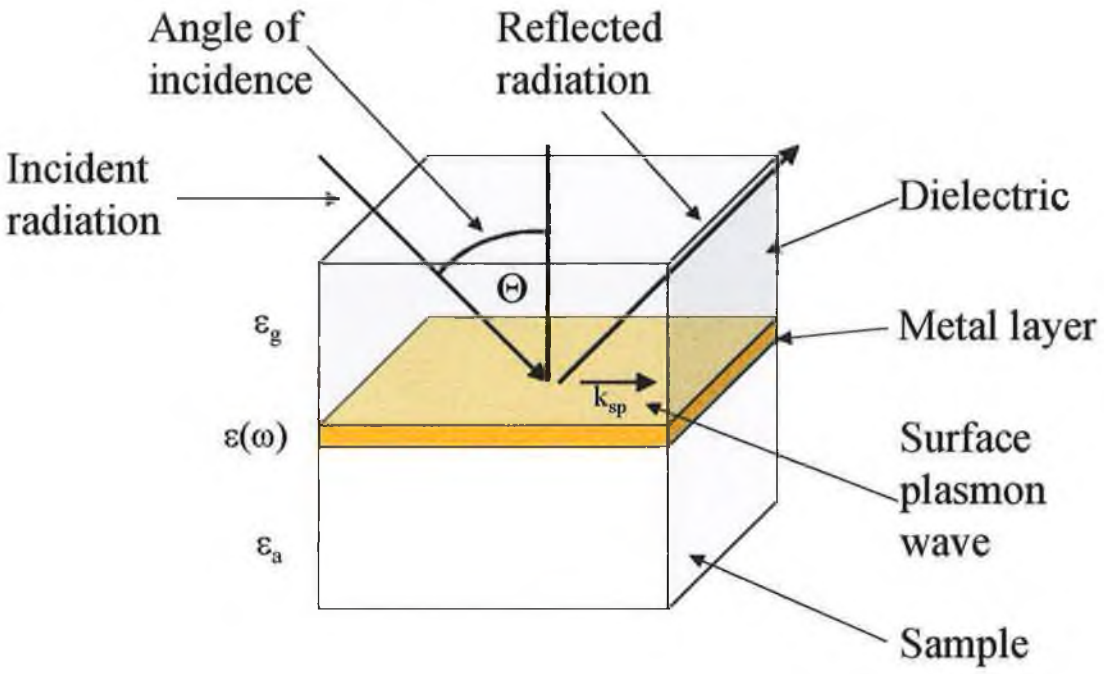

Figure 4.1: Schematic of the excitation of non-radiative surface plasmon resonance waves.

4.1.2 The evanescent wave

The evanescent wave is a decaying electric field extending into the ambient sample. Both the x and z components decay exponentially (Figure 4.7). The electric field E can be written as $E_z = E_z(0)\exp[-k_z z]$ where k_z can be expressed as[9]

$$k_z^2 = k_x^2 - \frac{\omega^2}{c^2}\varepsilon_a$$

Equation 4.4

When taking the optical constants of gold, $\varepsilon'(\omega)$=-13.15, and water, ε_a=1.77 at 632.8 nm (He-Ne), are substituted into Equation 4.4, the typical penetration depth is found at 190 nm.

Thus, the sensor device as described is sensitive to changes in the refractive index of the sample medium within 190 nm of the surface of the sensor (Figure 4.8).

Because the sensor can measure changes in refractive index beyond the immediate surface, most devices immobilise the biological surface in a dextran matrix on the sensor surface. The thickness of this matrix is often slightly greater than the actual penetration depth, but results in a more responsive system due to the larger volume available for immobilisation of recognition sites and also the increased availability and mobility of the recognition sites (Figure 4.1). When antibodies are immobilised directly on the sensor surface, many are unable to bind the analyte due to random orientation on the surface. This problem is negated by using such a matrix.

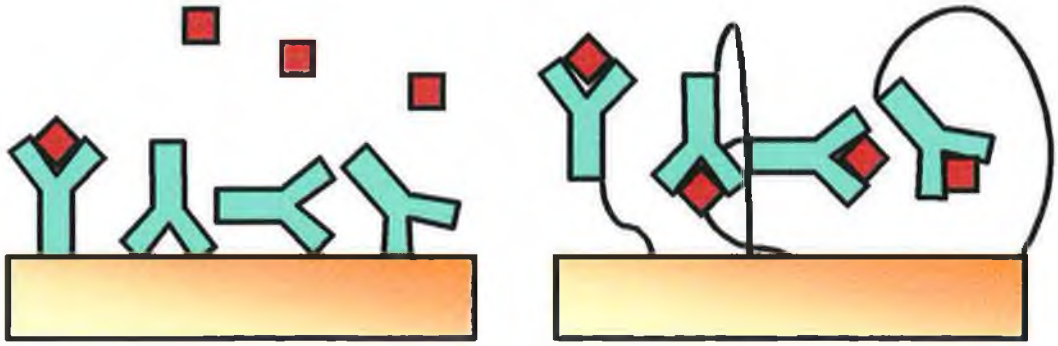

Figure 4.2: Schematic of the enhanced availability of antibodies using the coupling matrix approach.

4.1.3 Generation of a response curve

In order to facilitate antibody immobilisation, protein A is immobilised onto the surface (Figure 4.3, a). This is generally performed only once, with multiple further immobilisations possible onto the same protein A layer. The first step of each individual analysis is the immobilisation of the antibody itself (Figure 4.3, b). In reality, each protein A moiety can bind as many as six antibodies. This obviously results in much larger responses. The antibodies are immobilised within the range of the evanescent field penetration depth and thus, any refractive index changes are recorded by the sensor. After initial exposure, the sensor is washed to remove any non-specific binding. When the sensor complete with immobilised antibody is then exposed to a sample containing the required analyte, the antibody binds the analyte strongly, with a certain amount of non-specific binding between the analyte and either the dextran, protein A or the sensor surface itself (Figure 4.3, c). The shape of the curve generated with this step can be analysed to yield information about the kinetics of the interaction. However, before any real analytical information can be taken from this measurement, the sensor must be washed with a buffer solution (Tween) to remove all the weakly bound non-specific binding (Figure 4.3, d). The magnitude of the signal then present is due only to strongly bound antigens (Or whole blood cells). The analysis is then complete.

To prepare the sensor for another analysis, it is washed multiple times with HCl to remove any antibodies, after which the sensor surface returns to the satte indicated in Figure 4.3, a. The process is repeated from b-d for each and every analysis required.

A typical response curve thus generated can be seen, with corresponding steps in

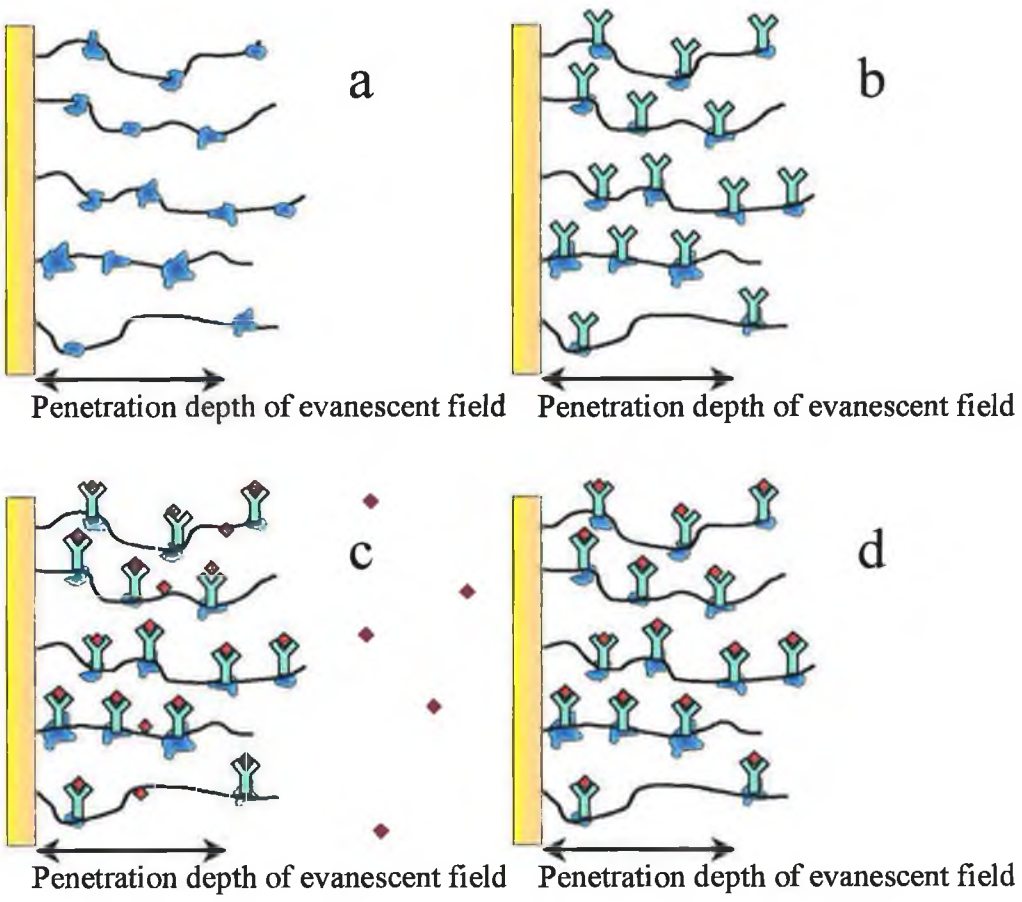

Figure 4.3: Processes involved in the generation of a typical response from a biological interaction analysis.

a) Initial immobilisation of Protein A (Blue)

b) Immobilisation of antibody (green) to the protein A (In reality up to six antibodies per protein A.

c) Interaction between the sensor and the target analyte (red), complete with a certain amount of non-specific binding.

d) Final state of the sensor after non-specific binding has been removed with buffer.

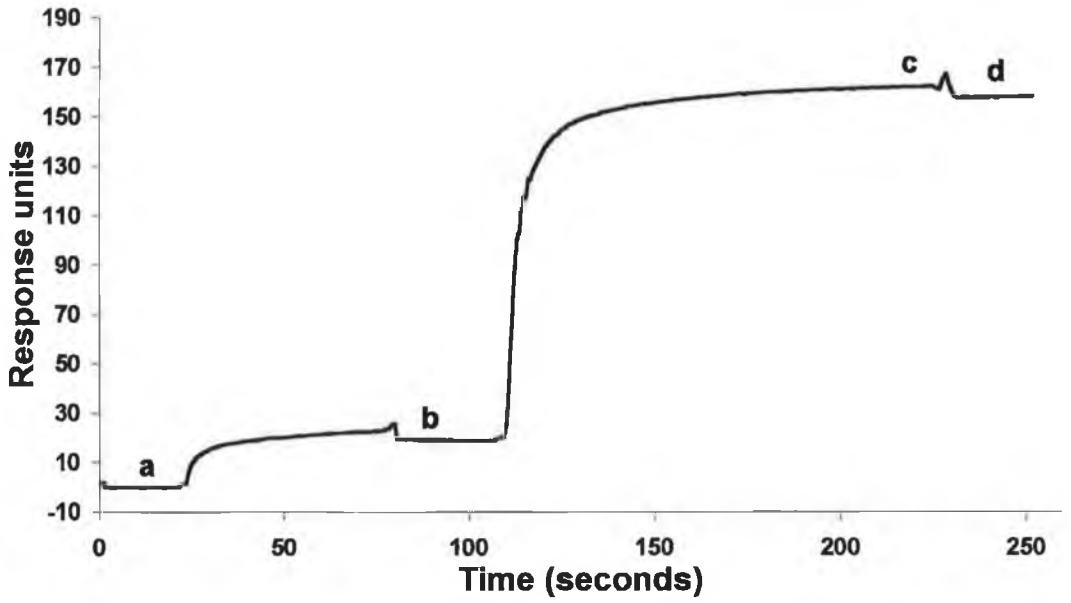

Figure 4.4: Example of a typical response (versus time) for an analysis. Points a-d correspond to the sensor states in Figure 4.3.

4.1.4 Generation of response profile from raw data

As explained earlier, SPR occurs when the vectors of incident radiation is equal to that of the surface plasmons. Traditionally, monochromatic light has been used to monitor the changes in refractive index as given in Equation 4.3. However, it is also possible to perform these measurements by using polychromatic light. Where traditionally, the term of $Sin\Theta_{sp}$ is used as indicator for changes in ε_a, with all other terms remaining constant, the polychromatic approach allows for $Sin\Theta_{sp}$ to remain constant. This removes the need to have any moving parts present in order to scan for the reflectance minimum. Instead, the function $\varepsilon'(\omega)$ changes with wavelength (or frequency) to compensate for any changes in ε_a. Thus, the surface plasmon resonance occurs at the same angle, but with the reflectance minimum existing at a different wavelength. By using a CCD array as the detector, this reflectance curve can easily be monitored (Figure 4.5).

Once the curve has been captured, the curve minimum must be found. The raw signal is noisy and a simple search for a minimum reflectance would not be reliable. Instead, a high-order (30^{th} order) polynomial curve is fitted to the experimental data. The advantage of this approach is that the noisy experimental curve is now replaced by a representative smooth curve with one clear minimum. Once the polynomial has been fitted to the data, the minimum can be easily found by searching for the minimum value (Figure 4.6).

When this process is repeated over time (every ~0.4 sec in these experiments) a profile of the reflectance minimum with respect to time can be generated. This can then be assumed to be a response curve proportional to the refractive index of the samples used (Figure 4.6).

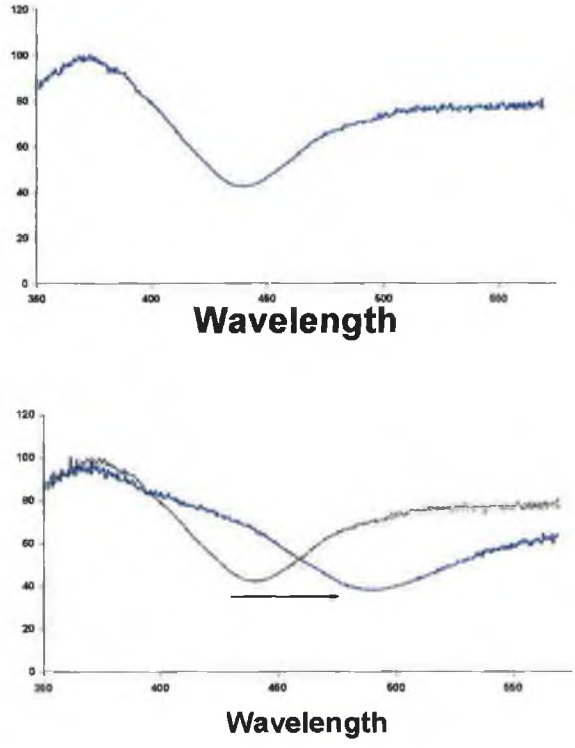

SPR according to:

$$\sqrt{\varepsilon_g}\sin\Theta_{sp} \approx \sqrt{\frac{\varepsilon'(\omega)\varepsilon_a}{\varepsilon_a + \varepsilon'(\omega)}}$$

Figure 4.5: How multiple wavelength interrogation can be used for SPR measurements.

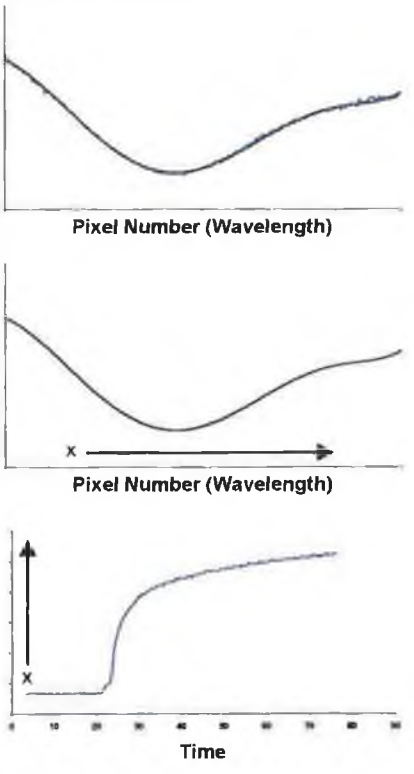

Wavelength scan and curve-fit

Curve-fit polynomial then used to solve for x minimum

As the SPR curve shifts, the value returned from the polynomial changes also. Plotted against time, this generates our response curve.

Figure 4.6: Example of how the SPR response profile is generated.

4.2 Applications of SPR

One of the first applications of this technique was in the sensing of gases[4]. A gas-absorbing medium was placed on the silver metal layer (silicon-glycol copolymer) which has its own defined refractive index. When this is exposed to a gaseous medium, the polymer layer traps much of the gas within its bulk, resulting in small changes in refractive index of the medium, which is then observed as a shift in the angle of reflectance of the minimum intensity. Initial bio-molecular interaction studies were also carried out in the same work. In this method, solutions of IgG were passed over the silver layer surface allowing for adsorption of a single monolayer on the silver surface. The refractive index change observed was from 1.33 (Water) to 1.47. However, once this monolayer is in place, it is then possible to monitor interactions of this system by then passing a solution of γ-globulin (a-IgG) over this surface, a further increase in refractive index at the surface is observed. This further increase is due to the selective binding of a-IgG to the previously immobilised IgG. Monitoring the change in refractive index with time allows the investigation of association rates. The observed refractive index change was seen to be similar to all concentrations of a-IgG, but the rate of association was seen to differ significantly. The calibration was performed with respect to degree change per concentration of a-IgG.

A review of the area of surface plasmon resonance as applied to analytical measurements can be found here[10].

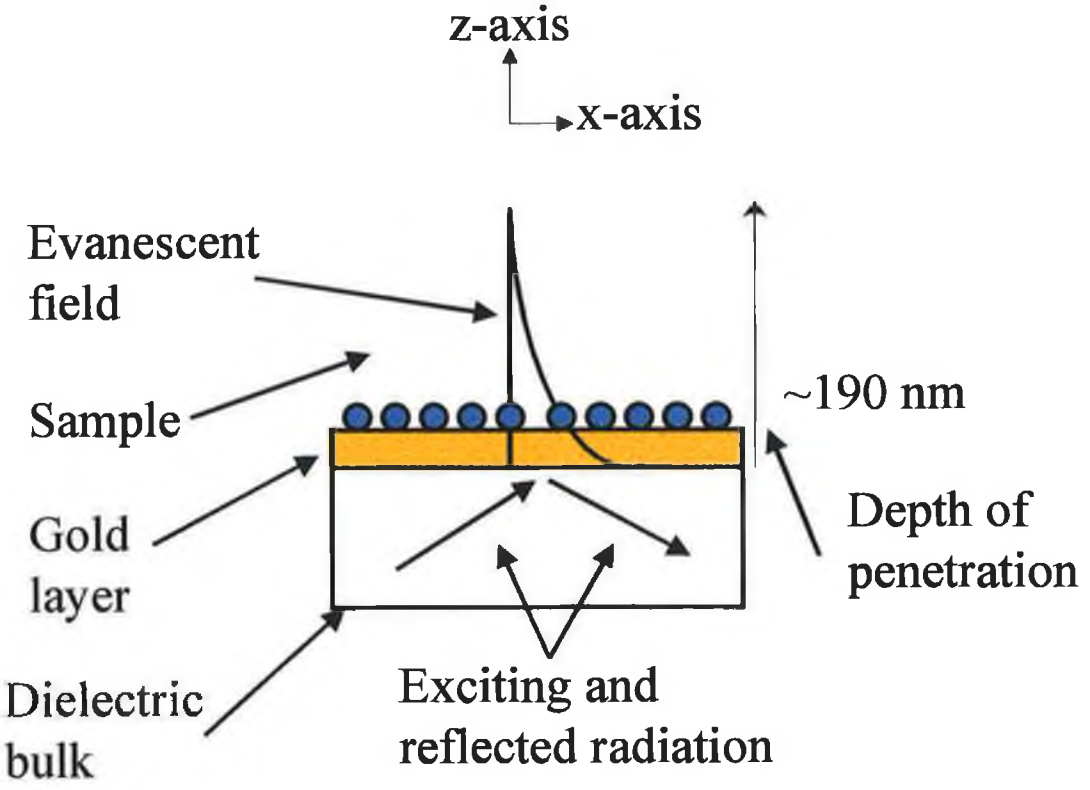

Figure 4.7: Diagram of the evanescent field penetration of the SPR sensor device

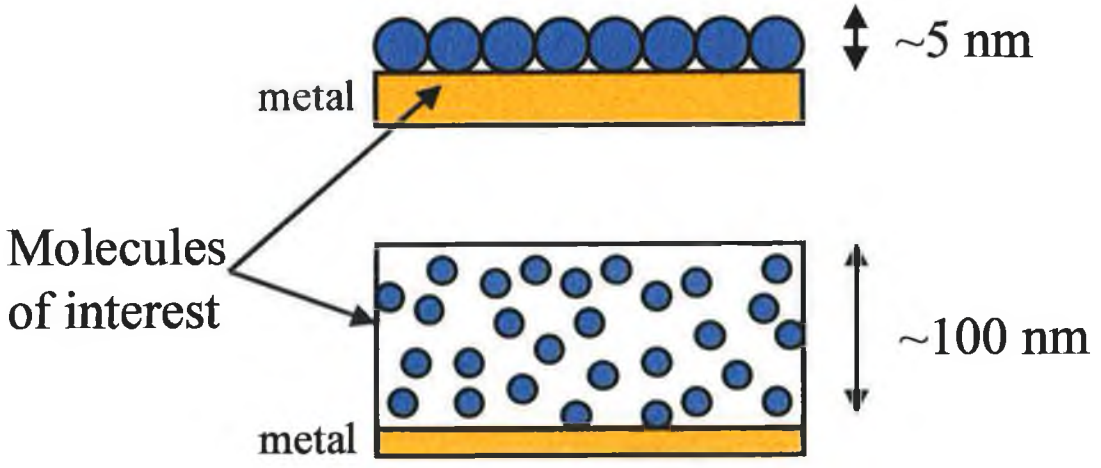

Figure 4.8: Direct immobilisation versus coupling matrix setups.

4.3 Equipment and apparatus[a]

Data was recorded using custom-written software written in LabVIEW (Chapter 5). The software was executed on a pentium class laptop computer. Data acquisition was performed by a National Instruments DAQ-Card 700 Multifunctional I/O card. A Heraeus Labofuge centrifuge 6000 was used in the preparation of the blood samples.

4.3.1 Reagents and materials

EDC-and N-hydroxy succinimide, ethanolamine, acetate buffer, phosphate buffer Tween and glycerol were supplied by Sigma. HCl was supplied by Aldrich. Phosphate buffer was supplied by Oxoid Ltd. Basingstoke, Hampshire, England.

4.4 Experimental[b]

4.4.1 Preparation of biological sensor surface

The fibre tip was supplied by BIA core AB, 2 Meadway court, meadway technological park, Stevenage, Herts, SG1 2EF. The fibre, mirrored end and dextran matrix were all pre-prepared. With the dextran matrix in palce, it is

[a] Sensor design and fabrication was carried out in conjunction with A. Doyle and J. Quinn, BEST Centre, DCU.

[b] Experimental was carried out in conjunction with A. Doyle and J. Quinn, BEST Centre, DCU.

necessary to immobilise protein A within the hydrogel. Protein A interacts with igG, and it is used within this work to allow immobilisation of the IgG antibody. This was done by amine coupling, using EDC-N-hydroxy succinimide as a linker. A solution of 50:50 0.4M EDC and 0.1M NHS was used to 'activate' the dextran matrix. Once this was performed, 20mg/ml solution of protein A (pK_a 4.6) in a 10 mM sodium acetate buffer pH 4.3 was introduced to the sensor surface. After equilibriation, ethanolamine was then used to 'deactivate' any residual dextran molecules not involved in binding to protein A. The sensor surface is then ready for use.

Experimental set-up was as shown in Figure 4.10 and Figure 4.11. Aqueous samples were introduced to the sensor by placing the sensor tip in the required solutions. No temperature control or compensation was carried out during the course of these experiments. For calibration with solutions of different refractive indices, no igG was deposited on the gold surface of the SPR sensor.

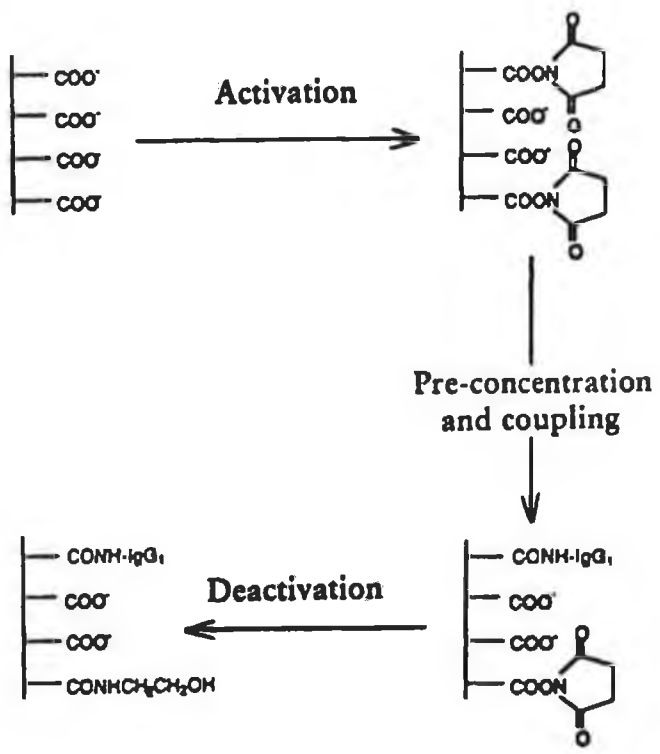

Figure 4.9: Scheme for the immobilisation of IgG to the dextran matrix.

4.4.2 Generation of antibody binding profile

Initially, the sensor is placed in a phosphate buffer solution (PBS). After a few minutes, the sensor is then placed in a solution of a defined concentration of igG to allow binding to the protein A. This is left to equilibrate for 4 minutes, after which, the sensor surface is washed with a PBS-Tween solution to remove any igG which is non-specifically bound. Once this is complete, the solution to be analysed is introduced to the sensor surface, when the antibodies bound to the protein A bind the analyte (whole blood cells for example). A response curve is generated and allowed to equilibrate for 5 minutes. After this time, the sensor surface is again washed with PBS-Tween to remove any unspecific binding. This response at this point of the curve is taken as the analysis value. Once this has again equilibrated, the sensor is washed initially with 20 mM HCl to remove any igG from the protein A. A solution of PBS is then used to verify that the sensor response has returned to its original value. This cleaning step is repeated as many times as is necessary to regenerate the sensor surface.

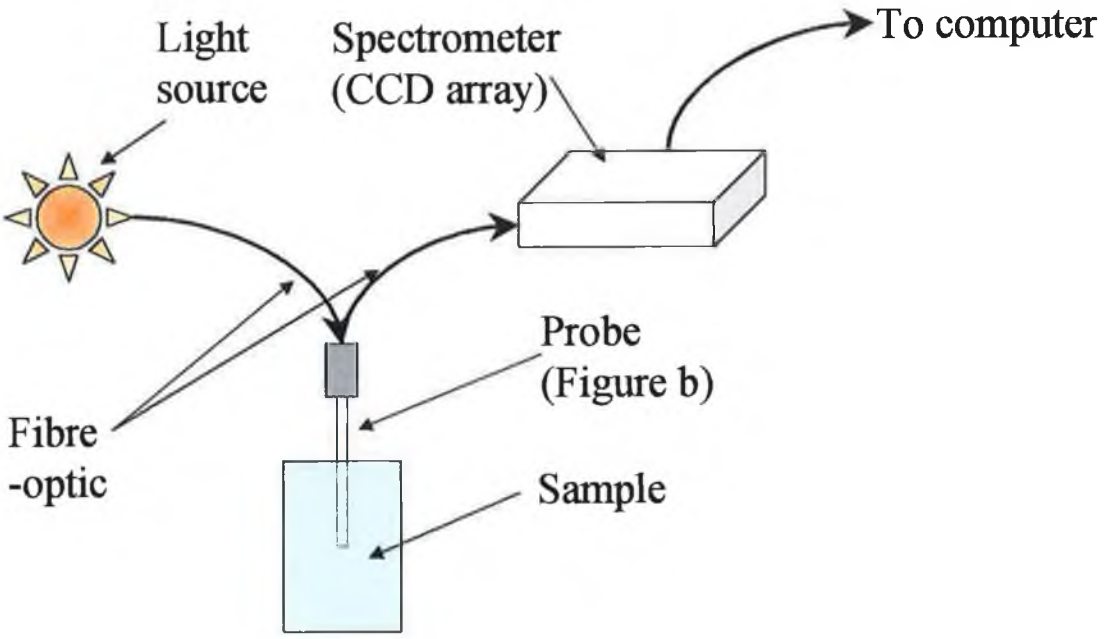

Figure 4.10: Schematic of Experimental set-up

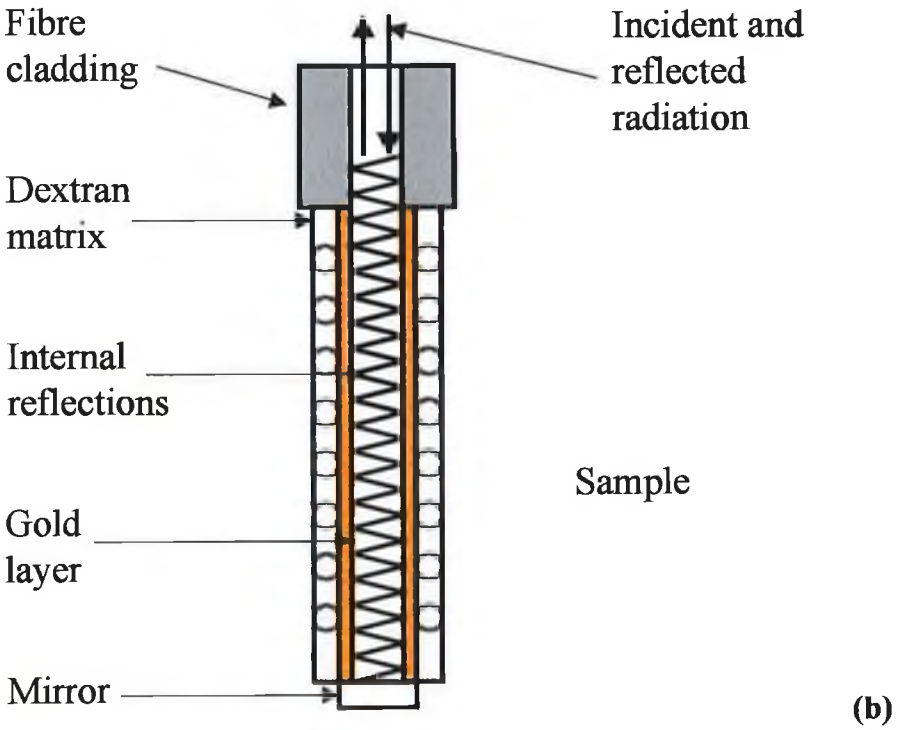

Figure 4.11: Expanded schematic of sensor-tip design.

4.5 Results and discussion

4.5.1 Refractive index calibration

The sensor was initially calibrated with respect to refractive index. In order to do this, solutions of varying refractive index ranging from 1.45 to 1.33 were prepared by mixing the required ratios of water (RI 1.33) and Glycerol (RI 1.45). The sensor output can be seen in Figure 4.12. The peak generated by surface plasmon resonance can be seen clearly in this figure and the shift of the peak with varying refractive index is also visible. After calculation of the location of the minimum of these peaks, which was performed in real-time (Chapter 5), the calibration of the system can be seen in Figure 4.13 with respect to refractive index, from time-dependent data shown in Figure 4.14. Successive baseline measurements were performed between each refractive index solution.

The baseline standard deviation is in the region of 0.9 response units. There are many factors which could be responsible for this deviation. Firstly, the curve-fit algorithm within the custom-written software has not been fully optimised. The standard deviation of the refractive index calibration solutions was reduced by altering the input variables for the curve-fitting, and also a slight change in the fitting method (Householder method[11]). Once this was performed, the average standard deviation of the baseline signal became only 0.3 response units. After some further optimisation involving more extensive changes to the signal processing, the final baseline standard deviation was measured at 0.08 response units. From this experimental data showing the effect of varying the parameters in this function has on the standard deviation of baseline signals, it is believed that this is perhaps the most significant area for improvement as regards final data quality.

Other factors include the effects of the bending of the fibre-optics involved, temperature variations, light source instability and the UV-Vis detector stability.

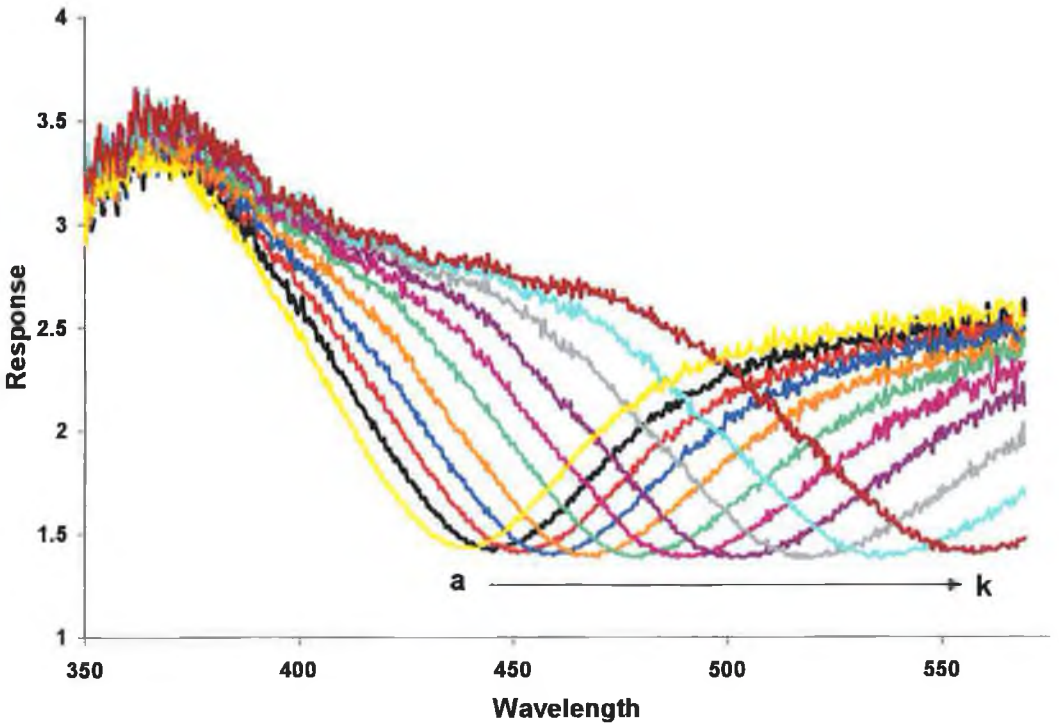

Figure 4.12: Scans obtained during refractive index calibration.
Sample refractive indices (Glycerol: water mixtures):

a. 1.331
b. 1.343
c. 1.355
d. 1.367
e. 1.370
f. 1.391
g. 1.403
h. 1.415
i. 1.427
j. 1.439
k. 1.451

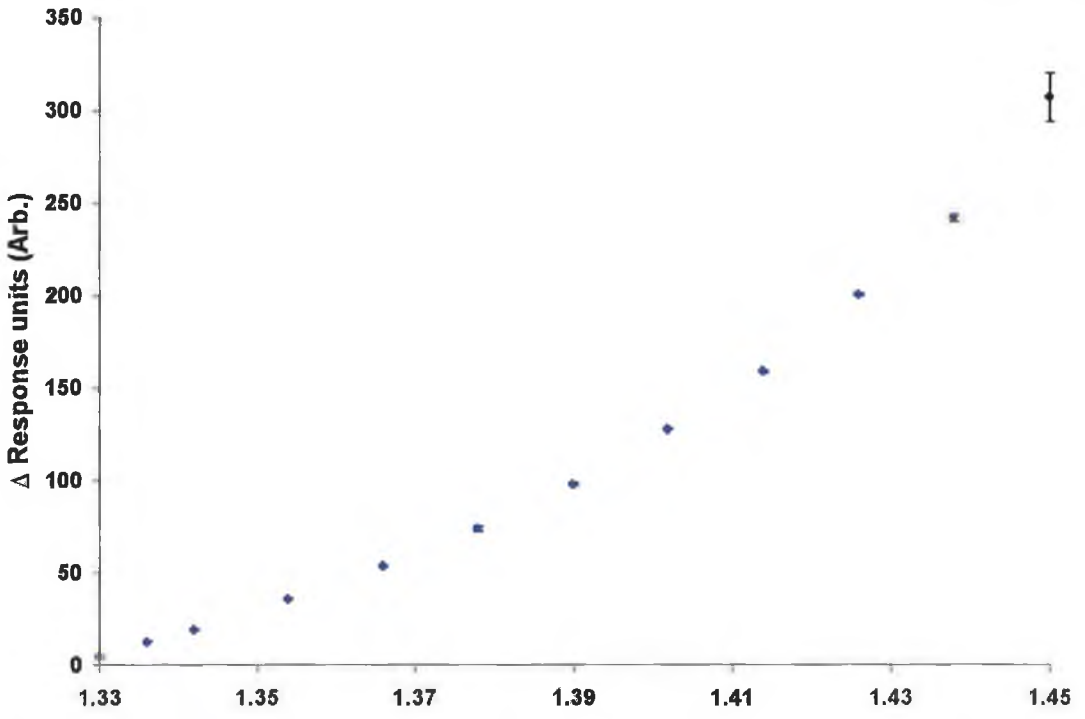

Figure 4.13: Calibration of SPR sensor with solutions of different refractive indices.

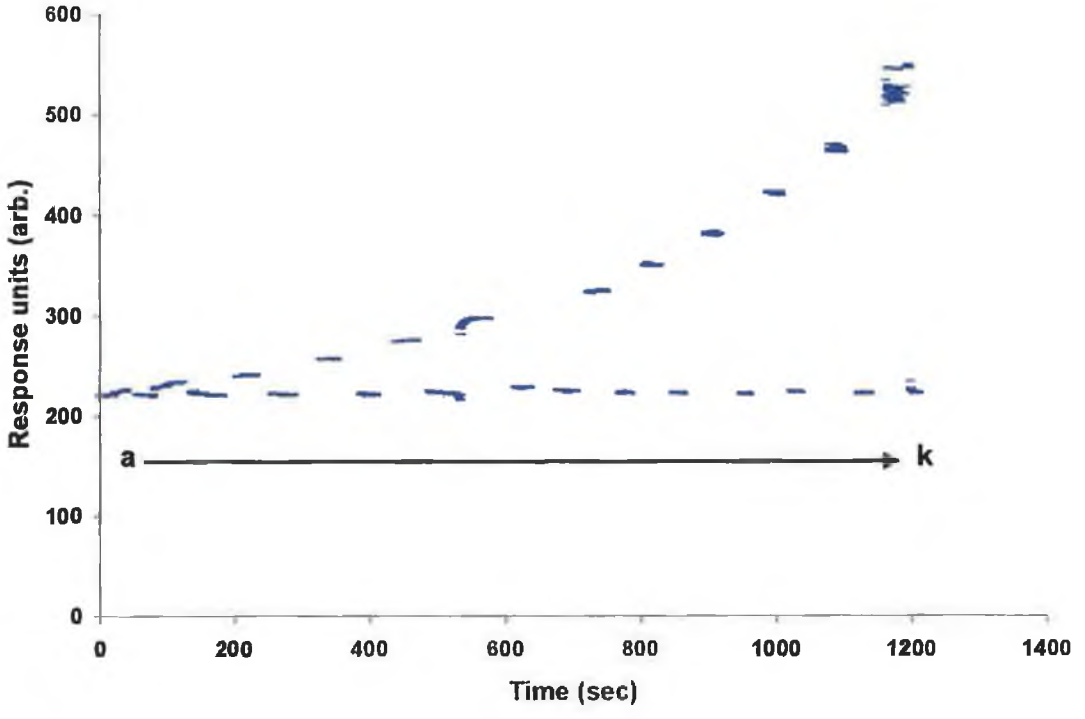

Figure 4.14: Response of sensor to solutions of different refractive index versus time.
Solutions a-k are indicated. (Figure 4.12)

4.5.2 Response to IgG

The sensor surface with protein A immobilised requires further modification before it can be used to measure the required analyte in solution. This involves immobilisation of an antibody on the protein A. In this case, Anti-A IgG2b was used. To investigate the effects of different concentrations of IgG used in this step, a calibration was performed where solutions containing different concentrations of IgG were used to prepare the sensor surface. The response profiles can be seen in Figure 4.15. This plot indicates that there is marginal non-specific binding at all concentrations of IgG except the two greatest. Although there is considerable non-specific binding at the highest concentration, after removal of the non-specifically bound antibody, there was a greater amount of immobilised antibody on the surface of the sensor. For this reason, this maximum concentration was used in all subsequent IgG immobilisation.

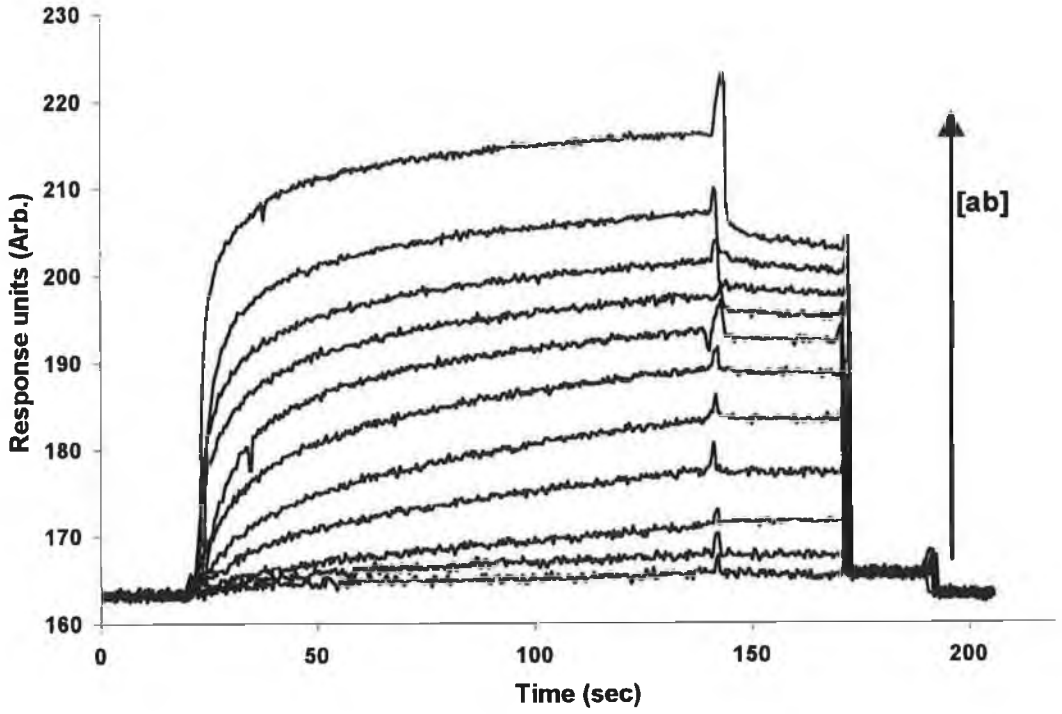

Figure 4.15: Response of SPR device to different concentrations of antigen.

4.5.3 Measurements in whole blood

Once the system had been shown to respond to changes in refractive index, an antibody was immobilised on the sensor within a dextran matrix. This immobilised antibody was then subjected to a series of solutions allowing for the adherence of whole blood cells to the sensor surface. The resulting changes in sensor output can be seen in Figure 4.16. The initial rise observed (until ~75 seconds) results from the binding of the actual antibody to the surface of the sensor. The following dip in response is due to a washing step to remove any non-specifically bound antibody. The surface is then ready for blood cell analysis. After 110 seconds, solutions of different percentages of whole blood were introduced to the sensor. The response from these solutions can be seen to show a clear distinction between the different concentrations of whole blood. The reproducibility of the antibody immobilisation was quite good (1.8 % between repetitions) but the reproducibility between blood cell interactions was not as good (~4.5% between repetitions). A clear reduction in the sensor response was visible with each subsequent analysis (Figure 4.17). This was attributed to the lysing of the blood cells within the solutions. This resulted in cell fragments remaining bound to the sensor surface, thus slightly increasing the refractive index of the bare sensor. The effect of the cell fragments also blocked many active sites for interaction on the sensor, thus reducing the overall response maximum from then on. This problem was greatest with the more concentrated blood solutions.

While the final response magnitude can be used to determine the concentration of whole blood in the unknown sample, the kinetics of the interaction can also be used quantitatively. A plot of the initial rate of response versus whole blood percentage gives yield to Figure 4.18 and Figure 4.19.

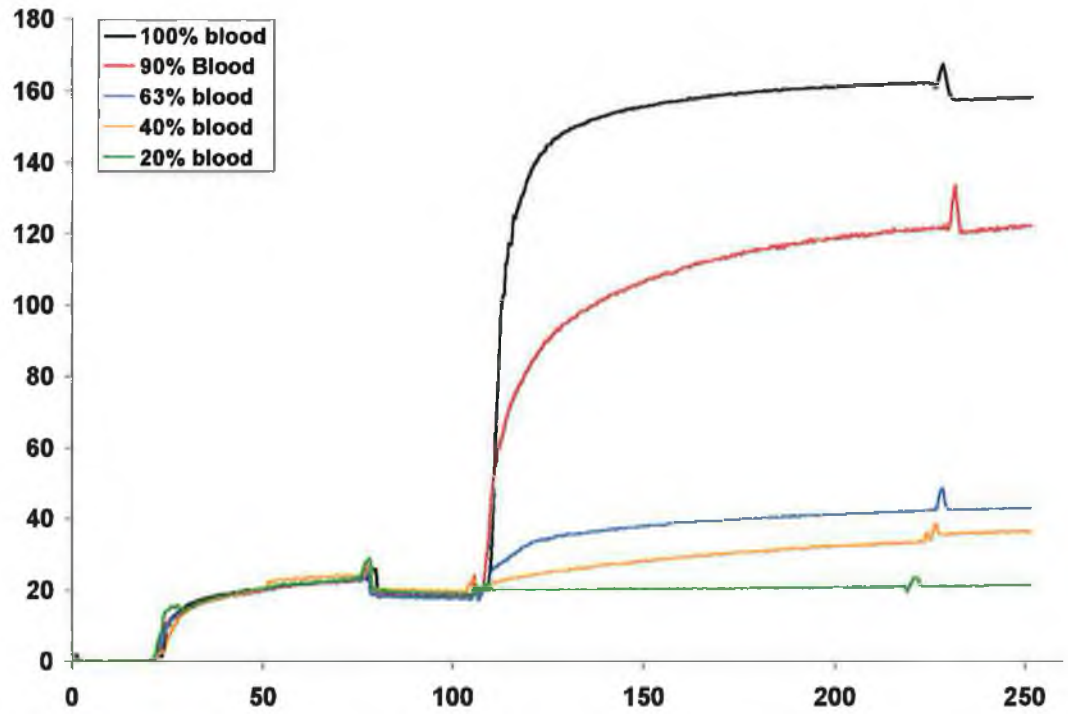

Figure 4.16: Response generated during whole blood response experiment.

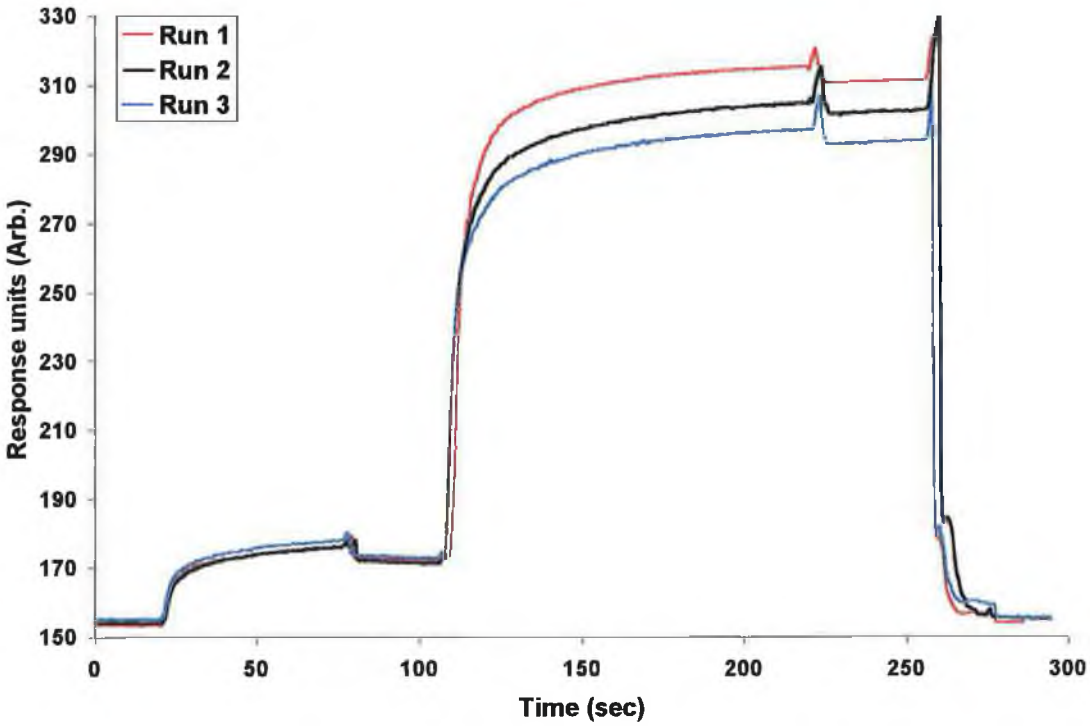

Figure 4.17: Repeatability of whole blood assays.
Deviations in response are due to lysing of the blood cells and fouling of the sensor surface.

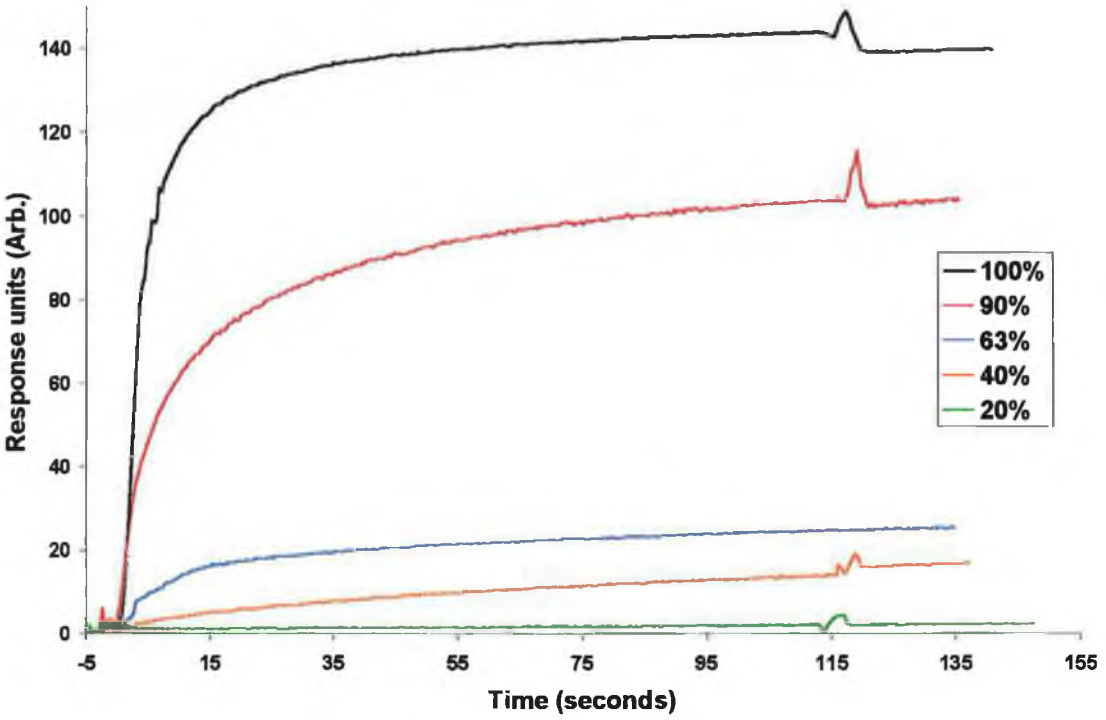

Figure 4.18: The rate of response of different dilutions of whole blood.

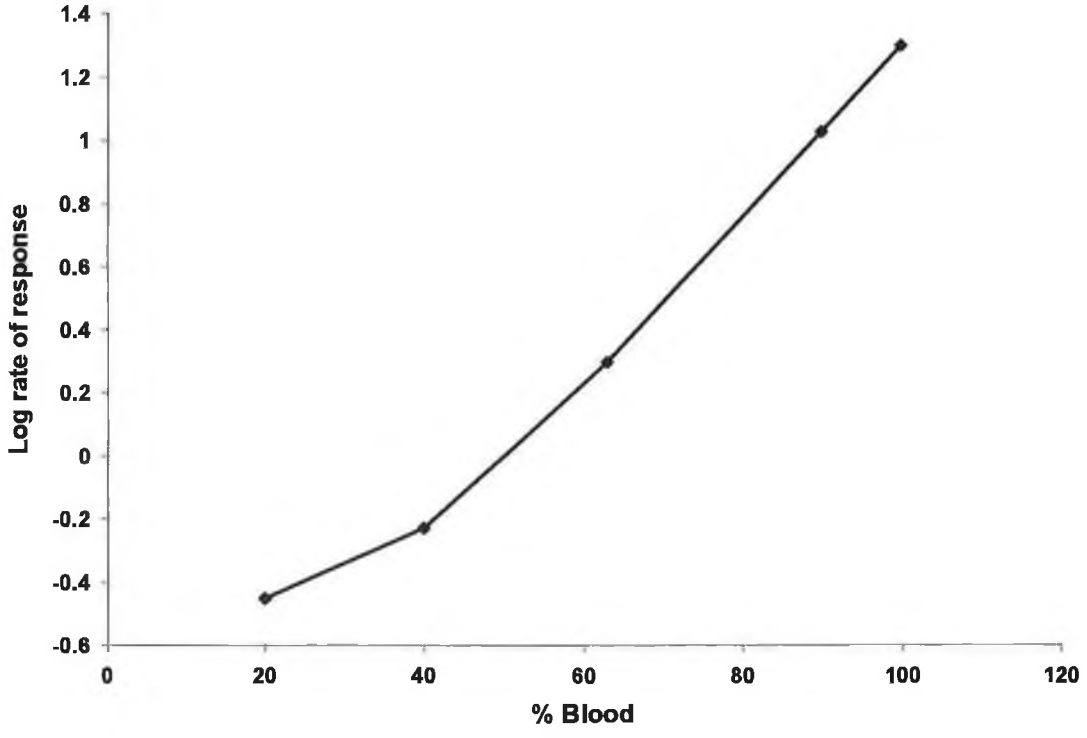

Figure 4.19: Plot of the rate of response vs. % whole blood.

4.6 Conclusions

A surface plasmon resonance device has been constructed and characterised. The response of the sensor to refractive index changes of the sample to which it was exposed has been demonstrated. The relationship between the refractive index changes and the shift in the absorbance minimum was shown to be non-linear.

Following this, a biological layer was immobilised on the sensor surface. This layer consisted of protein A covalently immobilised on the dextran sensor surface. The response of this surface to refractive index changes caused by localised aggregation of biological species has been demonstrated in relation to iGg antibody. The completed sensor layer, with the antibody in place was then shown to be a platform for measurements of whole blood cells.

When performing measurements in whole blood, the ability to perform calibrations based on either the steady-state response of the sensor, or the rate of response has been highlighted.

4.7 References

[1] B. Liedberg, I. Lundström, E. Stenberg, Sens. And Act. B., 11, 1993, 63-72

[2] P.B. Daniels, J.K. Deacon, M.J. Eddowes, D.G. pedley, Sens. And Act. B., 15, 1988, 11-18

[3] B. Liedberg, C. Nylander, I. Lundström., Biosensors and Bioelectronics, 10, 1995, i-ix

[4] B. Liedberg, C. Nylander, I. Lundström., Sens. And Act. B., 4, 1983, 299-304

[5] K. Matsubara., S. Kawata, S. Minami, Applied Optics, 27 (6), 1988, 1160-1163

[6] A. Otto, Zeitschrift für Physik, 216, 1968, 398-410

[7] R.J. Bell, B. Fischer, I.L. Tyler, Applied Optics, 12 (4), 1973, 832-836

[8] R.C. Jorgenson, S.S. Yee, Sens. And Act. B., 12, 1993, 213-220

[9] A.D. Boardman, Electromagnetic Surface Modes, Wiley, Chichester, 1982

[10] C.E.H. Berger., T.A.M. Beumer., R.P.H. Kooyman., J. Greve., Anal. Chem., 70(4), 1998, 703-706

[11] The numerical treatment of a single non-linear equation, A.S. Householder, Mc.Graw-Hill 1970.

5 LabVIEW programming in the analytical laboratory

5.1 Introduction

LabVIEW is a programming language supplied by National Instruments to allow engineers and scientists to effectively and quickly implement software solutions to many different acquisition and processing methods[1]. It is a full programming language, compiled directly into assembly language. It has a 32-bit parallel tasking compiler. It is also code-portable over many different platforms.

5.1.1 LabVIEW basics

Any program written within LabVIEW consists of two main parts. Firstly is the front panel, which is the visual aspect to the program, the part of the program the user will interact with once compiled. This is where all controls and graphs etc. are placed in order to allow input/output from the user. Each unit placed on the front panel is automatically inserted into the block diagram code. If the unit is a control, it serves as a source of data within the code diagram. If it is an indicator, it serves as a target for data. Careful attention must be made in assigning controls and indicators as, although they can be interchanged by the use of local variables, misuse can lead to inefficient code.

The second part is the block diagram. This is the actual code part of the program. Unlike most other languages however, LabVIEW maintains a graphical approach throughout the block diagram. These representations can be used as part of the code, and any changes made to the values stored within these items is immediately updated on the front panel. The order of code execution is determined by 'data dependency'. Data dependency is a term describing execution in conjunction with a flow of data. While this does not always queue operations exactly the way desired, it can be forced (Figure 5.1 and Figure 5.2). In this example, the system performs two updates to the string indicator, and performs some arithmetic. If required, dependency can be forced as in Figure 5.2.

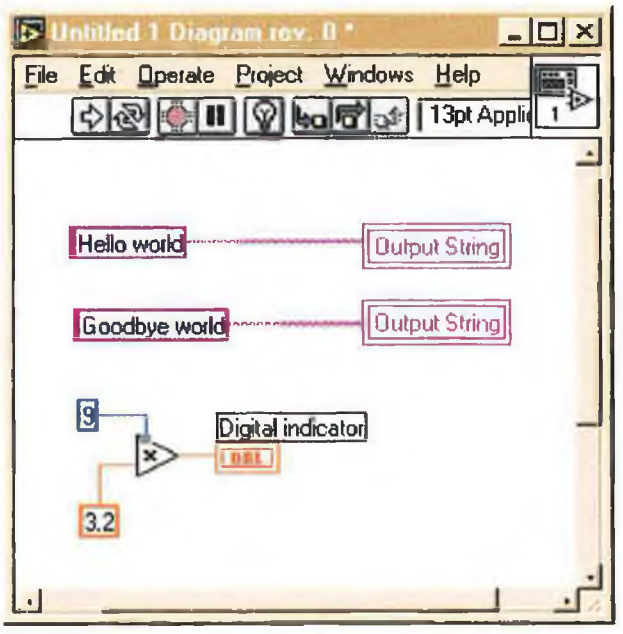

Figure 5.1: Example of a system with no inherent data dependency

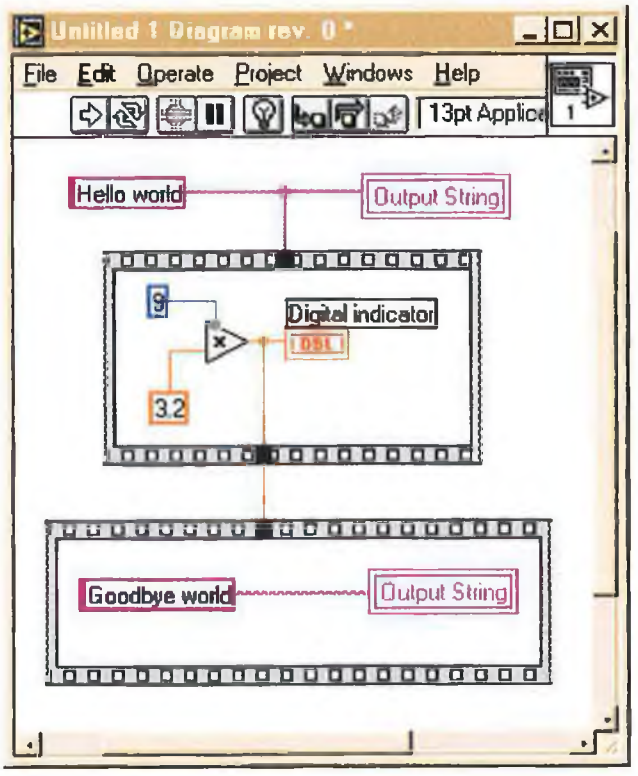

Figure 5.2: Example of a system with forced data dependency.

For simple examples where operations must be performed in a very ordered and not too complicated way (generally when the 'size' of the different portions are similar), a sequence structure can be used (Figure 5.3). A sequence structure is a structure into which code can be placed in successive panes numbered 0-n where there are n operations which need to be called in exact order. The order of execution in a sequence structure is always 0,1,2,....n. It is possible to share data between panes by using items called sequence locals, and these are either sources or targets of data. Unlike normal data types, they cannot be coerced into receiving data as a control or releasing data as an indicator.

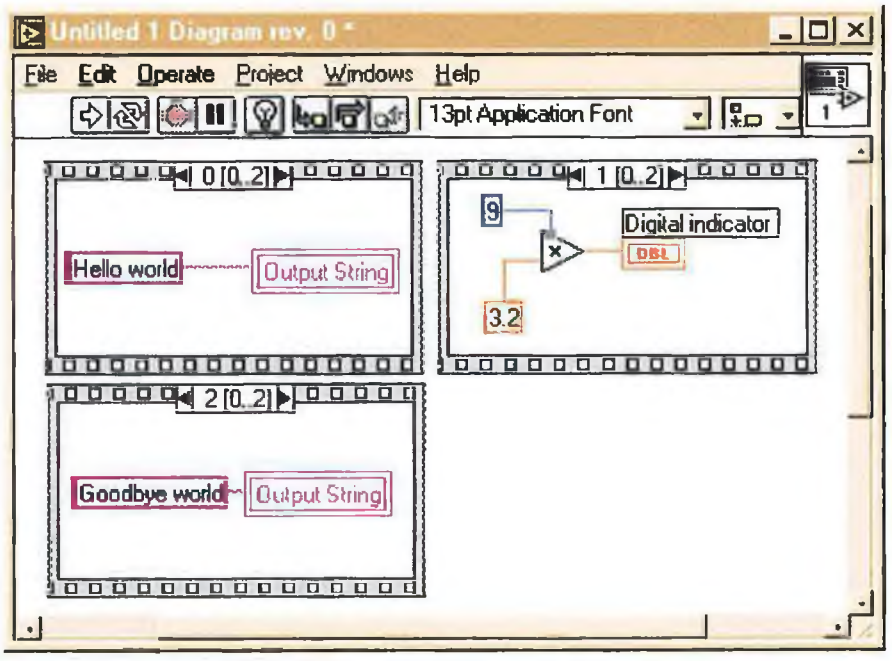

Figure 5.3: Example of a sequence structure with the three panes in order.

Other manipulations of the execution order can be achieved by use of the other structures available in LabVIEW. These are

- Case Structure. A Case structure behaves identically to a case statement in C or Pascal, allowing the program to perform a selective execution step. For a case statement (Usually for True or False) two sets of operations occur. Both sets of operations must output the same data or else data dependency will be violated. Once the input terminal is connected, the value passed to this determines which operations are called and thus a selective operation can be performed (Figure 5.4).

- For Loop. A For loop allows a certain operation to be performed N times. An example of this would be to perform an operation on each element of an array, with each array element being passed separately to the loop (Figure 5.5). However, the for loop has a special property called indexing. If an array is wired to a for loop as an input, then the for loop can automatically take the size of this array as the value for N. For example if a 100 unit array is connected to a for loop with the N terminal unwired, the loop will execute 100 times.

- While loop. A While loop is similar to a for loop except it executes indefinitely until a condition within the loop is met, at which time it exits. Examples of uses for this would be searching an array until a certain value is found (Figure 5.6).

Both loop types have the ability to index outputs. This means that every iteration of the loop adds another value to the output array, which (when the loop is finished), contains the results of every iteration. With this option not set, the loop returns only the last iteration result.

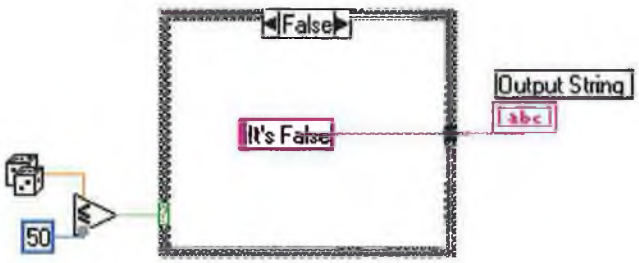

Figure 5.4: Example of a case statement execution returning a different string to an indicator depending on the state of a Boolean value.

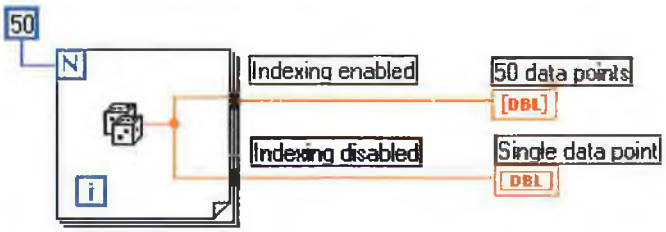

Figure 5.5: Example of a For loop execution which returns either an array of 50 random numbers (indexing enabled), or the last random number generated (Indexing disabled).

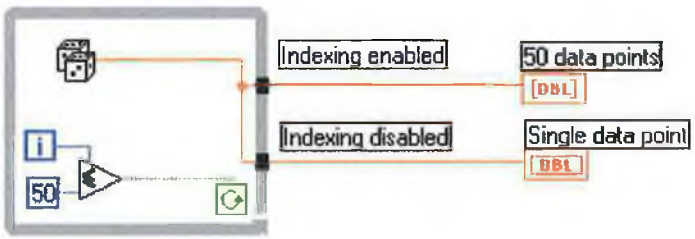

Figure 5.6: Example of a While loop execution returning an array of random numbers (Indexing enabled) or the last random number (Indexing disabled) once the variable i (Which contains a number corresponding to the number of times the loop has iterated) reaches 50.

5.1.2 Data Types

As with any programming language, data can be represented by many different types. In LabVIEW, the following data types are allowed

- Integer (Unsigned or signed 8 bit up to 32 bit integer)
- Real (Normal 16 bit real number up to extended precision floating point, 64 bits)
- Boolean (True or false)
- String (Collection of printable characters)
- Array (Collection of 1-n of one data type)
- Cluster (Collection of 1-n of any data types and may be mixed)

5.1.3 Data interoperability

Some programming languages are said to be strongly typed (Pascal) meaning that one cannot perform arithmetic using different types of data (Integers and Floating point). LabVIEW is not a strongly typed language, but markers appear where two different data types are being used together. There are some limitations to this however. One cannot, for example, multiply a string by a number (unlike C).

Wherever data of more than one type is being used together, LabVIEW automatically assigns a suitable common type. This process takes up memory and processor time. It is therefore advantageous to maintain data continuity throughout the code.

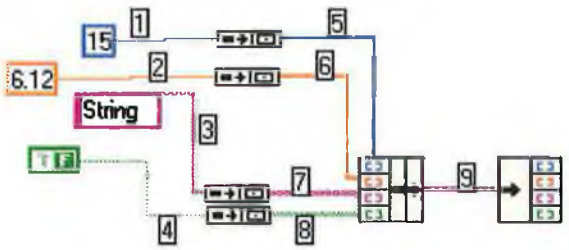

Figure 5.7: Wire types for different data types in LabVIEW.
Key. 1: Integer, 2: Floating Point unit, 3: String or Character, 4: Boolean, 5: Array of Integer, 6: Array of floating point, 7: Array of String, 8: array of Boolean, 9: Cluster of mixed data types.

5.2 Applications to analytical systems

LabVIEW offers an extremely fast path to generating custom code for anything from file read/write operations to inter-computer data sharing and synchronising across networks. In the analytical laboratory, these enable the everyday tasks such as file importing into commonly used packages[2] and data processing to be automated[3]. Spectral data can be zeroed, calibration curves automatically calculated and many separate files collated with very little programming. This approach allows for the almost complete removal of non-productive time-wasting chores.

Often, existing software performs 90% of the tasks required, and yet the remaining 10% of the work often takes longer than the measurements themselves. By incorporating LabVIEW programs into the sensing scheme, small changes can be made quickly and easily in order to make the program perform 100% of the functions required. This often requires each user of a sensor system maintaining their own software, which is tailored specifically for their own needs. This type of customisability is far too time-consuming and difficult to be implemented in other languages[4].

Once common file generation and data processing algorithms have been developed, they can simply be 'dropped into' new sensor programs, allowing for the automatic generation of data compatible with other software systems.

5.3 Real-time biological interaction monitoring

Surface Plasmon Resonance has been used for many years now to allow investigation of the binding properties of many different types of biological systems. The signal generated consists of a 'dip' in absorbance in the visible region, with the peak minimum shifting very slightly with changes in refractive index of the immediate environment of the sensor. A novel sensor for this

purpose has been prepared (Chapter 4), and the interfacing and processing software is outlined here.

5.3.1 Goals

The goal of this software is to provide real-time visual indications of the interactions between the biology of the sample and the sensor. Blank scan storage and retrieval as well as data storing in Excel compatible format are essential. Data acquisition was performed using a National Instruments Daq-700 PCMCIA I/O card.

5.3.2 Signal capture

Before any processing can be performed or results posted, the raw signal must first be recorded[5]. Modifications were made to existing driver software available from World Precision Instruments to allow for automatic detection of any I/O cards installed in the host computer system (Figure 5.8). Once this was performed, the data was collected directly from the spectrometer by calling the appropriate function within the assigned library.

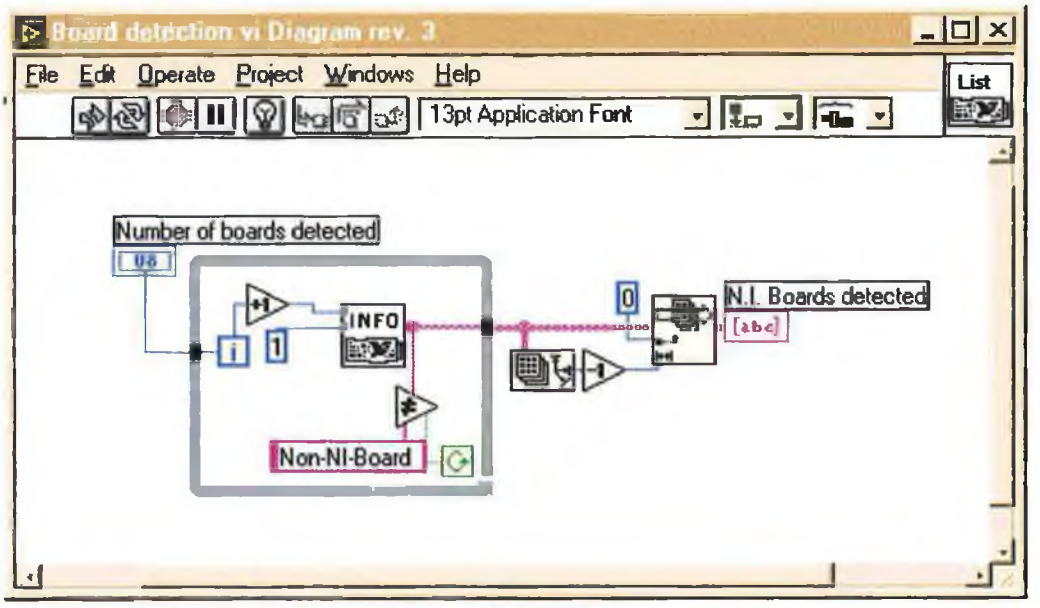

Figure 5.8: Sample of the changes made to existing driver software. This portion of code interrogates the system for information about any installed I/O cards in the computer and if only one is present automatically sets this to the default where it was normally required to manually select this option.

Once the data has been collected and stored in the computer memory, it is necessary to perform some smoothing and/or curve fitting in order to facilitate more accurate and reliable peak minimum determinations.

It was decided to perform a simple Nth order polynomial fit where N can be selected during execution to be any number from 1 to 100. The code responsible for performing the polynomial fit is supplied with LabVIEW and offers several fit methods. Method 3 (Householder curve fitting algorithm[6]) was found to give the most stable and reliable results. Once the polynomial fit coefficients are calculated, the curve must be re-generated in order to perform a peak minimum search. In order to allow this to be performed on any polynomial from 1st order to 100th order, a custom algorithm was prepared (Figure 5.9). This method automatically assigns the exponent for each fit coefficient, with the multiplier being provided by the output of the curve-fitting algorithm.

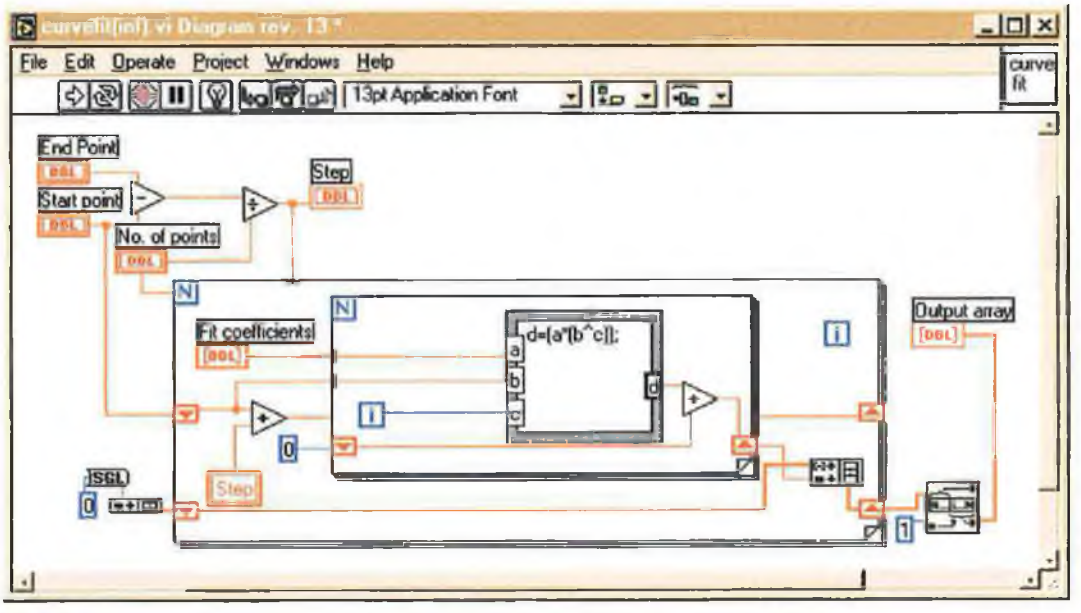

Figure 5.9: Sample of code permitting the re-generation of an Nth order polynomial where N can be any number and 'Fit Coefficients' are the 1-Nth polynomial coefficients.

Once the curve-fitted data had been reconstructed, the peak minimum was found by utilising another function supplied with LabVIEW, the PeakFind algorithm. This algorithm allows for the detection of peaks or valleys subject to certain input parameters such as the minimum peak height and width, along with selection of seraching for peaks or valleys.

While this value does represent the minimum of the data as presented to the function, it was found that the resolution of this value was only as good as the resolution of the generation of the fitted curve itself. It was decided to perform a second curve generation using the previously calculated coefficients for a portion of the curve from peak minimum - 1 to peak minimum + 1. This allowed a second peak find to generate a more accurate value for the of the original data set.

It was found that the best fit was obtained for a 30^{th} order polynomial fit as any value significantly above this (Figure 5.15) or below this (Figure 5.16) led to distortions of the fit. Fit type 3 (Householder method) was found to be the most suitable fitting algorithm (Figure 5.10 and Figure 5.11).

Results from this approach can be seen in Figure 5.12.

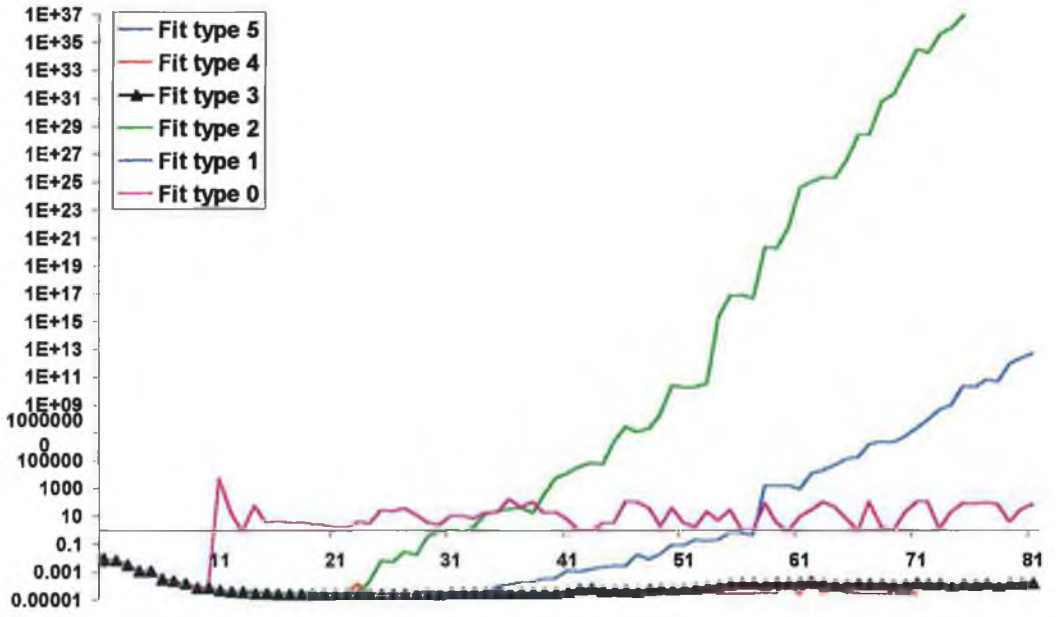

Figure 5.10. Plot of the residual error for curve fitting versus polynomial order for the size fit types investigated

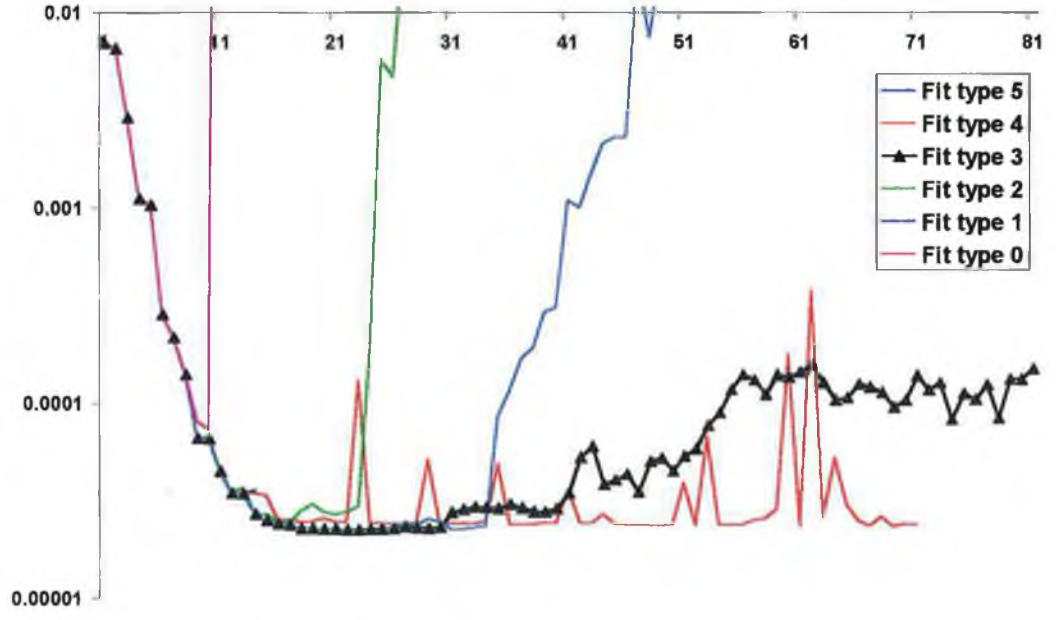

Figure 5.11: Expanded view of the variation of residual error versus polynomial order for the six fit types investigated.

5.3.3 Storage of results

The storage of the response trace was performed by outputting the data to a simple ASCII text file in the location chosen by the user. This data format is compatible with most spreadsheet programs and analysis packages (Tab delimited).

An option was also incorporated to allow for the actual sensor 'dip' to be saved onto computer disk for later analysis. These data were also saved in a spreadsheet compatible format.

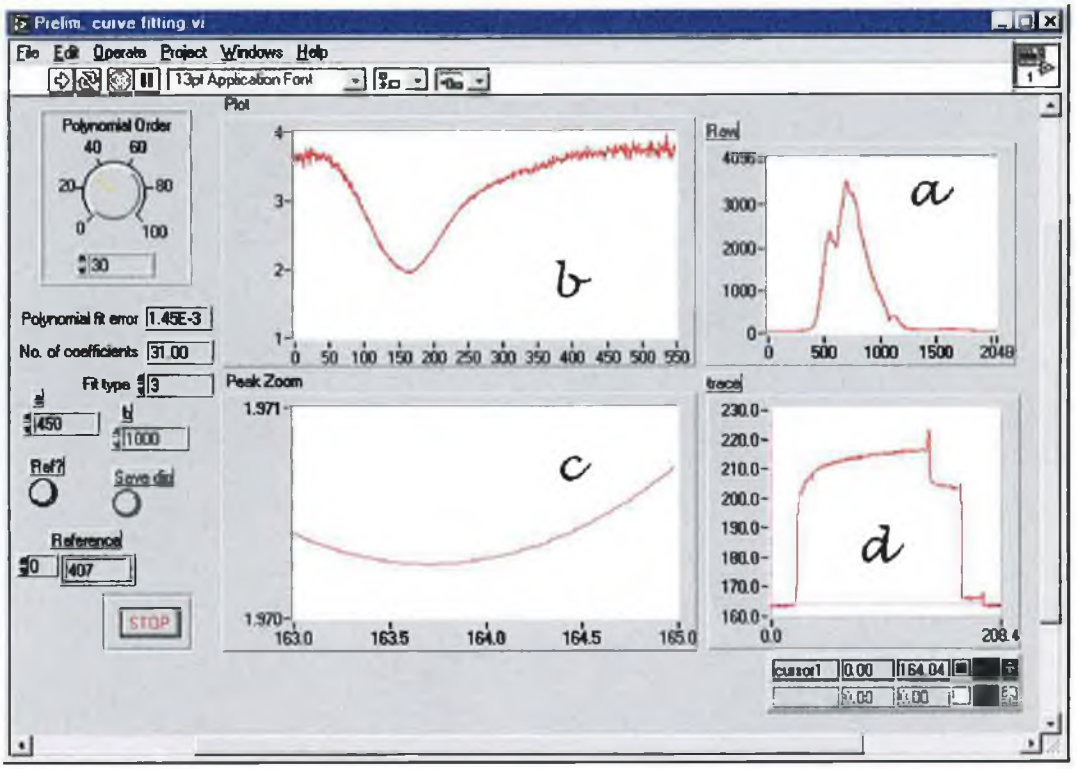

Figure 5.12: example of the output obtained from the biological interaction software during an assay.

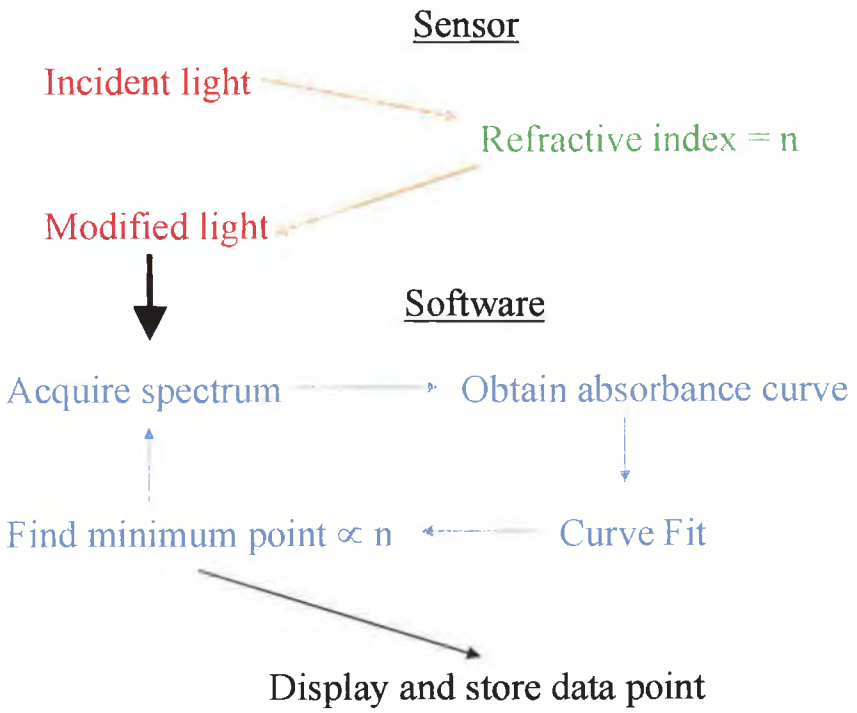

Figure 5.13: Schematic of the software pathways involved.
The modified light correlates to 'a' in figure 5.12, Obtaining the absorbance curve to 'b', Finding minimum point to 'c' and displaying points to 'd'.

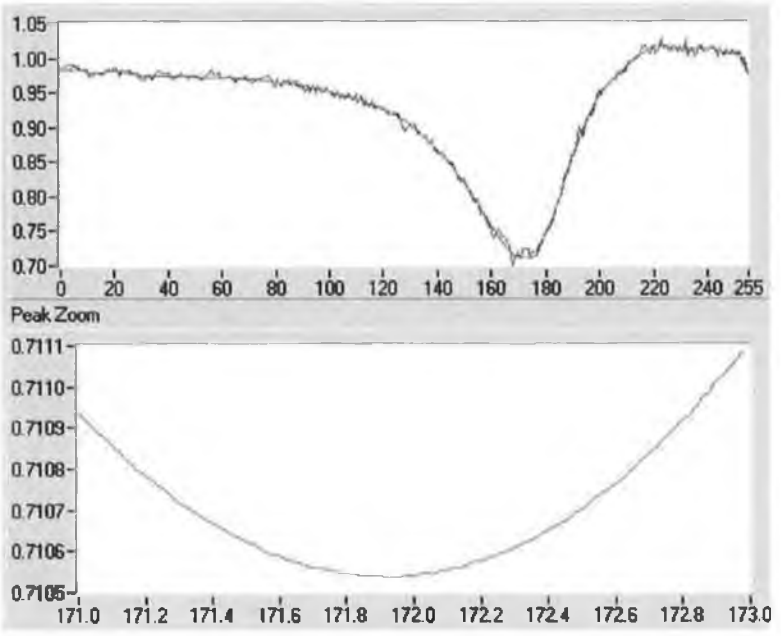

Figure 5.14: Example of a good fit to experimental 'dip' using a 30th order polynomial fit.
The lower peak is an expanded view of the dip minimum.

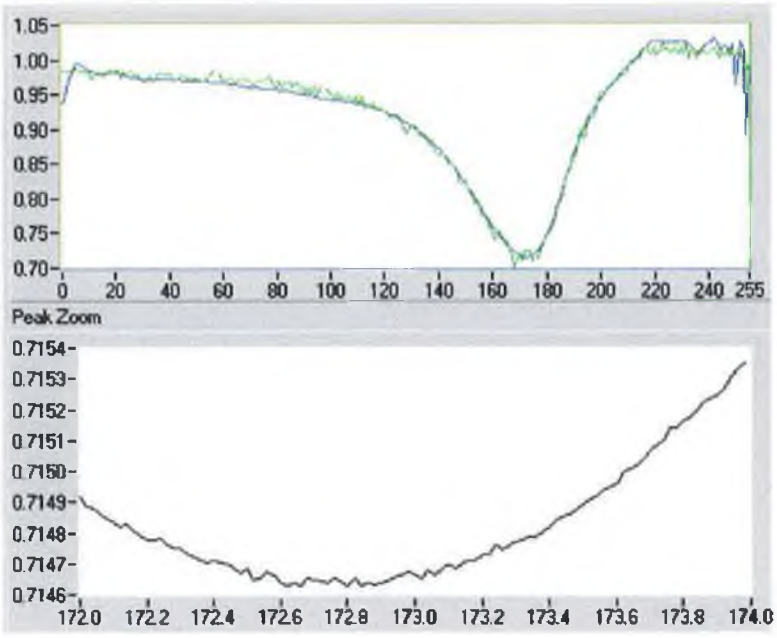

Figure 5.15: Example of an over-fit sample (80th order polynomial).
Note how the curve-fitting has begun to fit to the random noise in the trace.
The lower trace is an expanded view of the dip minimum.

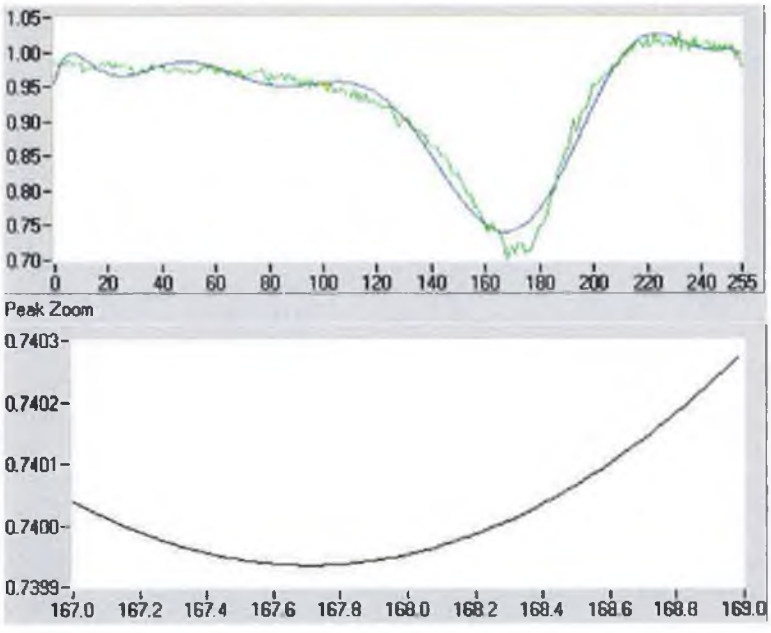

Figure 5.16: Example of an under-fit to experimental data (10th order polynomial).
The lower trace is an expanded view of the dip minimum.

5.4 Colour measurements with Digital cameras

There are analytical methods for many different analytes, which involve the generation of colour changes. Instrumental measurements of these systems have traditionally been limited to spectroscopy (preferably where the sample is non-turbid) or simple visual colour comparisons. Tests involving human judgement in distinguishing between colours can be troublesome. Such measurements are more subjective than quantitative. A more accurate method for the determination of colours and colour changes can be implemented through the use of colour CCD cameras. Software designed for the analysis of standard graphics files generated by a colour CCD camera is presented here. Experimental details can be found in Chapter 6.

5.4.1 Aims and objectives.

The aim of the software is firstly to enable the data to be read from a graphics file. Once the data has been read, there are many operations that can be performed, such as blank subtraction, sub-array selection (zoom), averaging, standard deviation, and some more advanced filtering and peak location. The data obtained must be saved in a spreadsheet compatible format (Tab delimited).

5.4.2 Data retrieval from Graphics files

The data from the colour measurement experiments were saved in a standard Bitmap file format. This is a widely used and well documented data file format. It exists in many forms, but the form of interest is the non-compressed 24-bit colour RGB bitmap. The file is made up of an initial header (56 bytes long) split up into many different parts including sections containing information about the picture height, width, colours etc. An initial problem is the form of storage of the data in the bitmap. In bitmaps, the values are stored in a reverse form in which

byte values consist of 8 individual bits in either little endian or big endian format[a] (Figure 5.17), but the organisation of values occupying more than one byte are different. In a bitmap file, the data are stored in the following way. Taking an example of a 16-bit number (2xbytes), the least significant byte is stored first, followed by the most significant byte. The arrangement of the bits within the individual bytes is the same as for other data types.

[a] Little endian and big-endian, outlined in Figure 17 are ways in which microprocessors handle data. Little endian has the 'least significant bit' in bit position 0, while big endian format has the 'most significant bit' in this position. In big endian format, the values of each bit are 128, 64, 32, 16, 8, 4, 2,1 from right to left as shown. These are reversed for little endian format.

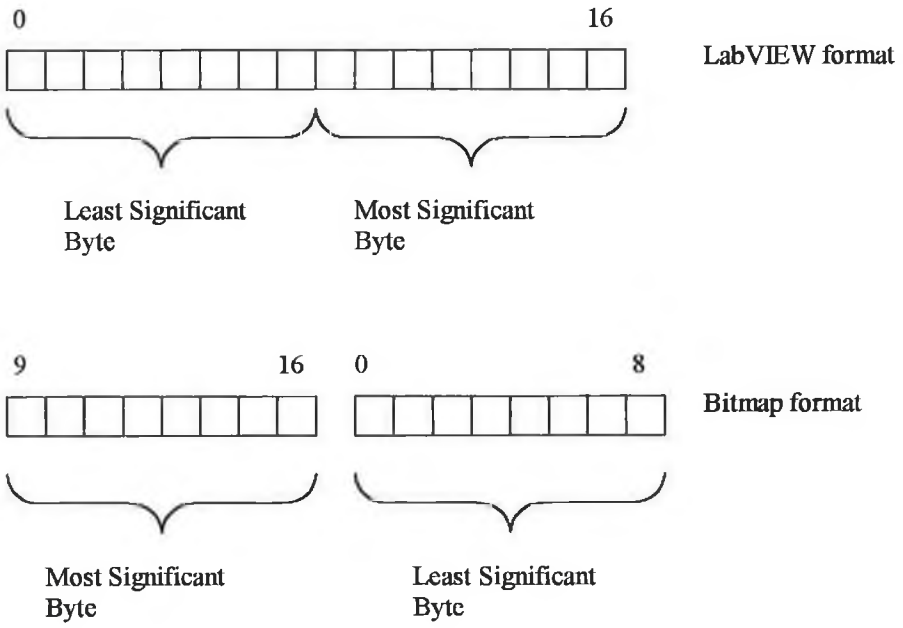

Figure 5.17: Schematic of the byte order in a Bitmap graphics file.

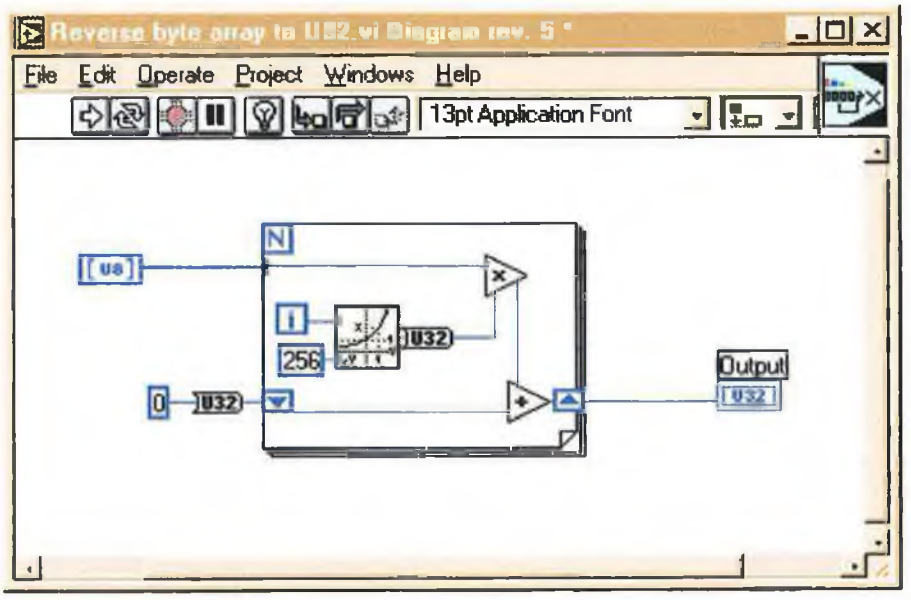

Figure 5.18: Code example to convert from Bitmap data storage format to LabVIEW data storage format.

Once this incompatibility was understood and overcome (Figure 5.18), it was possible to read in any information required from the bitmap file. From this, the software can automatically determine the size of the picture stored within, the number of colours within the picture (If not 16 million, generate an error). Once all ths relevant information has been read and converted, the picture data can be loaded.

5.4.3 Picture data retrieval.

The method of picture storage within a bitmap file is stored from the bottom left corner up. The first scan line is therefore the bottom horizontal line of the viewed picture, with the next line being the second bottom line and so on. In a 24-bit bitmap, the values for each pixel of the picture are stored in a 24 bit value with 8-bit values for red, green and blue. This means that a portion of the file of length 'picture width' x 3 bytes must be read in to allow for one complete scanline of the picture. This must then be repeated 'Picture height' times in order to get the entire picture into memory.

The process of reading entire bitmaps into memory can involve the use of large amounts of memory (data is stored within LabVIEW as floating point values, requiring 4 times the storage space as the parent bitmap). Therefore a method was devised which allowed for only the required portion (user-selectable) of the target bitmap to be read into memory by calculating the required offsets within the picture file and the lengths of each scanline to be read. This proved to greatly enhance the execution speed of the software.

5.4.4 Preliminary Data processing

Once the values for the picture have been stored in memory, the values are separated into the three 8-bit channels for red, green and blue for independent

manipulation and processing. After this, many different processes may take place which are summarised in the following sections.

5.4.5 Picture sub-array selection

It was thought advantageous to allow the user to graphically select sub-arrays from the picture stored in memory in order to facilitate the singling out of important features from within the picture. This was achieved by means of an Intensity Graph. An intensity graph within LabVIEW allows a 2-d array to be placed on the front panel. The value of each point in the array is then translated into a picture by means of a colour ramp. In these applications, the colour ramp was set to interpolate between 0 and 255 of the relevant colour. This allows automatic control of on-screen cursors, the locations of which can be monitored and controlled by the program. By identifying the location of these cursors, it was possible to communicate to the software which sub-section was required by the user.

5.4.6 Further analysis

It is possible for the software to then perform additional averaging and standard deviation measurements on the newly selected region of the picture, which allows for spatial comparisons to be made within the picture with respect to colour balances.

5.4.7 Blank correction.

Two different procedures were incorporated into the software to allow for blank correction of the membrane pictures.

5.4.7.1 Simple blank subtraction

In order to implement this approach, changes were made to the image processing software discussed above to allow for this procedure. It was decided to allow for the reading of more than one file to form a template light intensity map. These values were then stored in memory to be subtracted from the subsequently measured pictures.

With this method, the following is performed (Figure 5.19):

A sequence of blank files are chosen, resulting in the variable "Reference Files".
The colour intensities of each of these pictures are loaded and averaged resulting in the variable "Reference".
For this resulting picture, the average of the whole picture is subtracted from each individual pixel in the picture resulting in the variable "Blank".
This picture is then subtracted from the sample picture resulting in the final produce "Corrected Sample".

This process is performed automatically, and the same blank is used for each and every picture analysed in a given batch run.

In order for this to produce the required results, each picture in the analysis must have the same 'shape' of distorted light intensity.

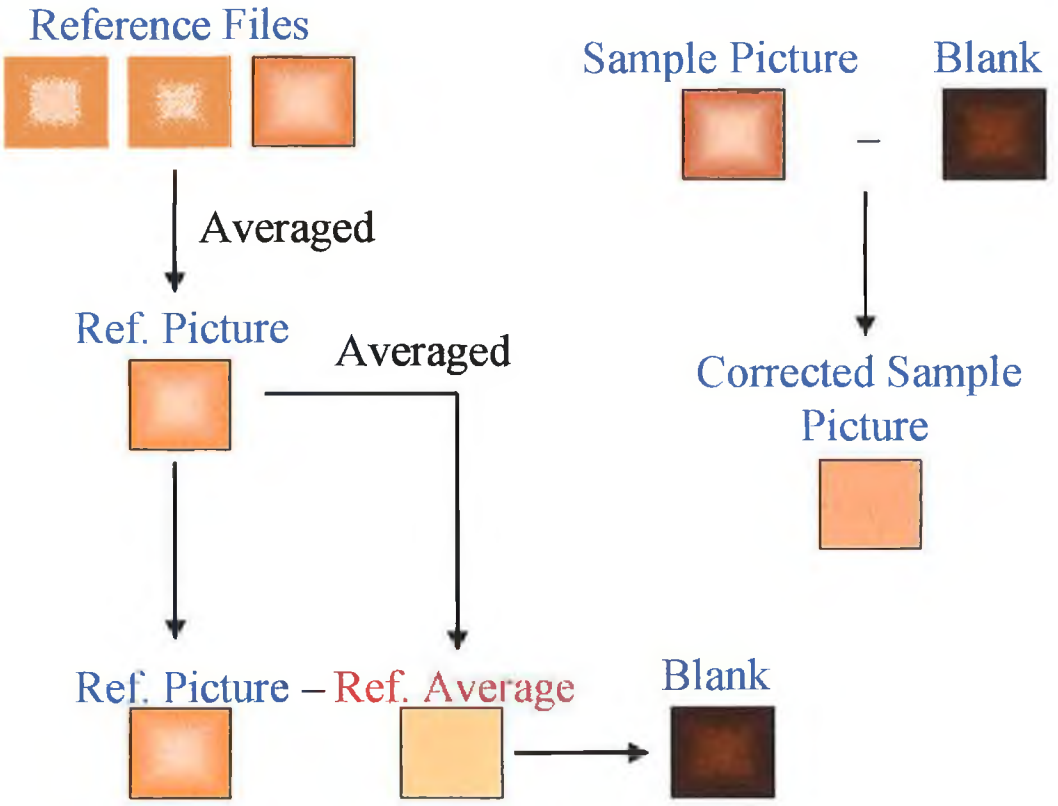

Figure 5.19: Flow chart describing the generation and implementation of the simple blank procedure.
Key: Blue = Picture value, Red = Number value, Black = Arithmetic operation.

5.4.7.2 Adaptive blank subtraction

The above solution is only applicable to situations where the magnitude of the distortion due to lighting is constant at every state of the membrane. Clearly this is not so. In order to attempt to correct for this, adaptive blank subtraction was implemented.

In this method, when preparing the blank as before, the entire picture (After average subtraction) is now also divided by the average of the entire blank picture. When this profile is then being used to be subtracted from the picture being analysed, it is simply multiplied by the average of the target picture in an attempt to adjust the magnitude of the distortion to that of the target picture.

With this method, the following is performed (Figure 5.20):

- A sequence of blank files are chosen, resulting in the variable "Reference Files".
- The colour intensities of each of these pictures are loaded and averaged resulting in the variable "Reference".
- For this "Reference", the average of the whole picture is subtracted from each individual pixel in the picture resulting in the variable "Blank".
- This picture is then divided by the average of the whole "Reference"(already calculated) to give the variable "Proportional Blank".
- This picture is then multiplied by the average of the entire sample picture to yield the "Adaptive Blank". This variable is then subtracted from the sample picture resulting in the final product "Corrected Sample".

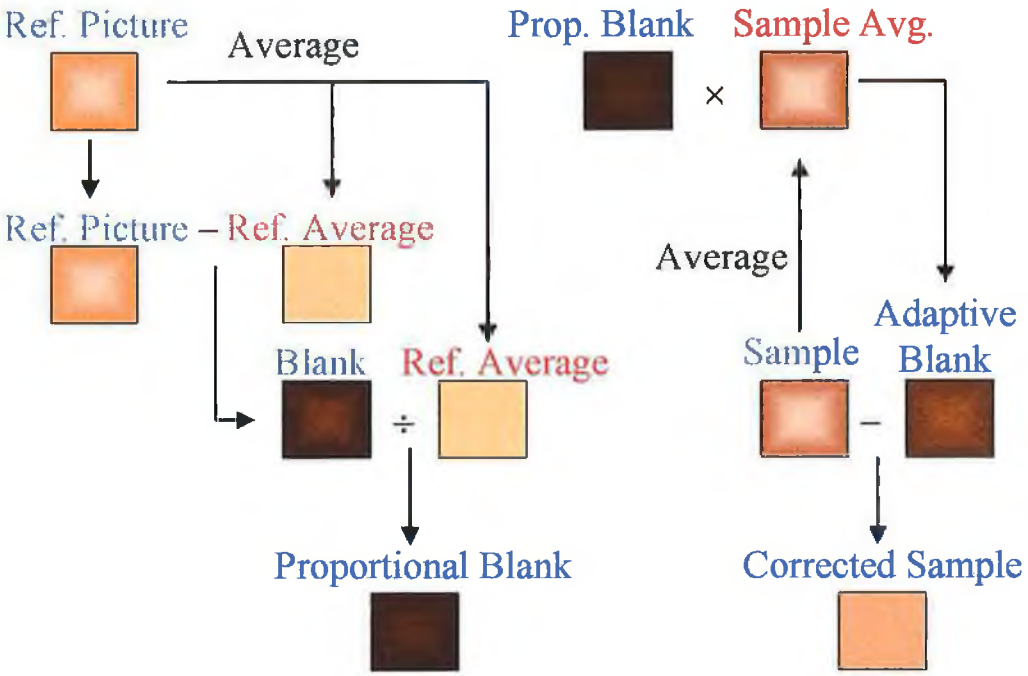

Figure 5.20: Flow chart describing the generation and implementation of the adaptive blank procedure.
Key: Blue = Picture value, Red = Number value, Black = Arithmetic operation.

5.4.8 Report generation

The software automatically tabulates the results from the above. It is possible to either print the data or export it directly to Microsoft Excel using Dynamic Data Exchange (DDE)[7].

5.4.9 Result Printing

The printing of results is easily achieved by sending the data to a sub-vi front panel and setting the vi properties to print the panel when complete.

5.4.10 Dynamic Data Exchenge (DDE)

As its name suggests DDE is a method whereby two programs can exchange data. In its most primitive form it can be used to input data directly into a Microsoft Excel worksheet instead of saving as text and then importing. However, functions within the target program cannot be accessed via DDE and as such it is quite limited.

Initially, it is necessary to have the target program running. A call is made from the program to the system to launch Excel. This ensures that whenever the DDE sub-VI is called, Excel will be running.

Once this has been achieved, a DDE 'Connect' call is made to the Excel system, and instructions are sent to order Excel to open a new workbook. After this is complete, the conversation is closed again. In order to transfer any data, another conversation must be opened, but this time, the target of the conversation is not the Excel system, but rather the workbook open within the system. When this is complete, the individual cells and ranges within the worksheets are accessible. The data is then passed directly to the required locations within the workbook, and the conversation is closed once again.

Such data transfers are performed exclusively through computer system memory. The system (Windows) allows for such programs to share information in this way. The system handles all protocol and data issues for communication between the two programs. Once communication has been opened, the two programs need to know what to do. Each program has different steps to be followed in order to achieve such transfers. Only the internal transfer protocol (DDE) is identical.

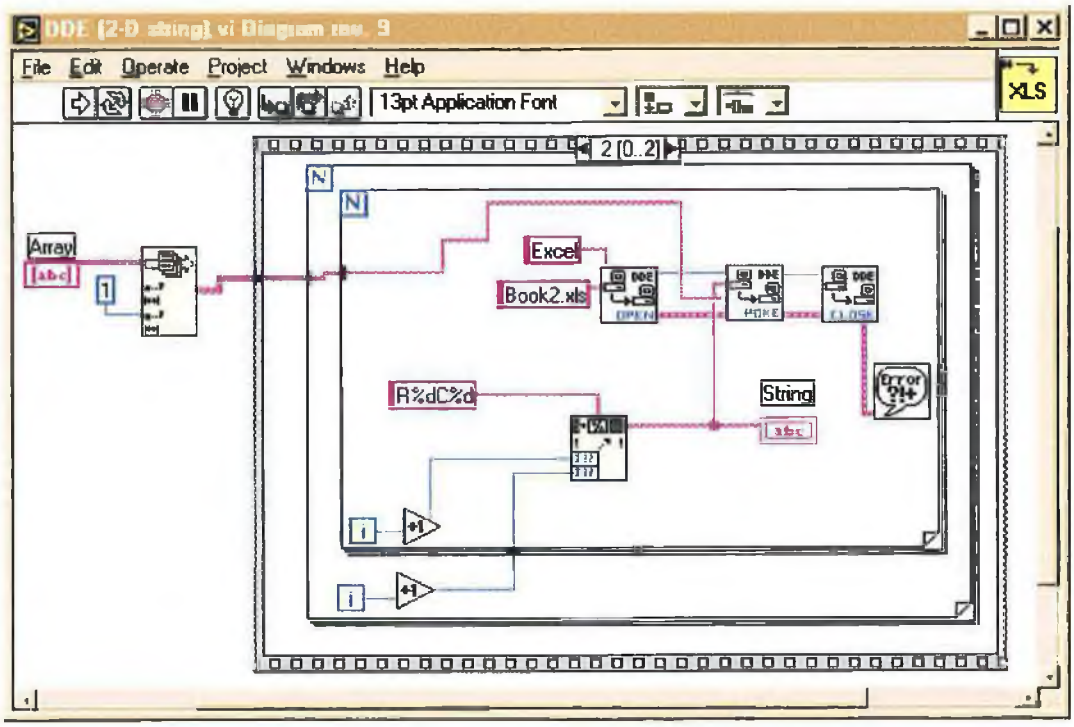

Figure 5.21: Example of the ability of LabVIEW to communicate with Microsoft Excel via DDE.

5.4.11 Advanced Processing techniques[6]

In order to make the software able to automatically measure small distinct areas of sensor colour it was decided to implement a low band-pass filter type of filtering scheme to eliminate noise. In order to do this Fourier transform techniques were employed.

5.4.12 Sample preparation

In order to allow this function to proceed, a single 'line' of spots must be selected by the user. This was achieved by utilising the picture sub-array selection method outlined previously. The data contained within this sub-array was then passed to the processing functions.

5.4.13 Fourier processing

The 2-d array sub-section is first vertically averaged to yield a 1-d array of average colour values. This array is then passed through a Fourier transform in order to change from the time to the frequency domain. Once the data is frequency separated, any unwanted frequencies can simply be removed. The frequency threshold for filter is determined automatically by inputting the number of spots within the sample. After the unwanted frequencies have been removed, the cleaned Fourier transform is passed back through an inverse Fourier transform to obtain a 'cleaned' signal. Peak height / valley depth measurements are then performed as before. We can see the code responsible in Figure 5.22 and the results in Figure 5.23. In Figure 5.23 'a' we see the raw data, 'b' is the cleaned data with frequency clean-up, 'c' is the responses after peak-finding and 'd' is the overall response profile.

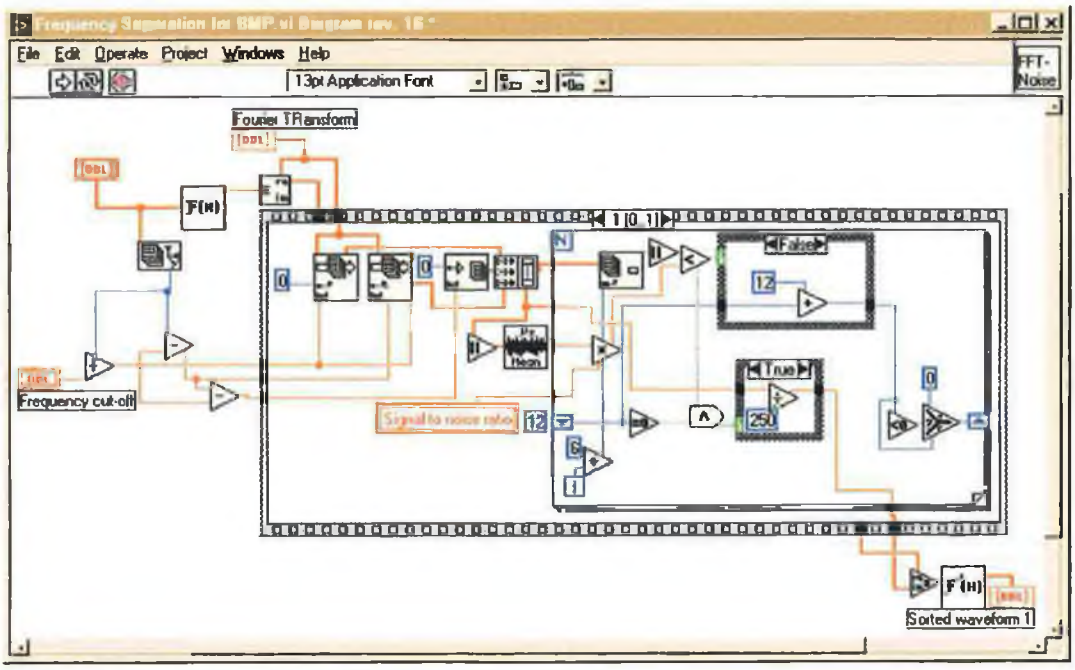

Figure 5.22: Example of the code for the automatic Fourier-cleaning of the selected sub-array for sensor 'spot' measurement

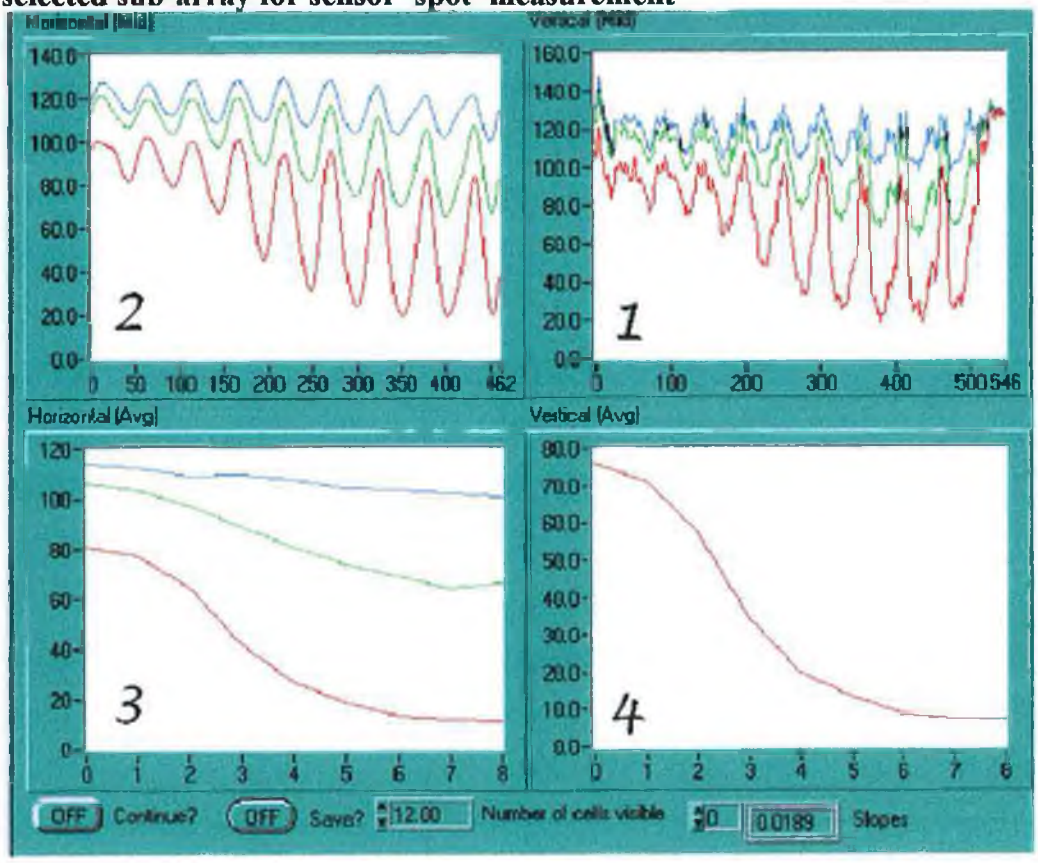

Figure 5.23: Example of Fourier cleanup of data taken from an ELISA plate picture.
The calibration curve below is calculated automatically with respect to the equation (Red*Green)/Blue

5.5 Conclusions

The ability to perform real-time biological interaction measurements with a relatively simple software design is testament to the power coupled to ease of programming which has always been a part of the LabVIEW system. Although the system runs at an acceptable rate (3-5 points per second with a 30^{th} order polynomial fit), it is believed that with further optimisation this could be improved.

Within the field of colour measurement and analysis, the ability to automate the interrogation of stored picture files is paramount. The possibility exists for these measurements to be made manually albeit with incredibly increased timespans and complexity. The automation of this method led to the development of an automatic 'spot' measurement technique which has shown itself to be a very useful tool.

The software reported here has been shown to function well for the intended usage. Above all, it is easily customised, a point which is essential in research as goals and requirements are constantly re-evaluated.

5.5.1 Future work

The ability to perform a better fit to the experimental data with the biological interaction software is very important. Presently, the polynomial fit produces good results, but a curve fit to a theoretically derived equation may prove more successful. Also, many more features can be added to the existing software to allow for more sophisticated analyses to be performed such as automatic tabling of results and report-generation.

With the software devised for the colour measurements with the digital camera, the ability to automatically 'find' colour spots within a 2-d space would be a tremendous advance in the software for colour analysis. This would allow automatic location and analysis of complete ELISA plates in one process. Also, execution speed and memory usage are areas where it is believed many improvements can be made. As with the biological interaction software, many new features could be added to the software to aid in the analysis of the raw data.

With both pieces of software however, since they are dealing with generic techniques, which may find application in many different areas, the ability of LabVIEW to form a central group of processing algorithms which can be re-used to build applications for specific tasks is a great advantage. The ability to create such custom software and the small times required make this approach near impossible with other programming languages.

5.6 References

[1] LabVIEW User Manual, National Instruments, 1996 part no. 320999B-01

[2] T. Starn., Lab. Robotics and Automation., 10(2), 998., 119-121

[3] J.P. Osborne., B. Erwin., M. Cyr., C. Rogers., Lab. Robotics and automation., 10(2)., 1998., 63-66

[4] D.M. McStravick., J.L. Kelly., Lab. Robotics and Automation., 10(2), 1998., 83-87

[5] LabVIEW Data Acquisition Basics Manual., National Instruments., 1996., Part no. 320997A-01

[6] LabVIEW Analysis VI Reference Manual., National Instruments., 1996., Part no. 320538C-01

[7] LabVIEW Communications VI Reference Manual., National Instruments., 1996., Part no. 320587C-01

6 Analytical measurements based on monitoring colour changes with digital cameras

6.1 Introduction

Much research has been performed in which linear-array CCD detectors are used to record UV-Vis/IR spectra or simple intensity maps of sensing layers[1-11]. Such CCD detectors have now become an accepted and affordable method to perform analytical measurements in the laboratory. In some applications however, the importance of wavelength specific data is superseded by that of spatially resolved data. In these cases, 2-D CCD detectors, usually responding only to a single wavelength or range of wavelengths, record a 2 dimensional topography of the target[12-18]. Being digital devices, these systems offer the ease and flexibility of use of digital post-processing techniques.

CCD cameras have evolved from this stage to include the possibility to measure colour[17]. Such cameras are now readily available on the market and have ever increasing quality (resolution, size, durability and colour reproduction) coupled with an ever decreasing price (Casio QV-10 : Jan '96 £800. Jan'98 <£200[19]). There are cameras with 24-bit (>16 million) colours available.

Offering very good resolution (Up to 1280x1024) and very accurate colour reproduction at a reasonable price, the application of such devices to the analytical measurement of an optical sensor responding in the visible spectrum is presented in this chapter.

6.2 Colour Digital Cameras

Colour digital cameras are based on CCD detectors[20]. A CCD (charge coupled device) has an output voltage proportional to the amount of incident light striking the surface. Traditional CCD detectors for spectrometers are constructed using a 1-D array and controlling the wavelengths of the light incident on each element, thus providing the user with a wavelength spectrum of the incident radiation[21].

Monochrome 2-D CCD devices are constructed in a similar way to conventional 1-D CCD detectors[21]. In this case however, there is no wavelength separation step. Instead, the light is incident directly on the detector. In order to allow these pixels to sense colour we must first recognise that human perception of colour is based on only three basic colours, red, green and blue[22].

6.2.1 Colour measurement with CCD arrays

Each 'pixel' (single dot in a picture) of a digitally recorded picture is composed of three values. Each of the red, green and blue channels has its own intensity value between 0 and 255. This gives 3x8 bit resolution, or what is commonly known as 24-bit colour or 'true colour'. In order for the camera to be able to record these data, the detector units in the 2-D CCD array are grouped into triplets with every third detector covered by a red, green and blue filter (Figure 6.1)[17]. Thus, each detector triplet measures one pixel of the final picture (Figure 6.2). This triplet of values is then interpreted by the camera's electronics and either stored in camera memory or transmitted to a host computer. The final pixel is then represented by a colour specified by the relative amounts of red, green and blue recorded.
The 'pixel fill factor' is a measure of how much of the incident light is actually recorded relative to its position. The pixel fill factor for this type of colour camera is said to be 33% or less. Monochrome detectors can often achieve pixel fill factors of upwards of 80%[17]. Using this three-filter approach for colour allows this figure for colour cameras to reach a maximum of 33.3%.

6.2.2 Data storage with CCD cameras

The digital information describing the target picture requires permanent storage in order to facilitate archiving and processing at a later date. Storage of the digital image of the target can be achieved in different ways.

6.2.2.1 Via PC card memory.

Many personal Colour CCD cameras on the market have 'smart media' cards allowing up to 4 megabytes worth of pictures to be stored within the camera. These can be removed and interchanged as needed. Cameras using this approach use compressed image types to allow many pictures to be stored in such a small memory space.

6.2.2.2 Via communication to Host PC.

Some cameras operate only through a direct connection and control to a PC. When a picture is taken, the digital information is sent immediately to the host computer where it can be displayed and stored at will. This type of camera is inherently less versatile as it requires an operating computer to be present at all times.

6.2.2.3 Combination

Most portable, personal cameras today have the option of operating via either of the above methods. For personal pictures, or for places where a computer is not available, the smart media can be used to store pictures, which can then be downloaded to computer at a later date.

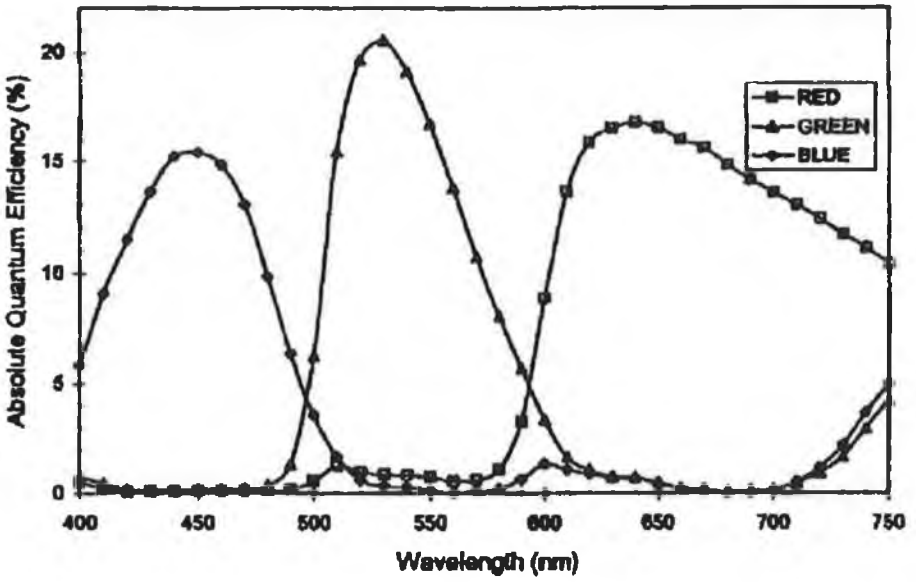

Figure 6.1: Typical red, green and blue filter response curves for a Kodak colour CCD camera.

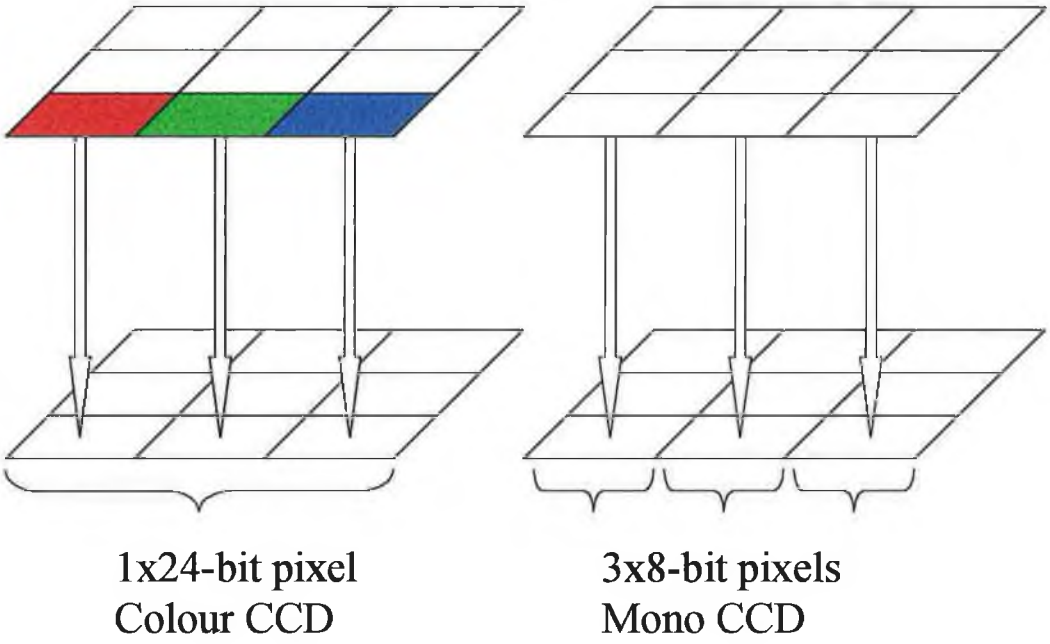

Figure 6.2: Schematic of the three-filter approach to colour CCD camera detection.
Each CCD detector records an 8-bit light intensity value.

6.3 Graphics file formats

Graphics files can be stored digitally in either compressed or uncompressed formats.

6.3.1 Uncompressed:

Uncompressed file types have the reassurance that each and every individual point of information within the picture (pixel) is stored individually and exclusively. These pictures can be modified and reproduced exactly.

6.3.2 Compressed:

Compressed file types can be further divided into two groups, those using lossy algorithms and those using lossless algorithms.

6.3.2.1 Lossy:

Lossy algorithms are types where advanced mathematical functions are used to 'simulate' the data represented in a picture, with the best fit equations being stored instead of the original data. The amount of compression can often be determined by the maximum allowable error between the best-fit model and the original data. While these can provide huge compression ratios (90% reductions in file size or better are common), they also lose some of the original data recorded, as the mathematical fits are never exact[23]. As the compression algorithms become more and more advanced, greater compression ration can be achieved with less distortion of the original picture[24].

6.3.2.2 Lossless:

Lossless algorithms on the other hand allow the parent picture to be recreated exactly from the compressed picture without any loss of the original data. Instead of performing a 'best-fit' with a defined maximum allowed error, an exact-fit

must be performed[25]. These generally do not yield the same reduction in file size as lossy types.

6.4 Bitmap File Format

In this work, the bitmap file format was chosen for storing of picture data because of its straightforward and logical storage of data. Bitmaps can be used in either normal or compressed mode. The compression algorithm used is that of run-length encoding and is of the lossless type. For the duration of this work, the normal uncompressed format was employed.

The bitmap file has a specific format consisting of a file header and the image data, and sometimes a colour palette. The file header is clearly defined and all the required information about the picture stored within can be read from this. The general structure of the file header is shown in Table 6-6.

Variable	Value(s)	Variable type	Data offset
File Header	'BM'	2xChar	0
File Size (Bytes)	0 to >4 billion	Long Int	2
Reserved	N/A	2xInt	6
Headersize	53	Long Int	12
InfoSize	N/A	long Int	14
Width	1 to >4 billion	long Int	18
Height	1 to >4 billion	long Int	22
biPlanes	N/A	short Int	26
Bits	24	short Int	28
biCompression	0	long Int	30
biSizeImage	Varies	long Int	34
biXpelspermeter	Varies	long Int	38
biYpelspermeter	Varies	long Int	42
biClrUsed	N/A	long Int	46
biClrImportant	N/A	long Int	50
Picture Data	3x8bit triplets	varies	54

Table 6-6: Format of Bitmap File header as used in 24-bit image files. Char, short Int and Long Int are different binary data types of 1, 2, and 4 bytes length respectively.

6.5 Analytical application of colour measurement

The advantage of using a colour CCD camera system is the ability to perform basic wavelength region resolved measurements. We know from Figure 6.1 that the red, green and blue colours represent specific wavelength ranges. Thus, colour changes which occur in these ranges can be measured by comparisons of the intensities of the three channels to each other. Ideally, two colour channels would respond equally well (or in opposition to each other) with the third channel acting as a reference.

6.5.1 Ion-selective optode membranes

Ion-selective optode membranes have been devised for many different species[24-26]. The colour changes associated with these sensors are typically in the visible region. Optical responses are normally in the form of a wavelength maximum shift, with this shift comprising often 100-200 nm. Such shifts give rise to colour changes from purple to blue, or red to orange or even blue to yellow. Such colour changes are easily visible with the naked eye[29]. Since the colour change is proportional to the log of activity of the required species, measuring the colour change in any way allows us to calculate the activity of an unknown sample by a single colour measurement. This type of measurement usually involves the entire picture area being occupied by a portion of the target membrane surface.

6.6 Sensor array imaging

Single-target systems are not the only systems for which colour CCD cameras can be applied. There are many cases where simultaneous calibration and unknown sample determination would be advantageous. In such a system, each colour-generating sensing spot could be immobilised or placed in a particular part of an overall pattern of spots allowing multiple measurements to be made in parallel.

6.6.1 Arrangement of sensor spots

As with any analytical technique, it is advantageous to present the original data in a form most suitable to the measurement technique. For this purpose, it involves regular and periodic spacing of the sensing regions throughout the target picture. A sub-section of the picture thus generated should generate a pseudo-square wave pattern of colour variation throughout the three colour channels. This allows us to apply a frequency filter to remove any unwanted noise.

6.7 Fourier-transform

The Fourier transform decomposes or separates a waveform or function into sinusoids of different frequencies which, when re-combined, yield the original waveform[30]. It can identify and distinguish different frequency sinusoids and their amplitudes. The Fourier transform is defined as

$$F(s) = \int_{-\infty}^{\infty} f(x)\exp(-ixs)dx \qquad \text{Equation 6.1}$$

where *F(s)* is the transformed sample at time *x*, i = $\sqrt{-1}$, *s* = the sample at any time *x*, *x* = the time of sample *s*, *s* is the frequency of the signal.

There are some functions which do not have a Fourier transform, but most physical systems do have a transform, especially when the transform represents a physical quantity.

Functions or waveforms can generally be split into even and odd parts as follows

$$f(x) = E(x) + O(x) \qquad \textbf{Equation 6.2}$$

where

$$E(x) = \tfrac{1}{2}[f(x) + f(-x)] \qquad \textbf{Equation 6.3}$$

$$O(x) = \tfrac{1}{2}[f(x) - f(-x)] \qquad \textbf{Equation 6.4}$$

and E(x) and O(x) are, in general, complex. An even function therefore has an even transform and an odd function has an odd transform. Other symmetrical properties are given below in Table 6-7[31].

Function	Transform
Real and even	Real and even
Real and odd	Imaginary and odd
Imaginary and even	Imaginary and even
Complex and even	Complex and even
Complex and odd	Complex and odd
Real and Asymmetrical	Complex and asymmetrical
Imaginary and symmetrical	Complex and asymmetrical
Real even plus imaginary odd	Real
Real odd plus imaginary even	Imaginary
Even	Even
Odd	Odd

Table 6-7: Symmetrical properties of functions and their Fourier transforms.

In the cases investigated in this work, the functions, resulting from real world data are generally Real and Asymmetrical meaning of course that the Fourier representation will be an asymmetrical complex function. Thus, and Fourier

transform calculations must be performed on both the real and imaginary portions of the transform.

6.7.1 Sampling

A signal which has no spectral components above a frequency B Hz is said to be a band-limited signal ($F(s)=0$ for $|s|>2\pi B$). The sampling theorem states that a signal can be correctly restored to its original without error from samples taken uniformly at a rate greater than 2B samples per second. This minimum sampling rate is called the Nyquist rate or the Nyquist frequency. The corresponding sampling interval is called the Nyquist interval. A signal sampled at a rate lower than the Nyquist rate is said to be under-sampled.

6.7.2 Aliasing

In practice, signals recorded are not band-limited as described above but rather are time-limited. As a result, such determinations of adequate sampling frequencies, which do not lose important information, are more difficult. However, in most experiments, the analytical signal is often of quite a low frequency and the sampling rate of quite a high frequency. Such a system is said to be over-sampled and removes the effect of aliasing.

6.7.3 Time and frequency domains

It can be useful to think of such functions and their transforms as occupying two domains. These are referred to as the function and transform domains, or the time and frequency domains. Operations performed in one domain have corresponding operations in the other. According to the convolution theorem, the convolution

operation in the time domain becomes a multiplication operation in the frequency domain and the reverse is also true. Such theorems allow movement between the two domains so that operations can be performed where they are easiest or most advantageous.

6.7.4 Signal vs. noise

In general, signals generated in most experiments are of a relatively low frequency, or are at least critically sampled. If an experiment is undersampled, information has already been lost. Most experiments in the modern laboratory are actually over-sampled.

An important influencing factor in many measurements is the presence of noise and its effect on the analytical signal. Most noise is of a high frequency, representing 'random' or 'shot' noise. The ability to move between the time and frequency domains allows one to filter out much of the high frequency noise in this way. It is often possible to reveal much more information about a sample than is immediately visible in the raw data.

In Figure 3 below, we see an example of using a Fourier transform to clean a somewhat corrupted signal. The input signal is the sum of two different frequencies, one of which is our analytical signal (Figure 6.3, 1). Further superimposed on this signal is random white noise. The frequencies and magnitudes present are defined by the values shown in Figure 6.3, 2. The Fourier transform of this function can be seen in (Figure 6.3, 3) above. The two main frequencies are clearly visible. By simply removing any values in the transform above a certain pre-determined point, we can remove the higher frequency signal components (Figure 6.3, 4) and then re-construct the original function without these frequencies. We can see in the cleaned signal that the original frequency and amplitude have been quite accurately restored (Figure 6.3, 5). The residuals of the original transform (found by subtraction) can be seen in Figure 6.3, 6.

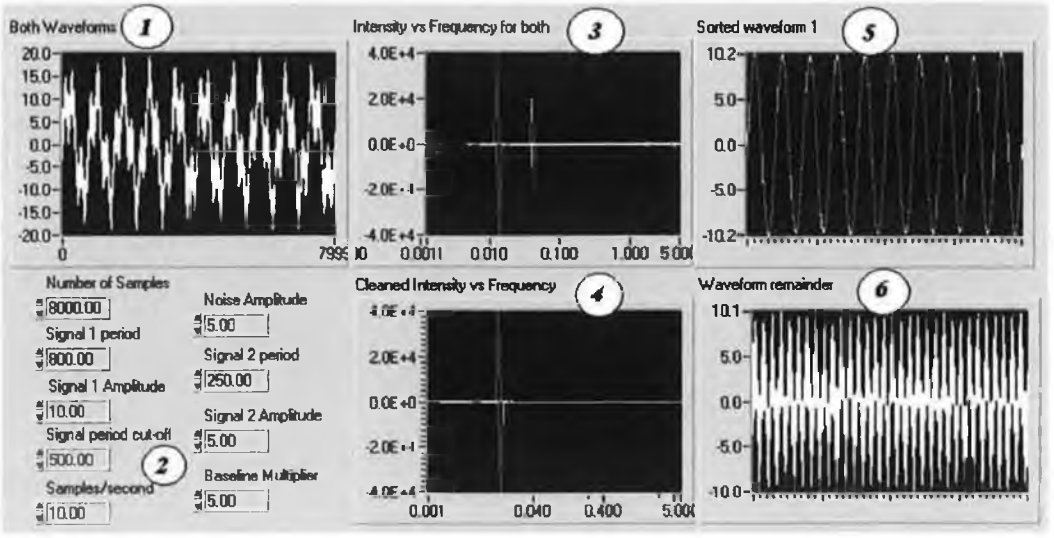

Figure 6.3: Example of Fourier Transform clean-up of a corrupted signal. 1: Input signal, 2: Parameters used for simulation of signal in (1) above and for separation, 3: Fourier transform of the input signal, 4: Cleaned Fourier transform with main interfering frequency removed, 5: Cleaned signal without higher frequency noise, 6: Residuals of the original signal.

6.7.5 Using Fourier transforms with sensor 'spots'

Taking a histogram or cross-section of a colour picture with immobilised 'spots' of activity results in a square wave or pseudo-square wave signal. Performing Fourier transform functions on this to remove high frequency signals can clean the signal but reduces the pseudo-square wave to a well defined sinusoid.

6.7.5.1 Square wave vs. Sine wave.

A parent sinusoid of frequency f and amplitude a can be modified by addition of another sinusoid of frequency f×3 and amplitude a/3. This can further be modified my adding a sinusoid of frequency f×5 and amplitude a/5. And the same is true for f×7, 9, 11, 13, 15 and so on for the odd numbers. The same pattern is repeated with the signal amplitude. The result of these additions is the construction of a square wave of the same frequency of the original, and an amplitude directly proportional to the original signal amplitude (Figure 6.4).

As we can see from Figure 6.5, the extra peaks and amplitudes are clearly visible (And resolved) from the original in the Fourier transform. These peaks can be removed by simply setting the points where these peaks are present to zero.

This fact allows us to treat any square wave (signal such as that taken from an ELISA plate picture cross-section, discussed later) as a group of sine waves, with one parent sine wave. By isolating this sine wave, we are accessing the overall change in signal, minus the high frequency components, which usually include random noise. The benefit of the Fourier transform is two-fold. Firstly, it allows the generation of a sine wave from a square wave, with one definite point for each peak/valley (which makes peak-finding by software much easier). Secondly, in removing the high frequency components, most or all of the random noise is then removed from the original signal.

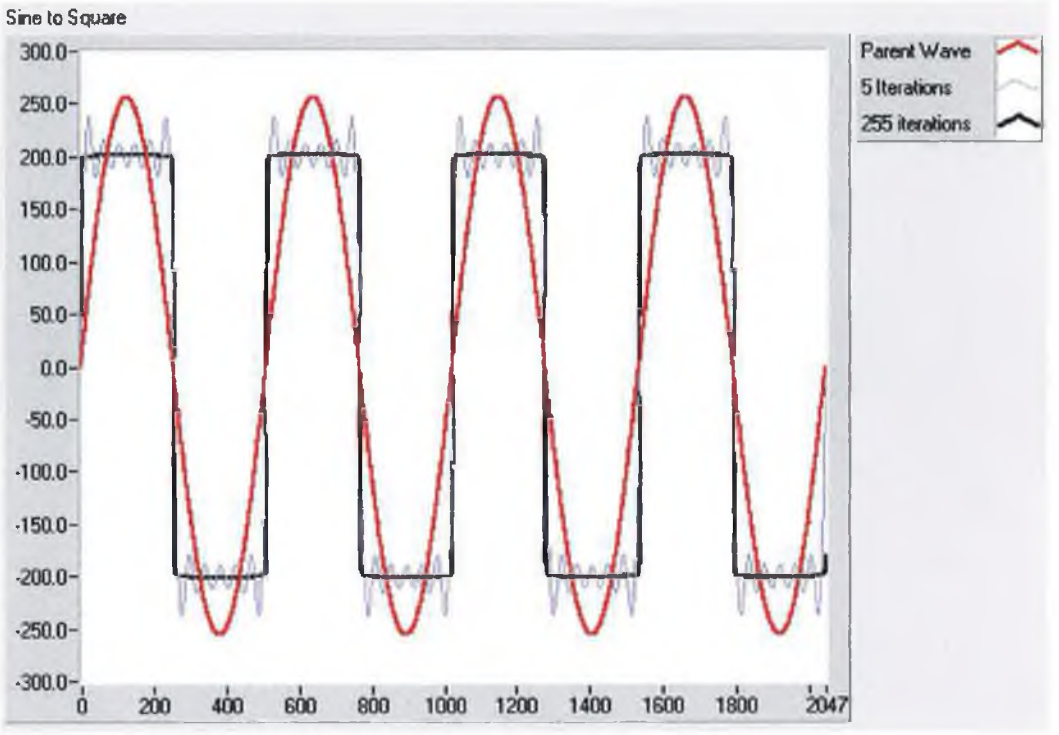

Figure 6.4: Diagram of the effect of successive iterations of the sine-addition method to construct a square wave from a parent sine wave.
Key: Red, Original wave, Purple, after only 5 iterations, Blue, after 255 iterations.

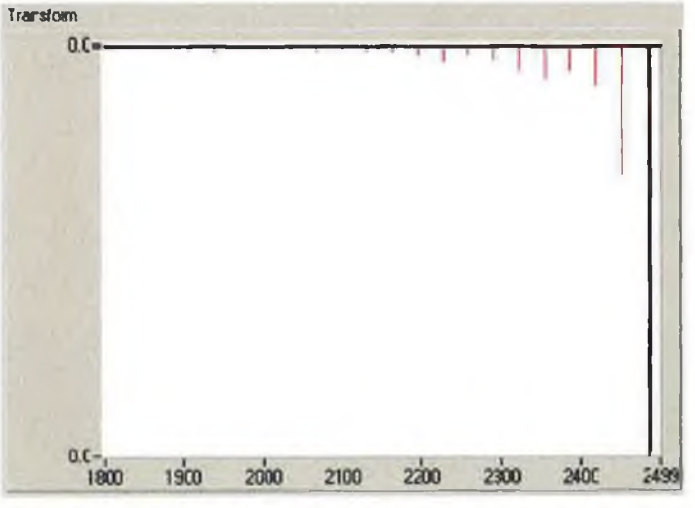

Figure 6.5: Fourier transform of original sine curve (Black) and curve after 255 iterations (Red).
Note the extra frequency peaks and the decreasing amplitudes.

6.8 Experimental

For acquisition of the colour digital pictures of the ion-selective optode membranes, a DIC-E CCD colour digital camera from World Precision Optics was used. This was in turn connected to a microscope, also supplied by World Precision Instruments to allow for focussing and magnification of the membrane surface. A ring-light adapter attached to the microscope objective (Lumina model, supplied by WPI) performed illumination of the membrane surface. A Gilson peristaltic pump was used for transfer and exchange of solutions in the flow-cell. A schematic of the experimental set-up can be seen in Figure 6.6. The sample handling system was identical to that in Chapter 3.

Colour pictures of the membrane held within the flow cell were taken using software supplied with the digital camera from World Precision Instruments. Measurements of the membranes during the course of a calibration (10^{-6}M sodium to 10^{-1}M sodium) were recorded in pentuplicate. These pictures were then saved directly onto the host computer in 24-bit bitmap (*.BMP) format. The software written in LabVIEW was then used to extract the colour information from the files. This data was then used for calculation of the calibration curve. A Pentium 166 computer with 32 megabytes of RAM was used throughout these experiments.

A Titertek Twinreader Plus Plate reader (Biological Instrumentation Services, Ltd., 8 Kirkham Trading Park, Freckleton Road, Kirkham, Lancs,PR4 3RB, united Kingdom) was used as the reference method in the ELISA studies.

For acquisition of the pictures of the ELISA analysis and also for the amine-sensitive experiment, an Olympus C-820L (Olympus Optical Co. UK Ltd., 2-8 Honduras St., London, EC1Y 0TX) digital camera was used for the capture of the picture. The pictures were stored automatically in the camera's memory and then downloaded to the host computer at a later date. The resolution of the pictures

taken was 1024x768. All pictures taken were taken in 'super high quality' mode. The pictures are stored internally as *.JPG, a lossy data type but were converted to *.BMP prior to analysis. There was no apparent image degradation upon conversion for *.JPG and back.

Aqueous solutions were prepared with Milli-Q equivalent water throughout and with salts of the highest purity available.
For membrane preparation, Poly(vinyl chloride) (PVC; High molecular weight), sodium tetrakis[3,5-bis(trifluoromethly)phenyl]borate ($NaTm(CF_3)_2PB$), di-butyl sebacate (DBS), 1,2-Benzo-7-(diethylamino)-3-(octadecanoylimino)phenoxazine (ETH 5294), and tetrahydrofuran (THF) were obtained from Fluka AG(Buchs, Switzerland). The styrylcyanine dye was synthesised in-house[32].

Optode membranes and solutions were prepared in identical manner to those outlined in Chapter 3.

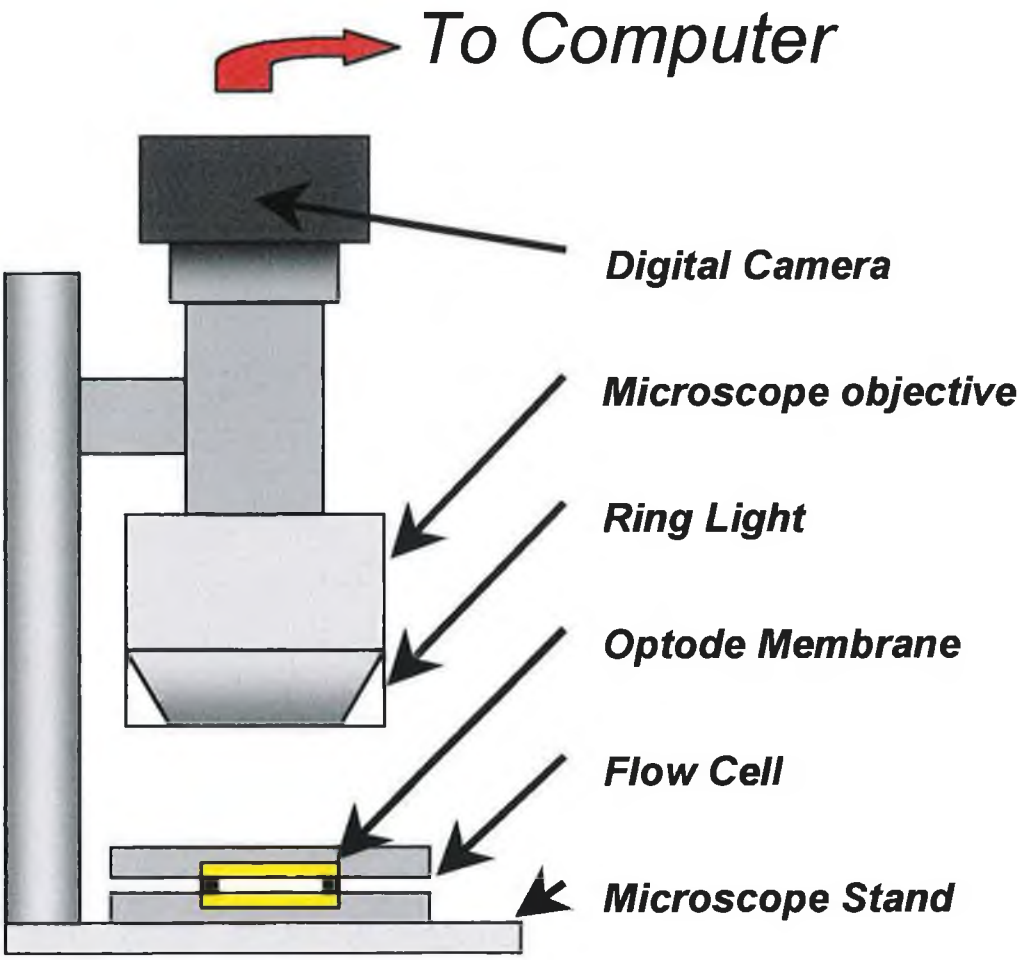

Figure 6.6: Schematic of experimental setup for digital camera measurements of ion-selective optode membranes.

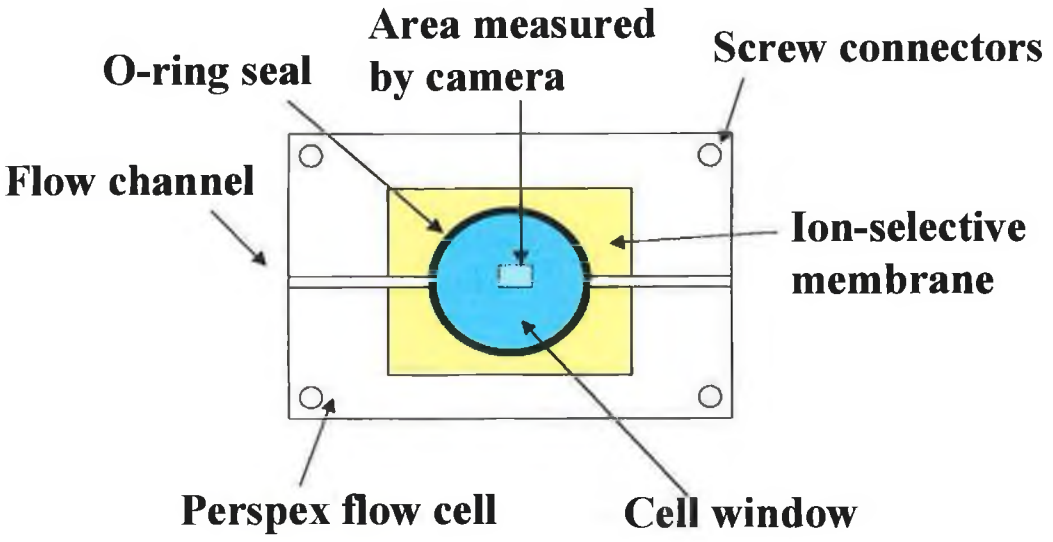

Figure 6.7: Close-up view of the flow cell used.

6.8.1 Camera and spectrometer comparison

In this work, the response of the ion-selective membrane is measured with a 2-dimensional CCD array. The wavelength-specific response is generated by the presence of three different wavelength filters (Previously discussed). This allows each picture pixel to represent a point in space as three colour values. Essentially, this is a sum of the membrane response over a particular wavelength region, as dictated by the filters in place (Figure 6.8 and Figure 6.9).

The spectrometer uses the same basic detector, a CCD, but instead of using filters, a diffraction grating is used to provide a splitting of the individual wavelengths. The result of this is a condition where each wavelength is directed at slightly different angles. These wavelengths are then incident upon the 1-D array so that each individual CCD determines a small defined region of the spectrum. In this example, the resolution of each CCD is around 0.9 nm.

The two methods can thus be compared as two different ways of implementing the same basic technology. The 1-D array allows for precise interrogation of the individual wavelengths, whereas the 2-D array allows for 2-dimensional imaging of the sensor surface. The 2-D array also has much less defined resolution of the wavelengths incident on it (Typical filter width is 100nm). However, for large shifts in the spectrum (100-200nm) this method is still valid as a tool for interrogating the spectrum. Its imaging ability, price and portability compensate for its lack of resolution. Also, the ability to measure many sensors simultaneously is discussed later.

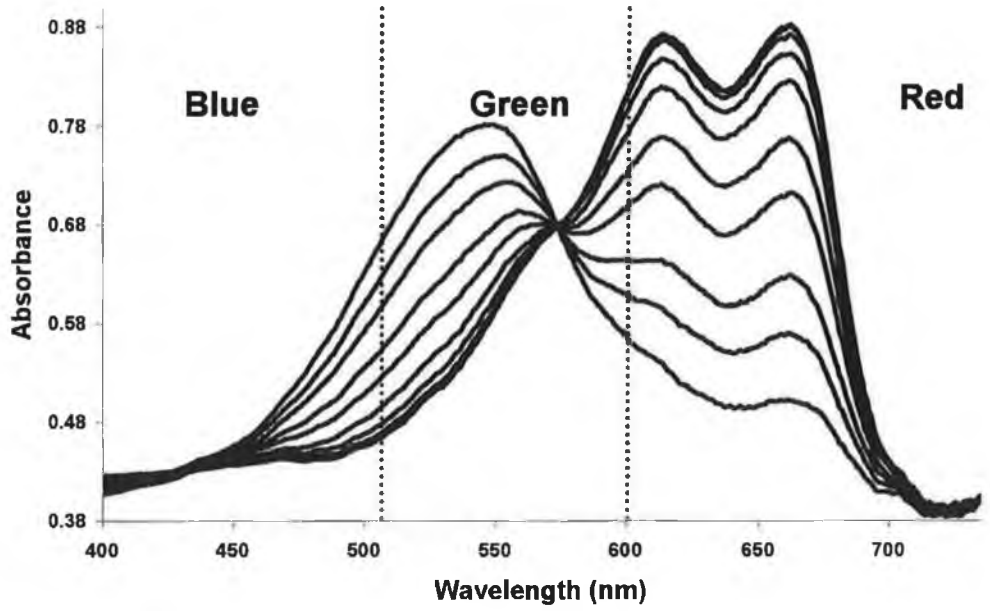

Figure 6.8: Overlay of spectral response of optode membrane incorporating dye 1 and colour digital camera filters.

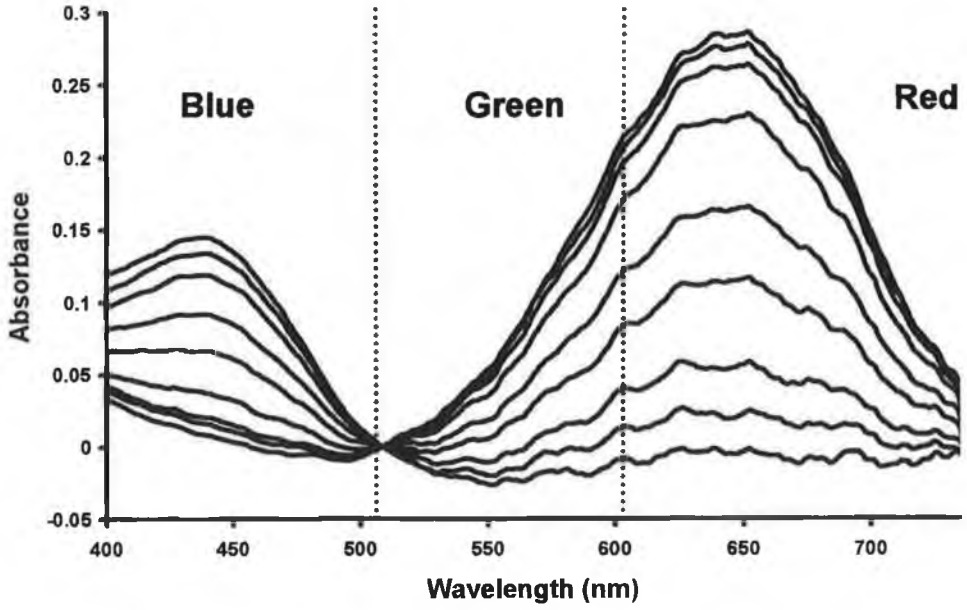

Figure 6.9: Overlay of spectral response of optode membranes incorporating dye 2 and colour digital camera filters.

6.9 Results and discussion

In order to maximise sensitivity, the light source intensity was varied to allow for saturation or near-saturation of the 8-bit channels when recording pictures of the ion-selective optode membranes. Once this intensity was chosen, it was kept constant throughout the experiments

The resulting pictures of the optode membranes in buffer can be seen in Figure 6.10 and Figure 6.11. Pentuplicate measurements made with these optode membranes can be seen in Figure 6.12 and Figure 6.13 for a range of primary ion concentrations from Buffer and 10^{-6}M to 1M.

The raw data generated from the averaging of these membrane pictures shown in Figure 6.12 andFigure 6.13 can be seen in Table 6-8 and Table 6-9.

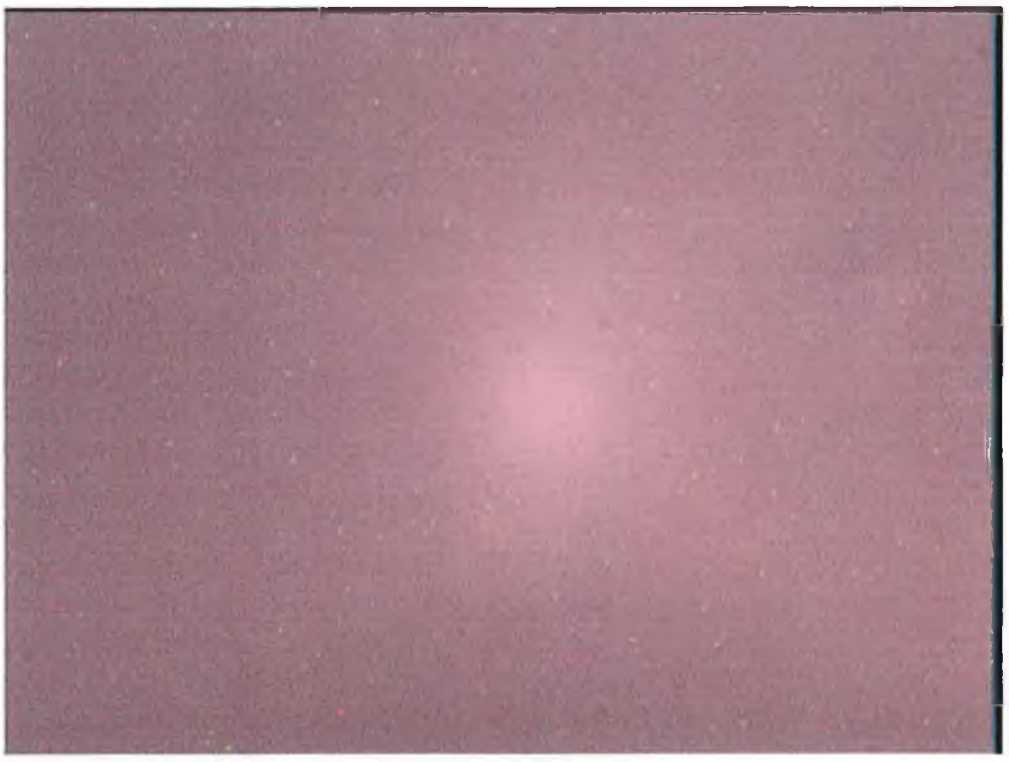

Figure 6.10: Picture of membrane 1 in buffer.
Red, Green and Blue channel averages are 140.0, 97.3, and 102.3 respectively.

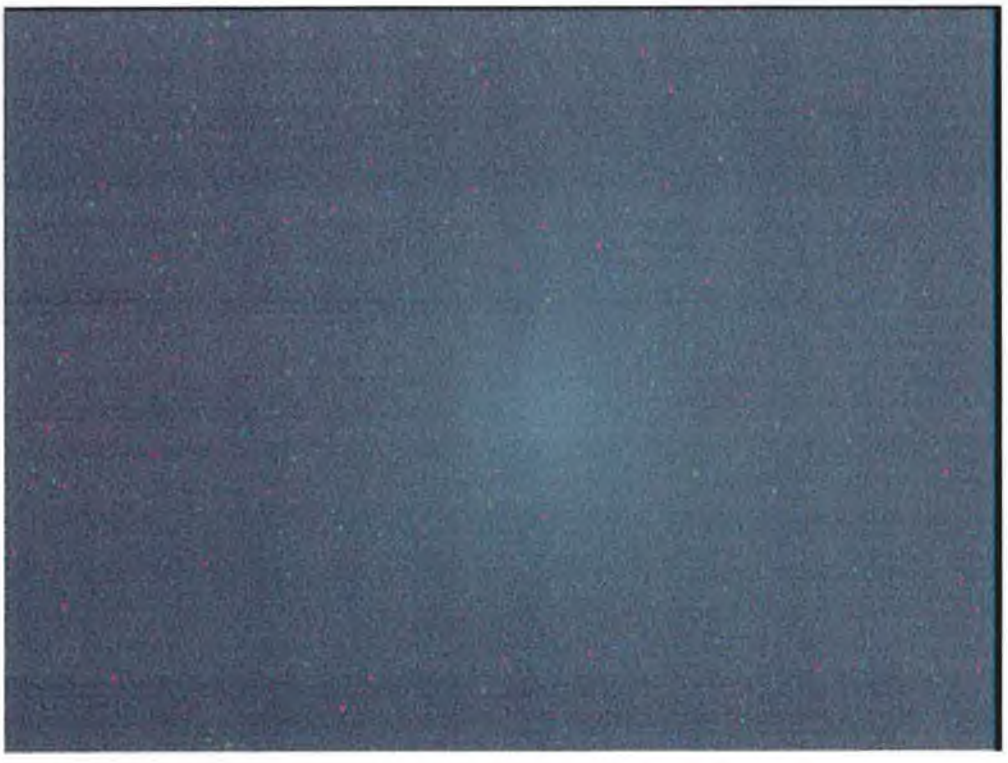

Figure 6.11: Picture of membrane 2 in buffer.
Red, Green and Blue channel averages are 70.5, 65.2, and 84.0 respectively

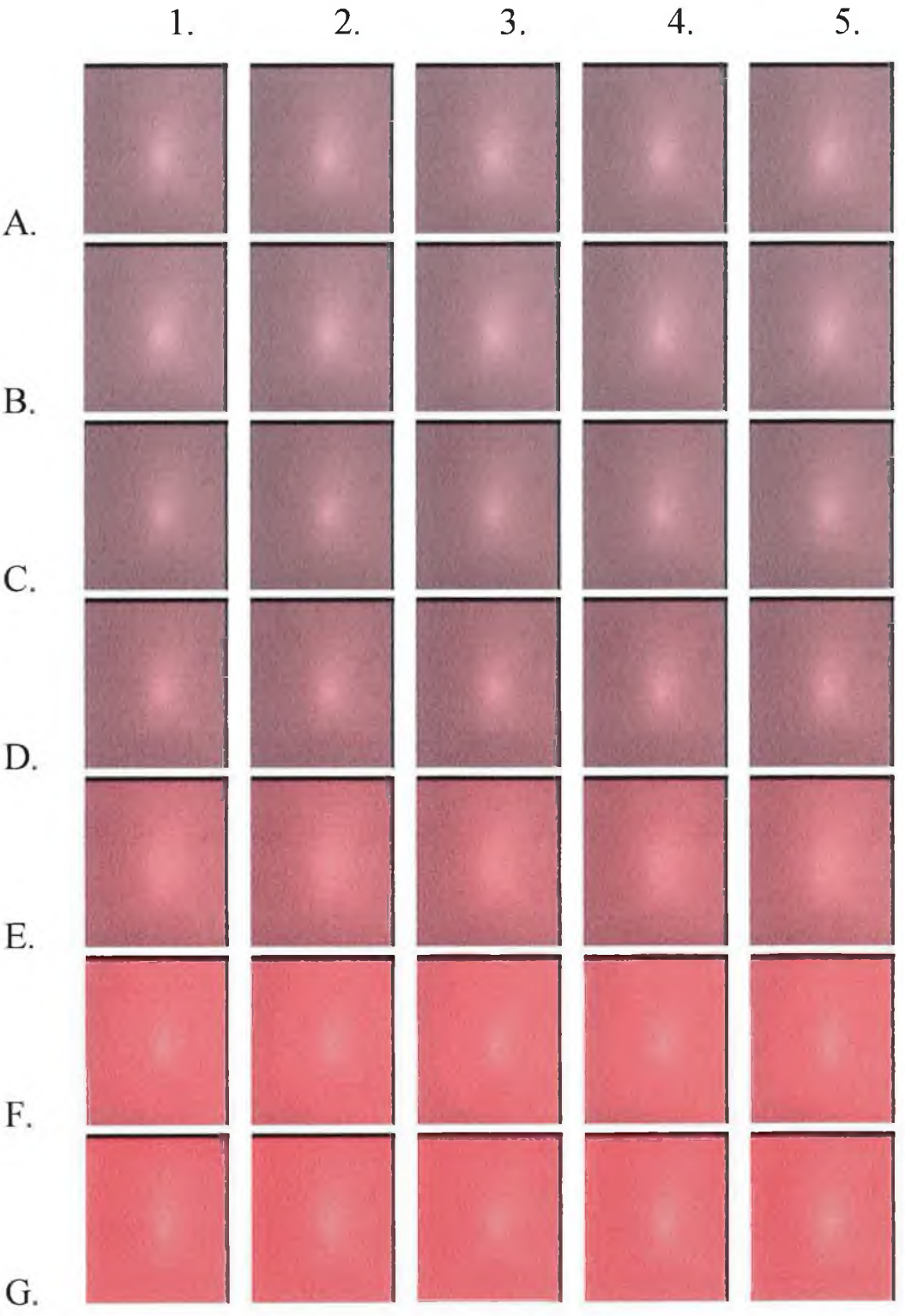

Figure 6.12 : Pictures obtained during calibration of Membrane 1 with sodium chloride solutions.
1-5 are replicate measurements at the respective concentration while A-G are Buffer, 10^{-6}M, 10^{-5}M, 10^{-4}M, 10^{-3}M, 10^{-2}M, 10^{-1}M and 1M respectively.

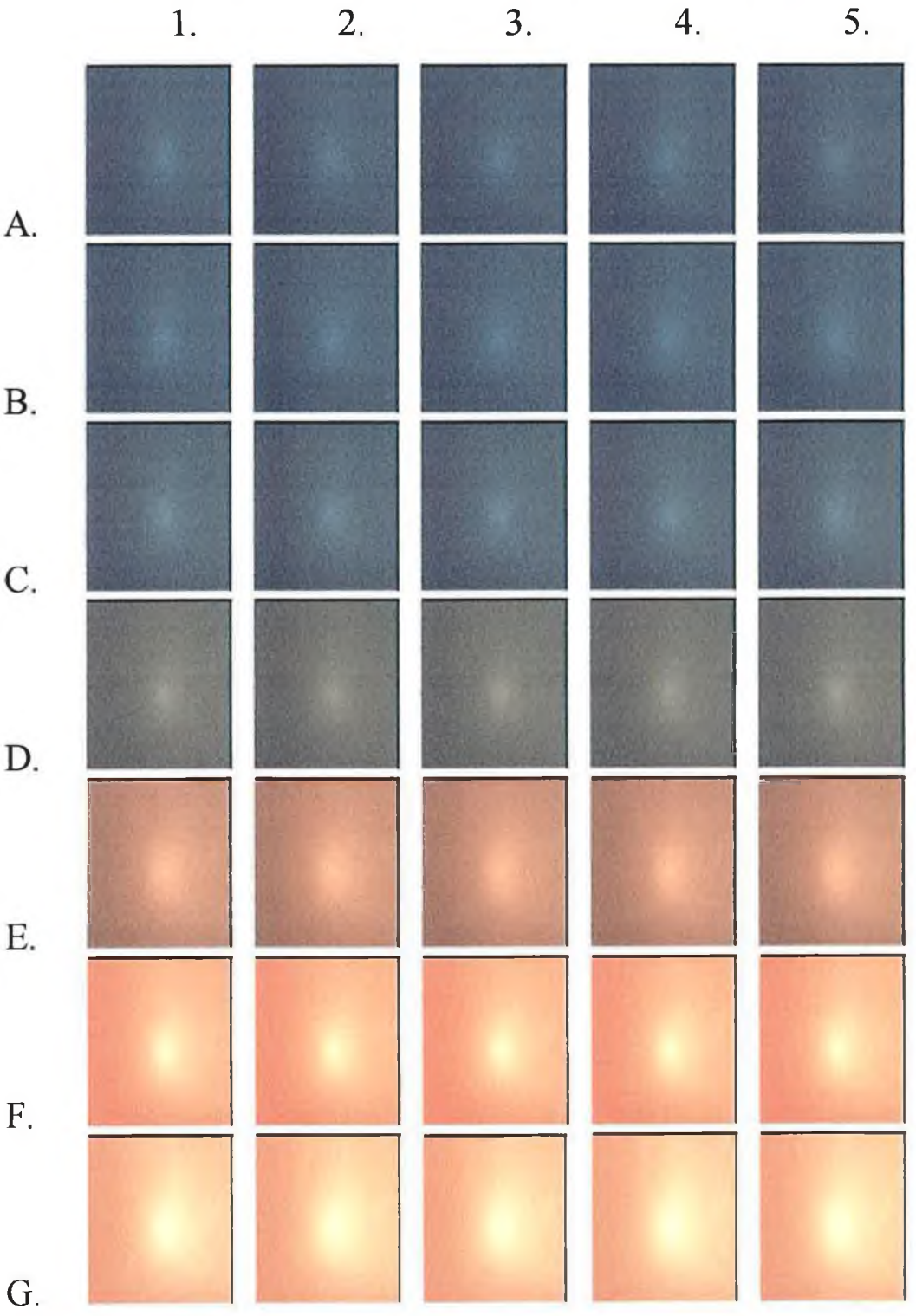

Figure 6.13 : Pictures obtained during calibration of Membrane 2 with sodium chloride solutions.
1-5 are replicate measurements at the respective concentration while A-G are Buffer, 10^{-6}M, 10^{-5}M, 10^{-4}M, 10^{-3}M, 10^{-2}M, 10^{-1}M and 1M respectively.

		Red		Green		Blue	
Conc	Repea	Avg	Stdev	Avg	Stdev	Avg	Stdev
1M	a	245.78	31.379	98.296	15.684	98.711	16.085
	b	245.76	31.381	98.224	15.681	98.640	16.079
	c	245.27	31.472	97.834	15.605	98.220	16.002
	d	245.28	31.477	97.873	15.614	98.203	16.005
	e	244.07	31.699	96.670	15.393	97.024	15.798
Stdev		0.6938	0.1306	0.6532	0.1190	0.6763	0.1164
10-1M	a	224.75	33.715	96.955	15.497	99.428	16.212
	b	225.46	33.715	97.307	15.559	99.739	16.284
	c	225.60	33.719	97.396	15.584	99.833	16.295
	d	224.70	33.732	96.914	15.490	99.338	16.203
	e	225.64	33.721	97.391	15.577	99.825	16.306
Stdev		0.4664	0.0069	0.2386	0.0445	0.2329	0.0486
10-2M	a	187.43	30.700	97.548	15.601	101.89	16.593
	b	186.60	30.581	97.150	15.527	101.46	16.507
	c	183.61	30.160	95.539	15.256	99.807	16.214
	d	185.52	30.429	96.593	15.436	100.86	16.423
	e	185.22	30.410	96.336	15.394	100.60	16.372
Stdev		1.4496	0.2033	0.7730	0.1316	0.8031	0.1435
10-3M	a	156.75	25.689	97.374	15.565	101.89	16.593
	b	157.25	25.776	97.786	15.647	102.32	16.664
	c	157.50	25.850	98.028	15.693	102.56	16.711
	d	156.64	25.692	97.413	15.586	101.89	16.601
	e	156.02	25.583	96.892	15.492	101.36	16.511
Stdev		0.5724	0.1007	0.4340	0.0772	0.4596	0.0762
10-4M	a	148.37	24.245	100.72	16.162	105.03	17.116
	b	148.73	24.322	100.97	16.212	105.27	17.162
	c	145.92	23.828	98.831	15.829	103.01	16.787
	d	145.43	23.757	98.473	15.762	102.60	16.701
	e	145.73	23.798	98.684	15.806	102.85	16.756
Stdev		1.5789	0.2705	1.2095	0.2145	1.2887	0.2168
10-5M	a	152.83	25.021	107.45	17.354	112.00	18.225
	b	153.28	25.110	107.79	17.423	112.29	18.292
	c	154.14	25.250	108.49	17.559	112.98	18.406
	d	153.18	25.101	107.68	17.409	112.14	18.281
	e	152.62	25.011	107.25	17.333	111.67	18.209
Stdev		0.5815	0.0961	0.4732	0.0886	0.4826	0.0774
10-6M	a	150.50	24.570	105.79	17.028	110.32	17.979
	b	150.21	24.526	105.56	17.002	110.07	17.966
	c	150.70	24.625	105.98	17.080	110.50	18.032
	d	151.14	24.720	106.32	17.140	110.88	18.111
	e	150.73	24.640	105.95	17.083	110.41	18.039
Stdev		0.3428	0.0738	0.2780	0.0535	0.2928	0.0575
Buffer	a	148.87	24.344	104.57	16.838	108.92	17.877
	b	151.26	24.757	106.45	17.167	110.93	18.185
	c	150.80	24.681	106.13	17.116	110.59	18.138
	d	151.07	24.741	106.30	17.152	110.76	18.158
	e	151.23	24.763	106.46	17.174	110.94	18.183
Stdev		1.0081	0.1780	0.8021	0.1421	0.8562	0.1308

Table 6-8: Membrane 1 results taking whole picture as sample

Conc	Repea	Red Avg	Stdev	Green Avg	Stdev	Blue Avg	Stdev
1M	a	251.27	30.581	193.31	33.717	124.02	20.884
	b	251.27	30.581	193.08	33.693	123.83	20.877
	c	251.27	30.581	195.35	33.996	125.17	21.090
	d	251.27	30.581	192.98	33.695	123.79	20.876
	e	251.27	30.581	193.94	33.835	124.35	20.966
Stdev		251.27	3.7E-	193.73	0.9782	124.23	0.5673
10-1M	a	250.78	30.635	176.40	31.059	114.12	19.331
	b	250.79	30.633	176.24	31.030	113.96	19.339
	c	250.70	30.643	175.25	30.874	113.43	19.228
	d	250.78	30.634	175.94	31.000	113.79	19.307
	e	250.81	30.630	176.41	31.094	113.98	19.352
Stdev		250.77	0.0420	176.05	0.4833	113.86	0.2682
10-2M	a	185.37	33.069	133.34	23.729	95.944	16.667
	b	187.10	33.354	134.59	23.966	96.640	16.806
	c	187.40	33.406	134.72	23.999	96.659	16.825
	d	186.15	33.228	133.59	23.794	95.964	16.682
	e	186.33	33.237	133.67	23.806	95.969	16.696
Stdev		186.47	0.8083	133.98	0.6276	96.235	0.3782
10-3M	a	99.733	17.197	93.542	15.630	87.939	14.893
	b	99.754	17.213	93.611	15.671	87.896	14.913
	c	99.724	17.215	93.508	15.649	87.809	14.901
	d	99.024	17.096	92.673	15.492	87.087	14.791
	e	98.502	17.020	92.003	15.383	86.524	14.710
Stdev		99.347	0.5644	93.068	0.7076	87.451	0.6236
10-4M	a	79.856	13.938	77.740	12.901	92.811	15.834
	b	79.877	13.967	77.863	12.943	92.913	15.870
	c	79.638	13.940	77.509	12.885	92.414	15.795
	d	79.730	13.945	77.717	12.926	92.671	15.840
	e	79.940	13.983	78.044	12.981	93.016	15.915
Stdev		79.808	0.1220	77.774	0.1970	92.765	0.2338
10-5M	a	75.846	13.400	73.120	12.115	93.813	16.020
	b	75.689	13.395	72.893	12.091	93.454	15.984
	c	76.051	13.442	73.516	12.208	94.315	16.145
	d	75.814	13.417	73.105	12.134	93.748	16.048
	e	75.859	13.422	73.184	12.151	93.865	16.079
Stdev		75.852	0.1300	73.164	0.2254	93.839	0.3102
10-6M	a	74.296	13.168	70.520	11.613	90.377	15.336
	b	74.941	13.257	71.632	11.830	91.817	15.602
	c	74.603	13.234	71.188	11.756	91.262	15.524
	d	74.578	13.232	71.082	11.741	91.089	15.496
	e	74.107	13.170	70.470	11.636	90.319	15.364
Stdev		74.505	0.3189	70.979	0.4876	90.973	0.6310
Buffer	a	75.198	13.323	72.361	11.979	90.809	15.446
	b	74.938	13.285	72.056	11.928	90.513	15.392
	c	74.763	13.280	71.854	11.906	90.247	15.354
	d	74.398	13.240	71.301	11.803	89.577	15.260
	e	74.540	13.264	71.484	11.843	89.780	15.283
Stdev		74.767	0.3171	71.811	0.4275	90.185	0.5085

Table 6-9: Membrane 2 results taking whole picture as sample

Taking whole-picture samples for determination of the average and standard deviation of the red, green and blue channels yielded some useful information, but the values for the standard deviation within measurements (sometimes as large as 20%) were unusually high (Table 6-8 and Table 6-9). There are a significant amount of 'dead' pixels present in the pictures (Figure 6.10 and Figure 6.11), and this could be responsible for raising the standard deviation slightly. The standard deviation between membrane measurements was significantly lower (typically around or below 0.5%) suggesting that the overall picture colour as recorded is quite reproducible.

The results from this experiment for membranes 1 and 2 can be seen plotted graphically in Figure 6.14 and Figure 6.15 respectively. In the case of membrane 1, the colour change recorded by the camera occurs almost exclusively in the red channel with the other channels remaining constant to serve as reference channels.

For membrane 2 also, the red channel response dominates, becoming saturated at 10^{-1}M sodium. However, unlike with membrane 1, both the green and blue channels respond also. The green channel does not reach saturation during the course of the experiment but does exhibit a significant response. This channel can also be used as an indicator of the membrane response. The blue channel as shown can be seen to shift slightly above 10^{-2}M sodium, but for the purpose of this experiment, was assumed constant. This channel was used as a reference channel.

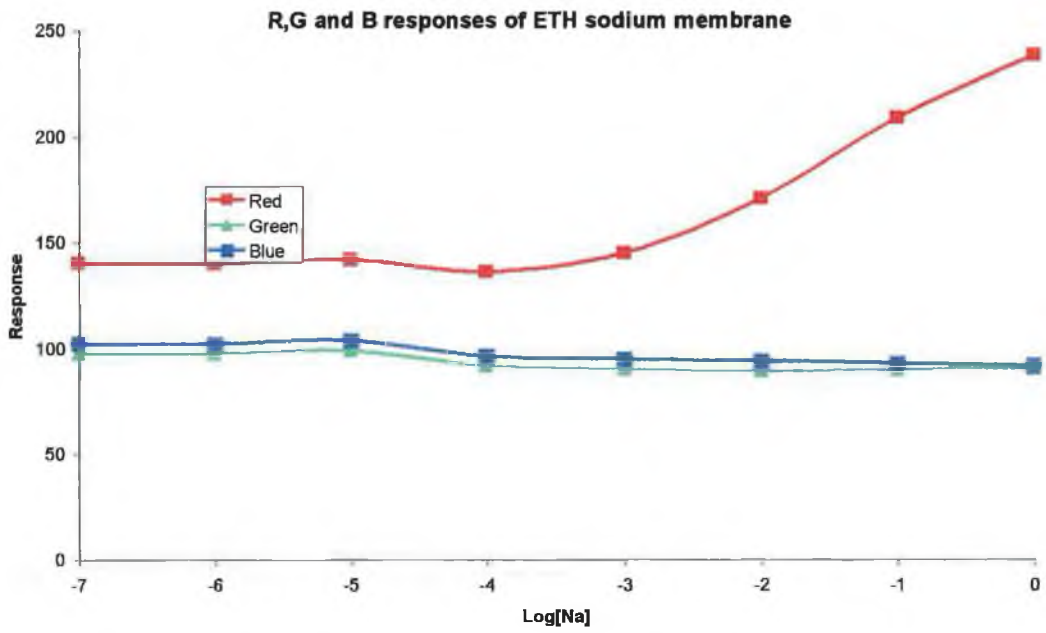

Figure 6.14: Raw channel Red, Green and Blue values for calibration of membrane 1 (pH 7.3).

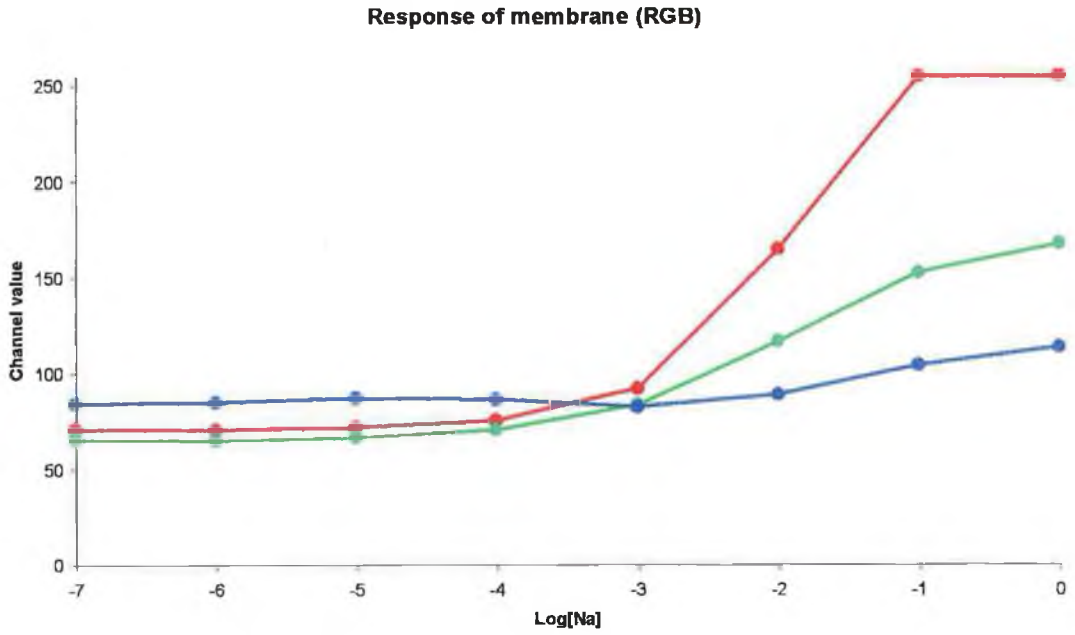

Figure 6.15: Raw channel Red, Green and Blue values for calibration of membrane 2 (pH 5.0).

6.9.1 Membrane calibration

In order to maximise sensitivity, and the allow for internal referencing to static colour channels, the results from all three colour channels for membranes 1 and 2 were combined according to the equations listed below.

6.9.1.1 Calculation for systems with membrane 1

$$Response = \frac{Red}{(Green + Blue)/2}$$ **Equation 6.5**

In this equation, only the red channel is taken as an indicator channel, with the average response of the other two channels being treated as reference channels. This produces the calibration curve shown in Figure 6.16. The similarity between this curve and the curve presented as recorded by a conventional linear array CCD spectrometer is clear.

6.9.1.2 Calculation for systems with membrane 2

$$Response = \frac{Red \times Green}{Blue}$$ **Equation 6.6**

For this equation, both the red and green channels must be considered as indicator channels, with the pseudo-constant blue channel being used as a reference. The calibration curve thus generated can be seen in Figure 6.17. Again there is a slight difference in sensitivity between the curves generated with the two different methods, but the general agreement is encouraging. This equation results in the calibration curve shown in Figure 6.17. Once again, there is a good similarity between the response generated by this method and the method using a conventional detector.

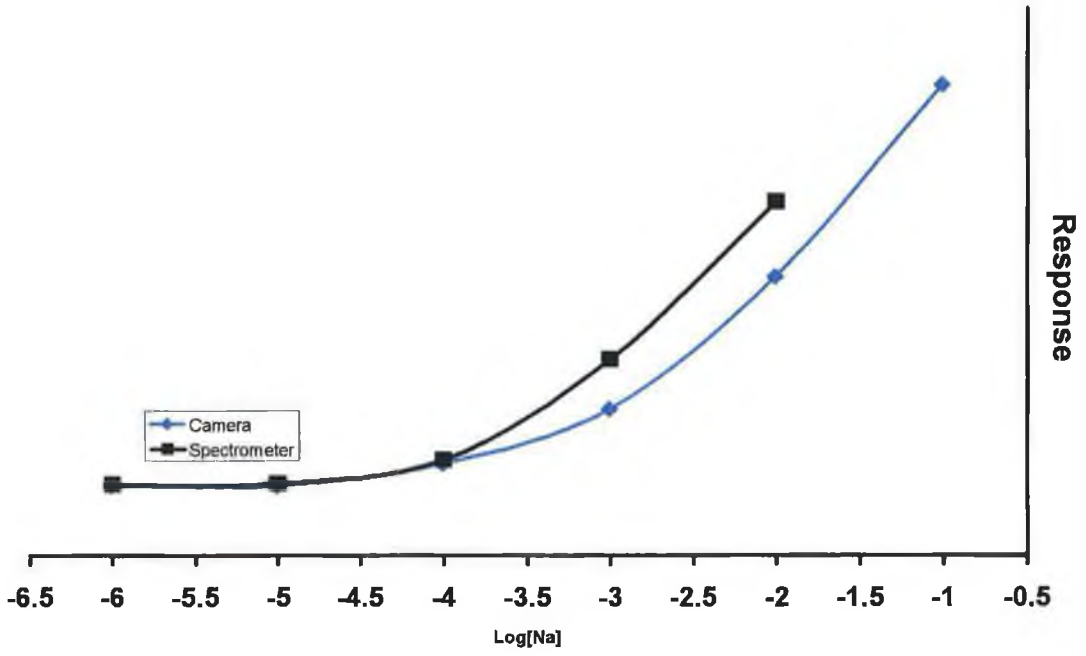

Figure 6.16: Calculated calibration for membrane 1. Calculation used was Red/(Average(Green+Blue))

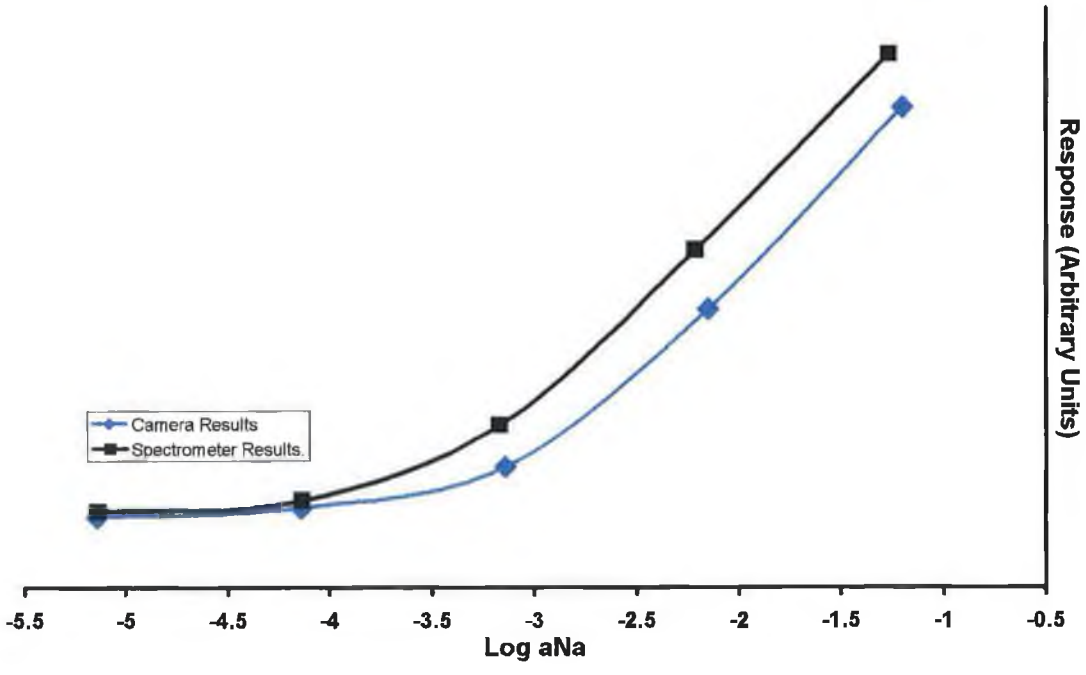

Figure 6.17: Calculated calibration for Membrane 2. Calculation used was (RedxGreen)/Blue.

6.9.2 Noise and standard deviation

By taking a 'slice' through the pictures recorded (Figure 6.18) we see that there is a significant amount of noise present in each scan line of the picture (Figure 6.18, top). Upon averaging, this noise is significantly reduced and the overall trend of the deviation across the surface of the membrane is visible (Figure 6.18, bottom). Even though random noise is never particularly welcome in an analytical signal, the sheer number of simultaneous measurements made with this method effectively allows for averaging out of the majority of this noise.

Apart from the random noise, there is a clear curve to the histogram as opposed to the flat line, which was expected. The non-uniform nature of the lighting used in the experiment was very important in this respect. The usefulness of extracting quantitative data from these pictures is therefore dependent on the 'location' of the sample. This is not an optimum condition, as the measurements become dependent on what part of the picture is chosen. There are two possible ways to correct for this

1. Sample only smaller portions of the sample, thus reducing the effect of the varying light intensity.

2. Incorporate some blank correction to remove the 'shape' of the non-uniform lighting and simulate uniform lighting.

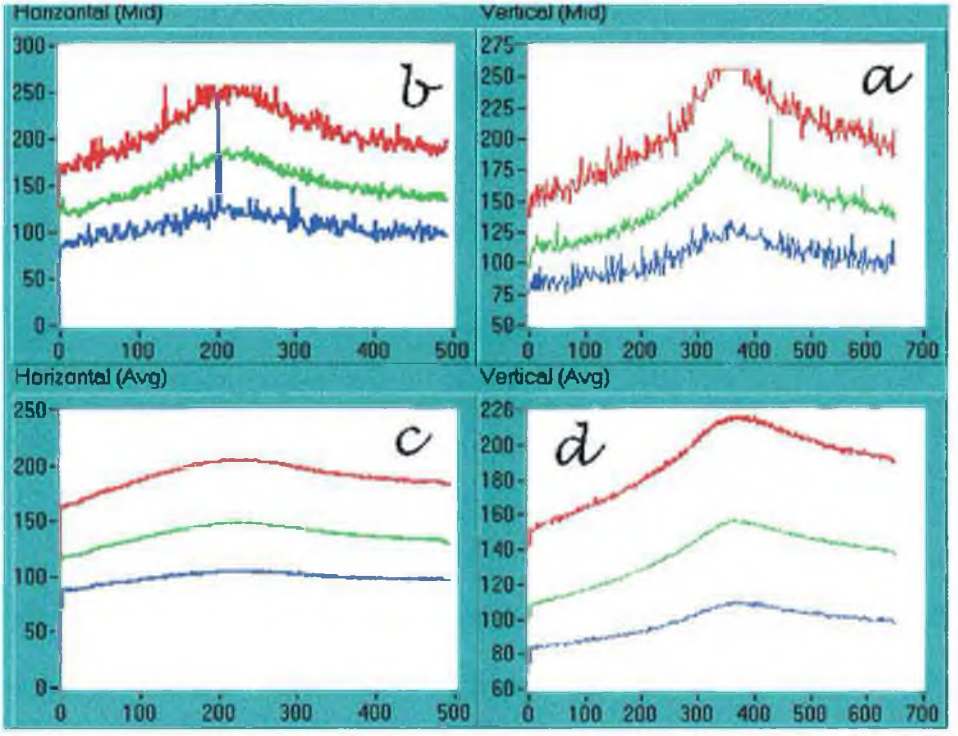

Figure 6.18: Histogram of average and single horizontal and vertical sections of Membrane 2 in buffer.
(See Figure 6.19)

a): Histogram of the middle lines vertically.

b): Histogram of the middle line horizontally.

c): Histogram of the average of the horizontal.

d): Histogram of the average of the vertical.

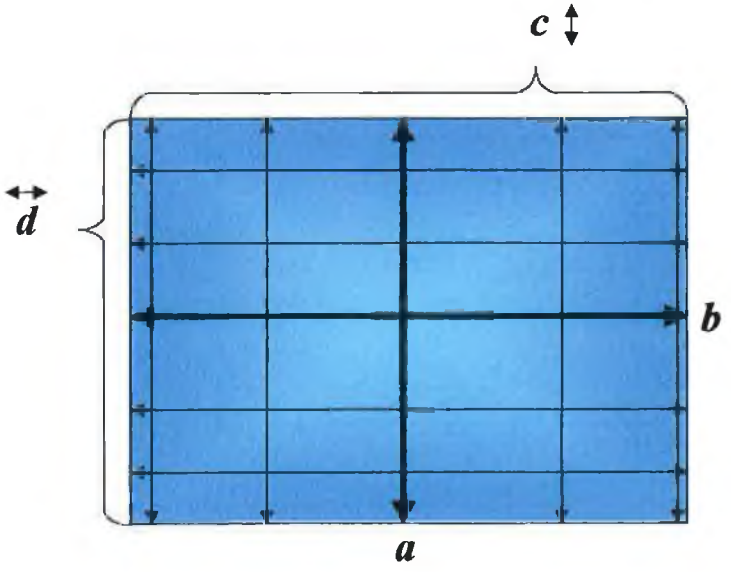

Figure 6.19: Diagram of the origins of a-d in Figure 6.18.

6.9.2.1 1. Sub-array sampling

The area of 10-110 on the X-scale and 10-110 on the Y-scale (Figure 6.20) was chosen for analysis. The variation in light intensity was quite small in this region of the pictures.

The values obtained for these measurements for membranes 1 and 2 can be seen in Table 6-10 and Table 6-11 respectively

One would have expected, with a smaller sample size to see a greater standard deviation than before if the main source of deviation is due to random noise. The fact that the smaller sample has a lower standard deviation indicates an overall shift in intensities across the membrane picture.

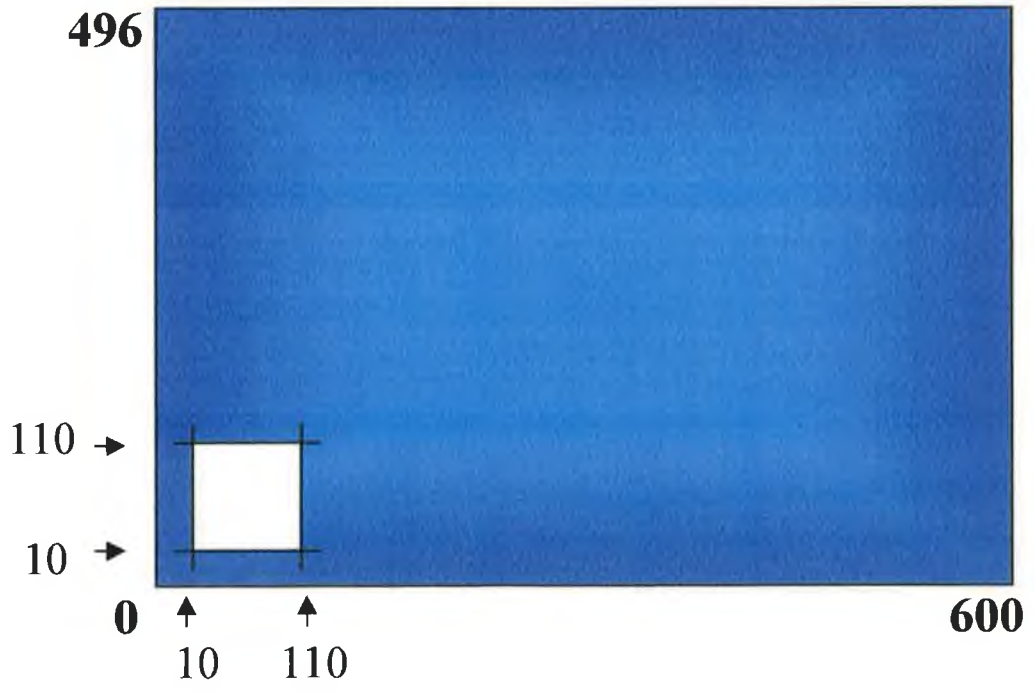

Figure 6.20: schematic of area chosen for membrane analysis.
The area chosen (shown in white, 10,000 points) was of the range 10-110 on both X and Y axis of the picture (shown in blue)

Colour		Red		Green		Blue	
Conc	Repea	Avg	Stdev	Avg	Stdev	Avg	StdDev
1M	a	232.19	10.203	87.146	4.7599	89.716	5.4163
	b	232.17	10.387	87.122	4.8278	89.757	5.4103
	c	230.91	10.269	86.747	4.7313	89.438	5.5341
	d	230.95	10.251	86.686	4.7362	89.279	5.3520
	e	228.02	10.319	85.851	4.7044	88.369	5.5073
St Dev		1.6965	0.0699	0.5241	0.0467	0.5629	0.0749
10-1M	a	200.17	9.3770	85.849	4.7536	90.238	5.3997
	b	200.81	9.4661	86.120	4.7090	90.413	5.4759
	c	200.92	9.5023	86.182	4.8200	90.496	5.3531
	d	200.07	9.4172	85.839	4.7200	90.257	5.3367
	e	201.02	9.4301	86.146	4.7671	90.528	5.3555
St Dev		0.4415	0.0477	0.1688	0.0439	0.1337	0.0563
10-2M	a	164.28	9.2758	85.901	4.8002	91.983	5.3585
	b	163.64	9.3157	85.671	4.7994	91.716	5.3238
	c	161.22	9.2957	84.382	4.7224	90.484	5.3681
	d	162.72	9.2860	85.187	4.7381	91.225	5.3719
	e	162.30	9.2483	84.976	4.8020	91.039	5.3176
St Dev		1.1888	0.0249	0.5976	0.0388	0.5869	0.0254
10-3M	a	138.36	9.1921	85.925	4.7964	92.056	5.3091
	b	138.67	9.1319	86.257	4.7529	92.342	5.3627
	c	138.94	9.1491	86.430	4.7751	92.499	5.4072
	d	138.17	9.2999	85.911	4.7444	91.990	5.3432
	e	137.76	9.2361	85.534	4.7685	91.608	5.3881
St Dev		0.4553	0.0680	0.3470	0.0202	0.3440	0.0383
10-4M	a	131.13	9.1775	88.688	4.8098	94.325	5.3862
	b	131.38	9.2435	88.863	4.8697	94.594	5.5394
	c	129.08	9.1879	87.068	4.8122	92.774	5.2586
	d	128.47	9.2304	86.772	4.7902	92.505	5.4417
	e	128.78	9.2215	86.957	4.8242	92.716	5.5070
St Dev		1.3758	0.0282	1.0169	0.0297	0.9925	0.1109
10-5M	a	134.86	9.0949	94.181	4.9412	99.876	5.8989
	b	135.06	9.0869	94.413	5.0007	100.09	5.8387
	c	135.88	9.1695	94.998	5.0185	100.60	5.9746
	d	135.00	9.1545	94.365	5.0080	99.900	5.8364
	e	134.67	9.0665	93.989	5.0042	99.667	5.8324
St Dev		0.4638	0.0449	0.3790	0.0305	0.3559	0.0614
10-6M	a	133.00	9.2085	92.943	5.0122	98.631	5.9093
	b	132.83	9.2634	92.768	5.0263	98.379	5.8049
	c	133.20	9.2714	93.115	5.0658	98.726	5.9368
	d	133.55	9.3054	93.365	5.0596	98.894	5.9837
	e	133.22	9.2256	93.015	5.0112	98.549	5.9120
St Dev		0.2688	0.0384	0.2210	0.0260	0.1925	0.0655
Buffer	a	131.52	9.4435	91.837	5.1422	97.278	6.0944
	b	133.57	9.4477	93.371	5.2068	98.909	6.2714
	c	133.21	9.4041	93.165	5.1369	98.645	6.1080
	d	133.23	9.3853	93.226	5.1159	98.793	6.1946
	e	133.58	9.4700	93.409	5.1434	98.916	6.2002
St Dev		0.8586	0.0345	0.6584	0.0341	0.6963	0.0729

Table 6-10: Membrane 1 results taking the section of 10-110 on both X and Y axes as sample

Colour Conc	Repea	Red Avg	Stdev	Green Avg	Stdev	Blue Avg	Stdev
1M	a	255	0	157.67	6.3366	105.44	6.6056
	b	255	0	157.44	6.4528	105.34	6.6716
	c	255	0	159.29	6.4279	106.43	6.6991
	d	255	0	157.41	6.3857	105.30	6.7752
	e	255	0	158.10	6.4129	105.71	6.5948
St Dev		0	0	0.7837	0.0444	0.4651	0.0736
10-1M	a	249.02	7.2846	143.29	6.1713	96.952	6.5477
	b	249.22	7.1360	143.13	6.2144	96.812	6.5337
	c	248.30	7.5870	142.33	6.2424	96.454	6.3492
	d	249.04	7.2865	142.83	6.2576	96.682	6.4901
	e	249.46	7.1154	143.31	6.2527	96.900	6.5175
St Dev		0.4310	0.1884	0.4084	0.0356	0.1992	0.0802
10-2M	a	150.04	10.121	107.24	5.7847	82.238	5.9686
	b	151.22	10.072	108.14	5.7709	82.805	5.9112
	c	151.52	10.121	108.22	5.7498	82.710	5.9482
	d	150.46	10.075	107.34	5.7014	82.255	5.9024
	e	150.64	10.111	107.45	5.7175	82.348	5.9294
St Dev		0.5954	0.0244	0.4650	0.0350	0.2669	0.0270
10-3M	a	86.213	10.378	78.121	5.1867	77.263	5.8165
	b	86.139	10.377	78.095	5.1900	77.188	5.8315
	c	86.195	10.429	78.050	5.1476	77.031	5.9040
	d	85.668	10.383	77.429	5.2177	76.541	5.7489
	e	85.281	10.466	76.882	5.2238	76.003	5.7940
St Dev		0.4119	0.0397	0.5468	0.0302	0.5292	0.0568
10-4M	a	71.065	10.650	65.724	4.8990	80.933	5.8852
	b	71.020	10.746	65.753	4.9189	80.952	5.8787
	c	70.832	10.748	65.490	4.9301	80.648	6.0242
	d	70.802	10.745	65.673	4.9078	80.871	6.0120
	e	71.104	10.781	65.851	4.9131	81.025	5.9449
St Dev		0.1382	0.0493	0.1334	0.0117	0.1439	0.0682
10-5M	a	67.973	10.764	62.463	4.8006	81.726	5.9864
	b	67.717	10.778	62.160	4.8488	81.254	5.9547
	c	68.026	10.761	62.682	4.8362	81.890	6.0036
	d	67.810	10.800	62.348	4.8194	81.494	5.9389
	e	67.846	10.778	62.410	4.8337	81.605	5.9359
St Dev		0.1248	0.0155	0.1890	0.0184	0.2401	0.0298
10-6M	a	66.895	10.762	60.629	4.7824	79.061	5.8638
	b	67.234	10.771	61.419	4.8020	80.202	5.8893
	c	67.022	10.836	61.106	4.8258	79.596	5.8590
	d	66.987	10.752	60.964	4.8431	79.654	5.8412
	e	66.684	10.789	60.590	4.8234	78.99	5.8959
St Dev		0.1999	0.0330	0.3450	0.0234	0.4948	0.0225
Buffer	a	67.484	10.769	61.928	4.7843	79.187	5.9410
	b	67.305	10.790	61.647	4.7888	79.079	5.8083
	c	67.142	10.779	61.45	4.7666	78.840	5.9381
	d	66.828	10.816	61.072	4.7762	78.354	5.8173
	e	66.978	10.819	61.199	4.8169	78.408	5.8964
St Dev		0.2592	0.0218	0.3436	0.0189	0.3800	0.0641

Table 6-11: Membrane 2 results taking the section of 10-110 on both X and Y axes as sample

6.9.2.2 2: Correction for non-uniform lighting

Many of the profiles shown for the membrane pictures shown so far have a distinctive curve due to non-uniform lighting.

A method to either reduce this effect or eliminate it totally was attempted. In order to measure the shape of the distortion, it was necessary in all cases to use some experimental data to aid the construction of 'blank' pictures. These pictures should hold only data for the variation of the light across the area of the picture. Their average should also be zero so they do not affect the overall average of the pictures they are being used to blank.

Two different methods were attempted as discussed in Chapter 5.

1. Simple blank subtraction

Results from this approach can be seen in Table 6-13 and Figure 6.21.

2. Adaptive blank subtraction.

Results from this method can be found in Table 6-14 and Figure 6.22.

Conc			Full Picture	10-110	200-300
10^{-1}M	Red	Avg	250.8	249	255.0
		Std	30.63	9.4	0
		Std	0.04	0.44	0
	Green	Average	176.1	143.0	190.4
		Std	31.04	4.7	11.6
		Std	0.48	0.17	0.55
	Blue	Average	113.9	96.8	121.5
		Std	19.3	5.3	10.3
		Std	0.27	0.13	0.34
10^{-2}M	Red	Average	186.5	150.8	202.5
		Std	33.3	9.3	13.5
		Std	0.81	1.19	0.91
	Green	Average	134.0	107.7	145.0
		Std	23.8	4.8	9.3
		Std	0.63	0.60	0.67
	Blue	Average	96.2	82.5	102.6
		Std	16.7	5.4	10.8
		Std	0.38	0.59	0.43
10^{-3}M	Red	Average	99.3	85.9	105.5
		Std	17.2	9.2	8.6
		Std	0.56	0.46	0.62
	Green	Average	93.0	77.7	99.5
		Std	15.5	4.8	6.3
		Std	0.71	0.35	0.80
	Blue	Average	87.5	76.8	92.1
		Std	14.8	5.3	10.3
		Std	0.62	0.34	0.66
10^{-4}M	Red	Average	79.8	71.0	83.7
		Std	14.0	9.2	7.6
		Std	0.12	1.38	0.10
	Green	Average	77.8	65.7	82.7
		Std	13.0	4.8	5.6
		Std	0.20	1.01	0.23
	Blue	Average	92.8	80.9	98.1
		Std	15.8	5.4	10.6
		Std	0.23	1.00	0.23
10^{-5}M	Red	Average	75.9	67.9	79.4
		Std	13.4	9.1	7.4
		Std	0.13	0.46	0.18
	Green	Average	73.2	62.4	77.7
		Std	12.1	5.0	5.6
		Std	0.23	0.38	0.25
	Blue	Average	93.8	81.6	99.3
		Std	16.0	5.9	10.6
		Std	0.31	0.36	0.34
Buffer	Red	Average	74.8	67.1	78.3
		Std	13.3	9.4	7.5
		Std	0.32	0.86	0.31
	Green	Average	71.8	61.5	76.3
		Std	12.0	5.2	5.6
		Std	0.43	0.66	0.49
	Blue	Average	90.2	78.8	95.4
		Std	15.4	6.1	10.5
		Std	0.51	0.70	0.56

Table 6-12: Comparison of results of different selection areas for membrane 2 without any blank correction employed.

			Full Picture	10-110	200-300
10^{-1}M	Red	Avg	250.8	256.6	251.5
		Std	14.6	10.6	7.11
		Std	0.06	0.43	0.00
	Green	Average	176.1	153.3	186.0
		Std	19.1	3.8	8.4
		Std	0.48	0.41	0.56
	Blue	Average	113.9	108.1	116.3
		Std	5.7	3.3	4.0
		Std	0.28	0.20	0.34
10^{-2}M	Red	Average	186.5	158.4	198.9
		Std	22.5	6.6	10.5
		Std	0.81	0.60	0.91
	Green	Average	134.0	118.0	140.5
		Std	12.6	2.8	5.6
		Std	0.62	0.47	0.67
	Blue	Average	96.2	93.9	97.3
		Std	3.6	2.9	3.6
		Std	0.37	0.27	0.43
10^{-3}M	Red	Average	99.35	93.5	101.9
		Std	5.8	3.1	4.0
		Std	0.56	0.41	0.62
	Green	Average	93.1	88.1	95.0
		Std	4.3	1.9	2.3
		Std	0.12	0.55	0.80
	Blue	Average	87.5	88.2	86.9
		Std	3.1	2.9	3.1
		Std	0.63	0.53	0.66
10^{-4}M	Red	Average	79.8	78.6	80.1
		Std	3.0	2.7	2.9
		Std	0.12	0.14	0.10
	Green	Average	77.8	76.0	78.2
		Std	2.0	1.6	1.8
		Std	0.2	0.13	0.23
	Blue	Average	92.8	92.3	92.8
		Std	3.2	2.9	3.3
		Std	0.23	0.14	0.23
10^{-5}M	Red	Average	75.9	75.5	75.9
		Std	2.8	2.7	2.9
		Std	0.13	0.12	0.18
	Green	Average	73.2	72.8	73.2
		Std	1.7	1.5	1.8
		Std	0.22	0.19	0.25
	Blue	Average	93.9	93.0	94.1
		Std	3.3	2.9	3.3
		Std	0.31	0.24	0.34
Buffer	Red	Average	74.8	74.8	74.8
		Std	2.3	2.2	2.3
		Std	0.32	0.26	0.31
	Green	Average	71.8	71.8	71.8
		Std	1.3	1.2	1.4
		Std	0.42	0.34	0.49
	Blue	Average	90.2	90.2	90.2
		Std	2.5	2.3	2.5
		Std	0.51	0.38	0.56

Table 6-13: Comparison of results of different selection areas for membrane 2 with simple blank correction employed.

Conc			Full Picture	10-110	200-300
10^{-1}M	Red	Avg	250 5	274 4	242 9
		Std	32 0	33 5	24 3
		Std	0 56	0 48	0 00
	Green	Average	175 4	163 6	178 4
		Std	11 03	5 8	9 3
		Std	0 48	0 47	0 52
	Blue	Average	113 6	109 0	114 5
		Std	4 7	3 3	5 7
		Std	0 28	0 22	0 32
10^{-2}M	Red	Average	185 7	166 1	192 9
		Std	20 2	14 7	15 0
		Std	0 80	0 66	0 87
	Green	Average	133 5	123 2	135 9
		Std	7 5	3 4	6 1
		Std	0 62	0 53	0 63
	Blue	Average	96 1	93 0	96 6
		Std	3 5	2 9	3 7
		Std	0 37	0 30	0 40
10^{-3}M	Red	Average	99 4	95 0	100 5
		Std	5 3	3 7	4 6
		Std	0 56	0 45	0 59
	Green	Average	93 0	89 0	93 2
		Std	2 8	1 9	2 8
		Std	0 71	0 63	0 74
	Blue	Average	87 5	86 5	86 7
		Std	3 1	2 9	3 1
		Std	0 63	0 60	0 62
10^{-4}M	Red	Average	79 8	78 2	79 7
		Std	3 0	2 7	3 1
		Std	0 12	0 15	0 10
	Green	Average	77 7	75 2	77 5
		Std	1 8	1 6	2 0
		Std	0 20	0 15	0 21
	Blue	Average	92 7	91 1	92 3
		Std	3 2	3 0	3 4
		Std	0 23	0 16	0 22
10^{-5}M	Red	Average	75 8	74 8	75 7
		Std	2 8	2 8	3 0
		Std	0 13	0 14	0 17
	Green	Average	73 1	71 4	72 8
		Std	1 7	1 6	1 8
		Std	0 22	0 22	0 23
	Blue	Average	93 8	91 9	95 6
		Std	3 2	3 0	3 4
		Std	0 31	0 27	0 32
Buffer	Red	Average	74 8	74 0	74 6
		Std	2 3	2 4	2 3
		Std	0 32	0 29	0 30
	Green	Average	71 8	70 3	71 5
		Std	1 3	1 4	1 5
		Std	0 42	0 40	0 46
	Blue	Average	90 2	88 7	89 9
		Std	2 5	2 4	2 6
		Std	0 51	0 43	0 53

Table 6-14: Comparison of results of different selection areas for membrane 2 with adaptive blank correction employed.

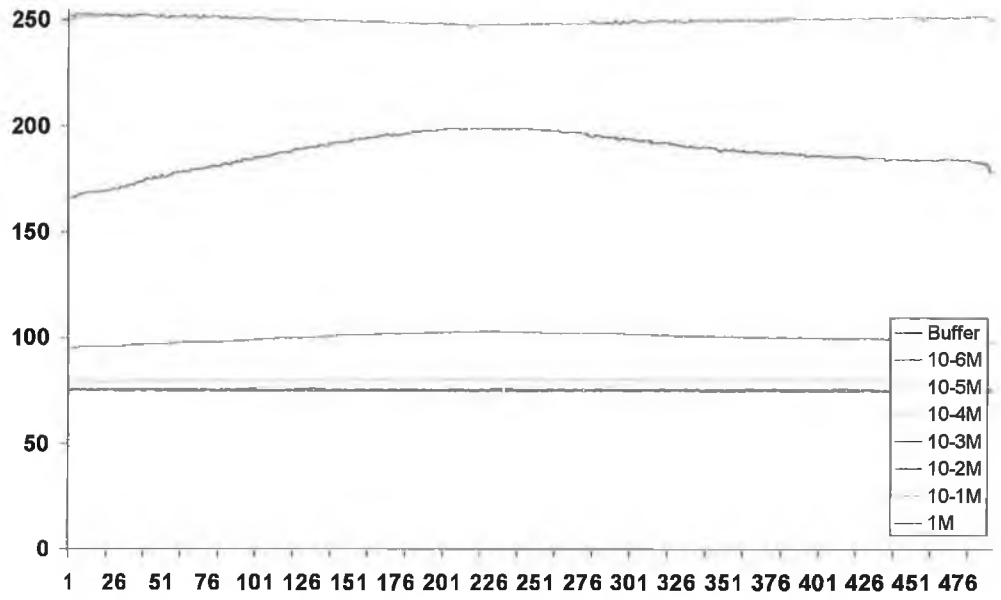

Figure 6.21: Variation of red channel intensity with different concentrations of sodium (Simple blank subtraction).
The saturated channel signal above 10^{-2}M shows a negative deviation due to the application of this method.

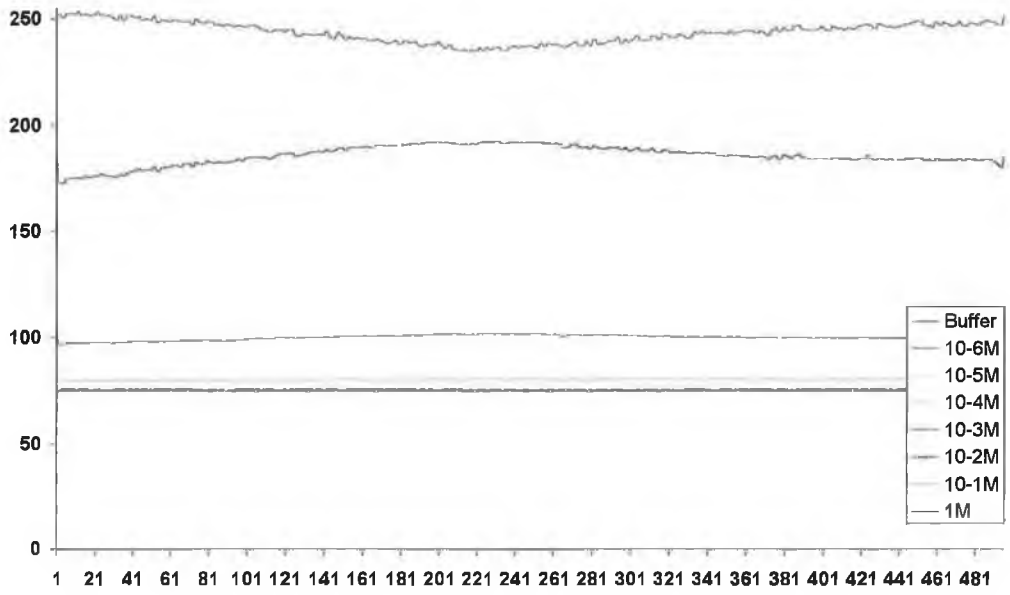

Figure 6.22: Variation of red channel intensity with different concentrations of sodium (Adaptive blank subtraction).
Again, the saturated signals above 10^{-2}M shows a negative deviation due to the application of this method.

6.9.2.3 Comparison of methods

As a method of comparison between the three methods, different portions of the picture were taken which were thought to signify high and low light intensities. These areas were whole picture, 10-110 on X and Y axes, and 200-300 on X and Y axes (Figure 6.23). The averages, standard deviation within and standard deviation between can all be seen in Table 6-12 to Table 6-14.

The differences between the red channel averages (standard deviation is not the factor being optimised with these methods) at 10^{-2}M was taken as an indicator of how well the non-uniform lighting was being corrected. For the case of the measurements performed without any blank, the difference between the maximum and minimum red channel average for the sample areas of 10-110 and 200-300 is 51.7 (Table 6-12). When we progress to the simple blank subtraction, this figure drops to 40.5 (Table 6-13). Clearly, the subtraction of the blank leads to a slightly more uniform red intensity throughout the area of the membrane picture. The standard deviations are not modified significantly.
When we move on to the adaptive blank subtraction, the difference in the red channel at 10^{-2}M is only 26.8 (Table 6-14). The difference has been reduced to nearly 50% of the original value without any blank.

While the effect of blank subtraction does not eliminate the effect of non-uniform lighting, it clearly reduces its effect. Further investigation into the characteristics of this distortion may yield a more satisfactory result.

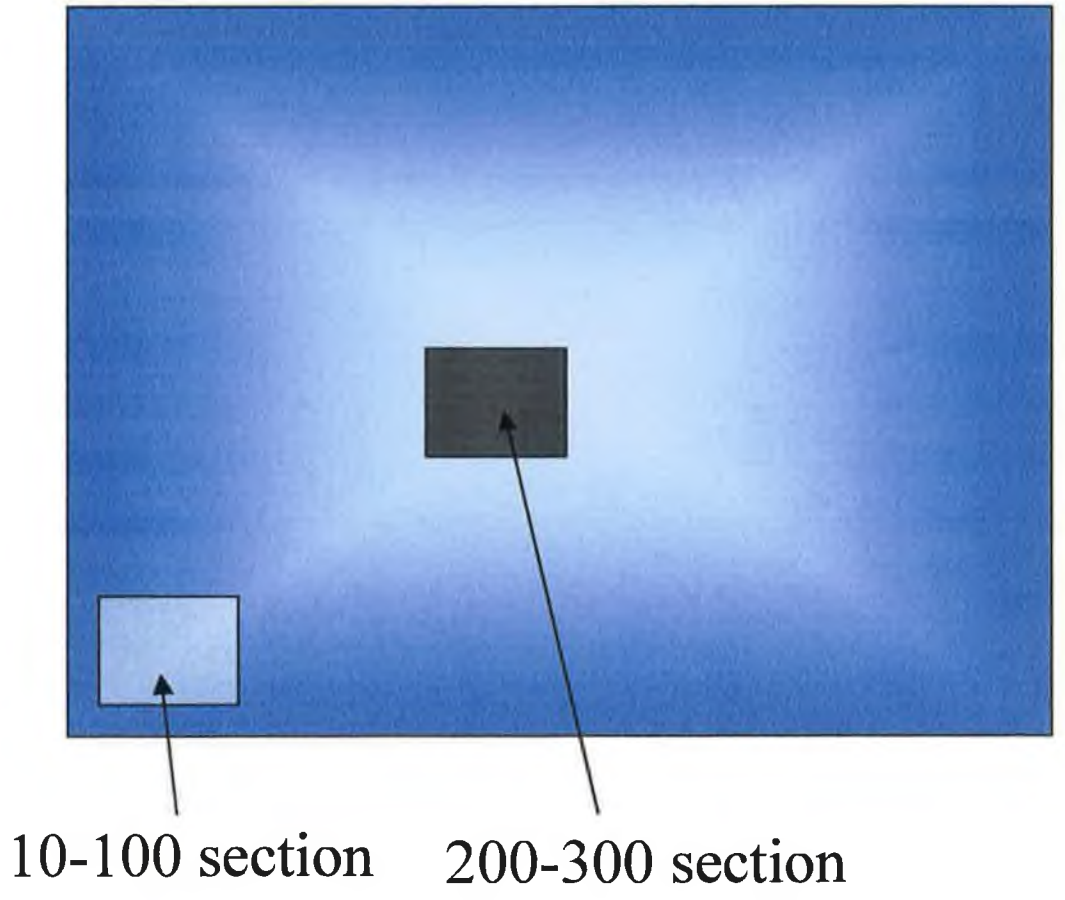

Figure 6.23: Diagram of the two sections used in the blanking comparisons in regard to the whole picture (See also Figure 6.20).

6.10 Application to 'spot' reading

In order to test the ability of the system to interpret automatically distinct spots of colour on a surface, and enzyme linked immuno-sorbent assay (ELISA) plate was used as a subject, and a picture was taken with a commercially available digital camera. The resultant picture was then used as a test to see if the software was able to separate out the parent sinusoids from the approximately square-wave data contained in the histogram.

6.10.1 Processing of ELISA Plate[a]

6.10.1.1 Generation of histogram

The histogram of the active area of the plate was performed using the graphical method of area selection outlined in the section describing this software (Figure 6.24). This array was then averaged (vertically) and passed to the Fourier transform function.

6.10.1.2 Frequency separation

The parameters required for frequency separations are crucial. It must allow the parent frequencies (When dealing with a complex real-world sample there are likely to be many parent frequencies) to be retained while removing any higher frequencies which may hinder the ability of the software to isolate distinct peaks and valleys. The following relationships were found to work quite well.

---

[a] Work was carried out in conjunction with Dr. G. Pennarun and Dr. B. Manning, BEST Centre, Dublin City University, Glasnevin, Dublin 9.

$$F_{crit} = 1.7\left(\frac{H_{size}}{N}\right)$$ Equation 6.7

Where

H_{size} = the width in pixels of the histogram

N = Number of cells visible in the selected region (Required)

In the transform, any frequencies above this critical frequency are removed and padded with zeroes. The filtered transform is then converted back into the time domain by applying an inverse Fourier transform. The resulting data is now cleaned and filtered.

The post-processed output can be seen in Figure 6.25.

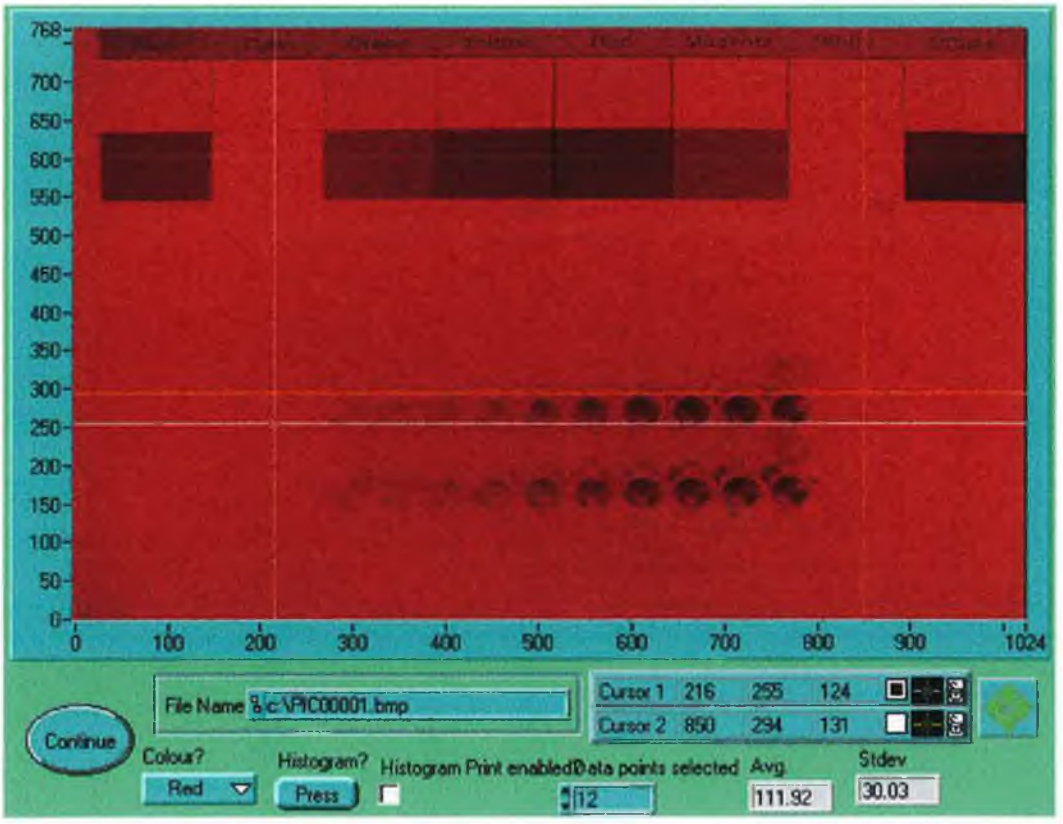

Figure 6.24: Selection of sub-array of an ELISA plate for generation of histogram to be processed by Fourier transform.

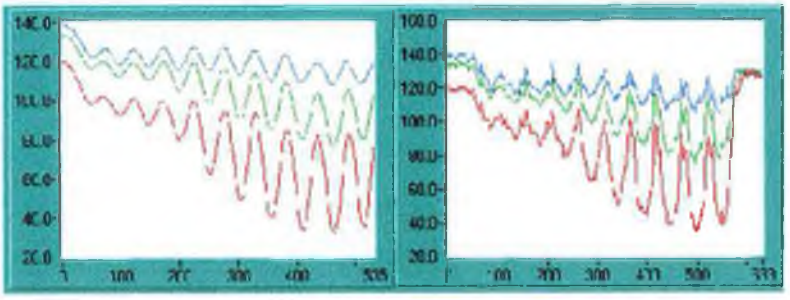

Figure 6.25: Example of a Cleaned signal (left) from the original signal (right) after using Fourier transform and frequency removal.

6.10.1.3 Generation of data

The overall reaction scheme for the ELISA system will not be discussed here. The overall interaction scheme is given in Figure 6.27.

The antigen used was Coumarin attached to BSA, the antibody used was rabbit anti-coumarin and the colour change observed was clear to yellow. The substrate used for the colour change (produced by reaction with horseradish peroxidase) was O-phenylenediamine dihydrochloride.

6.10.1.4 Data processing

Once the filtered Fourier transform has been converted back into the time domain, there is a clear maximum and minimum present for each high and low point present in the original square-wave signal. As a result of this clean signal, it is now possible for the software to perform an automatic peak find algorithm to find the location and magnitude of these peaks and valleys.

Once the peaks and valleys have been found, a standard curve can be prepared automatically (Figure 6.26). This assumes that the concentrations are uniformly distributed through the samples and they are in consecutive order.

The ability of the camera and software shown here to interrogate and quantify an full sequence of ELISA reactions allows for rapid and automatic ELISA measurements to be made. The absence of any moving parts and the ability to use micro-well arrays allow for the simultaneous measurement of very large numbers of measurements. This in turn allows for very small volumes of reagents, especially useful given the cost of enzymes and antibodies.

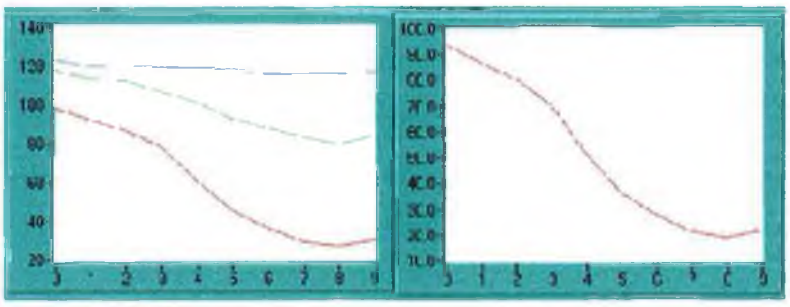

Figure 6.26: Example of an automatically generated standard curve for an ELISA calibration (From Figure 6.24 +Figure 6.25 above)

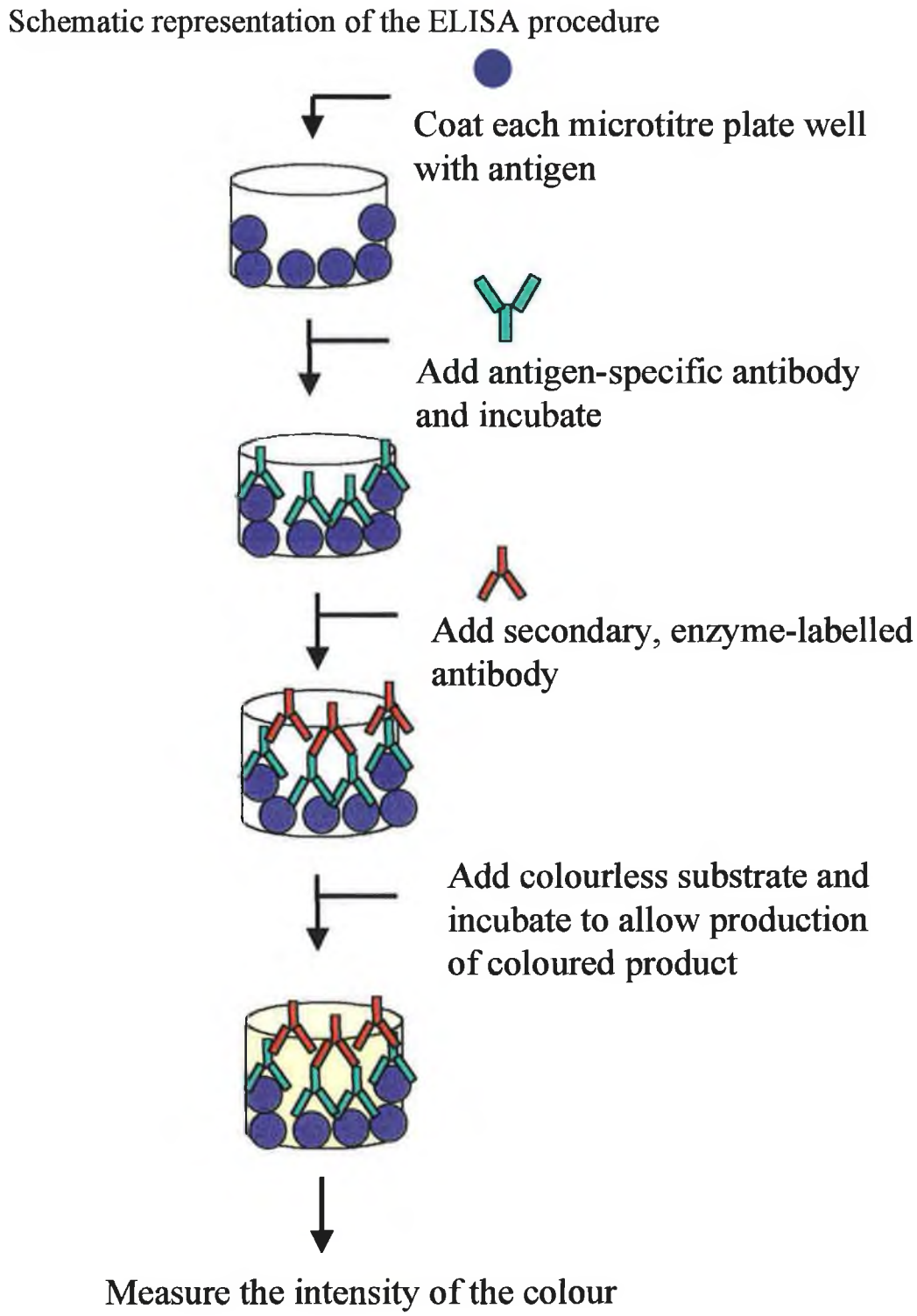

Figure 6.27: Schematic of the ELISA method used in the experiment.

6.10.1.5 Method comparison

The results of the ELISA plate with the camera and ELISA plate reader can be seen in Figure 6.28 and Figure 6.29.

Both systems seem to respond to the same trends on the ELISA plate. However, the shapes of the response curves vary slightly and the values taken from the cells at the 'edge' of the ELISA plate with the camera seem to have lower values than the others. It is believed this may be due to interference from outside the cell by ambient effects.

The map of the values recorded for the plate can be seen in Figure 6.30. this allows the shape of the two responses to be compared visually. The values recorded by the ELISA plate reader show a clear trend along the rows, with increased gradient from row 1 to row 6. The values recorded with the digital camera however reach a maximum gradient at row 4, after which it declines once more. It is possible that the effect of non-uniform lighting which was observed previously with ion-selective optode membranes could be affecting results here.

Incorporation of the blank subtraction scheme into the fourier analysis program may help to alleviate this problem. At present, the camera can be seen to generate an approximation to the actual values recorded by the plate reader. Perhaps with more careful experimental set-up, a closer match may be made.

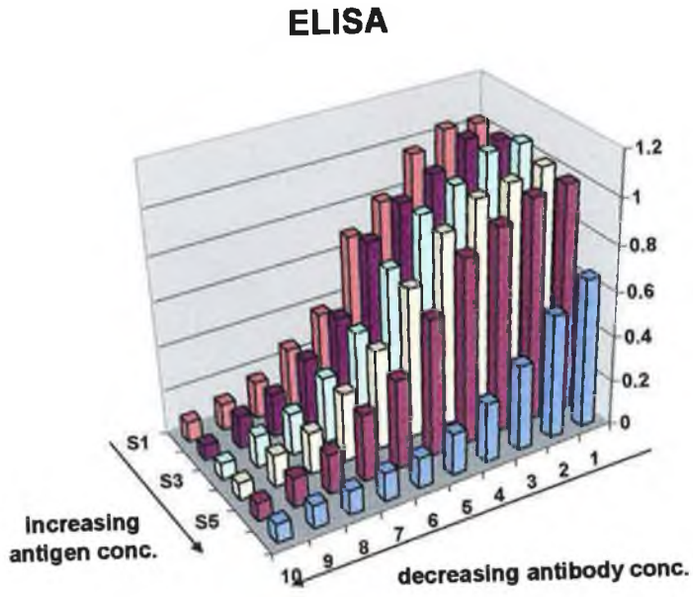

Figure 6.28: Measurement of the ELISA plate by the plate reader.

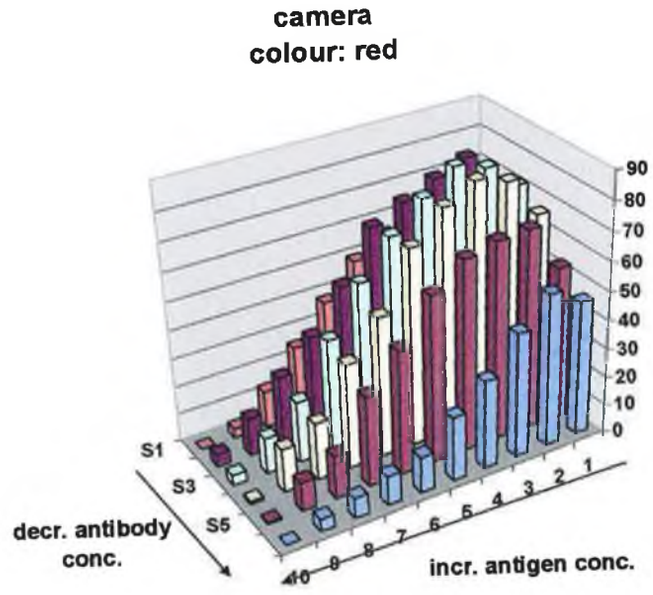

Figure 6.29: Measurement of the ELISA plate by the digital camera.

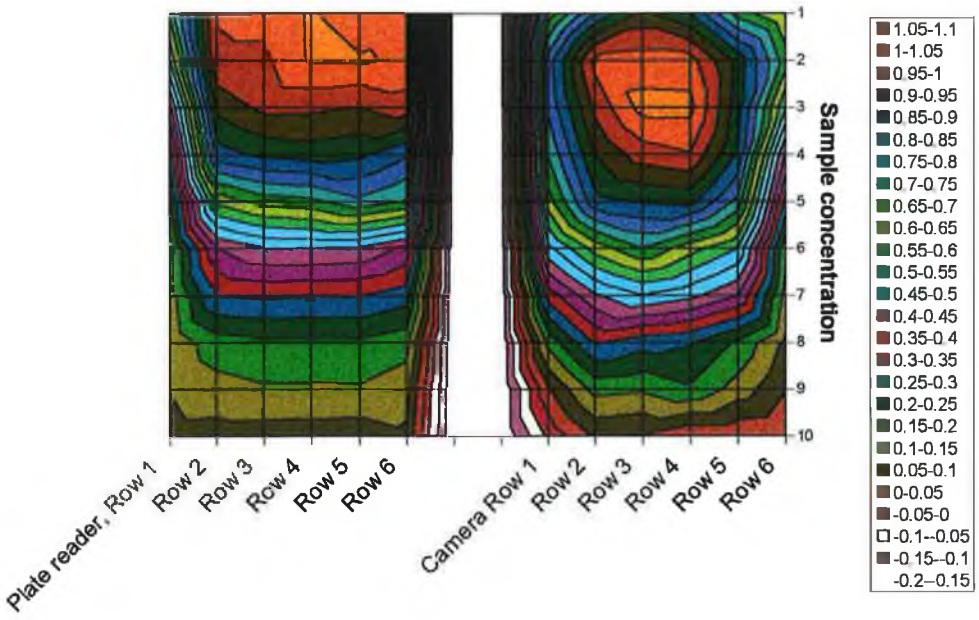

Figure 6.30: 'Map' of the values recorded by the two methods. Values recorded by the camera have been normalised to approximately match those of the plate reader.

6.10.2 Amine-sensitive discs[b]

While the results from the ELISA plate experiment are encouraging, it was decided to test the system with a more difficult task. Taking a picture of a non-optimised and somewhat non-regularly spaced experimental set-up, the same process was applied. The effects of non-uniform distribution of the sensor areas could therefore be estimated.

6.10.2.1 Sensing scheme.

Again, the detailed mechanism behind the generation of the colour in this experiment will not be discussed in detail.

In general, a calix[4]arene, complexed with Lithium was used as the sensing ligand (Figure 6.31, Figure 6.32). Attached to this ligand was an azo dye, whose colour changes upon complexation of the amines in the experiment. The calixarene complex was immobilised on filter paper and placed on the top of a small vial. The amine solutions used were placed within the vial and the colours measured.

The experiment presented here involved the measurement of amines present in the headspace above a small portion of fish flesh when stored on ice over a period of over 40 hours. Two types of fish were used, whiting and cod. The experiment was part of a series of experiments to illustrate the ability to measure the amount of amines released by the fish upon storage under different conditions.

---

[b] Work was carried out in conjunction with Dr. M. Loughran, BEST Centre, Dublin City University, Glasnevin, Dublin 9.

6.10.2.2 Histogram Generation

The picture used in this experiment consisted of several amine-selective optical discs, which change colour in proportion to the amount of amine present in the container. These are aligned roughly (Experiments were not performed for use with the Fourier processing technique) and are placed on backgrounds which are of a varying light intensity (Figure 6.39). As a result of the non-uniform nature of the placement of the discs, errors are to be expected due to variations in the sampling.

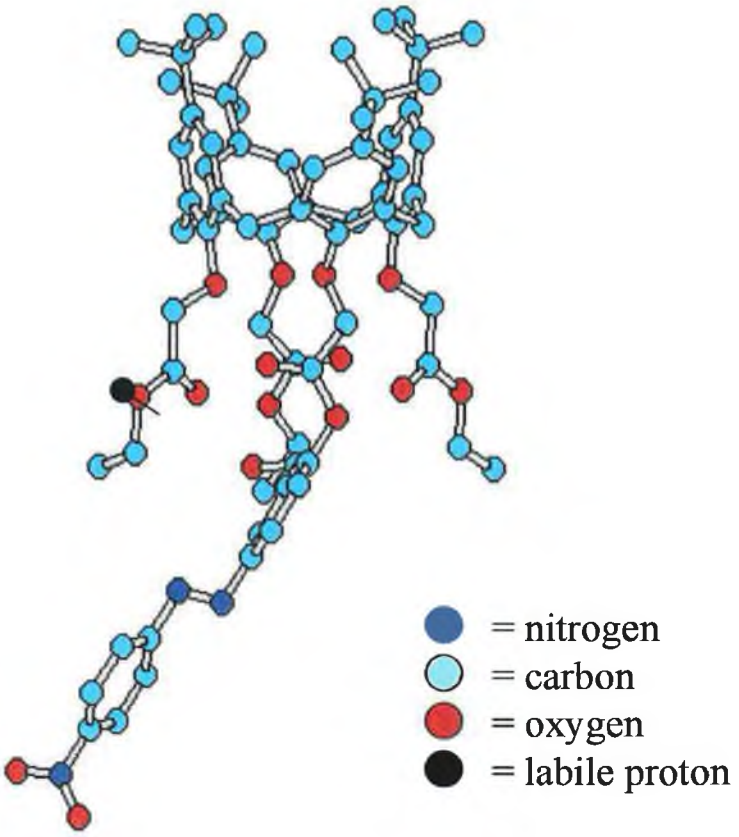

Figure 6.31: Side view of the calixarene complex used in this work (HyperChem v4.0)

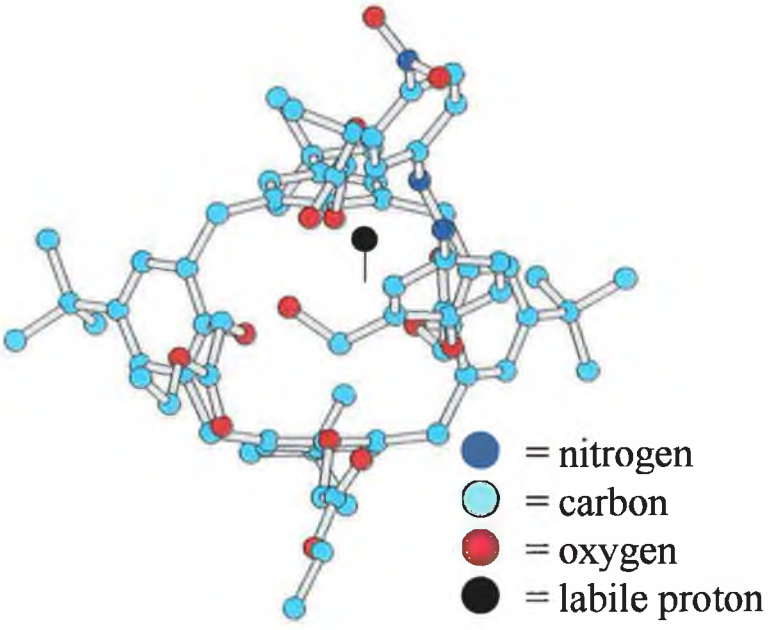

Figure 6.32: Top view of the calixarene complex used in this work (HyperChem v4.0)

6.10.2.3 Data processing

The normal method of taking small sub-sections of the picture was used with this experimental approach. The sample sizes are ca. 5,000-20,000 pixels. The software returns the mean and standard deviation of the sample selected. While this method can compensate for uneven sensor positioning, it is also prone to human errors of judgement. If any portion of the area sampled contains areas of the picture not covered by the coloured sensing discs, both the mean and standard deviation are altered.

Once the first method has been completed, an attempt was made to extract the colour intensities from the sample pictures by means of the Fourier transform sample treatment method. While the Fourier cleaned data is clearly more defined than the original (Figure 6.40), the fact that some of the immediate backgrounds to the discs are darker than the target disc and others are lighter poses a problem. Because of this, the data points required for measurements are divided among peaks and valleys. The ideal situation is where all peak maxima or minima contain the required information. In this situation, the software can automatically determine which values are sensor spots and which are not. It is therefore advisable to ensure that the background is either white or black to ensure that the data points are all either valleys or peaks respectively.

Unfortunately, since the cleaned signal contains only one point for each valley/peak, it is not possible to obtain a standard deviation. However, the calculations were found to be sensitive to the exact section of the picture taken. In order to investigate these, three different samples (boundaries shifted ± by ca. 50 pixels) were taken and analysed. Their variations can be seen in Figure 6.33, Figure 6.34, and Figure 6.35 with the actual picture used shown in Figure 6.36. While the calculations are therefore shown to be sensitive to the exact area selected, the standard deviation is less than that of the 'normal' method which was

achieved by manual selection of the disc and calculating the average and standard deviation within the sample.

The analysis was subsequently performed on a series of pictures recording the colour of an amine-sensitive disc over 43 hours exposed to a sample of fish (whiting). The results can be seen for the raw data (Figure 6.37) and for the data corrected by use of a white disc incorporated into each picture (Figure 6.38). The discs begin to respond at approximately 36 hours, and both sets of results reflect this change. In most cases, the values obtained for the colour intensities is within the range of the standard deviation of the normal method.

With this experiment, the method of Fourier transform and frequency filter worked quite well and allowed more rapid processing of data. This is in clear contrast to the method involving manual selection of the picture sections which proved laborious and time wasting. However, the uneven organisation of the discs and the problems with the disc supports highlights the importance of careful experimental design when using this approach.

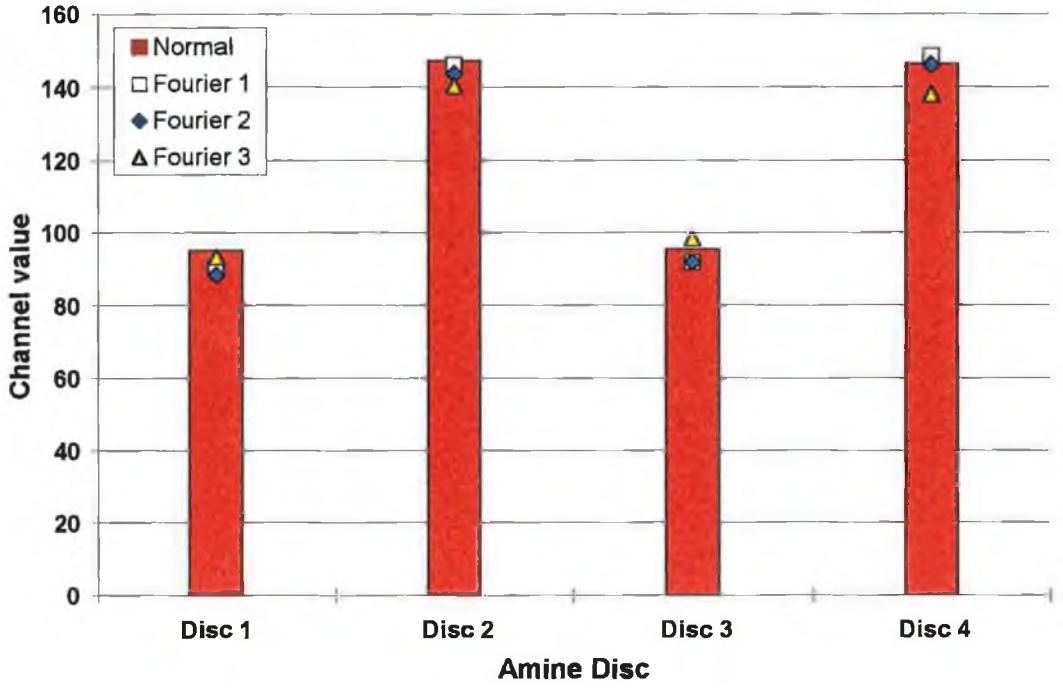

Figure 6.33: Comparison of the normal and Fourier analysis methods for red channel in the initial picture.

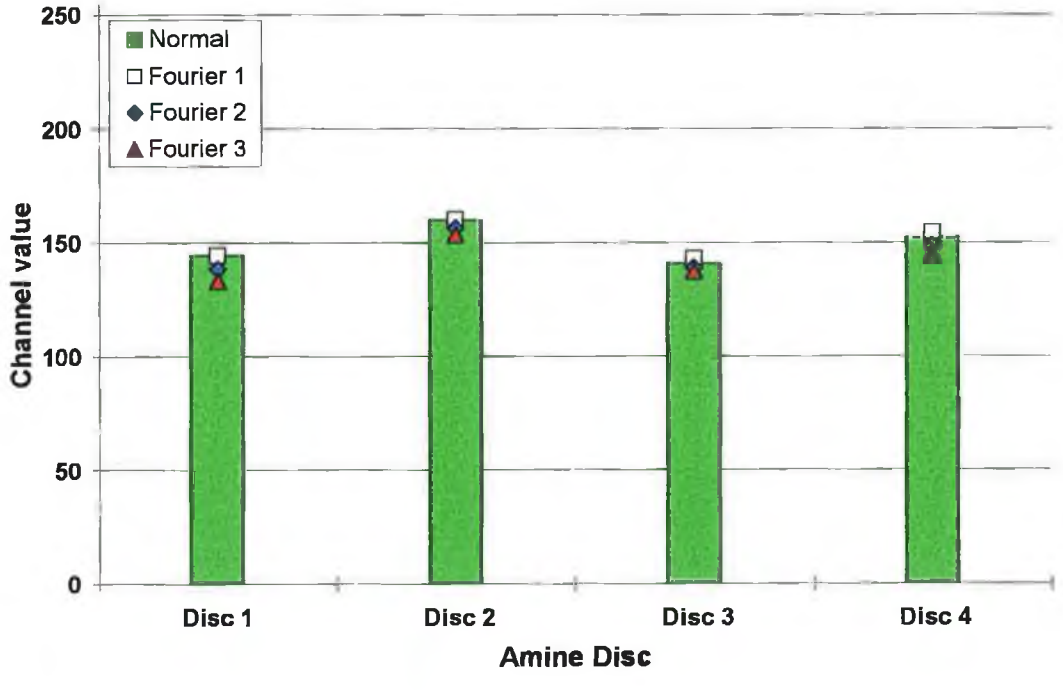

Figure 6.34: Comparison of the normal and fourier analysis methods for the green channel of the initial picture.

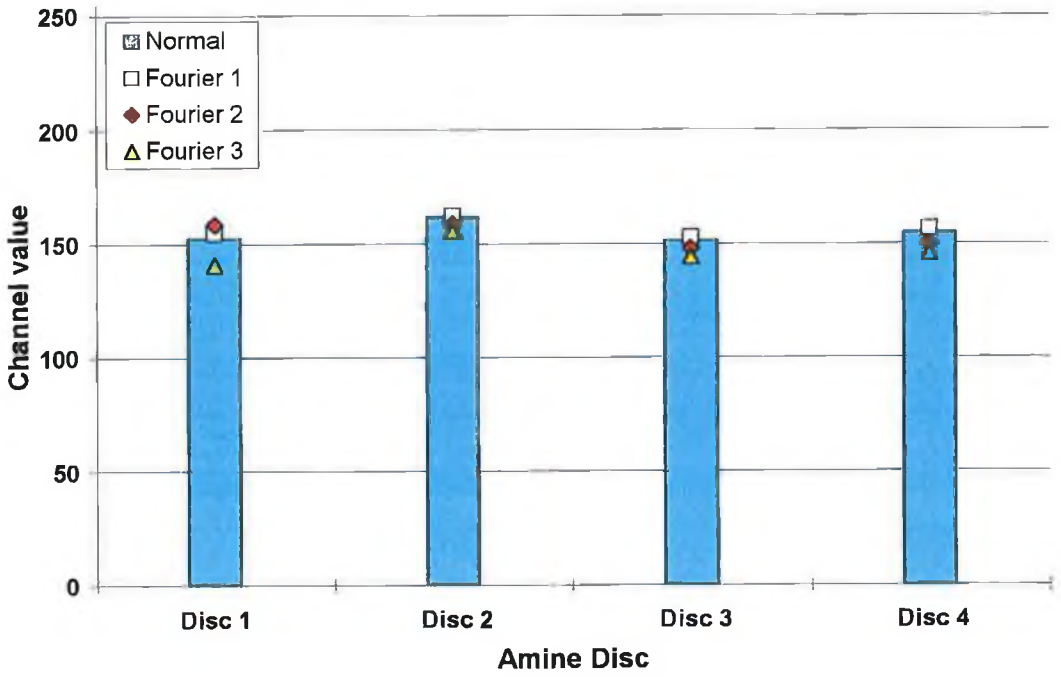

Figure 6.35: Comparison of the normal and fourier analysis methods for the blue channel of the initial picture.

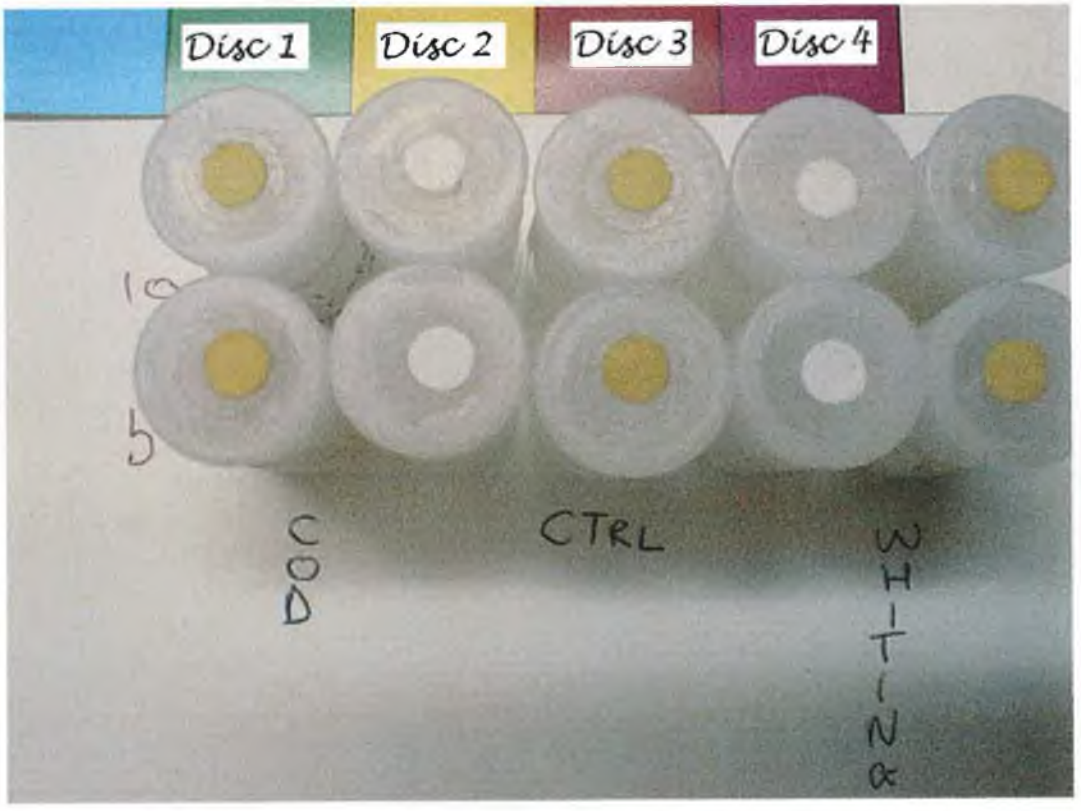

Figure 6.36: Initial picture used in comparing the two analysis methods and in the time-based response of the discs to fish samples.

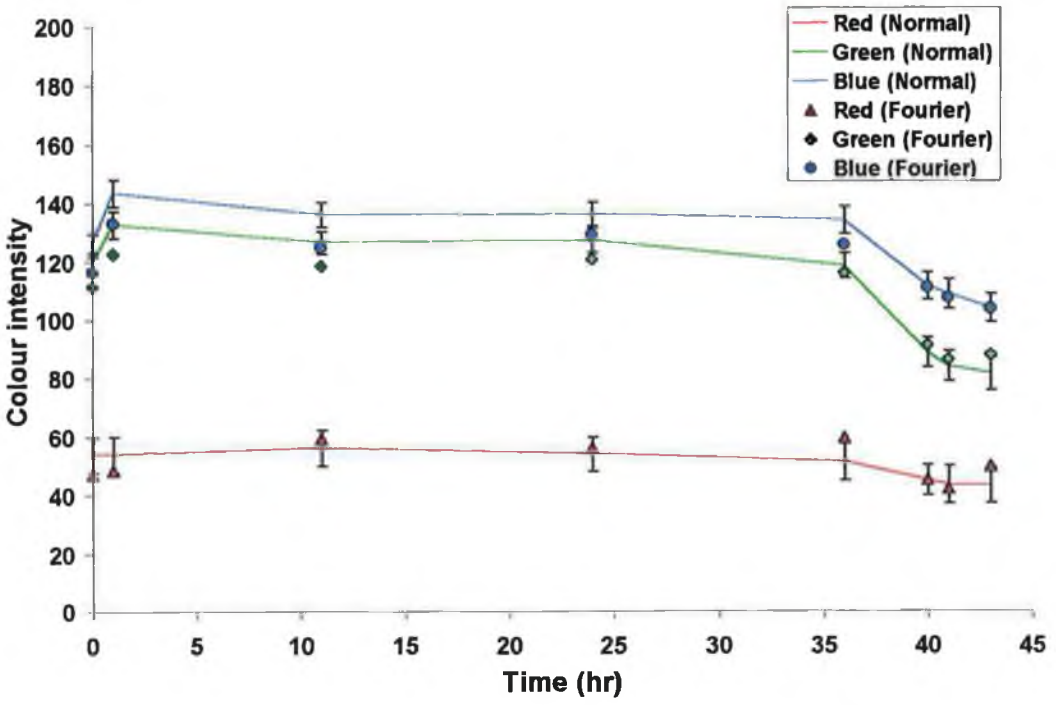

Figure 6.37: Comparison of normal and Fourier results for amine sensitive experiment monitoring whiting over a 43 hour period.
Standard deviation of the normal sampling method is shown.

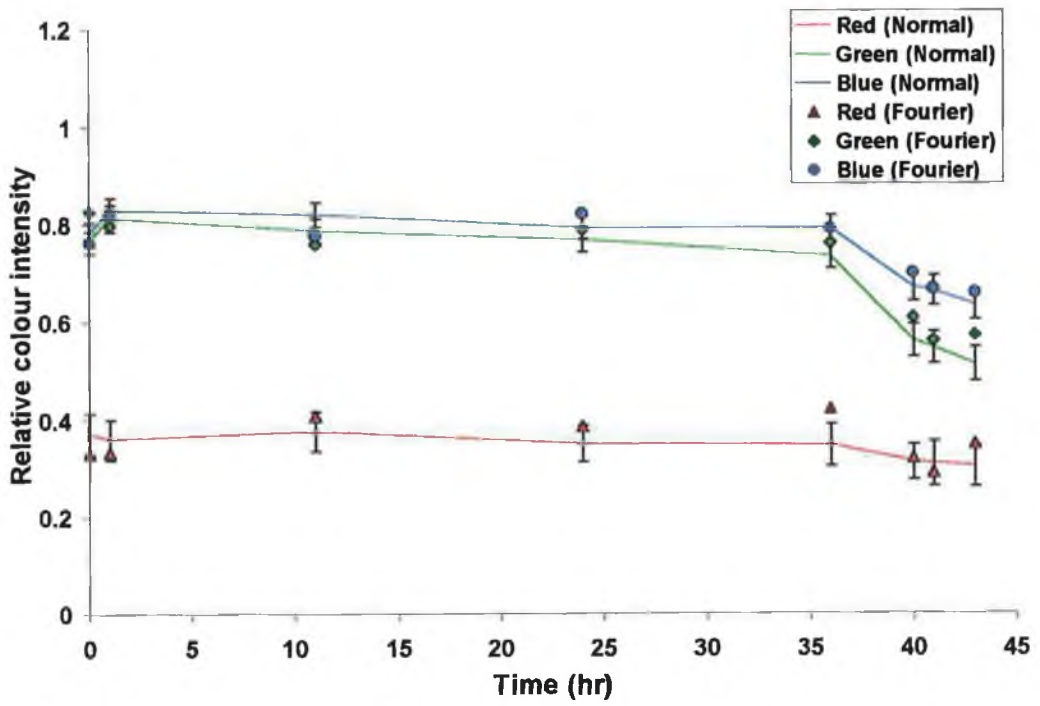

Figure 6.38: Comparison of normal and Fourier results after normalisation with respect to white blank.

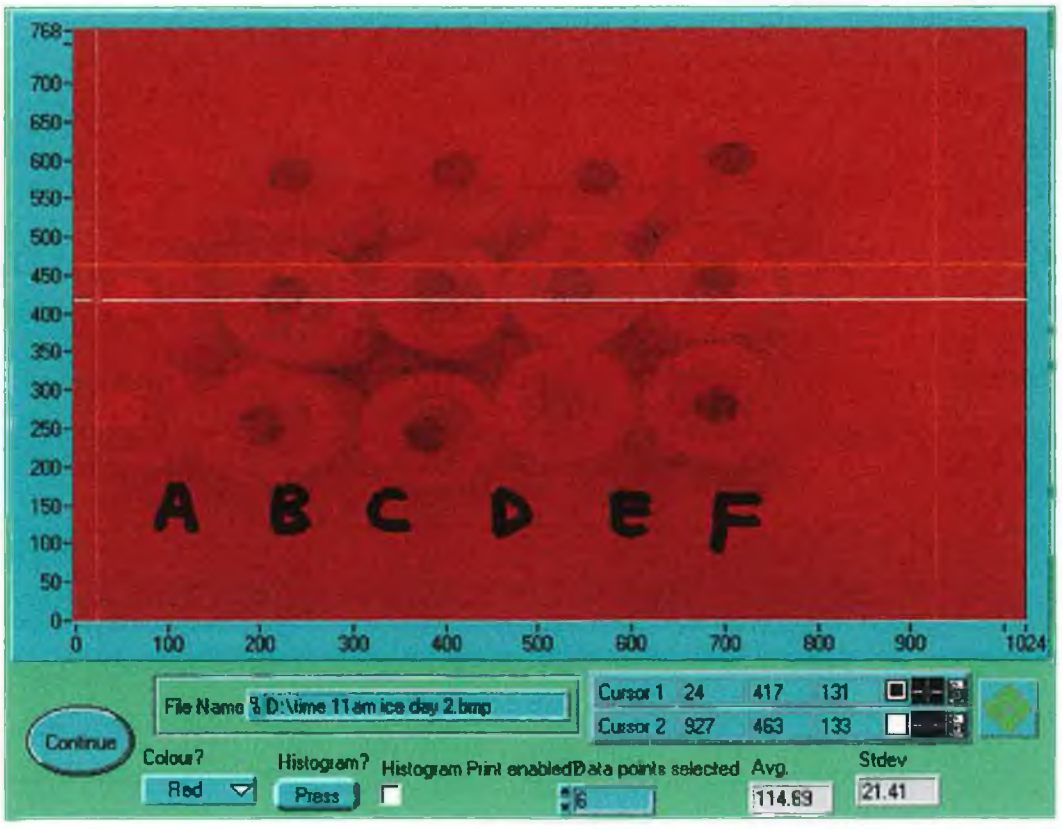

Figure 6.39: Selection of sub-array of amine-selective disc experiment

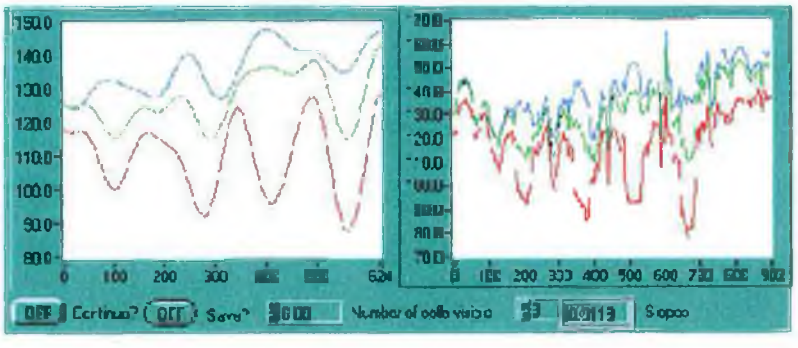

Figure 6.40: Results from Fourier clean-up of the histogram generated from Figure 23.
Peaks 1 and 3 (From left to right) on the cleaned plot for the blue channel are present as peaks whereas every other data point is present as a valley.

6.11 Conclusions

The ability of the colour CCD camera to extract and record colour data has been shown. It has also been demonstrated that the changes in colour recorded is accurate to the colour changes observed with other methods of measurement. With the sodium and calcium membranes, the principle of optode measurements has been shown. The ability to produce optodes of this type for almost every type of ion-selective electrode PVC membranes. The ability to produce sensor arrays for many analytes and the simple experimental set-up opens up the possibility for single-step screening of ions in solution. Also, this method can be applied to any existing test-strip method which generates a colour change (litmus paper for example).

Experimental arrangements must be made to reduce or eliminate the problem of non-uniform lighting which has shown itself to have an influence on the measurements made of the ion-selective optode membranes. Alternatively, further work on the blank subtraction algorithms outlined here may yield a sufficiently accurate and flexible method of correction to make this requirement unnecessary.

Finally, the ability to use a Fourier transform and subsequent frequency filter before performing the inverse Fourier transform has been shown to provide an excellent method for processing data from regularly spaced and well organised 'spot' sensors. The overall colour intensities and relationships between the individual colour channels is retained well. However, it is anticipated that non-uniform lighting will affect the ability of this method to produce reliable results.

6.12 References

[1] M. Hartnett, D. Diamond, L. Kiernan, J. Costello, *Anal Proc*, **29**, 1992, 52-53

[2] I. Nir, Y. Talmi, *Laser Focus World*, **August**, 1991, 111-120

[3] J.W. Olesik, G.M. Hieftje, *Anal. Chem*, **57**, 1985, 2049-2055

[4] Y. Wang, R.L. McCreery, *Anal. Chem.*, **61**, 1989, 2647-2651

[5] J.J. Sullivan, B.D. Quimby, *Anal. Chem*, **62**, 1990, 1034-1043

[6] N.F. Fell Jr., P.W. Bohn, *Anal. Chem.*, **65**, 1993, 3382-3388

[7] R.D. Waterbury, W. Yao, R.H. Byrne, *Anal. Chim. Acta*, **357**, 1997, 99-102

[8] E.J. Netto, J.I. Peterson, M. McShane, V. Hampshire, *Sens. and Act. B*, **29**, 1995, 157-163

[9] A. Brandenburg, *Sens. and Act. B*, **38-39**, 1997, 266-271

[10] T.E. Brook, M.N. Taib, R. Narayanswamy, *Sens and Act. B*, **38-39**, 1997, 272-276

[11] R.P. Podgorsek, T. Sterkenburgh, J. Wolters, T. Ehrenreich, S. Nischwitz, H. Franke, *Sens. and Act. B*, **38-39**, 1997, 349-352

[12] R.E. Neuhauser, U. Panne, R. Niessner, G. Petrucci, P. Cavalli, N. Omenetto, *Sens. and Act. B*, **38-39**, 1997, 344-348

[13] C.W. Earle, M.E. Baker, M.B. Denton, R.S. Pomeroy, *Trends in Analytical Chem.*, **12**, 1993, 395-403

[14] M.A. Hardisky, M.F. Gross, V. Klemas, *Biosciences*, 36, 1986, 453-460

[15] I. Amato, *Anal. Chem*, **60**, 1988, 1339-1344

[16] R.R. Klevecz, *The Scientist*, **12**, 1998, #15

[17] W.T. Lai, D.C. Bjorkquist, M.P. Abbott, A.A. Naqwi, *Meas. Sci. Technol.*, **9**, 1998, 297-308

[18] D. Slawinska, J. Slawinski, *Bioluminescence and Chemiluminescence*, **13**, 1998, 21-24

[19] *PC Pro magazine*, **15**, 1996, p96

[20] W. Boyle, G. Smith, *Bell Systems Technical Journal*, **49**, 1970, 587

[21] T.W. Woody, *Photonics Spectra*, **9**,1991, 167-172

[22] L.E. DeMarsh, E.J. Giorgianni, *Physics Today*, **9**,1989, 44-52

[23] V. Karhula., J. Reponen., J. Laurila., J. Perala., O. Tervonen., A Koivula., Computer Assisted Radiology., 1995, 1264

[24] F. Murtagh, J. Starck, M. Louys, *Imaging systems Tech.*, **9**, 1998, 38-45

[25] N.D. Memon., K. Sayood., Society of the Phot. Instr. Eng., (SPIE), 2418, 1995, 8-20

[26] U. Spichiger, W. Simon, E. Bakker, M. Lerchi, P. Bühlmann, J. Haug, M. Kuratli, S. Ozawa, S. West, *Sens. and Act. B*, **11**, 1993, 1-8

[27] U.E. Spichiger-Keller, *Sens. and Act. B.*, **38-39**, 1997, 68-77

[28] S. O'Neill, P. Kane, M.A. McKervey, D. Diamond, *Anal. Comm.*, **35**, 1998, 127-131

[29] Y. Kubo, N. Hirota, S. Maeda, S. Tokita, *Anal. Sci.*, **14**, 1998, 183-189

[30] J.W. Brault, O.R. White, *Astron. & Astrophys.*, **13**, 1971, 169-189

[31] R.N. Bracewell, *The Fourier Transform and its applications*, 1965, New York: McGraw Hill Book Company, p14

[32] S. O'Neill., S. Conway., O. Egan., D. Diamond., In Preparation